Technische Universität München
TUM School of Medicine and Health

An automated high-throughput drug screen for the identification of therapeutic vulnerabilities in pancreatic cancer cell lines

Hannah Lene Jakubowsky

Vollständiger Abdruck der von der TUM School of Medicine and Health der Technischen Universität München zur Erlangung eines

Doctor of Philosophy (Ph.D.)

genehmigten Dissertation.

Vorsitz: Prof. Dr. Thomas Korn

Betreuer: Prof. Dr. Dieter Saur

Prüfende der Dissertation:

1. Prof. Dr. Günter Schneider
2. Prof. Dr. Radu Roland Rad
3. Prof. Dr. Elisabeth Heßmann

Die Dissertation wurde am 30.11.2023 bei der TUM School of Medicine and Health der Technischen Universität München eingereicht und durch die TUM School of Medicine and Health am 09.06.2024 angenommen.

Contents

List of Tables

List of Figures

Abbreviations

%	Percentage
×g	Times gravity
°C	Degree Celsius
aCGH	array-based Comparative Genomic Hybridization
ADEX	Aberrantly differentiated endocrine exocrine
ADM	Acinar-to-ductal metaplasia
AHR	Aryl Hydrocarbon Receptor
AKT	Serine/Threonine Kinase
ARID1A	AT-Rich Interaction Domain 1A
AUC	Area under the curve
bp	Base pairs
BRAF	Rapidly accelerated fibrosarcoma isoform B
BRCA1	Breast Cancer 1, early-onset
BRCA2	Breast Cancer 2, early-onset
BSO	L-buthionine-S,R-sulfoximine
CAF	Cancer associated fibroblast
Cas	CRISPR associated
CDH1	Cadherin 1
CDKN2A	Cyclin-dependent kinase inhibitor 2A
CDX	Cell line derived xenograft
CNV	Copy number variation
CO_2	Carbon dioxide
CRISPR	Clustered Regularly Interspaced Short Palindromic Repeats
CTRP	Cancer Therapeutics Response Portal
$CuCl_2$	Copper(II) chloride
DMEM	Dulbecco’s modified Eagle’s medium
DMSO	Dimethyl sulfoxide
DNA	Deoxyribonucleic acid

dNTP	Deoxynucleotide triphosphate
DPBS	Dulbecco’s phosphate-buffered saline
DTT	1,4-Dithiothreitol
ECAR	Extracellular acidification rate
ECM	Extracellular matrix
ECOG	Eastern Cooperative Oncology Group
EDTA	Ethylenediaminetetraacetic acid
e.g.	example given
EGFR	Epidermal Growth Factor Receptor
Emax	Maximum efficacy, maximum drug effect
EMT	Epithelial-to-mesenchymal transition
ERK	Extracellular signal-regulated kinase
et al.	et alii (and others)
EtOH	Ethanol
FCS	Fetal calf serum
FDA	Food and Drug Administration
FDR	False discovery rate
Fer-1	Ferrostatin-1
Flp	Flippase
FOLFIRINOX	Fluorouracil, leucovorin, irinotecan, and oxaliplatin
FSF	frt-stop-frt
g	gram
GAP	GTPase-activating protein
GATA6	GATA Binding Protein 6
gDNA	genomic DNA
GDP	Guanosine diphosphate
GDSC	Genomics of Drug Sensitivity in Cancer
GEF	Guanine nucleotide exchange factor
GEMM	Genetically engineered mouse model

GLUT	glucose transporter
GPCR	G-protein coupled receptor
GSEA	Gene set enrichment analysis
GSH	Glutathione
GTP	Guanosine triphosphate
h	hours
H_2O	Water
HCl	Hydrochloric acid
HDAC	Histone deacetylase
HNF1A	HNF1 homeobox A
HSA	Highest single agent
IC50	Inhibitory concentration 50
IPMN	Intraductal papillary mucinous neoplasm
KRAS	Kirsten rat sarcoma virus
KRT81	Keratin 81
L	Liter
LCWGS	Low coverage whole genome sequencing
LDH	Lactate dehydrogenase
LSL	loxP-stop-loxP
M	Molar
mad	mean absolute deviation
max	maximum
MEK	Mitogen activated protein kinase
MCN	Mucinous cystic neoplasm
MDM2	Mouse Double Minute 2, E3 Ubiquitin-Protein Ligase
mg	Milligram
$MgCl_2$	Magnesium(II) chloride
min	minimum
mL	Milliliter

MLL3	Lysine Methyltransferase 2C
mM	Millimolar
mRNA	messenger-RNA
MSI	Microsatellite instability
MTOR	Mechanistic target of rapamycin kinase
multi	multiple
MUT	mutated
MYC	MYC Proto-Oncogene
n =	Number =
NA	not applicable
NAC	N-acetyl-l-cysteine
NaOH	Sodium hydroxide
nc	not calculable
Nec-1	Necrostatin-1
nM	Nanomolar
NTRK1	Neurotrophic Receptor Tyrosine Kinase 1
NTRK2	Neurotrophic Receptor Tyrosine Kinase 2
NTRK3	Neurotrophic Receptor Tyrosine Kinase 3
OCR	Oxygen consumption rate
PALB2	Partner And Localizer Of BRCA2
PanIN	Pancreatic intraepithelial neoplasia
PARP1	Poly(ADP-Ribose) Polymerase 1
PBS	Phosphate Buffered Saline
PCA	principal component analysis
PC1	first principal component
PC2	second principal component
PCR	Polymerase chain reaction
PDAC	Pancreatic ductal adenocarcinoma
PDX	Patient derived xenograft

Pdx1	Pancreatic And Duodenal Homeobox 1
PID	Pathway Interaction Database
PIK3CA	Phosphatidylinositol-4,5-Bisphosphate 3-Kinase Catalytic Subunit Alpha
pM	picomolar
PRISM	Profiling relative inhibition simultaneously in mixtures
Ptf1a	Pancreas Associated Transcription Factor 1a
qPCR	quantitative PCR
R26	Rosa26
RAF	Proto-Oncogene, Serine/Threonine Kinase
RNA	Ribonucleic acid
RNase	Ribonuclease
RNA-seq	RNA sequencing
rpm	Revolutions per minute
ROS	Reactive oxygen species
ROS1	ROS Proto-Oncogene 1, Receptor Tyrosine Kinase
RPMI	Roswell Park Memorial Institute Medium
RRID	Research Resource Identifiers
RTK	Receptor tyrosine kinase
SD	Standard deviation
SDS	Sodium dodecyl sulfate
SFM	Serum free medium
SLFN11	Schlafen Family Member 11
sgRNA	single guide RNA
SMAD4	Mothers against decapentaplegic homologue 4
SNP	Single-nucleotide polymorphism
ssGSEA	single sample Gene Set Enrichment Analysis
STR	Short Tandem Repeat
SURF1	Surfeit-Locus-Protein 1
TAE	Tris-acetate-EDTA

TCA	tricarboxylic acid
TCGA	The Cancer Genome Atlas
TE	Tris-EDTA
TGFB1	Transforming Growth Factor Beta 1
TGFBR2	Transforming Growth Factor Beta Receptor 2
TP53	Tumor Protein P53
Tris	Tris-(hydroxymethyl)-amino methane
TWIST1	Twist Family BHLH Transcription Factor 1
TWIST2	Twist Family BHLH Transcription Factor 2
µg	Microgram
µL	Microliter
µM	Micromolar
UV	Ultraviolet
V	Volt/Voltage
VCP	Valosin-containing protein, p97
vs	versus
v/v	Volume per volume
v/w	Volume per weight
WES	Whole exome sequencing
WGS	Whole genome sequencing
WGBS	Whole Genome Bisulfite Sequencing
WT	Wild-type
ZEB1	Zinc Finger E-Box Binding Homeobox 1
ZEB2	Zinc Finger E-Box Binding Homeobox 2
ZIP	Zero interaction potency

1 Abstract

Pancreatic ductal adenocarcinoma (PDAC) is a disease with a dismal prognosis and limited treatment options, encompassing to date mainly polychemotherapeutic regimens. One of the reasons for the difficulties in identifying promising targeted therapy approaches is thought to be the particularly high molecular heterogeneity found among PDAC tumors. This heterogeneity may translate into differential treatment responses and stratification of patients may be required for targeted therapies to be successful. In this study, an automated high-throughput drug screen was performed to comprehensively characterize the landscape of therapeutic vulnerabilities in a large cohort of murine pancreatic cancer cell lines. Insights derived from the murine drug screening data can be validated across species as sensitivity data for a cohort of primary human cell lines was additionally generated. Drug screening results furthermore obtained for a set of commercially available human cell lines demonstrate that our data is similarly robust to existing pharmacogenomic datasets. The high-throughput drug screening data was shown to represent a valuable resource which can be used, for example, for the identification of efficacious drugs in PDAC and of subgroup-specific vulnerabilities as well as to gain insights into drugs' mechanisms of action. The highly efficient drug NSC319726 was investigated in more detail and it could be demonstrated that while this compound was originally identified as a p53 mutant reactivator, mitochondrial respiration and copper may play important roles in the mechanism of action of this compound in our PDAC cohort. An additional application of the high-throughput drug screening data aimed at the identification of biomarkers is the integration with other large-scale datasets such as transcriptomic data. Computational approaches were used to define associations between the expression of single genes or pathway activation on the one hand and drug response on the other hand. It was shown exemplarily that the generated predictive models can be validated by different techniques such as combinatorial drug screening and CRISPR/Cas9-based negative selection screens. Overall, we present the largest dataset of drug sensitivity in pancreatic cancer known to date which provides manifold application opportunities for further studies encompassing multi-omics data integration, biomarker discovery and personalized medicine approaches.

2 Zusammenfassung

Das duktale Adenokarzinom des Pankreas (PDAC) ist eine Erkrankung mit einer schlechten Prognose und begrenzten Behandlungsmöglichkeiten, die zurzeit hauptsächlich Polychemotherapien umfassen. Einer der Gründe für die Schwierigkeiten bei der Identifizierung vielversprechender zielgerichteter Therapieansätze ist die molekulare Heterogenität von PDAC-Tumoren. Diese Heterogenität kann ein unterschiedliches Ansprechen auf verschiedene Medikamente zur Folge haben, sodass eine Stratifizierung von Patienten notwendig sein könnte, damit zielgerichtete Therapien in Zukunft erfolgreich sein können. In dieser Arbeit wird ein automatisierter Hochdurchsatz-Wirkstoffscreen vorgestellt, der mit dem Ziel durchgeführt wurde, die Vulnerabilitäten einer großen Anzahl von murinen PDAC-Zelllinien umfassend zu charakterisieren. Erkenntnisse, die aus den Wirkstoffscreens der murinen Zelllinien gewonnen wurden, können artübergreifend validiert werden, da außerdem Sensitivitätsdaten für eine Kohorte primärer humaner Zelllinien generiert wurden. Die Ergebnisse des Wirkstoffscreenings für eine Reihe kommerziell verfügbarer humaner Zelllinien zeigen, dass unsere Daten ähnlich robust sind wie die anderer bereits publizierter pharmakogenetischer Screens. Es wurde gezeigt, dass die Hochdurchsatz-Wirkstoffscreening-Daten eine wertvolle Ressource darstellen, die unter anderem für die Identifizierung von effizienten Wirkstoffen in PDAC und von Subgruppen-spezifischen Vulnerabilitäten sowie für Studien zum Wirkmechanismus von Medikamenten genutzt werden kann. Der besonders effiziente Wirkstoff NSC319726 wurde genauer untersucht und es wurde gezeigt, dass obwohl er ursprünglich als ein Reaktivator von mutiertem p53 identifiziert wurde, die mitochondriale Atmung und Kupfer eine wichtige Rolle im Wirkmechanismus dieser Substanz in unserer PDAC-Kohorte spielen könnten. Eine weitere Anwendungsmöglichkeit der Daten aus dem Hochdurchsatz-Wirkstoffscreening, die auf die Identifizierung von Biomarkern abzielt, ist die Integration mit anderen großen Datensätzen wie zum Beispiel dem Transkriptom. Mit Hilfe computergestützter Ansätze wurden Zusammenhänge zwischen der Expression einzelner Gene oder der Aktivierung von Signalwegen einerseits und dem Ansprechen auf ein Medikament andererseits definiert. Es wurde beispielhaft gezeigt, dass die generierten Modelle durch verschiedene Techniken wie kombinatorische Wirkstoffscreens und CRISPR/Cas9-basierte Screens validiert werden können. Zusammenfassend präsentieren wir den größten bisher bekannten Datensatz zu Vulnerabilitäten im Bauchspeicheldrüsenkrebs, der vielfältige Anwendungsmöglichkeiten für weitere Studien bietet, die die Integration von Multi-omics-Daten, die Identifizierung von Biomarkern und Ansätze der personalisierten Medizin umfassen.

3 Introduction

3.1 Pancreatic ductal adenocarcinoma (PDAC)

Pancreatic ductal adenocarcinoma (PDAC) is the most prevalent type of pancreatic cancer accounting for more than 90 % of all neoplastic diseases of the pancreas (Kleeff et al. 2016). PDAC is the fourth most common cause of cancer-related deaths (Siegel et al. 2022) and is projected to become the second most common cancer-related death reason by 2030 (Rahib et al. 2021). It has one of the lowest five-year survival rates of all cancers which is currently at around 11 % (Siegel et al. 2022). Risk factors that have been reported for this disease include advanced age, smoking, obesity, heavy alcohol consumption, pancreatitis and diabetes mellitus (Kleeff et al. 2016; Bosetti et al. 2012; Behrens et al. 2015; Tramacere et al. 2010; Bosetti et al. 2014; Turati et al. 2013).

There are several reasons for the particularly poor prognosis of pancreatic cancer which include late diagnosis, limited surgical and treatment options, but also a high genetic heterogeneity and a dense and complex tumor microenvironment (Frappart and Hofmann 2020; Orth et al. 2019). Due to the lack of early and specific symptoms, PDAC is usually diagnosed at advanced stages when the disease presents with distant metastases that preclude curative surgical resection (Kleeff et al. 2016; Jiang and Sohal 2023). Only 20 % of patients are eligible for curative intent surgery at the time of diagnosis (Hosein et al. 2022; Gobbi et al. 2013). Additionally, PDAC displays resistance to most treatment options such as chemotherapy, radiotherapy and molecularly targeted therapy (Kleeff et al. 2016). Nevertheless, polychemotherapies are currently the standard of care treatments for PDAC. Gemcitabine has been approved by the US FDA for pancreatic cancer therapy since 1997 (Burris et al. 1997). In 2011, the combination of folinic acid, 5-Fluorouracil, Irinotecan and Oxaliplatin (FOLFIRINOX) was shown to significantly improve overall survival compared to Gemcitabine monotherapy (Conroy et al. 2011). Due to significant toxicities associated with this polychemotherapeutic regimen, however, its application is limited to patients with an excellent ECOG performance status (Kleeff et al. 2016). Another clinical study, published in 2013, showed improved efficacy of the combination of Gemcitabine and albumin-bound Paclitaxel (Hoff et al. 2013), a regimen which despite significant toxicities can be considered as a treatment option for patients with worse performance status (Kleeff et al. 2016). Notwithstanding these advances in poly-chemotherapy treatment protocols, the prognosis for affected patients is still poor with median overall survival rates for metastatic patients remaining at approximately one year (Orth et al. 2019; Conroy et al. 2011; Hoff et al. 2013).

3.2 Biological hallmarks of PDAC

3.2.3 Pancreatic cancer progression model and genetics

The nature of the cell of origin for PDAC is currently still being debated (Backx et al. 2022). The adult pancreas consists of cells belonging to the exocrine (acinar), epithelial (ductal) and endocrine compartment and displays a high degree of plasticity (Da Silva et al. 2022; Orth et al. 2019). A process called acinar-to-ductal metaplasia (ADM) describes the transdifferentiation of acinar cells to a ductal-like phenotype (Da Silva et al. 2022). A current model suggests that PDAC can arise both from the ductal epithelium as well as acinar cells undergoing ADM (Da Silva et al. 2022; Backx et al. 2022).

Precursor lesions of invasive PDAC include pancreatic intraepithelial neoplasia (PanIN) or larger pre-neoplastic lesions such as intraductal papillary mucinous neoplasms (IPMNs) or mucinous cystic neoplasms (MCNs) (Kleeff et al. 2016). PanINs can be graded in different stages ranging from PanIN-1A and PanIN-1B that are both classified as low-grade to PanIN-2 (intermediate grade) and high grade PanIN-3 (Hruban et al. 2000).

The most common genetic alterations in PDAC are activating mutations in *Kirsten rat sarcoma virus (KRAS)* which can be found in more than 90 % of tumors (Kleeff et al. 2016). Other driver oncogenes that have been reported for smaller subsets of patients are mutated *B-Raf Proto-Oncogene* (*BRAF)* and *Phosphatidylinositol-4,5-Bisphosphate 3-Kinase Catalytic Subunit Alpha (PIK3CA)* (Witkiewicz et al. 2015; Payne et al. 2015). *KRAS* mutations are not only a very frequent alteration, but are also considered as an initial step during PDAC development (Kanda et al. 2012). In genetically engineered mouse models (GEMMs), the expression of oncogenic *KRAS* in the pancreas has been shown to be sufficient to induce and recapitulate the full spectrum of human PanIN formation followed by the development of invasive pancreatic cancer (Hingorani et al. 2003).

RAS proteins belong to the family of guanine nucleotide binding membrane-bound regulatory proteins (G proteins) and control various important intracellular downstream signalling pathways (Huang et al. 2021; Takai et al. 2001; Román et al. 2018). KRAS switches between inactive guanosine diphosphate (GDP) and active guanosine triphosphate (GTP) binding states, which is controlled by guanine nucleotide exchange factors (GEFs) and GTPase-activating proteins (GAPs) (Pylayeva-Gupta et al. 2011; Bos et al. 2007). Upon stimulation by cell surface receptors such as EGFR, other receptor tyrosine kinase receptors or G-protein coupled receptors (GPCRs), KRAS switches to its activated state and can in turn activate the rapidly accelerated fibrosarcoma (RAF)-mitogen-activated protein kinase (MEK)-extracellular regulated protein kinases (ERK) signaling pathway, phosphoinositide 3-kinase (PI3K)-protein kinase B (AKT)—mammalian target of rapamycin (mTOR) signaling pathway, and the Ral

guanine nucleotide exchange factor pathway (Gimple and Wang 2019; Pylayeva-Gupta et al. 2011; Huang et al. 2021). KRAS thereby regulates several essential cellular processes such as proliferation, cell survival and cell growth (Pylayeva-Gupta et al. 2011; Gimple and Wang 2019).

In addition to early occurring mutations in *KRAS*, *CDKN2A* alterations are also commonly found in early stages during PDAC progression (Hezel et al. 2006). *CDKN2A* encodes for two different tumour suppressor genes by using alternative reading frames, namely $p16^{INK4A}$ and $p14^{ARF}$ (Mao et al. 1995; Quelle et al. 1995; Stott et al. 1998). $p16^{INK4A}$ acts by preventing S phase entry whereas $p14^{ARF}$ inhibits MDM2, thereby activating p53 (Sharpless 2005). p53 protein in turn acts as a tumour suppressor by regulating key processes such as DNA repair, cell cycle arrest and apoptosis (Riley et al. 2008).

Mutations in *TP53* and *SMAD4* occur in later stages of PDAC progression (Hruban et al. 2000). *TP53* mutations are found in around 70 % of PDAC cases and are mostly missense mutations which lead to inactivation of the gene (Maddalena et al. 2021; Integrated Genomic Characterization of Pancreatic Ductal Adenocarcinoma 2017). *SMAD4* is another tumour suppressor gene which is inactivated in around 60 % of PDAC cases (Hahn et al. 1996; Dardare et al. 2020). It acts as an important effector of the transforming growth factor ß (TGFß) signaling pathway which is also altered in 47 % of PDAC cases and regulates cellular processes such as cell cycle arrest and apoptosis (Dardare et al. 2020; Bailey et al. 2016; Zhao et al. 2018).

In addition to mutations in *KRAS*, *CDKN2A*, *TP53* and *SMAD4*, other genes including *AT-Rich interaction domain 1A* (*ARID1A), myeloid/lymphoid or mixed-lineage leukemia protein 3 (MLL3)* and *transforming growth factor beta receptor 2 (TGFBR2)* are mutated in PDAC at a prevalence of around 10 % (Kleeff et al. 2016). Apart from these commonly mutated genes, however, PDAC is characterized by a highly heterogenous genetic landscape with a large number of infrequently mutated genes that are found in less than 2 % of tumors (Kleeff et al. 2016). These include, for example, mutations in genes belonging to DNA damage repair signalling pathways, such as *BRCA1, BRCA2* and *PALB2*, chromatin modification genes and additional oncogenes such as *MYC* (Integrated Genomic Characterization of Pancreatic Ductal Adenocarcinoma 2017; Waddell et al. 2015).

3.2.4 Molecular subtypes of PDAC

As described previously, PDAC is a highly heterogeneous disease, which complicates the development of effective treatment strategies. Novel stratification approaches are therefore

thought to be required to design therapeutic strategies for subgroups of PDAC patients (Orth et al. 2019).

Based on structural variations identified by whole genome sequencing and copy number variation (CNV) analysis, Waddell et al. have classified PDAC into four different subtypes termed stable, locally rearranged, scattered and unstable (Waddell et al. 2015). In addition, various subtyping efforts based also on transcriptomic profiling have already been undertaken (Waddell et al. 2015; Bailey et al. 2016; Connor et al. 2017; Moffitt et al. 2015; Collisson et al. 2011; Puleo et al. 2018; Chan-Seng-Yue et al. 2020). While the numbers of identified subtypes vary between the different studies, two major lineages were consistently described (Collisson et al. 2019). The commonly identified classical/canonical subtype is characterized by epithelial-like (such as *GATA6*) gene expression as opposed to the quasi-mesenchymal/basal-like subtype which displays overexpression of mesenchymal genes (Orth et al. 2019; Collisson et al. 2019). Additionally identified subtypes in different studies may be explained by varying input materials and assumptions underlying the performed analyses (Collisson et al. 2019).

The first gene expression-based subtyping study in PDAC by Collisson et al. from 2011 used microdissected epithelium from untreated, primary resected tumors and identified three molecular subtypes, namely quasi-mesenchymal, classical and exocrine-like subtypes (Collisson et al. 2011). The quasi-mesenchymal subtype with mesenchymal-associated gene expression correlated with a poorer prognosis (Collisson et al. 2011). In a second subtyping study from 2015, Moffitt et al. also identified two major subtypes which they designated basal-like and classical and, in addition, two stromal subtypes called normal and activated (Moffitt et al. 2015). In 2016, Bailey et al. assessed bulk tissue including the tumor microenvironment and defined four subtypes which they termed squamous, pancreatic progenitor, aberrantly differentiated endocrine exocrine (ADEX) and immunogenic (Bailey et al. 2016). The Cancer Genome Atlas (TCGA) Research Network demonstrated in 2017 that the immunogenic and ADEX subtypes strongly correlated with lower tumor purity (Integrated Genomic Characterization of Pancreatic Ductal Adenocarcinoma 2017). When using only high purity samples they observed a strong overlap of the squamous classification by Bailey et al. and the basal-like subtype termed by Moffitt et al. (Integrated Genomic Characterization of Pancreatic Ductal Adenocarcinoma 2017). Pancreatic progenitor (Bailey et al.) and classical (Collisson et al.) subtypes on the other hand were shown to correspond largely with the Moffitt et al. classical subtype (Integrated Genomic Characterization of Pancreatic Ductal Adenocarcinoma 2017). Contributing to the debate on whether the description of subtypes such as ADEX stem from normal tissue contaminations of examined tumors, Puleo et al. published a study in 2018 in which they investigated formalin-fixed paraffin embedded

PDACs with both high and low cellularity (Puleo et al. 2018). When analyzing only high-cellularity samples, they identified two subtypes (Basal-like and Classical) and within the Classical subtype, two subgroups which they called “Immune Classical” and “Pure Classical” (Puleo et al. 2018). An analysis based on all samples, including those with low cellularity, identified two additional stromal subtypes which they termed “Stroma Activated” and “Desmoplastic” (Puleo et al. 2018; Collisson et al. 2019). Both stromal subtypes showed characteristics of basal-like and classical subtypes, which precluded a clear conclusion on whether these are indeed independent subtypes (Puleo et al. 2018; Collisson et al. 2019). Another study from 2020 confirmed the major classification into classical and basal-like subtypes (Chan-Seng-Yue et al. 2020). These previously identified subtypes, however, were in this case subcategorized in basal-like-A and basal-like-B as well as classical-A and classical-B groups (Chan-Seng-Yue et al. 2020). In their study, Chan-Seng-Yue et al. analyzed both genomic and transcriptomic data and were able to link molecular subtypes to copy number alterations in genes such as *KRAS* and *GATA6* (Chan-Seng-Yue et al. 2020).

These different subtypes are suggested to be associated with prognostic outcome as well as differential drug responsiveness (Frappart and Hofmann 2020). In a study published by Collisson et al., the quasi-mesenchymal subtype was shown to be more sensitive to Gemcitabine treatment and more resistant to Erlotinib compared to the classical subtype (Collisson et al. 2011). The group of Prof. Saur has also shown that MEK inhibition is more effective in the classical subtype (Falcomatà et al. 2022). Furthermore, in a clinical trial published in 2018, patients with different transcriptomic and genomic subtypes have been reported to show varying responses to chemotherapy (Aung et al. 2018). In this study, *GATA6* expression was significantly increased in classical subtype tumors and was proposed as a robust biomarker for distinguishing the two major subtypes, thereby also potentially predicting chemosensitivity (Aung et al. 2018). Further clinical trials are ongoing that will evaluate the response to chemotherapy in different molecular subtypes (e.g. clinical trial NCT04469556: Pancreatic Adenocarcinoma Signature Stratification for Treatment (PASS-01)) (Knox et al. 2022; Hosein et al. 2022). In another study, immunohistochemistry-based subtype stratification using *HNF1A* and *KRT81* expression was likewise shown to be associated with different responses to chemotherapy and these were thus proposed as potential biomarkers (Muckenhuber et al. 2018).

Therefore, even though these subtype classifications do not yet routinely inform clinical decisions, their potential value has already been shown. Overall, the identification of subgroups with differential responses to therapy and the stratification of such patient cohorts for personalized medicine approaches could potentially help to improve the so far dismal prognosis of PDAC patients.

3.2.5 Metastasis

As discussed previously, one of the features of PDAC which are causative for its high lethality is the high prevalence of metastasis at the time of diagnosis (Kleeff et al. 2016). Common sites of metastasis include the peritoneum, the liver and lungs (Yachida et al. 2012). In a mouse model of pancreatic cancer that allows for tracing of pancreatic epithelial cells, a strong association of dissemination and epithelial-to-mesenchymal transition (EMT) has been demonstrated (Rhim et al. 2012). EMT is defined as the biological process in which polarized epithelial cells lose their cell-cell adhesion and convert to a mesenchymal phenotype characterized by an enhanced migratory capacity and invasiveness which promotes metastasis (Kalluri and Weinberg 2009). EMT plays a role during implantation, embryogenesis, organ development, tissue regeneration and organ fibrosis as well as cancer progression and metastasis (Kalluri and Weinberg 2009). Several studies have demonstrated that the majority of circulating tumor cells express both epithelial and mesenchymal markers which strengthens the notion of an essential role of EMT during carcinoma dissemination (Wang et al. 2017; Khoo et al. 2015; Yu et al. 2013; Thiery and Lim 2013). EMT is regulated by complex networks of epigenetic modifications, transcription factors and transcription regulators (Wang et al. 2017). Among EMT-inducing transcription factors, *snail family zinc finger protein SNAI1 and 2 (SNAI1/2), zinc finger E-box-binding homeobox 1 and 2 (ZEB1/2)* and *twist-related protein 1 and 2 (TWIST1/2)* are common examples (Wang et al. 2017; Orth et al. 2019). In addition, microRNAs have also been shown to regulate EMT (Orth et al. 2019; Giovannetti et al. 2017; Mees et al. 2010).

In pancreatic cancer, the quasi-mesenchymal subtype which is associated with mesenchymal gene expression is linked to a poorer prognosis, which may further point to the involvement of mesenchymal gene expression programs in accelerated metastasis formation (Orth et al. 2019; Moffitt et al. 2015; Collisson et al. 2011).

3.2.6 Tumor microenvironment

Another hallmark of PDAC which is highly relevant for the paucity of effective treatment strategies is the dense desmoplastic tumor stroma which can constitute up to 90 % of the tumor volume (Orth et al. 2019; Dougan 2017). PDAC stroma is highly heterogeneous, consisting of acellular and cellular components including extracellular matrix (ECM), vasculature, growth factors and cytokines, cancer-associated fibroblasts (CAFs), myofibroblasts, pancreatic stellate cells and immune cells (Feig et al. 2012; Hosein et al. 2020). It is thought to be a critical mediator of PDAC progression, during which it can constantly change its composition, thereby further increasing the complex nature of the

desmoplastic reaction (Feig et al. 2012; Hosein et al. 2020). This so-called microenvironment of PDAC is recognized as an important contributor to therapy resistance (Feig et al. 2012), as for example the ECM can act as a physical barrier to effective drug delivery (Hosein et al. 2020). PDAC vasculature is a complex system and is also characterized by desmoplasia-associated hypovascularization which generates a hypoxic environment (Hosein et al. 2020; Orth et al. 2019). The existence of multiple CAF subtypes with distinct roles further increases the complexity of the tumor microenvironment, which additionally complicates the development of effective therapies (Hosein et al. 2020).

3.3 Precision medicine approaches for PDAC treatment

As discussed in Chapter 3.2.3, genomic analyses have revealed a high heterogeneity of mutations in PDAC that occur at a low prevalence or are patient-specific in nature (Sivapalan et al. 2022).

The previously described molecular profiling and subtyping efforts have also revealed that up to 25 % of pancreatic cancers present with an actionable molecular alteration (Aguirre et al. 2018; Bailey et al. 2016; Biankin et al. 2012; Collisson et al. 2011; Lowery et al. 2017; Moffitt et al. 2015; Waddell et al. 2015; Witkiewicz et al. 2015; Pishvaian et al. 2020). By definition, actionable mutations are alterations for which a specific therapy exists, which is supported by clinical or strong preclinical evidence (Pishvaian et al. 2020). The largest identified fraction of these actionable alterations in pancreatic cancer can be assigned to DNA damage response pathways (Pishvaian et al. 2020). These have been recognized as beneficial biomarkers, since it has been shown that patients with DNA mismatch-repair lesions or high microsatellite instability (MSI-H) show robust responses to immune checkpoint inhibitors (Le et al. 2015; Pishvaian et al. 2020; Nevala-Plagemann et al. 2020). Additionally, patients with germline *BRCA1* or *BRCA2*-mutated pancreatic cancer are eligible for treatment with the PARP inhibitor Olaparib (Golan et al. 2019; Pishvaian et al. 2020).

Another example of targeted therapy approaches in pancreatic cancer informed by molecular markers is the treatment of patients that display *ROS1, NTRK1, NTRK2*, and *NTRK3* gene fusions with TRK inhibitors (Laetsch et al. 2018; Pishvaian et al. 2020; Nevala-Plagemann et al. 2020). Evidence also suggests that patients with $BRAF^{V600E}$ mutated pancreatic cancer benefit from treatment with RAF-MEK-targeted therapy (Guan et al. 2018; Pishvaian et al. 2020).

In 2020, Pishvaian et al. published the results of the so-called “Know Your Tumor (KYT)” programme in the USA in which they analyzed more than 1000 patients with pancreatic

cancer regarding, among others, the overall survival outcomes for patients with actionable molecular alterations who were treated with a molecularly matched therapy (Pishvaian et al. 2020). They could demonstrate that for a subgroup of pancreatic cancer patients, median overall survival rates could indeed be significantly improved by treatments with molecularly matched therapeutics (Pishvaian et al. 2020). This study therefore provides a strong indication that precision oncology approaches for pancreatic cancer patients are a valuable strategy for improving overall survival rates for this disease, that molecular profiling should be performed routinely and should also guide prospective clinical trials (Pishvaian et al. 2020). Nevertheless, only 25 % of pancreatic cancer patients have an actionable molecular alteration, which also shows the limitations of these approaches (Pishvaian et al. 2020).

3.4 Pancreatic cancer models and high-throughput drug screens

The promise of precision medicine approaches for pancreatic cancer treatment has already been discussed in Chapter 3.3. The stratification of patients based on their molecular profiles could be guided by specific biomarkers of drug sensitivity. Large-scale screening efforts in preclinical model systems have already been undertaken to identify such putative predictors of drug response (Barretina et al. 2012; Garnett et al. 2012; Haverty et al. 2016; Seashore-Ludlow et al. 2015; Yu et al. 2016; Niepel et al. 2019; Corsello et al. 2020).

Preclinical model systems of pancreatic cancer include patient-derived cell line and xenograft models, organoid cultures as well as cell lines derived from genetically engineered mouse models (GEMMs) (Kleeff et al. 2016).

A classic GEMM for PDAC is based on the expression of oncogenic *KRAS*^{G12D} in the pancreas using the *Cre/loxP* system and the pancreas-specific promoter *Pdx1* or *Ptf1a* (Hingorani et al. 2003). In this model, *KRAS*^{G12D} expression is prevented by an upstream stop cassette flanked by *loxP* sites (*loxP-stop-loxP, LSL*), except in the pancreas where this stop cassette is excised by Cre recombinase under the control of the pancreas-specific promoters (Hingorani et al. 2003). Using this system, *KRAS*^{G12D} expression could be shown to be sufficient to induce and recapitulate the full spectrum of human PanIN formation leading to the development of invasive pancreatic cancer and even the formation of metastases (Hingorani et al. 2003). Since then, GEMMs have also been generated for other altered genes such as *Cdkn2a*, *Trp53*, *Smad4, Snail* or *Braf* (Aguirre et al. 2003; Hingorani et al. 2005; Bardeesy et al. 2006; Paul et al. 2023; Rad et al. 2013). Next-generation mouse models using a dual-recombinase system also allow for sequential genetic changes in tumor cells or to target the microenvironment, thereby further improving the recapitulation of the human disease (Schönhuber et al. 2014). The Saur laboratory has derived more than 1000

novel mouse PDAC cell lines from such GEMMs with various different genotypes including the expression of oncogenes with or without the additional deletion of tumour suppressors (Mueller et al. 2018). Genes that are altered exclusively or in combination with others in these cell lines include *Kras*, *Braf*, *Pik3ca*, *Trp53, Smad4*, *Cdkn2a* and *Tgfßr2*. These cell lines therefore comprehensively capture the genetic landscape of PDAC. In addition, they display different morphologies that reflect classical/epithelial, quasi-mesenchymal and mesenchymal subtypes with different degrees of expression of EMT signatures and range from differentiated to more undifferentiated histology (Mueller et al. 2018). These cell lines represent a valuable resource that can greatly extend the limited number of available human PDAC cell line models.

Interspecies differences between mouse- and human-derived models are expected and must be considered. These can represent a major limitation of GEMMs, whereas an important advantage is the low passage number of this cell line cohort. Commercially available human cell lines have commonly been subjected to prolonged culturing periods and previous studies have demonstrated that the passage number can affect the cell line's characteristics (O'Driscoll et al. 2006). Passage number can for instance influence cellular morphology, growth rate and gene expression (O'Driscoll et al. 2006) and lead to accumulation of somatic mutations over time (Kim et al. 2017). Therefore, these cell lines may not accurately retain key characteristics of their tumors of origin (Garcia et al. 2020).

As both human and murine cell lines are relatively cost effective and easy to maintain and propagate (Garcia et al. 2020), they can, for example, conveniently be used for the screening of large compound libraries in a high-throughput fashion. Nevertheless, they remain simplified models with additional limitations. For example, they cannot account for effects of the tumor microenvironment and the interaction with the immune system, which has been shown to play an important role in promoting tumor growth and metastasis as well as providing a barrier to drug delivery (Feig et al. 2012). Patient-derived xenograft models (PDX) are an alternative, which is generated by direct implantation of human tumor tissue into immunocompromised mice (Garcia et al. 2020) and can more closely reflect the tumor-stroma interaction in patients (Bleijs et al. 2019). On the other hand, these *in vivo* PDX models are labor and cost intensive and only a small number of drugs can be tested (Bleijs et al. 2019; Hirt et al. 2022).

More recently, 3D organoid models have emerged which can strike a balance between the advantages of 2D cell lines and PDX models (Hirt et al. 2022; Baker et al. 2016; Boj et al. 2015). These organoid models have been shown to convincingly represent drug response in patients (Hirt et al. 2022; Tiriac et al. 2018; Driehuis et al. 2019). Extensive PDAC organoid biobanks are currently being established and drug screening experiments have also already been undertaken (Hirt et al. 2022). Limitations in resources, however, still hamper the scale

of these efforts due to the relatively high cost of components needed for organoid growth, especially Matrigel (Hirt et al. 2022).

2D models, as discussed previously, are currently more cost effective and are the basis for several large-scale screening datasets that are publicly available. The CCLE (Barretina et al. 2012; Pharmacogenomic agreement between two cancer cell line data sets 2015), the GDSC (Iorio et al. 2016; Picco et al. 2019), the CTRP CTD^2 (Seashore-Ludlow et al. 2015; Rees et al. 2016) and the PRISM Repurposing datasets represent major efforts that provide drug response data for large sets of molecularly characterized cancer cell lines from diverse tumor entities, which are available on the DepMap Portal (https://depmap.org/portal/).

The idea of the DepMap project is to integrate the drug sensitivity data which is available for hundreds of cancer cell line models with other large-scale datasets to identify genetic targets for therapeutic development and to allow for stratification of patients responding to specific therapies based on biomarkers (https://depmap.org/portal/depmap/) (Tsherniak et al. 2017; Meyers et al. 2017; Behan et al. 2019; Krill-Burger et al. 2023).

Using the CCLE cohort, for example, Barretina et al. combined gene expression and drug sensitivity data to demonstrate associations between *AHR* expression and MEK inhibitor efficacy and between *SLFN11* expression and sensitivity to topoisomerase inhibitors, respectively (Barretina et al. 2012). Characterization of this cohort has since then been expanded and now includes RNA sequencing, whole-exome sequencing, whole-genome sequencing, reverse-phase protein array, reduced representation bisulfite sequencing, microRNA expression profiling and global histone modification profiling data as well as abundance measures of metabolites (Ghandi et al. 2019). Integration of these data with drug sensitivity profiles as well as short hairpin RNA knockdown and CRISPR-Cas9 knockout data has revealed potential targets for cancer drugs and associated biomarkers (Ghandi et al. 2019).

Loss-of-function genetic screens using CRISPR-Cas9 or shRNA knockdown based approaches can complement drug response measurements by adding another layer of vulnerability profiling in cancer cells (Meyers et al. 2017; Tsherniak et al. 2017; Hart et al. 2015; Behan et al. 2019). Ideally, biomarker studies could therefore be independently supported by both drug response and gene fitness measurements (Gonçalves et al. 2020). Furthermore, integration of these two types of datasets, loss-of-function genetic screens and drug response, has also been shown to allow for investigations of drug mechanism of action (Gonçalves et al. 2020; Deans et al. 2016).

The reproducibility and the utility of such large-scale screening efforts have been the matter of scientific discussion (Pharmacogenomic agreement between two cancer cell line data sets 2015; Haibe-Kains et al. 2013; Bouhaddou et al. 2016; Niepel et al. 2019). Harmonization of

methodologies has been addressed as an important factor to improve the comparability of different large-scale screening efforts (Pharmacogenomic agreement between two cancer cell line data sets 2015). In that regard, several confounders of drug response measures have already been identified. Media composition and volume as well as cell density are such variables that can influence the biology of drug response (Haverty et al. 2016; Hafner et al. 2016). These factors as well as intrinsic differences can cause variability in growth rate which has been identified as a strong confounder of drug response measures (Niepel et al. 2019; Hafner et al. 2016; Hafner et al. 2017). Cell density has also been shown to in turn influence media condition and the strength of autocrine signaling which can affect drug response in certain cases (Wilson et al. 2012; Yonesaka et al. 2008; Niepel et al. 2019). Batch effects caused by the microtiter plates (Niepel et al. 2017) and edge effects caused by temperature gradients and uneven evaporation of media (Bushway et al. 2010) are additional variables that can have an influence on drug screening results (Niepel et al. 2019).

Quality control measures that can help standardization and comparability of the results include the authentication of cell lines and compounds, standardization of consumables such as media, additives and plates and the use of automation to improve reliability (Niepel et al. 2019).

Analytical tools to calculate sensitivity values can also lead to discordant results between studies (Pharmacogenomic agreement between two cancer cell line data sets 2015). Most commonly, cells are exposed to drug treatment using different concentrations and cell viability is measured at the end of the assay (Hafner et al. 2016). The cell viability counts in the presence of drug are then divided by control counts (e.g. untreated samples) and fitted to a sigmoidal curve from which parameters of drug sensitivity can be derived (Hafner et al. 2016). These include the concentration of drug at which the cell count is half the control (IC50), the normalized cell count at the highest drug concentration (Emax) and the area under the dose response curve (AUC) (Fallahi-Sichani et al. 2013; Sebaugh 2011; Hafner et al. 2016). As discussed previously, these metrics, IC50, Emax and AUC, can vary extensively depending on the number of cell divisions occuring during the course of an assay (Hafner et al. 2016). Hafner et al. have developed growth-rate independent metrics to correct for this confounder and make drug response data more reproducible and therefore more useful for personalized medicine approaches developed across different institutes (Hafner et al. 2016). Other approaches to harmonize drug response data obtained from different assays and institutes have likewise been published (Pharmacogenomic agreement between two cancer cell line data sets 2015; Pozdeyev et al. 2016; Bouhaddou et al. 2016).

3.5 Drug resistance and combinatorial drug screens

Another pitfall of the precision medicine approaches discussed in Chapter 3.3 is the emergence of drug resistance towards targeted therapy (Vasan et al. 2019). Various mechanisms have been suggested to lead to drug resistance, including tumor burden, tumor heterogeneity, physical barriers, the immune system and therapeutic pressure (Vasan et al. 2019).

Drug resistance mechanisms can be categorized into intrinsic resistance, where the patient is unresponsive from the beginning of the treatment, and acquired resistance which develops over time after the patient initially showed a response (Jin et al. 2022). Acquired resistance can for example arise from changes in gene expression or from mutations, which can occur in the drug target itself ("on-target" mutations), upstream or downstream of the drug target or in parallel pathways (Jin et al. 2022). Tumors can for example circumvent MAPK inhibition by activating PI3K/AKT signaling (Villanueva et al. 2010). Intra-tumoral heterogeneity poses further challenges as selection of resistant subclones can occur under therapeutic pressure (Jin et al. 2022; McGranahan and Swanton 2017).

One way to combat both intrinsic and acquired drug resistance is the use of combinations of compounds (Al-Lazikani et al. 2012; Lopez and Banerji 2017; Jaaks et al. 2022; Jin et al. 2022). An additional advantage of the use of combination regimens is that the compounds can potentially also be used at lower doses as if used as monotherapies, thereby reducing treatment side-effects (Ianevski et al. 2020; Wood et al. 2014; Law et al. 2003).

The vast number of possible combinations that could be tested, however, poses a major challenge to this approach (Jin et al. 2022). Functional genetic approaches can help to rationally design combination regimens (Jin et al. 2022). The identification of genes whose inactivation leads to lethality to a compound can help to determine reasonable drug targets for combinations (Jin et al. 2022; Mainardi et al. 2018; Prahallad et al. 2012).

Rational approaches can also encompass strategies based on comprehensive knowledge of involved signaling pathways (Jin et al. 2022). The finding that BRAF inhibition leads to mutations in downstream players of the MAPK pathway has for example resulted in the use of BRAF-MEK combination strategies (Flaherty et al. 2012). In addition, computational approaches have also been applied to predict which drug combinations have the highest potential for being effective (Jin et al. 2022; Menden et al. 2019; Lotfollahi et al. 2023).

High-throughput combinatorial drug screening is another established strategy to identify potentially synergistic drug combinations (Jin et al. 2022; Ianevski et al. 2020; Holbeck et al. 2017; Jaaks et al. 2022), i.e. combinations with higher than expected effects (Ianevski et al.

2020). Synergy or the opposing antagonism can be quantified by comparing the drug combination response which is observed in the experiment to the response which is expected according to a reference model assuming no interaction between the drugs (Ianevski et al. 2020).The most commonly used reference models comprise the Bliss (BLISS 1939), Loewe (LOEWE 1953), HSA (highest single agent) (Berenbaum 1989) and ZIP (Zero interaction potency) (Yadav et al. 2015) models. A useful drug combination identified in clinical trials across a patient cohort can, however, also stem from patient-to-patient variability in response to single drugs (Palmer and Sorger 2017). By giving more than one drug, chances are increased that the patient receives a drug that is effective (Palmer and Sorger 2017).

A recently published high-throughput combinatorial drug screen analyzing breast, colon and 29 pancreatic cancer cell lines has shown that overall, synergy between drugs is the exception rather than the rule, with 7.2 % of the tested combination – pancreatic cancer cell line pairs being classified as synergistic (Jaaks et al. 2022). Subsets of combinations were generally more synergistic, including combinations comprising the compound Navitoclax and inter-pathway targeting of MAPK and PI3K pathways (Jaaks et al. 2022). Jaaks et al. could also demonstrate that biomarkers can be identified for specific combinations such as an association between low *CDH1* gene expression and irinotecan plus AZD7762 sensitivity in pancreatic cancer cell lines (Jaaks et al. 2022). The results from this high-throughput combinatorial drug screen showed that targeted drugs with weak single-agent activity are most likely to be synergistic and could provide a basis for the design of rational combinatorial therapies, of future screens and for novel computational approaches (Jaaks et al. 2022).

3.6 Aim of this work

PDAC is a disease with an urgent unmet clinical need. The prognosis for PDAC patients is dismal and treatment options are currently very limited (Kleeff et al. 2016). One of the major challenges to the development of effective therapeutic strategies is the high molecular heterogeneity that can be found among PDAC tumors (Juiz et al. 2019). It is suggested that the identification of subgroups of patients with specific vulnerabilities and associated biomarkers allowing for stratification would be an important strategy to successfully employ targeted therapy approaches and improve the poor prognosis of PDAC patients (Kleeff et al. 2016). The aim of this thesis was therefore to characterize the landscape of therapeutic vulnerabilities in a large cohort of pancreatic cancer cell lines by high-throughput drug screening. The drug response data was correlated with the molecular characteristics of the cell lines to identify associations and biomarkers of drug sensitivity or resistance. To validate the results obtained from a computational pipeline integrating the drug screening data and transcriptomics data, combinatorial drug screens and CRISPR/Cas9-based screens were performed.

4 Materials

4.1 Technical equipment

Table 4-1: Technical equipment.

Device	Source
AxioCam HRc	Carl Zeiss AG, Oberkochen, Germany
Analytical balance A 120 S	Sartorius AG, Göttingen, Germany
Analytical balance BP 610	Sartorius AG, Göttingen, Germany
Analytical balance	Kern & Sohn GmbH, Balingen, Germany
Autoclave 2540 EL	Tuttnauer Europe B.V., Breda, Netherlands
Autoclave Systec VX-75	NeoLab Migge GmbH, Heidelberg, Germany
Centrifuge 220R	Hettich AG, Bäch, Switzerland
Centrifuge Rotina 380	Hettich AG, Bäch, Switzerland
Centrifuge Multifuge X3 FR	Thermo Fisher Scientific, Inc., Waltham, MA, USA
CO_2 incubator HERAcell ® 240	Thermo Fisher Scientific, Inc., Waltham, MA, USA
CO_2 incubator HERAcell® VIOS 160i	Thermo Fisher Scientific, Inc., Waltham, MA, USA
CO_2 incubator HERAcell® VIOS 250i	Thermo Fisher Scientific, Inc., Waltham, MA, USA
CO_2 incubator MCO-17AIC	Sanyo Denki K.K., Moriguchi, Japan
CyBio® FeliX pipetting platform	Analytik Jena, Jena, Germany
CyBio FeliX head R 96/250 µL	Analytik Jena, Jena, Germany
Cytomat™ 24C automated incubator	Thermo Fisher Scientific, Inc., Waltham, MA, USA
Electrophoresis power supply Power Pac 200	Bio-Rad Laboratories, Munich
Electrophoresis power supply EV243	Consort bvba, Turnhout, Belgium
Electrophoresis system, Compact L/XL	Biometra, Göttingen, Germany
Gel Doc™ XR+ system	Bio-Rad Laboratories GmbH, Munich, Germany
Glass ware, Schott Duran®	Schott AG, Mainz, Germany
Heating cabinet	Memmert GmbH + Co. KG, Schwabach, Germany
Heidolph Rotamax 120 Orbital Shaker	Heidolph Instruments GmbH & Co. KG, Schwabach, Germany
Horizontal shaker	Henning Berlin GmbH, Berlin, Germany
Laminar flow hood	BDK Luft- und Reinraumtechnik GmbH, Sonnenbühl-Genkingen, Germany
Laminar flow hood	Envair Technology, Cheshire, UK
Luminescence microplate reader CLARIOstar	BMG Labtech Germany, Ortenberg, Germany
Luminescence microplate reader FLUOstar OPTIMA	BMG Labtech Germany, Ortenberg, Germany
Luminescence microplate reader Infinite® 200 PRO	Tecan Group AG, Männedorf, Switzerland
Magnetic stirrer, Ikamag®RCT	IKA®Werke GmbH & Co. KG, Staufen, Germany
Magnetic stirrer, 2mag magnetic motion	2mag AG, Munich, Germany
Masterflex EasyLoad pump	Thermo Fisher Scientific, Inc., Waltham, MA, USA
Microscope Axio Imager.A1	Carl Zeiss AG, Oberkochen, Germany
Microscope Axiovert 25	Carl Zeiss AG, Oberkochen, Germany

Device	Source
Microscope DM LB	Leica Microsystems GmbH, Wetzlar, Germany
Microscope Primovert	Carl Zeiss AG, Oberkochen, Germany
Microtome Microm HM355S	Thermo Fisher Scientific, Inc., Waltham, MA, USA
Microwave	GGV Handelsgesellschaft mbH & Co. KG, Kaarst, Germany
Microwave	Imtron GmbH, Ingolstadt, Germany
Multidrop™ Combi Reagent Dispenser	Thermo Fisher Scientific, Inc., Waltham, MA, USA
Multiway Valve	Thermo Fisher Scientific, Inc., Waltham, MA, USA
Nanophotometer®	Implen GmbH, Munich, Germany
Neubauer chamber (Hemocytometer)	Lo-Labortechnik GmbH, Friedrichsdorf, Germany
pH meter 521	WTW Wissenschaftlich-Technische Werkstätten GmbH, Weilheim, Germany
Pintool 96-well	Analytik Jena, Jena, Germany
Pipettes Eppendorf	Research Plus, Eppendorf AG, Hamburg, Germany
Pipetus Hirschmann	Hirschmann Laborgeräte GmbH & Co. KG, Eberstadt, Germany
Pump, Masterflex L/S® Easy-Load®	Cole-Parmer Instrument Company, Vernon Hills, USA
Qubit®2.0 Fluorometer	Invitrogen GmbH, Karlsruhe, Germany
Schott Duran Glass ware	Schott AG, Mainz, Germany
Schutzmagazin OL3316-11-200	Analytik Jena, Jena, Germany
Seahorse XFe96 Analyzer	Agilent, CA, USA
Spectrophotometer NanoDrop 1000	Peqlab Biotechnologie GmbH, Erlangen, Germany
Spinnaker automation system	Thermo Fisher Scientific, Inc., Waltham, MA, USA
Stripettor™ Plus pipetting controller	Corning Inc., Corning, NY, USA
Stripettor™ Ultra pipetting controller	Corning Inc., Corning, NY, USA
Thermocycler T100	Bio-Rad Laboratories GmbH, Munich, Germany
Thermocycler TOne	Biometra GmbH, Göttingen, Germany
Thermocycler Tpersonal	Biometra GmbH, Göttingen, Germany
Thermocycler Tprofessional	Biometra GmbH, Göttingen, Germany
Thermomixer compact	Eppendorf AG, Hamburg, Germany
UVP UVsolo touch Transilluminator	Analytik Jena, Jena, Germany
UVsolo TS Imaging System	Biometra, Göttingen, Germany
Vortex Genius 2	Scientific Industries, Inc., Bohemia, USA
Washing station 96 DW	Analytik Jena, Jena, Germany
Water bath 1003	GFL Gesellschaft für Labortechnik mbH, Burgwedel, Germany

4.2 Disposables

Table 4-2: Disposables.

Disposable	Supplier
Cell scrapers	TPP Techno Plastic Products AG, Trasadingen, Switzerland
BioPur® Safe-lock reaction tubes	Eppendorf AG, Hamburg, Germany
CELLSTAR® Cell culture multiwell plate (6, 12, 24, 48, 96 well)	Greiner Bio-One GmbH, Kremsmünster, Austria
CELLSTAR® Cell culture flasks (T25, T75, T175)	Greiner Bio-One GmbH, Kremsmünster, Austria
Costar® Multiple Well Cell Culture Plates (6, 12, 24, 48, 96 well)	Corning Inc., Corning, NY, USA
Cell strainer 70 µm	Greiner Bio-One, Kremsmünster, Austria
Combitips BioPur®	Eppendorf AG, Hamburg, Germany
Conical tubes, 15 mL	Greiner Bio-One, Kremsmünster, Austria
Conical tubes, 50 mL	Greiner Bio-One, Kremsmünster, Austria
CryoPure tubes	Sarstedt AG & Co., Nümbrecht, Germany
CyBio-Tips OL-3811-25-637-S	Analytik Jena, Jena, Germany
Dispensing Cassette Standard Tube	Steinle Labtechnology, Rodgau, Germany
Dispensing Cassette for Multidrop™ Combi Reagent Dispenser	Thermo Fisher Scientific, Inc., Waltham, MA, USA
Disposable scalpels	Feather Safety Razor Co., Ltd., Osaka, Japan
DNA LoBind® Tubes	Eppendorf AG, Hamburg, Germany
Filtermax vacuum filtration system	TPP Techno Plastic Products AG, Trasadingen, Schwitzerland
Filtropur S 0.2	Sarstedt AG & Co., Nümbrecht, Germany
Masterblock	Greiner Bio-One, Kremsmünster, Austria
Microtome blades S35 and C35	Feather Safety Razor Co., Ltd., Osaka, Japan
Microplate 384-well, barcoded	Greiner Bio-One, Kremsmünster, Austria
Pasteur pipettes	Hirschmann Laborgeräte GmbH & Co. KG, Eberstadt, Germany
Parafilm M	Brand GmbH & Co. KG, Wertheim, Germany
PCR reaction tubes	Brand GmbH + Co. KG, Wertheim; Eppendorf AG, Hamburg, Germany
Plate covers	Greiner Bio-One, Kremsmünster, Austria
Pipette tips	Sarstedt AG & Co., Nümbrecht, Germany
Reaction tubes, 0.5 mL, 1.5 mL and 2 mL	Eppendorf AG, Hamburg, Germany
Robotic reservoirs, convoluted bottom	Thermo Fisher Scientific, Inc., Waltham, MA, USA
Seahorse XFe96 FluxPak	Agilent Technologies, Santa Clara, USA
Serological pipettes	Sarstedt AG & Co., Nümbrecht, Germany
Single use needles Sterican® 27 gauge	B. Braun Melsungen AG, Melsungen, Germany
Tissue Culture Dish (6cm, 10cm, 15cm)	TPP AG, Trasadingen, Switzerland
Western Blotting Filter Paper	Bio-Rad Laboratories GmbH, Munich, Germany

4.3 Chemicals, reagents and solutions

Table 4-3: Chemicals, reagents and solutions.

Reagent	Supplier
1,4-Dithiothreitol (DTT)	Carl Roth GmbH + Co. KG, Karlsruhe, Germany
2-Desoxy-D-glucose	Sigma-Aldrich Chemie GmbH, Taufkirchen, Germany
2-Mercaptoethanol, 98%	Sigma-Aldrich Chemie GmbH, Taufkirchen, Germany
2-Propanol	Sigma-Aldrich Chemie GmbH, Taufkirchen, Germany
Advanced DMEM/F-12	Thermo Fisher Scientific, Inc., Waltham, MA, USA
Agarose	Carl Roth GmbH & Co. KG, Karlsruhe, Germany
Agarose Standard for DNA/RNA electrophoresis	Carl Roth GmbH & Co. KG, Karlsruhe, Germany
Aqua B. Braun	B.Braun Melsungen AG, Melsungen, Germany
Buthionine sulfoximine (BSO)	Sigma-Aldrich Chemie GmbH, Taufkirchen, Germany
Cherry-pick compound library	Selleck Chemicals GmbH, Planegg, Germany
Copper chloride ($CuCl_2$)	Sigma-Aldrich Chemie GmbH, Taufkirchen, Germany
Crystal violet	Sigma-Aldrich Chemie GmbH, Taufkirchen, Germany
D-galactose	Thermo Fisher Scientific, Inc., Waltham, MA, USA
D-glucose	Thermo Fisher Scientific, Inc., Waltham, MA, USA
Dimethyl sulfoxide	Sigma-Aldrich Chemie GmbH, Taufkirchen, Germany
Dimethyl sulfoxide for cell culture	AppliChem, Darmstadt, Germany
dNTP mix, 10mM each	Sigma-Aldrich Chemie GmbH, Taufkirchen, Germany
Dodecylsulfate Na-salt in pellets (SDS)	Serva Electrophoresis GmbH, Heidelberg, Germany
Dulbecco's phosphate buffered saline (1x DPBS) solution	Sigma-Aldrich Chemie GmbH, Taufkirchen, Germany
Dulbecco's Modified Eagle Medium (DMEM) - High Glucose	Sigma-Aldrich Chemie GmbH, Taufkirchen, Germany
Dulbecco's Modified Eagle Medium (DMEM) – No glucose	Thermo Fisher Scientific, Inc., Waltham, MA, USA
Ethanol (100%)	Merck KGaA, Darmstadt, Germany
Ethidium Bromide	Sigma-Aldrich Chemie GmbH, Taufkirchen, Germany
Fetal calf serum (FCS)	Sigma-Aldrich Chemie GmbH, Taufkirchen, Germany
Fetal calf serum (FCS), dialyzed	Thermo Fisher Scientific, Inc., Waltham, MA, USA
Gel loading dye, blue	New England Biolabs GmbH, Frankfurt am Main, Germany
GeneRuler™ 100bp DNA ladder	Thermo Fisher Scientific, Inc., Waltham, MA,

Reagent	Supplier
	USA
Histoclear	Carl Roth GmbH & Co. KG, Karlsruhe, Germany
Hydrochloric acid (HCl)	Merck KGaA, Darmstadt, Germany
KAPA HiFi HotStart ReadyMix	Roche Deutschland Holding GmbH, Grenzach-Wyhlen, Germany
Keratinocyte SFM	Thermo Fisher Scientific, Inc., Waltham, MA, USA
Multiscribe Reverse Transcriptase	Thermo Fisher Scientific, Munich, Germany
MycoRAZOR®	Biontex Laboratories GmbH, Munich, Germany
N-acetyl cysteine (NAC)	Sigma-Aldrich Chemie GmbH, Taufkirchen, Germany
Penicillin/Streptomycin	Sigma-Aldrich Chemie GmbH, Taufkirchen, Germany
Polybrene	Sigma-Aldrich Chemie GmbH, Taufkirchen, Germany
Proteinase K, recombinant, PCR grade	Roche Deutschland Holding GmbH, Grenzach-Wyhlen, Germany
Puromycin	Sigma-Aldrich Chemie GmbH, Taufkirchen, Germany
Random Hexamers	Hoffmann-La Roche, Basel, Switzerland
RNase-free DNase set	Qiagen GmbH, Hilden, Germany
RNase Inhibitor	Thermo Fisher Scientific, Inc., Waltham, MA, USA
RPMI 1640 Medium, GlutaMAX™ Supplement	Thermo Fisher Scientific, Inc., Waltham, MA, USA
Seahorse XF Base Medium	Agilent Technologies, Santa Clara, USA
Seahorse XF Calibrant Solution	Agilent Technologies, Santa Clara, USA
Sodium hydroxide solution (NaOH)	Merck KGaA, Darmstadt, Germany
TaqMan RT Buffer	Thermo Fisher Scientific, Inc., Waltham, MA, USA
TE buffer, pH 8.0	AppliChem GmbH, Darmstadt, Germany
Triton® X 100	Sigma-Aldrich Chemie GmbH, Taufkirchen, Germany
Trypan Blue	Thermo Fisher Scientific, Inc., Waltham, MA, USA
TrypLE™ Express	Thermo Fisher Scientific, Inc., Waltham, MA, USA
Trypzean	Sigma-Aldrich Chemie GmbH, Taufkirchen, Germany
Tween® 20	Carl Roth GmbH & Co. KG, Karlsruhe, Germany
V&P Solution	V&P Scientific, Inc., San Diego, CA, USA

4.4 Buffers and solutions

Table 4-4: Buffers and solutions.

Name	Ingredients
Freezing medium	Dulbecco´s Modified Eagles Medium, high glucose 10% (v/v) FCS 10% (v/v) DMSO
10x Gitschier's buffer	670 mM Tris, pH 8.8 166 mM $(NH_4)_2SO_4$ 67 mM $MgCl_2$
Soriano lysis buffer	0.5 % TritonX-100 1 % 2-Mercaptoethanol 1x Gitschier's buffer 400 µg/ml Proteinase K (add prior to use)

4.5 Kits

Table 4-5: Kits.

Kit	Company
Caspase-Glo® 3/7 Assay	Promega, Walldorf, Germany
CellTiter-Glo® Luminescent Cell Viability Assay	Promega, Walldorf, Germany
GenElute™ Mammalian Genomic DNA Miniprep Kit	Sigma-Aldrich, Taufkirchen, Germany
Monarch PCR & DNA Cleanup Kit	New England Biolabs, Ipswich, USA
RNeasy Mini Kit	Qiagen, Hilden, Germany
QIAGEN Blood & CellCulture DNA MaxiKit	QIAGEN GmbH, Hilden, Germany
QIAmp DNA Micro Kit	Qiagen, Hilden, Germany

4.6 Compounds used for high-throughput drug screening

All compounds used in the high-throughput drug screen were purchased as 10 mM stocks in DMSO or H_2O from Selleck Chemicals LLC (Houston, TX, USA) and are listed in Table 4-6.

Table 4-6: Compounds used for high-throughput drug screening.

Product Name	Target detailed	Target broad	Pathway
(+)-JQ1	Epigenetic Reader Domain	Epigenetic Reader Domain	Epigenetics
4E1RCat	eIF4E/eIF4G interaction	eIF4E/eIF4G interaction	PI3K/Akt/mTOR
4EGI-1	eIF4E/eIF4G interaction	eIF4E/eIF4G interaction	PI3K/Akt/mTOR
A-1155463	Bcl-2	Bcl	Apoptosis
A-1210477	Bcl-2	Bcl	Apoptosis

Product Name	Target detailed	Target broad	Pathway
A-366	Histone Methyltransferase	Histone Methyltransferase	Epigenetics
A-769662	AMPK, Fatty Acid Synthase	AMPK	PI3K/Akt/mTOR
Abexinostat (PCI-24781)	HDAC	HDAC	Epigenetics
ABT-751 (E7010)	Microtubule Associated	Microtubule Associated	Cytoskeletal Signaling
Adavosertib _MK-1775_	Wee1	Wee1	Cell Cycle
Afatinib (BIBW2992) Dimaleate	EGFR, HER2	Multi-RTK	Protein Tyrosine Kinase
AGI-5198	Dehydrogenase	Dehydrogenase	Metabolism
AGI-6780	Dehydrogenase	Dehydrogenase	Metabolism
AICAR (Acadesine)	AMPK	AMPK	PI3K/Akt/mTOR
Alectinib hydrochloride	ALK	ALK	Protein Tyrosine Kinase
Alisertib (MLN8237)	Aurora Kinase	Aurora Kinase	Cell Cycle
Allopurinol Sodium	ROS	ROS	Immunology & Inflammation
Alogliptin	DPP-4	DPP-4	Proteases & ER
Alpelisib (BYL719)	PI3K	PI3K	PI3K/Akt/mTOR
AMI-1	Histone Methyltransferase	Histone Methyltransferase	Epigenetics
Anastrozole	Aromatase	Aromatase	Endocrinology & Hormones
Apabetalone (RVX-208)	Epigenetic Reader Domain	Epigenetic Reader Domain	Epigenetics
Apitolisib (GDC-0980, RG7422)	mTOR, PI3K	PI3K/mTOR	PI3K/Akt/mTOR
Apocynin	NADPH-oxidase	NADPH-oxidase	Metabolism
Apoptosis Activator 2	Caspase	Caspase	Apoptosis
APR-246 (PRIMA-1MET)	p53	p53/Mdm2	Apoptosis
AT13148	Akt, S6 Kinase, ROCK, PKA	AKT	PI3K/Akt/mTOR
AT7519 HCl	CDK	CDK	Cell Cycle
ATN-161 (Ac-PHSCN-NH2)	Integrin	Integrin	Cytoskeletal Signaling
Avagacestat (BMS-708163)	Beta Amyloid, Gamma-secretase	Gamma-secretase	Stem Cells & Wnt
Axitinib	c-Kit, PDGFR, VEGFR	Multi-RTK	Protein Tyrosine Kinase
AZ 628	Raf	Raf	MAPK
AZ191	DYRK	DYRK	Protein Tyrosine Kinase
Azacitidine	DNA Methyltransferase	DNA Methyltransferase	Epigenetics
AZD1208	Pim	Pim	JAK/STAT
AZD1480	JAK	JAK	JAK/STAT
AZD3965	MCT1	MCT1	Metabolism
AZD4547	FGFR	FGFR	Protein Tyrosine Kinase

Product Name	Target detailed	Target broad	Pathway
AZD5153	Epigenetic Reader Domain	Epigenetic Reader Domain	Epigenetics
AZD6482	PI3K	PI3K	PI3K/Akt/mTOR
AZD6738	ATM/ATR	ATM/ATR	DNA Damage
AZD7762	Chk	Chk	Cell Cycle
Bafetinib (INNO-406)	Bcr-Abl	Bcr-Abl	Protein Tyrosine Kinase
b-AP15	DUB	DUB	Ubiquitin
Barasertib (AZD1152-HQPA)	Aurora Kinase	Aurora Kinase	Cell Cycle
BAW2881 (NVP-BAW2881)	VEGFR, Raf, c-RET	Multi-RTK	Protein Tyrosine Kinase
BAY 11-7082	E2 conjugating, I_B/IKK	NF-_B	NF-_B
BAY 87-2243	HIF	HIF	Angiogenesis
BAY-61-3606	Syk	Syk	Angiogenesis
BAY-876	GLUT	GLUT	Metabolism
BI-78D3	JNK	JNK	MAPK
BI-847325	MEK, Aurora Kinase	MEK	MAPK
BI-D1870	S6 Kinase	S6 Kinase	PI3K/Akt/mTOR
Binimetinib (MEK162, ARRY-162, ARRY-438162)	MEK	MEK	MAPK
Birinapant	IAP	IAP	Apoptosis
Bisindolylmaleimide IX (Ro 31-8220 Mesylate)	PKC	PKC	TGF-beta/Smad
BLZ945	CSF-1R	CSF-1R	Protein Tyrosine Kinase
BML-190	Cannabinoid Receptor	Cannabinoid Receptor	GPCR & G Protein
BMS202 (PD-1PD-L1 inhibitor 2)	PD-1/PD-L1	PD-1/PD-L1	Immunology & Inflammation
BMS-345541	I_B/IKK	I_B/IKK	NF-_B
BMS-777607	TYRO3, AXL, MER, c-Met	Multi-RTK	Protein Tyrosine Kinase
BMS-794833	c-Met, VEGFR	Multi-RTK	Protein Tyrosine Kinase
BMS-986205	IDO1	IDO	Metabolism
BPTES	Glutaminase	Glutaminase	Metabolism
BQU57	Rho	Rho/ROCK	Cytoskeletal Signaling
BRD4770	Histone Methyltransferase	Histone Methyltransferase	Epigenetics
Brivanib (BMS-540215)	FGFR, VEGFR	Multi-RTK	Protein Tyrosine Kinase
Bromopyruvic acid	Hexokinase	Hexokinase	Metabolism
Bromosporine	Epigenetic Reader Domain	Epigenetic Reader Domain	Epigenetics
BTB06584	ATPase	ATPase	Transmembrane Transporters
Busulfan	DNA alkylator	DNA alkylator	DNA Damage

Product Name	Target detailed	Target broad	Pathway
BX-795	I_B/IKK, PDK	PDK	PI3K/Akt/mTOR
BX-912	PDK	PDK	PI3K/Akt/mTOR
C646	Histone Acetyltransferase	Histone Acetyltransferase	Epigenetics
Cabozantinib malate (XL184)	TYRO3, AXL, MER, VEGFR	Multi-RTK	Protein Tyrosine Kinase
Capmatinib (INCB28060)	c-Met	c-Met	Protein Tyrosine Kinase
Carfilzomib (PR-171)	Proteasome	Proteasome	Proteases & ER
CB-5083	ATPase	ATPase	Transmembrane Transporters
CB-839	Glutaminase	Glutaminase	Metabolism
CC-115	DNA-PK,mTOR	DNA-PK	DNA Damage
CCF642	Thioredoxin	Thioredoxin	Metabolism
C-DIM12	Immunology & Inflammation related, Dopamine Receptor	NF-_B	NF-_B
Cediranib (AZD2171)	VEGFR	VEGFR	Protein Tyrosine Kinase
Celecoxib	COX	COX	Metabolism
CEP-32496	CSF-1R, Raf	Raf	MAPK
Ceritinib (LDK378)	ALK	ALK	Protein Tyrosine Kinase
CGP 57380	MNK	MNK	MAPK
Chaetocin	Histone Methyltransferase	Histone Methyltransferase	Epigenetics
Chk2 Inhibitor II (BML-277)	Chk	Chk	Cell Cycle
CID755673	CaMK	CaMK	Apoptosis
Cisplatin	DNA/RNA Synthesis	DNA/RNA Synthesis	DNA Damage
Cobimetinib (GDC-0973, RG7420)	MEK	MEK	MAPK
Colchicine	Microtubule Associated	Microtubule Associated	Cytoskeletal Signaling
CP-673451	PDGFR	PDGFR	Protein Tyrosine Kinase
CPI-169	Histone Methyltransferase	Histone Methyltransferase	Epigenetics
CPI-203	Epigenetic Reader Domain	Epigenetic Reader Domain	Epigenetics
CPI-455 HCl	Histone Demethylase	Histone Demethylase	Epigenetics
CPI-613	Dehydrogenase	Dehydrogenase	Metabolism
Crenigacestat (LY3039478)	Gamma-secretase	Gamma-secretase	Stem Cells & Wnt
Crizotinib (PF-02341066)	ALK, c-Met	c-Met	Protein Tyrosine Kinase
CUDC-101	EGFR, HDAC, HER2	Multi-RTK	Protein Tyrosine Kinase
CW069	Microtubule Associated	Microtubule Associated	Cytoskeletal Signaling
Cyclophosphamide Monohydrate	DNA alkylator	DNA alkylator	DNA Damage

Product Name	Target detailed	Target broad	Pathway
Dabrafenib (GSK2118436)	Raf	Raf	MAPK
Dalcetrapib (JTT-705, RO4607381)	CETP	CETP	Metabolism
Danusertib (PHA-739358)	Aurora Kinase, Bcr-Abl, c-RET, FGFR	Aurora Kinase	Cell Cycle
Dapagliflozin	SGLT	SGLT	GPCR & G Protein
DASA-58	PKM	PKM	Metabolism
Dasatinib hydrochloride	Abl/Src	Src	Protein Tyrosine Kinase
DBeQ	p97	p97	Ubiquitin
DDR1-IN-1	DDR1	DDR1	Protein Tyrosine Kinase
Decitabine	DNA Methyltransferase	DNA Methyltransferase	Epigenetics
Defactinib (VS-6063, PF-04554878)	FAK	FAK	Cytoskeletal Signaling
Degrasyn (WP1130)	Bcr-Abl, DUB	Bcr-Abl	Protein Tyrosine Kinase
Deguelin	Mitochondrial complex I	Mitochondrial complex I	Metabolism
Dibenzazepine (YO-01027)	Gamma-secretase	Gamma-secretase	Stem Cells & Wnt
Dinaciclib (SCH727965)	CDK	CDK	Cell Cycle
DMOG	Hydroxylase, HIF	Hydroxylase	Metabolism
Dovitinib (TKI258) Lactate	FLT3, c-Kit, FGFR, PDGFR, VEGFR	Multi-RTK	Protein Tyrosine Kinase
Doxorubicin (Adriamycin) HCl	Topoisomerase	Topoisomerase	DNA Damage
Droxinostat	HDAC	HDAC	Epigenetics
EED226	Epigenetic Reader Domain	Epigenetic Reader Domain	Epigenetics
eFT-508 (eFT508)	MNK	MNK	MAPK
EI1	Histone Methyltransferase	Histone Methyltransferase	Epigenetics
Elacridar (GF120918)	P-gp	P-gp	Transmembrane Transporters
Elesclomol (STA-4783)	ROS	ROS	Immunology & Inflammation
Eltanexor (KPT-8602)	CRM1	CRM1	Transmembrane Transporters
Enasidenib (AG-221)	Dehydrogenase	Dehydrogenase	Metabolism
Entinostat (MS-275)	HDAC	HDAC	Epigenetics
Entospletinib (GS-9973)	Syk	Syk	Angiogenesis
Entrectinib (RXDX-101)	Trk receptor, ALK	Trk receptor	Protein Tyrosine Kinase
Enzastaurin (LY317615)	PKC	PKC	TGF-beta/Smad
Epacadostat (INCB024360)	IDO	IDO	Metabolism
EPZ004777	Histone	Histone	Epigenetics

Product Name	Target detailed	Target broad	Pathway
	Methyltransferase	Methyltransferase	
EPZ005687	Histone Methyltransferase	Histone Methyltransferase	Epigenetics
EPZ020411 2HCl	Histone Methyltransferase	Histone Methyltransferase	Epigenetics
Erastin	Ferroptosis	Ferroptosis	Metabolism
Erdafitinib (JNJ-42756493)	FGFR	FGFR	Protein Tyrosine Kinase
Erlotinib	EGFR	EGFR	Protein Tyrosine Kinase
Etoposide	Topoisomerase	Topoisomerase	DNA Damage
ETP-46464	ATM/ATR, mTOR	ATM/ATR	DNA Damage
FH535	PPAR, Wnt/beta-catenin	Wnt/beta-catenin	Stem Cells & Wnt
FLI-06	Gamma-secretase	Gamma-secretase	Stem Cells & Wnt
Fluorouracil (5-Fluoracil, 5-FU)	DNA/RNA Synthesis	DNA/RNA Synthesis	DNA Damage
Fluvastatin Sodium	HMG-CoA Reductase	HMG-CoA Reductase	Metabolism
FR 180204	ERK	ERK	MAPK
FX1	Bcl-6	Bcl	Apoptosis
Galunisertib (LY2157299)	TGF-beta/Smad	TGF-beta/Smad	TGF-beta/Smad
Ganetespib (STA-9090)	HSP (e.g. HSP90)	HSP (e.g. HSP90)	Proteases & ER
GDC-0152	IAP	IAP	Apoptosis
GDC-0994	ERK	ERK	MAPK
Gemcitabine	DNA/RNA Synthesis,Autophagy	DNA/RNA Synthesis	DNA Damage
Glesatinib (MGCD265)	c-Met, Tie-2, VEGFR	Multi-RTK	Protein Tyrosine Kinase
GMX1778 (CHS828)	NAMPT	NAMPT	Metabolism
GSK J1	Histone Demethylase	Histone Demethylase	Epigenetics
GSK126	Histone Methyltransferase	Histone Methyltransferase	Epigenetics
GSK1324726A (I-BET726)	Epigenetic Reader Domain	Epigenetic Reader Domain	Epigenetics
GSK1904529A	IGF-1R	IGF-1R	Protein Tyrosine Kinase
GSK2256098	FAK	FAK	Cytoskeletal Signaling
GSK2334470	PDK	PDK	PI3K/Akt/mTOR
GSK2606414	PERK	PERK	Apoptosis
GSK2656157	PERK	PERK	Apoptosis
GSK2801	Epigenetic Reader Domain	Epigenetic Reader Domain	Epigenetics
GSK2830371	Wip1 phosphatase	Wip1 phosphatase	DNA Damage
GSK461364	PLK	PLK	Cell Cycle
GSK503	Histone Methyltransferase	Histone Methyltransferase	Epigenetics
GSK583	NF-_B	NF-_B	NF-_B
GSK591	Histone	Histone	Epigenetics

Product Name	Target detailed	Target broad	Pathway
	Methyltransferase	Methyltransferase	
GSK650394	SGK1, SGK2 inhibitor	SGK	PI3K/Akt/mTOR
GSK690693	Akt	AKT	PI3K/Akt/mTOR
GSK923295	Kinesin	Kinesin	Cytoskeletal Signaling
GSK963	NF-_B, TNF-alpha	NF-_B	NF-_B
GW0742	PPAR	PPAR	Metabolism
GW3965 HCl	Liver X Receptor	Liver X Receptor	Metabolism
GW441756	Trk receptor	Trk receptor	Protein Tyrosine Kinase
GW9662	PPAR	PPAR	Metabolism
HA15	HSPA5	HSP (e.g. HSP90)	Proteases & ER
HLCL-61 HCL	Histone Methyltransferase	Histone Methyltransferase	Epigenetics
HTH-01-015	AMPK	AMPK	PI3K/Akt/mTOR
I-BET-762	Epigenetic Reader Domain	Epigenetic Reader Domain	Epigenetics
I-BRD9	Epigenetic Reader Domain	Epigenetic Reader Domain	Epigenetics
Ibrutinib (PCI-32765)	BTK	BTK	Protein Tyrosine Kinase
ID-8	DYRK	DYRK	Protein Tyrosine Kinase
Ilomastat (GM6001, Galardin)	MMP	MMP	Proteases & ER
Importazole	Importin-_ (Karyopherin beta)	Importin-_ (Karyopherin beta)	Transmembrane Transporters
Indirubin	GSK-3	GSK-3	PI3K/Akt/mTOR
INH1	Microtubule Associated	Microtubule Associated	Cytoskeletal Signaling
Iniparib (BSI-201)	PARP	PARP	DNA Damage
IOX1	Histone Demethylase	Histone Demethylase	Epigenetics
IPA-3	PAK	Rho/ROCK	Cytoskeletal Signaling
Irinotecan HCl Trihydrate	Topoisomerase	Topoisomerase	DNA Damage
Ispinesib (SB-715992)	Kinesin	Kinesin	Cytoskeletal Signaling
IWP-L6	Wnt/beta-catenin	Wnt/beta-catenin	Stem Cells & Wnt
IWR-1-endo	Wnt/beta-catenin	Wnt/beta-catenin	Stem Cells & Wnt
Ixazomib Citrate (MLN9708)	Proteasome	Proteasome	Proteases & ER
JIB-04	Histone Demethylase	Histone Demethylase	Epigenetics
JNJ-26854165 (Serdemetan)	E3 Ligase, p53	p53/Mdm2	Apoptosis
JNK-IN-8	JNK	JNK	MAPK
JSH-23	NF-_B	NF-_B	NF-_B
Ki16425	LPA Receptor	LPA Receptor	GPCR & G Protein
KU-0063794	mTOR	mTOR	PI3K/Akt/mTOR
KU-55933 (ATM Kinase Inhibitor)	ATM/ATR	ATM/ATR	DNA Damage

Product Name	Target detailed	Target broad	Pathway
KU-60019	ATM/ATR	ATM/ATR	DNA Damage
KX2-391	Src	Src	Protein Tyrosine Kinase
KYA1797K	Wnt/beta-catenin	Wnt/beta-catenin	Stem Cells & Wnt
Lapatinib (GW-572016) Ditosylate	EGFR, HER2	Multi-RTK	Protein Tyrosine Kinase
LCL161	IAP	IAP	Apoptosis
Linifanib (ABT-869)	CSF-1R, PDGFR, VEGFR	Multi-RTK	Protein Tyrosine Kinase
Linsitinib (OSI-906)	IGF-1R	IGF-1R	Protein Tyrosine Kinase
LJH685	S6 Kinase	S6 Kinase	PI3K/Akt/mTOR
LLY-507	Histone Methyltransferase	Histone Methyltransferase	Epigenetics
Lonidamine	Hexokinase	Hexokinase	Metabolism
LTX-315	Mitochondrial membrane	Mitochondrial membrane	Apoptosis
Luminespib (AUY-922, NVP-AUY922)	HSP (e.g. HSP90)	HSP (e.g. HSP90)	Proteases & ER
Luteolin	PDE	PDE	Metabolism
LY2090314	GSK-3	GSK-3	PI3K/Akt/mTOR
LY2109761	TGF-beta/Smad	TGF-beta/Smad	TGF-beta/Smad
Lys05	Autophagy	Autophagy	Autophagy
Maraviroc	CCR	CCR	Microbiology
Masitinib (AB1010)	c-Kit, PDGFR	Multi-RTK	Protein Tyrosine Kinase
MCB-613	Steroid receptor coactivators	Steroid receptor coactivators	Metabolism
Mdivi-1	Dynamin	Dynamin	Metabolism
Melphalan	DNA alkylator	DNA alkylator	DNA Damage
MI-2 (MALT1 inhibitor)	MALT	MALT	Immunology & Inflammation
MI-463	Histone Methyltransferase	Histone Methyltransferase	Epigenetics
MI-503	Histone Methyltransferase	Histone Methyltransferase	Epigenetics
Milciclib (PHA-848125)	CDK	CDK	Cell Cycle
Mivebresib(ABBV-075)	Epigenetic Reader Domain	Epigenetic Reader Domain	Epigenetics
MK-0752	Beta Amyloid,Gamma-secretase	Gamma-secretase	Stem Cells & Wnt
MK-2206 2HCl	Akt	AKT	PI3K/Akt/mTOR
MK-8776 (SCH 900776)	CDK, Chk	Chk	Cell Cycle
MK-886 (L-663,536)	Lipoxygenase	Lipoxygenase	Metabolism
ML264	KLF5	KLF5	MAPK
ML323	DUB	DUB	Ubiquitin
ML324	Histone Demethylase	Histone Demethylase	Epigenetics
ML390	Dehydrogenase	Dehydrogenase	Metabolism
MLN2480	Raf	Raf	MAPK

Product Name	Target detailed	Target broad	Pathway
Motolimod (VTX-2337)	TLR	TLR	Immunology & Inflammation
MS023	Histone Methyltransferase	Histone Methyltransferase	Epigenetics
MS436	Epigenetic Reader Domain	Epigenetic Reader Domain	Epigenetics
Mubritinib (TAK 165)	HER2	HER2	Protein Tyrosine Kinase
MX69	Mdm2	p53/Mdm2	Apoptosis
Napabucasin	STAT	STAT	JAK/STAT
NCT-501	Dehydrogenase	Dehydrogenase	Metabolism
NCT-503	Dehydrogenase	Dehydrogenase	Metabolism
Neratinib (HKI-272)	EGFR, HER2	Multi-RTK	Protein Tyrosine Kinase
Nintedanib (BIBF 1120)	FGFR, PDGFR, VEGFR	Multi-RTK	Protein Tyrosine Kinase
Nintedanib Ethanesulfonate Salt	VEGFR, FGFR, PDGFR	Multi-RTK	Protein Tyrosine Kinase
NLG919	IDO	IDO	Metabolism
NMS-873	p97	p97	Ubiquitin
NSC 319726	p53	p53/Mdm2	Apoptosis
NSC348884	p53	p53/Mdm2	Apoptosis
NSC59984	p53	p53/Mdm2	Apoptosis
NSC87877	SHP-1 and SHP-2	SHP-1 and SHP-2	MAPK
NT157	IGF-1R	IGF-1R	Protein Tyrosine Kinase
NU7026	DNA-PK	DNA-PK	DNA Damage
NU7441 (KU-57788)	DNA-PK, PI3K	DNA-PK	DNA Damage
Nutlin-3	E3 Ligase, Mdm2	p53/Mdm2	Apoptosis
NVP-BHG712	Bcr-Abl, Ephrin receptor, Raf, Src	Multi-RTK	Protein Tyrosine Kinase
NVP-CGM097	Mdm2	p53/Mdm2	Apoptosis
OF-1	Epigenetic Reader Domain	Epigenetic Reader Domain	Epigenetics
Olaparib (AZD2281, Ku-0059436)	PARP	PARP	DNA Damage
Olmutinib (HM61713, BI 1482694)	EGFR, BTK	Multi-RTK	Protein Tyrosine Kinase
ON123300	CDK	CDK	Cell Cycle
Onalespib (AT13387)	HSP (e.g. HSP90)	HSP (e.g. HSP90)	Proteases & ER
Oprozomib (ONX 0912)	Proteasome	Proteasome	Proteases & ER
Orantinib (TSU-68, SU6668)	PDGFR	PDGFR	Protein Tyrosine Kinase
OSI-930	c-Kit, CSF-1R, VEGFR	Multi-RTK	Protein Tyrosine Kinase
Osimertinib (AZD9291)	EGFR	EGFR	Protein Tyrosine Kinase
OTS514 hydrochloride	TOPK	TOPK	MAPK
OTX015	Epigenetic Reader Domain	Epigenetic Reader Domain	Epigenetics

Product Name	Target detailed	Target broad	Pathway
Oxaliplatin	DNA/RNA Synthesis	DNA/RNA Synthesis	DNA Damage
P22077	DUB	DUB	Ubiquitin
P5091 (P005091)	DUB	DUB	Ubiquitin
Paclitaxel	Autophagy, Microtubule Associated	Microtubule Associated	Cytoskeletal Signaling
Palbociclib (PD0332991) Isethionate	CDK	CDK	Cell Cycle
Panobinostat (LBH589)	HDAC	HDAC	Epigenetics
Pelitinib (EKB-569)	EGFR	EGFR	Protein Tyrosine Kinase
Pevonedistat (MLN4924)	E1 Activating	E1 Activating	Ubiquitin
PF-00562271	FAK	FAK	Cytoskeletal Signaling
PF-3758309	PAK	Rho/ROCK	Cytoskeletal Signaling
PF-3845	FAAH	FAAH	Metabolism
PF-4708671	S6 Kinase	S6 Kinase	PI3K/Akt/mTOR
PF-543	S1P Receptor	Sphingosine Kinase 1	Kinase
PFI-1 (PF-6405761)	Epigenetic Reader Domain	Epigenetic Reader Domain	Epigenetics
PFI-4	Epigenetic Reader Domain	Epigenetic Reader Domain	Epigenetics
PFK15	Autophagy	Autophagy	Autophagy
PHT-427	Akt, PDK	AKT	PI3K/Akt/mTOR
Pictilisib (GDC-0941)	PI3K	PI3K	PI3K/Akt/mTOR
PIK-93	PI3K	PI3K	PI3K/Akt/mTOR
Pinometostat (EPZ5676)	Histone Methyltransferase	Histone Methyltransferase	Epigenetics
Plinabulin (NPI-2358)	VDA	Microtubule Associated	Cytoskeletal Signaling
PluriSIn 1 (NSC 14613)	Dehydrogenase	Dehydrogenase	Metabolism
PLX-4720	Raf	Raf	MAPK
Ponatinib (AP24534)	Bcr-Abl, FGFR, PDGFR, VEGFR	Multi-RTK	Protein Tyrosine Kinase
Poziotinib (HM781-36B)	HER2, EGFR	Multi-RTK	Protein Tyrosine Kinase
PR-619	DUB	DUB	Ubiquitin
Pracinostat (SB939)	HDAC	HDAC	Epigenetics
PRIMA-1	p53	p53/Mdm2	Apoptosis
PRT4165	E3 Ligase, BMI-1	BMI-1	Ubiquitin
PS-1145	I_B/IKK	I_B/IKK	NF-_B
PTC-209 HBr	BMI-1	BMI-1	Ubiquitin
PX-12	Thioredoxin	Thioredoxin	Metabolism
PX-478 2HCl	HIF	HIF	Angiogenesis
PYR-41	E1 Activating	E1 Activating	Ubiquitin
Quisinostat (JNJ-	HDAC	HDAC	Epigenetics

Product Name	Target detailed	Target broad	Pathway
26481585) 2HCl			
Quizartinib (AC220)	FLT3	FLT3	Angiogenesis
Rabusertib (LY2603618)	Chk	Chk	Cell Cycle
Ralimetinib (LY2228820)	p38 MAPK	p38 MAPK	MAPK
RBC8	RalA and RalB	RalA and RalB	GPCR & G Protein
Rebastinib (DCC-2036)	Bcr-Abl	Bcr-Abl	Protein Tyrosine Kinase
Regorafenib (BAY 73-4506)	c-RET, VEGFR	Multi-RTK	Protein Tyrosine Kinase
Remodelin	Histone Acetyltransferase	Histone Acetyltransferase	Epigenetics
RGFP966	HDAC	HDAC	Epigenetics
RHPS 4 methosulfate	Telomerase	Telomerase	DNA Damage
RI-1	RAD51	RAD51	DNA Damage
Ribociclib (LEE011)	CDK	CDK	Cell Cycle
Rigosertib (ON-01910)	PLK	PLK	Cell Cycle
RITA (NSC 652287)	E3 Ligase, p53	p53/Mdm2	Apoptosis
RKI-1447	ROCK	Rho/ROCK	Cytoskeletal Signaling
RO5126766 (CH5126766)	Raf	Raf	MAPK
Romidepsin	HDAC	HDAC	Epigenetics
Roxadustat (FG-4592)	HIF	HIF	Angiogenesis
RRx-001	Dehydrogenase	Dehydrogenase	Metabolism
RSL3	Ferroptosis	Ferroptosis	Metabolism
Ruxolitinib (INCB018424)	JAK	JAK	JAK/STAT
Sabutoclax	Bcl-2	Bcl	Apoptosis
Salermide	Sirtuin	Sirtuin	Epigenetics
Salirasib	Rho	Rho/ROCK	Cytoskeletal Signaling
Sapanisertib (INK 128, MLN0128)	mTOR	mTOR	PI3K/Akt/mTOR
Saracatinib (AZD0530)	Src	Src	Protein Tyrosine Kinase
SB202190 (FHPI)	p38 MAPK	p38 MAPK	MAPK
SB216763	GSK-3	GSK-3	PI3K/Akt/mTOR
SB743921 HCl	Kinesin	Kinesin	Cytoskeletal Signaling
SC144	P-gp	P-gp	Transmembrane Transporters
SC79	Akt	AKT	PI3K/Akt/mTOR
SCH58261	Adenosine Receptor	Adenosine Receptor	GPCR & G Protein
Selisistat (EX 527)	Sirtuin	Sirtuin	Epigenetics
Selonsertib (GS-4997)	ASK1	ASK	Apoptosis
Selumetinib	MEK	MEK	MAPK

Product Name	Target detailed	Target broad	Pathway
(AZD6244)			
SF1670	PTEN	PTEN	PI3K/Akt/mTOR
SF2523	PI3K, DNA-PK, Epigenetic Reader Domain, mTOR	PI3K/mTOR	PI3K/Akt/mTOR
SGC 0946	Histone Methyltransferase	Histone Methyltransferase	Epigenetics
SGC707	Histone Methyltransferase	Histone Methyltransferase	Epigenetics
SGC-CBP30	Epigenetic Reader Domain	Epigenetic Reader Domain	Epigenetics
SGI-1027	DNA Methyltransferase	DNA Methyltransferase	Epigenetics
SGI-1776 free base	Pim	Pim	JAK/STAT
SGI-7079	VEGFR	VEGFR	Protein Tyrosine Kinase
SGX-523	c-Met	c-Met	Protein Tyrosine Kinase
SHP099 dihydrochloride	SHP-1 and SHP-2	SHP-1 and SHP-2	MAPK
Silmitasertib (CX-4945)	Casein Kinase	Casein Kinase	Metabolism
SMER28	Autophagy	Autophagy	Autophagy
Sodium dichloroacetate (DCA)	Dehydrogenase	Dehydrogenase	Metabolism
Sorafenib Tosylate	PDGFR, Raf, VEGFR	Multi-RTK	Protein Tyrosine Kinase
Sotrastaurin	PKC	PKC	TGF-beta/Smad
SP2509	Histone Demethylase	Histone Demethylase	Epigenetics
SP600125	JNK	JNK	MAPK
Spebrutinib (CC-292, AVL-292)	BTK	BTK	Protein Tyrosine Kinase
SRPIN340	SRPK	SRPK	Kinase
SRT1720 HCl	Sirtuin	Sirtuin	Epigenetics
STF-083010	IRE1_	IRE1_	Kinase
STF-118804	NAMPT	NAMPT	Metabolism
STF-31	GLUT	GLUT	Metabolism
Sulfabenzamide	Anti-infection	Anti-infection	Microbiology
TAK-700 (Orteronel)	P450 (e.g. CYP17)	P450 (e.g. CYP17)	Metabolism
Taladegib (LY2940680)	Hedgehog, Hedgehog/Smoothened	Hedgehog	Stem Cells & Wnt
TAPI-1	ADAM17/TACE, MMP	MMP	Proteases & ER
Tazemetostat (EPZ-6438)	Histone Methyltransferase	Histone Methyltransferase	Epigenetics
Tezacaftor (VX-661)	CFTR	CFTR	Transmembrane Transporters
TH287	MTH1	MTH1	DNA Damage
TH588	MTH1	MTH1	DNA Damage
Thiamet G	O-GlcNAcase	O-GlcNAcase	Epigenetics

Product Name	Target detailed	Target broad	Pathway
Thiomyristoyl	Sirtuin	Sirtuin	Epigenetics
Tipifarnib	Farnesyltransferase	Farnesyltransferase	Metabolism
Tofacitinib (CP-690550,Tasocitinib)	JAK	JAK	JAK/STAT
Topotecan HCl	Topoisomerase	Topoisomerase	DNA Damage
Tozasertib (VX-680, MK-0457)	Aurora Kinase	Aurora Kinase	Cell Cycle
TPX-0005	Src, ALK	Src	Protein Tyrosine Kinase
Trametinib (GSK1120212)	MEK	MEK	MAPK
Tretinoin	Retinoid Receptor	Retinoid Receptor	Metabolism
U-104	Carbonic Anhydrase	Carbonic Anhydrase	Metabolism
Ulixertinib (BVD-523, VRT752271)	ERK	ERK	MAPK
UNC0379	Histone Methyltransferase	Histone Methyltransferase	Epigenetics
UNC1215	Epigenetic Reader Domain	Epigenetic Reader Domain	Epigenetics
UNC1999	Histone Methyltransferase	Histone Methyltransferase	Epigenetics
UNC669	Epigenetic Reader Domain	Epigenetic Reader Domain	Epigenetics
Uprosertib (GSK2141795)	Akt	AKT	PI3K/Akt/mTOR
Vactosertib (TEW-7197)	TGF-beta/Smad	TGF-beta/Smad	TGF-beta/Smad
Vatalanib (PTK787) 2HCl	VEGFR	VEGFR	Protein Tyrosine Kinase
VE-822	ATM/ATR	ATM/ATR	DNA Damage
Veliparib (ABT-888)	PARP	PARP	DNA Damage
Vemurafenib (PLX4032, RG7204)	Raf	Raf	MAPK
Venetoclax (ABT-199, GDC-0199)	Bcl-2	Bcl	Apoptosis
Vincristine sulfate	Autophagy, Microtubule Associated	Microtubule Associated	Cytoskeletal Signaling
Vinorelbine Tartrate	Microtubule Associated	Microtubule Associated	Cytoskeletal Signaling
Vismodegib (GDC-0449)	Hedgehog/Smoothened	Hedgehog	Stem Cells & Wnt
Vistusertib (AZD2014)	mTOR	PI3K/mTOR	PI3K/Akt/mTOR
VLX1570	DUB	DUB	Ubiquitin
Volasertib (BI 6727)	PLK	PLK	Cell Cycle
VO-Ohpic trihydrate	PTEN	PTEN	PI3K/Akt/mTOR
Voxtalisib (XL765, SAR245409)	mTOR, PI3K	PI3K/mTOR	PI3K/Akt/mTOR
VPS34-IN1	PI3K	PI3K	PI3K/Akt/mTOR
WH-4-023	Src	Src	Protein Tyrosine Kinase
WIKI4	Wnt/beta-catenin	Wnt/beta-catenin	Stem Cells & Wnt

Product Name	Target detailed	Target broad	Pathway
WZ4003	AMPK	AMPK	PI3K/Akt/mTOR
Xanthohumol	COX	COX	Metabolism
XAV-939	Wnt/beta-catenin	Wnt/beta-catenin	Stem Cells & Wnt
XL413 (BMS-863233)	CDK	CDK	Cell Cycle
XMD16-5	Tnk2	Tnk2	Protein Tyrosine Kinase
Y-27632 2HCl	Autophagy, ROCK	Rho/ROCK	Cytoskeletal Signaling
YM155 (Sepantronium Bromide)	Survivin	Survivin	Apoptosis
ZCL278	Rho	Rho/ROCK	Cytoskeletal Signaling
Zibotentan (ZD4054)	Endothelin Receptor	Endothelin Receptor	GPCR & G Protein
Zileuton	Lipoxygenase	Lipoxygenase	Metabolism
ZSTK474	PI3K	PI3K	PI3K/Akt/mTOR

4.7 Compounds used for additional experiments

Table 4-7: Additional compounds.

Compound	Distributor
Antimycin A	Sigma-Aldrich Chemie GmbH, Taufkirchen
Bortezomib (PS-341)	Selleck Chemicals LLC (Houston, TX, USA)
FCCP	Selleck Chemicals LLC (Houston, TX, USA)
Ferrostatin-1	Selleck Chemicals LLC (Houston, TX, USA)
Necrostatin-1	Selleck Chemicals LLC (Houston, TX, USA)
Oligomycin A	Selleck Chemicals LLC (Houston, TX, USA)
Rotenone	Selleck Chemicals LLC (Houston, TX, USA)
Z-VAD-FMK	Selleck Chemicals LLC (Houston, TX, USA)

4.8 Primers

All oligonucleotides were synthesized by Eurofins MWG GmbH (Ebersberg) and diluted in H_2O to a concentration of 10 µM.

Primers used for cell line authentication (regenotyping) are shown in Table 4-8.

Table 4-8: Regenotyping primers.

PCR name	Primer name	Sequence (5' → 3')
Ptf1a-Cre	p48-Cre-GT-LP-URP	CCTCGAAGGCGTCGTTGATGGACTGCA
	p48-Cre-GT-wt-UP	CCACGGATCACTCACAAAGCGT

PCR name	Primer name	Sequence (5' → 3')
	p48-Cre-GT-mut-UP-neu	GCCACCAGCCAGCTATCAA
Pdx1-Cre	Pdx-Prom-UP2	GCTCATTGGGAGCGGTTTTG
	V-Cre-LP2	ACATCTTCAGGTTCTGCGGG
	PdxKON-LP1	CACGTGGTTTACCCTGGAGC
Pdx-Flp	pdx5ut-scUP	AGAGAGAAAATTGAAACAAGTGCAGGT
	Flpopt-scLP	CGTTGTAAGGGATGATGGTGAACT
	Gabra-UP	AACACACACTGGAGGACTGGCTAGG
	Gabra-LP	CAATGGTAGGCTCACTCTGGGAGATGATA
LSL-Kras^{G12D}	Kras-WT-UP1	CACCAGCTTCGGCTTCCTATT
	Kras-URP-LP1	AGCTAATGGCTCTCAAAGGAATGTA
	KrasG12Dmut-UP	CCATGGCTTGAGTAAGTCTGC
FSF-Kras^{G12D}	Kras-WT-UP1	CACCAGCTTCGGCTTCCTATT
	Kras-URP-LP1	AGCTAATGGCTCTCAAAGGAATGTA
	R26-Tva-SA-mut	GCGAAGAGTTTGTCCTCAACC
LSL-Trp53^{R172H}	Trp53R172H-WT-UP2	AGCCTTAGACATAACACACGAACT
	Trp53R172H-URP-LP	CTTGGAGACATAGCCACACTG
	Trp53R172H-mut-UP4	GCCACCATGGCTTGAGTAA
LSL-Trp53^{R172H} (deleted stop cassette)	p53R172H-LoxUP	AGCCTGCCTAGCTTCCTCAGG
	p53R172H-LoxLP	CTTGGAGACATAGCCACACTG
Trp53^{lox}	p53 berns Up-E	CACAAAAAACAGGTTAAACCCAGC
	p53 berns LP-F	GCACCTTTGATCCCAGCACATA
Trp53^{frt}	p53-ftr1	CAAGAGAACTGTGCCTAAGAG
	p53-frt2	CTTTCTAACAGCAAAGGCAAGC
Pik3ca^{H1047R}	Soriano_SA_UP	CAGTAGTCCAGGGTTTCCTTGATG
	PI3K-genotyp-RevPr	AAATAGCCGCAGGTCACAAAGTCTCCG
	pGL3-pA-pause4645-UP	TGAATAGTTAATTGGAGCGGCCGCAATA
Cdkn2a^{lox}	INK4A-UP	CCAAGTGTGCAAACCCAGGCTCC
	INK4A-LP	TTGTTGGCCCAGGATGCCGACATC
LSL-Braf^{V637E}	BR_UP	TTTATCATAGTAGGGCTTGCTGTCTTGCTT
	BR_WT-LP	CAAATATGTTTTGAGCAAGACCTTTGTTCT
	BR_SA-LP	CCACTGACCAGAAGGAAAGTGGT
p16^{Ink4a*}	VBC_Ink4a_PM-UP	GCAGTGTTGCAGTTTGAACCC
	VBC_Ink4a_PM-LP	TGTGGCAACTGATTCAGTTGG

Primers used for human contamination test are shown in Table 4-9.

Table 4-9: Primers used to test for human contamination.

PCR name	Primer name	Sequence (5' → 3')
Human contamination test	Kras_hu_G12D_fw	AAAGGTACTGGTGGAGTATTTGATAGTG
	Kras_hu_G12D_rev	GGTCCTGCACCAGTAATATGCA

Primers used for human contamination test are shown in Table 4-10.

Table 4-10: Primers used to test for murine contamination of human cell cultures.

PCR name	Primer name	Sequence (5' → 3')
Murine contamination test	hKRAS_ex2_flank_Fw	GGTACTGGTGGAGTATTTGATAGTG
	hKRAS_ex2_flank_Rv	GGTCCTGCACCAGTAATATGCA
	mKras_ex2_flank_Fw	TCCTTTGAGAGCCATTAGCTGCT
	mKras_ex2_flank_Fw	TTTACAAGCGCACGCAGACTGTA

Primers used for mycoplasma tests are shown in Table 4-11.

Table 4-11: Primers for mycoplasma tests.

PCR name	Primer name	Sequence (5' → 3')
Mycoplasma	5' primer 1	CGC CTG AGT AGT ACG TTC GC
	5' primer 2	CGC CTG AGT AGT ACG TAC GC
	5' primer 3	TGC CTG GGT AGT ACA TTC GC
	5' primer 4	TGC CTG AGT AGT ACA TTC GC
	5' primer 5	CGC CTG AGT AGT ATG CTC GC
	5' primer 6	CAC CTG AGT AGT ATG CTC GC
	5' primer 7	CGC CTG GGT AGT ACA TTC GC
	3' primer 1	GCG GTG TGT ACA AGA CCC GA
	3' primer 2	GCG GTG TGT ACA AAA CCC GA
	3' primer 3	GCG GTG TGT ACA AAC CCC GA

Primers used for virus contamination tests are shown in Table 4-12.

Table 4-12: Primers used for virus contamination tests.

PCR name	Primer name	Sequence (5' → 3')
HIV-1	F-HIV	ATAATCCACCTATCCCAGTAGGAGAAAT
	R-HIV	TTTGGTCCTTGTCTTATGTCCAGAATGC
	hKras-fw	GGTACTGGTGGAGTATTTGATAGTG
	hKras-rv	GGTCCTGCACCAGTAATATGCA
HIV-2	F-HIV2	CCTCAATTCTCTCTTTGGAAAAGACC
	R-HIV2	AAATGTTGATTGGGGTATCTCCTGTC
	R-HIV2-2	AAATGTTGATTGGGGTATCTCCTATC
	hBraf-fw	GAAGAGCCTTTACTGCTCGCC
	hBraf-rv	TTTCTAGTAACTCAGCAGCATCTCA
HBV	F-HEBP	AAGCTGTGCCTTGGGTGGCTT
	R-HEBP	CGAGATTGAGATCTTCTGCGAC
	hKras-fw	GGTACTGGTGGAGTATTTGATAGTG
	hKras-rv	GGTCCTGCACCAGTAATATGCA
HCV	F-HCV	GCCATGGCGTTAGTATGAGT
	F-HCV-2	GCCATGGCGTTAGTATGAG
	R-HCV	GTGCACGGTCTACGAGACCT
	Fw-beta-actin	CGCGGCGATATCATCATC
	Rv-beta-actin	CCTCGCCTTTGCCGATCC

4.9 Primers used for CRISPR/Cas9 screens

Primers used for amplification of sgRNAs from CRISPR screens are shown in Table 4-13. Different forward and reverse primers were obtained by variable indexing sequences (denoted as NNNNNN, Table 4-13).

Table 4-13: Primers used for sgRNA amplification.

Primer name	Sequence (5' → 3')
sgRNA_NGS_P5	AATGATACGGCGACCACCGAGATCTACAC**NNNNNN**CACCG ACTCGGTGCCACTTTT
sgRNA_NGS_P7	AATGATACGGCGACCACCGAGATCTACAC**NNNNNN**CACCG ACTCGGTGCCACTTTT

4.10 Plasmids

Plasmids used for this thesis are listed in Table 4-14. The plasmid "pEX-128-HA-MS-2" is a customized plasmid containing the following sequence from HIV-2:

CCTCAATTCTCTCTTTGGAAAAGACCAGTAGTCACAGCATACATTGAGGGCCAGGCAGTAGAGGTCCTATTA
GATACAGGGGCTGATGATTCAATAGTAGCAGGAATAGAGTTAGGGAATGATTATAGTCCAAAAGTAGTAGGG
GGAATAGGGGGATTCATAAATACCAAAGAATACAAAAATGTAGAGATAAAAGTGTTAAATAAAAGAGTAAGAG
CCACCATAATGATAGGAGATACCCCAATCAACATTT

Table 4-14: Plasmids.

Plasmid	Source	RRID
The mouse CRISPR Knockout Brie pooled Library (#73632)	Addgene, Watertown, MA, USA	n/a
psPAX2 #12260	Addgene, Watertown, MA, USA	Addgene_12260
HBV 1.3-mer WT replicon #65459	Addgene, Watertown, MA, USA	n/a
pFR_HCV_xb #11510	Addgene, Watertown, MA, USA	RRID:Addgene_11510
pEX-128-HA-MS-2	Thermo Fisher Scientific, Waltham, Massachusetts, USA	

4.11 Murine cell lines

Murine PDAC cell lines used for this thesis were isolated from PDAC mouse models by members of the laboratories of Prof. Saur, Prof. Rad and Prof. Schneider. Isolation was performed as described previously (Burstin et al. 2009; Eser et al. 2013). The mouse models were based on the *Cre-loxP* and *Flp-frt* recombination systems. By interbreeding tissue-specific *Cre* strains or *Flp* mouse strains with mice carrying transgenes flanked by *loxP*-sites

or *frt*-sites or silenced by a *loxP-stop-loxP (LSL)* or *frt-stop-frt (FSF)* cassette, mice with expression or deletion of the target gene(s) were obtained. All animals were on a mixed *C57Bl/6*; *129S6/SvEv* genetic background.

The following mouse strains were used and have previously been reported as indicated: *Pdx1-Cre* (Hingorani et al. 2003), *Ptf1a*$^{Cre/+}$ (Nakhai et al. 2007), *Pdx1-Flp* (Schönhuber et al. 2014), *LSL-Kras*$^{G12D/+}$ (Jackson et al. 2001; Hingorani et al. 2003), *FSF-Kras*$^{G12D/+}$ (Schönhuber et al. 2014), *LSL-PIK3CA*$^{H1047R/+}$ (Eser et al. 2013), *LSL-Rosa26*$^{Snail/+}$ (Paul et al. 2023), *LSL-Braf*$^{V637E/+}$ (Rad et al. 2013), *Cdh1*$^{fl/+}$ (Derksen et al. 2006), *LSL-Trp53*$^{R172H/+}$ (Hingorani et al. 2005; Olive et al. 2004), *Trp53*$^{lox/+}$ (Jonkers et al. 2001), *Trp53*$^{frt/+}$ (Lee et al. 2012), *p16*$^{Ink4a*/+}$ (Krimpenfort et al. 2001), *Cdkn2a*$^{lox/+}$ (Aguirre et al. 2003), *Tgfß2*$^{lox/+}$ (Chytil et al. 2002), *Smad4*$^{lox/+}$ (Bardeesy et al. 2006) and *LSL-Rosa26*$^{Tgfß1/+}$ (developed by the Saur laboratory).

For this thesis, murine cell lines isolated from mouse models with the genotypes listed in Table 4-15 were used. For the purposes of this thesis (e.g. to improve readability), genotypes were categorized in genotype groups as also shown in Table 4-15.

Table 4-15: Overview of genotype groups.

Genotype group	Detailed genotypes
PK	*Ptf1a*$^{Cre/+}$*;LSL-Kras*$^{G12D/+}$ *Pdx1-Cre;LSL-Kras*$^{G12D/+}$ *Pdx1-Flp;FSF-Kras*$^{G12D/+}$ *Pdx1-Flp-o;FSF-Kras*$^{G12D/+}$
PPI3K	*Ptf1a*$^{Cre/+}$*;Pdx1-Cre;LSL-Pik3ca*$^{H1047R/+}$ *Ptf1a*$^{Cre/+}$*;LSL- Pik3ca*$^{H1047R/+}$ *Pdx1-Cre;LSL-Pik3ca*$^{H1047R/+}$ *Pdx1-Flp;FSF-Pik3ca*$^{H1047R/+}$
PKPI3K	*Ptf1a*$^{Cre/+}$*;LSL-Kras*$^{G12D/+}$*;Pik3ca*$^{H1047R/+}$
PPI3KP	*Ptf1a*$^{Cre/+}$*; LSL-Pik3ca*$^{H1047R/+}$*;Trp53*$^{R172H/+}$ *Ptf1a*$^{Cre/+}$*;Pdx1-Cre; LSL-Pik3ca*$^{H1047R/+}$*;Trp53*$^{R172H/+}$ *Pdx1-Cre;LSL-Pik3ca*$^{H1047R/+}$*;Trp53*$^{R172H/+}$ *Pdx1-Cre;LSL-Pik3ca*$^{H1047R/+}$*;Trp53*$^{lox/lox}$ *Pdx1-Cre;LSL-Pik3ca*$^{H1047R/+}$*;Trp53*$^{lox/+}$
PKPI3KP	*Ptf1a*$^{Cre/+}$*;LSL-Kras*$^{G12D/+}$*;Pik3ca*$^{H1047R/+}$*;Trp53*$^{R172H/+}$
PPI3KPC	*Pdx1-Cre;LSL-Pik3ca*$^{H1047R/+}$*;Trp53*$^{R172H/}$*; Cdkn2a*$^{lox/+}$
PKP	*Ptf1a*$^{Cre/+}$*;LSL-Kras*$^{G12D/+}$*;Trp53*$^{R172H/+}$ *Pdx1-Cre;LSL-Kras*$^{G12D/+}$*;Trp53*$^{R172H/+}$ *Ptf1a*$^{Cre/+}$*;Pdx1-Cre;LSL-Kras*$^{G12D/+}$*; Trp53*$^{R172H/+}$ *Pdx1-Flp;FSF-Kras*$^{G12D/+}$*;LSL-Trp53*$^{R172H/+}$ *Pdx1-Flp-o;FSF-Kras*$^{G12D/+}$*;LSL-Trp53*$^{R172H/+}$ *Ptf1a*$^{Cre/+}$*;LSL-Kras*$^{G12D/+}$*;Trp53*$^{lox/+}$ *Ptf1a*$^{Cre/+}$*;LSL-Kras*$^{G12D/+}$*;Trp53*$^{lox/lox}$ *Pdx1-Cre;LSL-Kras*$^{G12D/+}$*;Trp53*$^{lox/+}$ *Pdx1-Cre;LSL-Kras*$^{G12D/+}$*;Trp53*$^{lox/lox}$ *Pdx1-Flp;FSF-Kras*$^{G12D/+}$*;Trp53*$^{frt/+}$ *Pdx1-Flp;FSF-Kras*$^{G12D/+}$*;Trp53*$^{frt/frt}$

Genotype group	Detailed genotypes
PBRC	*Pdx1-Cre;LSL-Braf$^{V637E/+}$;p16$^{Ink4a*/+}$* *Pdx1-Cre;LSL-Braf$^{V637E/+}$;p16$^{Ink4a*/Ink4a*}$* *Pdx1-Cre;LSL-Braf$^{V637E/+}$;Cdkn2a$^{lox/lox}$*
PBRPC	*Pdx1-Cre;LSL-Braf$^{V637E/+}$;p16$^{Ink4a*/+}$;Trp53$^{R172H/+}$*
PKC	*Ptf1a$^{Cre/+}$;LSL-Kras$^{G12D/+}$;Cdkn2a$^{lox/+}$* *Ptf1a$^{Cre/+}$;LSL-Kras$^{G12D/+}$;Cdkn2a$^{lox/lox}$* *Ptf1a$^{Cre/+}$;LSL-Kras$^{G12D/+}$; p16$^{Ink4a*/+}$*
PKCSm	*Pdx1-Flp;FSF-Kras$^{G12D/+}$;Cdkn2a$^{lox/+}$;Smad4$^{lox/+}$*
PKPCSm	*Pdx1-Flp;FSF-Kras$^{G12D/+}$;Cdkn2a$^{lox/+}$; Smad4$^{lox/lox}$;Trp53$^{lox/+}$* *Pdx1-Flp;FSF-Kras$^{G12D/+}$;Cdkn2a$^{lox/lox}$;Smad4$^{lox/+}$;Trp53$^{lox/lox}$* *Pdx1-Flp;FSF-Kras$^{G12D/+}$;Cdkn2a$^{lox/lox}$;Smad4$^{lox/lox}$;Trp53$^{lox/+}$* *Pdx1-Flp;FSF-Kras$^{G12D/+}$;Cdkn2a$^{lox/lox}$;Smad4$^{lox/+}$;Trp53$^{lox/+}$*
PKE	*Pdx1-Flp;FSF-Kras$^{G12D/+}$;Cdh1$^{fl/fl}$*
PKPE	*Pdx1-Cre;LSL-Kras$^{G12D/+}$;Trp53$^{R172H/+}$;Cdh1$^{fl/fl}$*
PKPT	*Ptf1a$^{Cre/+}$;LSL-Kras$^{G12D/+}$;Tgfβr2$^{lox/lox}$;Trp53$^{R172H/+}$* *Ptf1a$^{Cre/+}$;LSL-Kras$^{G12D/+}$;Tgfβr2$^{lox/+}$;Trp53$^{R172H/+}$*
PKS	*Pdx1-Cre;LSL-Kras$^{G12D/+}$;Rosa26$^{Snail/Snail}$* *Pdx1-Cre;LSL-Kras$^{G12D/+}$;Rosa26$^{Snail/+}$* *Ptf1a$^{Cre/+}$;LSL-Kras$^{G12D/+}$;Rosa26$^{Snail/+}$*
PKSC	*Ptf1a$^{Cre/+}$;LSL-Kras$^{G12D/+}$;Rosa26$^{Snail/+}$; p16$^{Ink4a*/+}$* *Ptf1a$^{Cre/+}$;LSL-Kras$^{G12D/+}$; Rosa26$^{Snail/+}$; p16$^{Ink4a*/Ink4a*}$* *Pdx1-Cre;LSL-Kras$^{G12D/+}$;Rosa26$^{Snail/+}$; p16$^{Ink4a*/+}$* *Ptf1a$^{Cre/+}$;LSL-Kras$^{G12D/+}$; Rosa26$^{Snail/+}$; Cdkn2a$^{lox/+}$* *Ptf1a$^{Cre/+}$;LSL-Kras$^{G12D/+}$; Rosa26$^{Snail/+}$; Cdkn2a$^{lox/lox}$*
PKSm	*Ptf1a$^{Cre/+}$;LSL-Kras$^{G12D/+}$;Smad4$^{lox/+}$*
PKT	*Ptf1a$^{Cre/+}$;LSL-Kras$^{G12D/+}$; Tgfβr2$^{lox/lox}$* *Ptf1a$^{Cre/+}$;LSL-Kras$^{G12D/+}$; Tgfβr2$^{lox/+}$*
PKTo	*Ptf1a$^{Cre/+}$;LSL-Kras$^{G12D/+}$; LSL-Rosa26$^{Tgfβ1/+}$*
PKTSm	*Ptf1a$^{Cre/+}$;LSL-Kras$^{G12D/+}$; Tgfβr2$^{lox/+}$;Smad4$^{lox/+}$*

All murine cell lines that were used for this thesis are listed in Table 4-16. All murine cell lines were authenticated by re-genotyping PCR as described in Chapter 5.3.7. Genotypes are listed in more detail in Table 9-1. Only confirmed cancer cell lines were used in this thesis. In the future, genome sequencing data for all cell lines will be available, providing even more detailed information on the presence of mutations and deletions of genes.

Fibroblast contamination as indicated in Table 4-16 was determined based on the presence of unrecombined alleles according to re-genotyping PCRs (Table 9-1). As demonstrated in Figure 31, fibroblast contamination did not affect drug response and fibroblast contaminated cell lines were therefore not removed from analyses.

All murine cell lines used in this thesis were tested negative for contamination with human cells (tested according to Chapter 5.3.9). Additionally, all murine cell lines were tested negative for mycoplasma contamination (described in more detail in Chapter 5.3.8). The cell line 8349 was initially mycoplasma positive (passage 12) and was used only after being

confirmed negative after mycoplasma removal (passage 29-30) (mycoplasma removal performed according to Chapter 5.1.3).

The morphology of the cell lines as indicated in Table 4-16 was determined by microscopy.

Table 4-16: Overview of murine cell lines used in this thesis with information on genotype group, fibroblast contamination and morphology.

Cell line	Genotype group	Fibroblast contamination	Morphology
10092	PPI3K	negative	quasi-mesenchymal
10139	PKP	negative	mesenchymal
10158	PPI3K	negative	quasi-mesenchymal
10161	PPI3K	negative	epithelial
10193	PPI3KP	negative	mesenchymal
10232	PKP	negative	quasi-mesenchymal
10350	PPI3K	negative	quasi-mesenchymal
10502	PKP	negative	quasi-mesenchymal
10587	PPI3KP	negative	epithelial
10593	PPI3KP	negative	quasi-mesenchymal
10632	PPI3KP	negative	quasi-mesenchymal
10688	PPI3KP	negative	mesenchymal
10725	PPI3KP	negative	quasi-mesenchymal
10729	PPI3KP	positive	quasi-mesenchymal
10731	PPI3KP	positive	mesenchymal
11343	PKP	negative	epithelial
11363-2	PKPI3K	negative	quasi-mesenchymal
11440	PPI3KP	positive	mesenchymal
11600	PPI3KP	negative	quasi-mesenchymal
11602	PPI3KP	positive	mesenchymal
11714	PPI3KP	negative	mesenchymal
11987	PPI3KP	positive	mesenchymal
12047	PPI3K	negative	quasi-mesenchymal
12128	PPI3KP	positive	mesenchymal
12508	PK	negative	quasi-mesenchymal
12690	PPI3K	negative	quasi-mesenchymal
13474	PPI3KP	negative	quasi-mesenchymal
13871	PKP	negative	mesenchymal
14169	PKP	negative	quasi-mesenchymal
14193	PKP	negative	quasi-mesenchymal
14311	PKP	negative	epithelial
16990	PK	negative	quasi-mesenchymal
16992	PK	negative	mesenchymal
1712	PKP	negative	epithelial
1778	PKP	negative	epithelial
2259	PK	negative	quasi-mesenchymal
271-105	PKPCSm	negative	quasi-mesenchymal
271-91	PKPCSm	negative	quasi-mesenchymal
2937	PKPE	negative	mesenchymal

Cell line	Genotype group	Fibroblast contamination	Morphology
3139	PKP	negative	mesenchymal
3202	PK	negative	mesenchymal
3250	PK	negative	mesenchymal
3862	PPI3KP	negative	quasi-mesenchymal
4072	PK	negative	quasi-mesenchymal
4130	PPI3KP	negative	mesenchymal
4134	PPI3K	negative	mesenchymal
4140	PPI3K	negative	epithelial
4706	PK	negative	quasi-mesenchymal
4888	PPI3K	negative	quasi-mesenchymal
4900	PK	negative	quasi-mesenchymal
4912	PK	negative	quasi-mesenchymal
4971	PKP	negative	epithelial
5123	PK	negative	quasi-mesenchymal
5320	PK	negative	mesenchymal
53578	PK	negative	quasi-mesenchymal
53631	PK	negative	epithelial
53646	PK	negative	epithelial
53704	PK	negative	quasi-mesenchymal
53909	PK	negative	mesenchymal
5671	PK	negative	epithelial
5748	PK	negative	quasi-mesenchymal
6021	PKP	negative	quasi-mesenchymal
6034	PKP	negative	epithelial
6075	PK	negative	quasi-mesenchymal
6127	PK	negative	epithelial
6605	PKP	positive	mesenchymal
6719	PKP	negative	epithelial
7725	PKP	negative	epithelial
7968	PK	negative	mesenchymal
8013	PKP	negative	quasi-mesenchymal
8028	PK	negative	mesenchymal
8182	PK	negative	quasi-mesenchymal
8248	PK	negative	mesenchymal
8296	PK	negative	epithelial
8305	PK	negative	mesenchymal
8349	PK	negative	mesenchymal
8442	PK	negative	epithelial
8513	PK	negative	mesenchymal
8570	PK	negative	mesenchymal
8661	PK	negative	epithelial
8927	PPI3K	negative	quasi-mesenchymal
8932	PPI3K	negative	quasi-mesenchymal
9063	PKP	negative	epithelial with fibroblasts
9091	PK	negative	mesenchymal
9172	PKP	negative	mesenchymal

Cell line	Genotype group	Fibroblast contamination	Morphology
9203	PK	negative	epithelial
9255	PKP	positive	mesenchymal
9366	PKP	negative	epithelial
9471	PPI3K	negative	quasi-mesenchymal
9580	PPI3K	negative	quasi-mesenchymal
9591	PK	negative	epithelial
9784	PKP	positive	mesenchymal
9793	PKPI3KP	positive	mesenchymal
9794	PK	positive	quasi-mesenchymal
9795	PKPI3K	negative	quasi-mesenchymal
9924	PKP	positive	mesenchymal
9960	PPI3K	negative	quasi-mesenchymal
9964	PK	negative	epithelial
9965	PKPI3K	negative	quasi-mesenchymal
AA120	PKC	negative	quasi-mesenchymal
AA1229	PKC	negative	quasi-mesenchymal
AA1261	PKC	negative	quasi-mesenchymal
AA1377	PKC	negative	epithelial
AA1467	PKC	negative	quasi-mesenchymal
AA168	PKC	negative	epithelial
AA169	PKC	negative	epithelial
AA172	PKC	negative	epithelial
AA199	PKC	negative	quasi-mesenchymal
AA651	PKC	negative	quasi-mesenchymal
AA765	PKC	negative	mesenchymal
AA766	PKC	negative	mesenchymal
AA785	PKP	negative	quasi-mesenchymal
AA821	PKC	negative	mesenchymal
AA852	PKC	negative	epithelial
AA854	PKC	negative	epithelial
AA966	PKP	negative	epithelial
AK1301	PPI3K	negative	mesenchymal
AK453	PPI3KP	negative	mesenchymal
AK496	PPI3KP	negative	mesenchymal
AK501	PPI3KP	negative	mesenchymal
AK5299	PPI3K	negative	epithelial
AK594	PPI3KP	negative	quasi-mesenchymal
AK596	PPI3KP	negative	quasi-mesenchymal
AK635	PPI3KP	negative	mesenchymal
AK693	PPI3KP	negative	quasi-mesenchymal
B127	PKP	positive	mesenchymal
B191	PKP	negative	quasi-mesenchymal
B212	PKP	negative	mesenchymal
B231	PKP	negative	epithelial
B590	PK	negative	epithelial
BR19	PBRC	negative	epithelial
BR230	PBRC	negative	mesenchymal

Cell line	Genotype group	Fibroblast contamination	Morphology
BR55	PBRC	negative	epithelial
BR63	PBRPC	negative	epithelial with fibroblasts
C065	PKT	negative	quasi-mesenchymal
C1232	PKE	negative	epithelial
C147	PKPT	negative	epithelial
C1530	PK	negative	quasi-mesenchymal
C1607	PK	negative	mesenchymal
C1609	PK	negative	mesenchymal
C1612	PKPT	negative	epithelial
C1696	PK	negative	mesenchymal
C1763	PKPT	negative	quasi-mesenchymal
C2118	PK	negative	quasi-mesenchymal
C2473	PKP	negative	epithelial
C2514	PKP	negative	epithelial
C2532	PKT	negative	mesenchymal
C2552	PKP	negative	epithelial
C2675	PKP	negative	quasi-mesenchymal
C2677	PKP	negative	epithelial
C2810	PKT	negative	epithelial
C2922	PKT	negative	epithelial
C3356	PKT	negative	quasi-mesenchymal
C3443	PKT	negative	epithelial
C4430	PKP	negative	epithelial
C4466	PKT	negative	quasi-mesenchymal
C4557	PKP	negative	epithelial
C4617	PKP	negative	epithelial
C4692	PKP	negative	epithelial
C4722	PKP	negative	epithelial
C5081	PKT	negative	quasi-mesenchymal
C5310	PKP	negative	epithelial with fibroblasts
C5315	PKP	negative	quasi-mesenchymal
C5389	PKP	negative	mesenchymal
C5599	PK	negative	epithelial
C5835	PKP	negative	mesenchymal
C6037	PKPT	negative	epithelial
CF001-1	PKPI3K	negative	quasi-mesenchymal
CF001-2	PKPI3K	negative	quasi-mesenchymal
CF002-1	PKPI3K	negative	epithelial
CF002-2	PKPI3K	negative	epithelial
CR15798	PK	negative	epithelial
E126	PPI3K	positive	quasi-mesenchymal
E208	PPI3K	positive	mesenchymal
E234	PPI3K	negative	epithelial
E440	PPI3KPC	negative	mesenchymal
E915	PKPI3K	negative	epithelial

Cell line	Genotype group	Fibroblast contamination	Morphology
KG471	PKT	negative	quasi-mesenchymal
KG486	PKPT	negative	quasi-mesenchymal
KG513	PKP	negative	epithelial
KG564	PKP	negative	epithelial with fibroblasts
KG6290	PKP	negative	quasi-mesenchymal
MG172	PBRC	negative	epithelial
MG846	PKP	negative	mesenchymal
MZ1380	PKTo	negative	quasi-mesenchymal
MZ1730	PKTo	negative	quasi-mesenchymal
P1162	PKSC	negative	epithelial
P1956	PKSC	negative	mesenchymal
P2313	PKC	negative	mesenchymal
P2324	PKS	negative	quasi-mesenchymal
P2345	PKS	negative	mesenchymal
P2347	PKS	negative	mesenchymal
P3066	PKSC	negative	epithelial
P3272	PKS	negative	mesenchymal
P348	PKS	negative	mesenchymal
P3532	PKP	negative	quasi-mesenchymal
P4162	PKS	negative	epithelial
P4470	PKSC	negative	epithelial
P4492	PKP	negative	quasi-mesenchymal
P4828	PKS	negative	quasi-mesenchymal
P5078	PKC	negative	epithelial
P5142	PKSC	negative	mesenchymal
P5166	PKSC	negative	mesenchymal
P5187	PKSC	negative	mesenchymal
R1035	PK	negative	epithelial
R211	PKP	negative	quasi-mesenchymal
R254	PKP	negative	epithelial
R259	PKP	negative	epithelial
R4694	PKP	negative	epithelial
R4765	PKP	negative	epithelial
R6827	PKCSm	negative	epithelial
R6888	PKCSm	negative	quasi-mesenchymal
R7024-2	PKPCSm	negative	quasi-mesenchymal
R7102	PKPCSm	negative	quasi-mesenchymal
R7108	PKPCSm	negative	epithelial
R7121	PKPCSm	negative	epithelial
R7136-1	PKPCSm	negative	epithelial
R7136-2	PKPCSm	negative	epithelial
R7153	PKPCSm	negative	epithelial
S1145	PKP	negative	epithelial
S134	PK	negative	mesenchymal
S302	PK	negative	quasi-mesenchymal
S411	PK	negative	mesenchymal

Cell line	Genotype group	Fibroblast contamination	Morphology
S559	PK	negative	mesenchymal
S821	PK	negative	quasi-mesenchymal
S908	PKP	negative	mesenchymal
S914	PK	negative	mesenchymal
SB1381-1	PKT	negative	epithelial
SB1382-1	PKSm	negative	mesenchymal
SB1382-2	PKSm	negative	mesenchymal
SB1382-3	PKSm	negative	quasi-mesenchymal
SB1412-1	PKPT	negative	epithelial
SB1437-1	PKT	negative	quasi-mesenchymal
SB1516-2	PKPT	negative	epithelial
SB1551-1	PKT	negative	epithelial
SB1614-5	PKSm	negative	mesenchymal
SB1672-2	PKTSm	negative	mesenchymal
SB1751-1	PKSm	negative	epithelial
SB1751-4	PKSm	negative	epithelial
SB1751-5	PKSm	negative	epithelial
SC3701	PKC	negative	quasi-mesenchymal
SC5406	PKC	negative	quasi-mesenchymal
SC5711	PKSC	negative	quasi-mesenchymal
SC5815	PKSC	negative	mesenchymal
SC5847	PKC	negative	quasi-mesenchymal
SC5877	PKC	negative	mesenchymal
SC5881	PKSC	negative	quasi-mesenchymal
SC6039	PKSC	negative	quasi-mesenchymal
V4706	PK	negative	epithelial
W22	PKP	negative	mesenchymal

4.12 Human cell lines

All human cell lines used in this thesis were authenticated as described in Chapter 5.3.5. Only verified and unique cell lines were used. All primary human cell lines were confirmed to be free of murine contamination by PCR as described in Chapter 5.3.10. The cell line SMJ98 was initially murine contaminated and was only used after confirmed removal of the contamination which was performed according to Chapter 5.1.4. All human cell lines used in this thesis were tested negative for mycoplasma contamination (tested as described in Chapter 5.1.2, 5.3.8). The cell line SMJ7 was initially mycoplasma positive (passage 8) and was used only after being confirmed negative after mycoplasma removal (passage 23). All primary human cell lines were tested negative for contamination with pathogenic viruses (tested as described in Chapter 5.3.11). Commercial cell lines were provided free of virus contamination by the vendor.

Table 4-17: Overview of human cell lines used for this thesis with information on source, culturing conditions and RRID number.

Cell line	Source	Medium	FCS	RRID number
AsPC1	AG Rad (TUM)	RPMI	10 %	CVCL_0152
B250	AG Reichert (TUM)	RPMI	20 %	NA
B403	AG Reichert (TUM)	RPMI	20 %	NA
BxPC3	AG Rad (TUM)	RPMI	10 %	CVCL_0186
Capan1	AG Rad (TUM)	DMEM	10 %	CVCL_0237
DanG	AG Rad (TUM)	RPMI	10 %	CVCL_0243
EngB	AG Saur (TUM) (Eser et al. 2013)	RPMI	20 %	NA
GCDX13	AG Hessmann (UMG)	RPMI	20 %	NA
HPAC	AG Rad (TUM)	RPMI	10 %	CVCL_3517
Hs766T	AG Rad (TUM)	DMEM	10 %	CVCL_0334
HucK	AG Saur (TUM) (Eser et al. 2013)	RPMI	20 %	NA
Hupt4	AG Rad (TUM)	DMEM	10 %	CVCL_1300
IMIM-PC1	AG Rad (TUM)	RPMI	10 %	CVCL_4061
KP4	AG Rad (TUM)	RPMI	10 %	CVCL_1338
LohC	AG Saur (Eser et al. 2013)	RPMI	20 %	NA
MiaPaca2	AG Rad (TUM)	DMEM	10 %	CVCL_0428
Pacadd119	DSMZ	RPMI	20 %	CVCL_1848
Pacadd135	DSMZ	RPMI	20 %	CVCL_1849
Pacadd137	DSMZ	RPMI	20 %	CVCL_1850
Pacadd159	DSMZ	RPMI	20 %	CVCL_M465
Pacadd161	DSMZ	RPMI	20 %	CVCL_M466
Pacadd165	DSMZ	RPMI	20 %	CVCL_M467
Panc1	AG Rad (TUM)	DMEM	10 %	CVCL_0480
Panc0327	AG Rad (TUM)	RPMI	10 %	CVCL_1635
Panc0403	AG Rad (TUM)	RPMI	10 %	CVCL_1636
Panc1005	AG Rad (TUM)	RPMI	10 %	CVCL_1639
Patu8902	AG Rad (TUM)	RPMI	10 %	CVCL_1845
Patu8988S	AG Rad (TUM)	DMEM	10 %	CVCL_1846
PDC40	AG Kong (Ulm)	Advanced DMEM	10 %	NA
PDC49	AG Kong (Ulm)	Advanced DMEM	10 %	NA
PDC56	AG Kong (Ulm)	Advanced DMEM	10 %	NA
PL45	AG Rad (TUM)	RPMI	10 %	CVCL_3567
Psn1	AG Rad (TUM)	RPMI	10 %	CVCL_1644
SMJ7	AG Saur (Eser et al. 2013)	RPMI	20 %	NA
SMJ31	AG Saur (Eser et al. 2013)	RPMI	20 %	NA
SMJ98	AG Saur (Eser et al. 2013)	RPMI	20 %	NA
SW1990	AG Rad (TUM)	DMEM	10 %	CVCL_1723
YAPC	AG Rad (TUM)	RPMI	10 %	CVCL_1794

4.13 Software

Table 4-18: Software.

Software	Source
CyBio® Composer	Analytik Jena, Jena, Germany
Excel, RRID:SCR_016137	Microsoft Corporation, Redmont, WA, USA
GraphPad Prism 5, RRID:SCR_002798	Graphpad Software, Inc, La Jolla, CA, USA
Momentum Integration Software	Thermo Fisher Scientific, Waltham, Massachusetts, USA
RStudio, RRID:SCR_000432	RStudio, Inc., Boston, Massachusetts, USA
Seahorse Wave 4.2.2, RRID:SCR_014526	Agilent Technologies, Santa Clara, USA
Snapgene Viewer, RRID:SCR_015052	GSL Biotech LLC, San Diego, USA
Unipro Ugene, RRID:SCR_005579	Unipro LLC, Akademgorodok, Russia
ZEN 2 (blue edition), RRID: SCR_013672	Carl Zeiss AG, Oberkochen, Germany

5 Methods

5.1 Cell culture

5.1.1 Culture of PDAC cell lines

Cells were cultured in cancer cell medium (DMEM, Advanced DMEM or RPMI supplemented with 10 % or 20 % FCS and 1 % penicillin/streptomycin) at 37 °C, 5 % CO_2 and 100 % humidity.

For passaging of cells, the medium was aspirated, the cells were washed with PBS and then incubated with Trypzean® solution at 37 °C. To stop the trypsinization reaction, medium was added, and the cell suspension was transferred to a falcon tube and centrifuged at 1000 rpm for 5 minutes. The supernatant was removed, and the cells were resuspended in medium and seeded into a new vessel at an appropriate dilution depending on the experiment. Cell numbers were determined by a Neubauer hemacytometer.

For cryopreservation, cells were trypsinized, resuspended and centrifuged at 1000 rpm for 5 minutes. The supernatant was discarded, and the cell pellet was resuspended in ice-cold freezing medium (DMEM with 20 % FCS and 10 % DMSO) and transferred to CryoPure tubes. The cells were frozen at -80°C and subsequently stored in liquid nitrogen.

5.1.2 Mycoplasma test

For mycoplasma testing, cells were cultivated in 6-well plates in medium without antibiotics for at least two weeks until the cells were almost 100 % confluent. 2 ml of supernatant were taken and centrifuged at 250×g for 2 minutes. The supernatant was transferred in new tube and centrifuged at 20’000×g for 10 minutes. The supernatant was discarded, and the pellet resuspended in 50 µl PBS and heated to 95 °C for 3 minutes. The samples were then used for mycoplasma test PCRs (Chapter 5.3.8).

All cell lines used for this thesis were routinely tested for mycoplasma contamination and only those with a confirmed negative result were used in experiments. All cell lines were tested during expansion for the automated high-throughput drug screen (Chapter 5.2), so that only cells from a confirmed negative stock were used for the drug screening procedure. Mycoplasma tests were repeated for the vial of cells used for the screen and a negative result was confirmed for all used cell lines.

5.1.3 Mycoplasma removal

MycoRAZOR® antibiotics reagent was used to remove mycoplasma contamination from cell cultures. The manufacturer's instructions were followed. 1:25 and 1:50 dilutions of the reagent were used. The cell lines 8349 (positive at passage 12, negative at passage 29) and SMJ7 (positive at passage 8, negative at passage 23) were subjected to mycoplasma removal by this procedure.

5.1.4 Removal of murine contamination by differential trypsinization

The cell line SMJ98 used in this thesis was initially tested positive for murine contamination (tested according to 5.3.10). As murine cells generally detach faster upon Trypzean® treatment than human cells, a method called differential trypsinization was used to remove the contamination. To this end, the normal procedure for passaging of cells was followed (Chapter 5.1.1), but before all cells were detached, the trypsinization reaction was stopped by adding medium. After removal of the first fraction of cells, Trypzean® solution was added again to detach the second fraction. This procedure was repeated several times until murine contamination could no longer be detected by PCR (Chapter 5.3.10). The cell line SMJ98 was tested positive at passage 8 and was used at passage 37-38 after repeated confirmation of murine cell removal.

5.1.5 CellTiter-Glo® Assay

CellTiter-Glo® Assay was performed to assess cell viability. Cells were seeded in appropriate densities (500-3000 cells/well) in 96-well plates. At the end of the assay, 25 µl CellTiter-Glo® reagent was added to each well, the plates were incubated for 10 minutes on a shaker protected from light and luminescence was measured in a plate reader.

5.1.6 Caspase-Glo® 3/7 Assay

Caspase-Glo® 3/7 Assay was performed to assess apoptosis. 1000 cells per well were seeded in 96-well plates. On the next day, the cells were treated with inhibitors. 24 hours after the start of the treatment, 100 µl Caspase-Glo® was added to each well, the contents were mixed for 30 seconds on a shaker and then plates were incubated for 30 minutes protected from light. Luminescence was measured according to the manufacturer's instructions.

5.1.7 Clonogenic assays

For clonogenic assays, 1000-2000 cells per well, depending on the growth rate of the cell line, were seeded into 24-well plates. Drug treatment was started the following day. The plates were incubated at 37 °C and 5 % CO_2. Depending on the confluence of the vehicle-treated control, 7-13 days after the beginning of the drug treatment, the cells were washed with PBS and stained with Crystal Violet solution (2.5 % (v/v) EtOH and 4 % (w/v) Crystal Violet in H_2O). After incubating on a shaker at room temperature for 30 minutes, the wells were washed three times with tap water and then dried. Visualization of the stained colonies was performed using a photo scanner. For quantification, crystal violet stain was solubilized with 1 % SDS and absorbance was measured at 595 nm.

5.1.8 Culturing of cells in glucose/galactose conditions

For experiments in glucose/galactose conditions, DMEM medium lacking glucose was supplemented with dialyzed FCS and either 10 mM glucose or 10 mM galactose.

5.1.9 Seahorse Assay – Cell Mito Stress Test and Glycolytic Stress Test

For Seahorse assay analyses, 5000 cells per well were seeded in quadruplets in 80 µl DMEM (supplemented with 10 % FCS and 1 % Penicillin/Streptomycin) in a Seahorse cell culture plate. The wells at the four edges were left empty. As a control for cell viability, a 96-well plate was prepared in the same manner for Cell Titer Glo measurement. On the next day, NSC319726 and DMSO for the control wells were added in 20 µl medium. One day prior to the final measurement, the cartridge was hydrated by adding 200 µl H_2O to each well. The cartridge and the calibration solution were incubated overnight at 37 °C and 0 % CO_2. The H2O in the cartridge was changed to 200 µl pre-warmed calibration solution at least one hour before the measurement. For the Mito stress test, 5 g/L glucose was added to the Seahorse medium and the pH was adjusted to 7.4. The medium in the Seahorse plate was changed to 180 µl of the glucose supplemented Seahorse medium one hour before the measurement. The loading of the Seahorse plate ports was as follows: Port A) 20 µl of 20 µg/ml Oligomycin; Port B) 22 µl of 10 µM FCCP and 50 mM Pyruvate; Port C) 25 µl of 25 µM Rotenone and 25 µM Antimycin-A. For the glycolytic stress test, one hour before the measurement, the medium in the Seahorse plate was changed to Seahorse medium without glucose supplementation. The ports were loaded as follows: A) 20 µl of 100 mM Glucose; Port B) 22 µl of 20 µg/ml Oligomycin; Port C) 25 µl of 1 mM 2-desoxy-D-glucose. Analysis of the

Seahorse plate was done in a Seahorse XFe96 Analyzer. Cell viability in the parallelly prepared 96-well plate was measured using CellTiter-Glo® Assay. The ECAR and OCR values were calculated in relation to cell viability. Calculation of the different parameters was done as described by the manufacturer.

5.1.10 Growth curves and doubling time calculation

Cells were counted and cell suspensions with 5000, 10000 and 20000 cells/ml were prepared. Five 96-well plates with 3 wells of each concentration in 100 µl were seeded. On each of the following days, one plate was used for CellTiter-Glo® Assay as described in Chapter 5.1.5. After collecting the data for all time points for all concentrations, each time point was normalized to the first day of measurement (day 0). The normalized values were plotted using the GraphPad Prism software. Doubling times were calculated using the following formula:

$$DoublingTime = 72\ hours * \frac{\log(2)}{\log\left(\frac{mean\ Cell\ Titer\ Glo\ value\ on\ Day\ 3}{mean\ Cell\ Titer\ Glo\ value\ on\ Day\ 0}\right)}$$

5.2 Automated high-throughput drug screening

5.2.1 Automated cell seeding

Before changing the seeded cell line, each valve of the Multiway Valve attached to the Multidrop™ Combi Reagent Dispenser equipped with a Standard Tube Dispensing Cassette was routinely washed with water and ethanol.

Cells were detached as described in Chapter 5.1.1. After centrifugation and resuspension in medium, the cells were filtered using a 70 µm filter. The cells were counted using Trypan Blue Solution and a Neubauer counting chamber. The medium supplemented with FCS and Penicillin/Streptomycin was filtered using a 0.22 µm filter top. The same batch of FCS was used for the entire screen. A cell suspension with 7500-30000 cells/mL was prepared. The cells were seeded in technical duplicates in 96-well plates using 100 µl/well using the Multiway Valve and Multidrop™ Combi Reagent Dispenser. The plates were transferred onto the Multidrop™ Combi Reagent Dispenser and afterwards into a Cytomat™ 24C automated incubator using a Spinnaker automation system. The cells were incubated overnight at 37 °C and in 88 % humidity and 5 % CO_2.

After cell seeding, each valve of the Multiway Valve attached to the Multidrop™ Combi Reagent Dispenser was routinely washed with PBS, water and 0.1 % Tween in water.

5.2.2 Automated drug treatment

The drug library was diluted beforehand in barcoded 384-well plates using a CyBio® FeliX pipetting platform equipped with a pipetting adaptor. Each drug was diluted to seven concentrations (3-fold dilution series, highest concentration in the "source" plate 10 mM). To reduce edge effects (Mansoury et al. 2021), the highest concentrations of each drug were kept at the edge of the plate (rows A and H) and the DMSO control was pipetted into row D. All stock solutions were purchased from SelleckChem dissolved at 10 mM either in DMSO or water. The drug library was used for up to ten freeze-thaw cycles.

Drug treatment with the compound library was performed after overnight incubation of the cells using the CyBio® FeliX pipetting platform equipped with a 96-well Pintool. The Pintool was initially washed with V&P solution and water. The plates were loaded into the CyBio® FeliX pipetting platform using the Spinnaker automation system. The Pintool was used to transfer the diluted drugs from the barcoded 384-well plate to the cell culture plate. 100 nL of drug were transferred (highest final concentration 10 µM). After each treated cell culture plate, the Pintool was washed with DMSO:H2O (1:1) and Isopropanol using a Masterflex Easy-Load pump connected to washing stations. At the end of the day, the Pintool was again washed with V&P solution and water.

5.2.3 Automated cell viability measurement

Cell viability was measured on the third day after drug treatment using CellTiter-Glo® Luminescent Cell Viability Assay. The Multidrop™ Combi Reagent Dispenser was washed with water and then connected to the filtered (using a 0.22 µm filter) CellTiter-Glo® reagent. Using the Spinnaker automation system, the plates were transferred from the Cytomat™ 24C automated incubator to the Multidrop™ Combi Reagent Dispenser where 25 µl of CellTiter-Glo® Luminescent Cell Viability Assay reagent were added to each well. After incubation at room temperature for 10 minutes, luminescence was measured using a microplate reader.

5.2.4 Primary analysis of high-throughput drug screening data

The raw data obtained as described in Chapters 5.2.1-5.2.3. was processed using the R package GRmetrics (version 4.0.3) (Hafner et al. 2016; Clark et al. 2017). The AUC values derived from this initial analysis were used in further downstream analyses. The AUC values for three cell line – drug pairs were excluded from all analyses (mean AUC > 3, C1530 treated with GSK923295 and Oprozomib, W22 treated with Thiomyristoyl) as they would strongly bias for example principal component analyses. Their respective dose response curves are shown in Figure 32. Standard deviations for the AUC values between replicates ranged between 8 and 1015 for these pairs indicating non-reliable data.

5.2.5 Automated combinatorial drug screening

Cells were seeded as described in Chapter 5.2.1. One technical replicate each was seeded for monotherapy and combination treatment. Drug treatment was performed as described in Chapter 5.2.2, except that for the combination treatment, the Pintool was used to transfer drugs from the 384-well plate containing library drugs, then washed and subsequently used to transfer the “anchor drugs” from another manually diluted 384-well plate. The anchor drugs were given in one concentration (Afatinib: 0.2 µM, Paclitaxel: 0.01 µM). Cell viability measurements were performed after 72 hours as described in Chapter 5.2.3.

5.2.6 Analysis of combinatorial drug screening

The R package GRmetrics (version 4.0.3) (Hafner et al. 2016; Clark et al. 2017) was used to generate dose-response curves and calculate AUC values for both monotherapy and combination treatment. The Bliss independence model (BLISS 1939) was used to calculate expected AUC values for the combinations. Delta AUC values, calculated by subtraction of expected AUC values from observed AUC values, were used as proxy for synergy.

5.2.7 Comparison of drug screening data to publicly available datasets

GDSC2 (Picco et al. 2019), CTRP (Seashore-Ludlow et al. 2015; Rees et al. 2016) and PRISM (Corsello et al. 2020) datasets were downloaded from the DepMap Portal website (https://depmap.org/portal/download/all/, downloaded in November 2022). Compound names

were manually curated and harmonized between the datasets. Pearson correlation values were calculated across all AUC values for overlapping cell line – drug pairs.

5.3 Molecular biology techniques

5.3.1 DNA isolation from cells for genotyping PCRs

Cells were pelleted at 1000 rpm for 5 minutes. The medium was removed, and the pellet washed with PBS. After centrifugation at 1000 rpm for 5 minutes, the supernatant was discarded, and the pellet was resuspended in 50 µl Soriano lysis buffer supplemented with DTT. The samples were briefly centrifuged and incubated at 55 °C for 2 hours and 95 °C for 15 minutes. Afterwards, the samples were vortexed and centrifuged at 4 °C at full speed for 10 minutes. 40 µl of the supernatants were pipetted into PCR strips which were briefly centrifuged and stored at -20 °C. The maximum volume used for PCR was 1 µl.

5.3.2 Genomic DNA isolation from cells for sequencing and genotyping PCRs

Genomic DNA was isolated using the GenElute™ Mammalian Genomic DNA Miniprep Kit. A cell pellet was obtained by trypsinization and centrifugation in a 1.5 ml tube at 1000 rpm for 5 minutes. The cell culture medium was removed, and the cell pellet resuspended in 200 µl resuspension solution. 20 µl of Proteinase K were added, followed by 200 µl of lysis solution C. The sample was mixed by vortexing for about 15 seconds and incubated at 70 °C for 10 minutes. The GenElute™ Miniprep Binding Column was prepared by adding 500 µl of Column Preparation Solution followed by centrifugation at 12000×g for 1 minute. The flow-through was discarded. 200 µl 100 % ethanol were added to the lysate which was subsequently mixed thoroughly by vortexing for 10 seconds. The entire lysate was transferred to the pre-treated GenElute™ Miniprep Binding Column and centrifuged at 7000×g for 1 minute. The binding column was placed in a new 2 ml collection tube and washed with 500 µl Wash solution. After centrifugation at 7000×g for 1 minute, the flowthrough was discarded, and the binding column was placed in a new 2 ml collection tube. The column was washed with another 500 µl of Wash Solution and centrifuged at 16000×g for 3 minutes. 80 µl of Elution Solution were added to the binding column, then it was incubated for 5 minutes at room temperature and finally centrifuged at 7000×g for 1 minute. The concentration of genomic DNA was then measured using a NanoPhotometer® or Qubit device.

5.3.3 Genomic DNA isolation from tails for sequencing and genotyping PCRs

Genomic DNA from tails was isolated using the GenElute™ Mammalian Genomic DNA Miniprep Kit. Frozen mouse tails were cut into small pieces using a scalpel and placed in a 1.5 ml tube. 180 ml of Lysis Solution T were added, followed by 20 µl of Proteinase K. The sample was incubated shaking at 55 °C overnight. 200 µl of Lysis Solution C were added and the sample was subsequently vortexed. The GenElute™ Miniprep Binding Column was prepared as described in Chapter 5.3.2. All subsequent steps were followed as described in Chapter 5.3.2. The concentration of genomic DNA was then measured using a NanoPhotometer® or Qubit device.

5.3.4 Isolation of DNA from formalin-fixed, paraffin-embedded tissue for sequencing and genotyping PCRs

At least 5 sections of 10 µm thickness were cut from tissue blocks using a cryotome and collected in a 1.5 ml Eppendorf tube. The tube was centrifuged at full speed for one minute. 1 ml Histoclear was added, the samples were vortexed for 10 seconds and centrifuged at full speed for one minute. The supernatant was discarded and 0.5 ml Histoclear were added. The samples were again vortexed for 10 seconds and centrifuged at full speed for one minute. The supernatant was discarded, and the pellet was washed with 1 ml 100 % Ethanol. After vortexing and centrifugation at full speed for one minute, the supernatant was discarded. The ethanol wash was repeated once. Residual ethanol was removed using a 10 µl pipette, the tube was opened, and the pellet dried at 37 °C for 10 minutes. The pellet was resuspended in 180 µl buffer ATL and 20 µl proteinase K. The sample was vortexed and incubated at 56 °C and 800 rpm for three hours and subsequently at 90 °C for one hour. The samples were briefly centrifuged and 200 µl buffer AL was added. After vortexing 200 µl 100 % Ethanol were added and the lysate was transferred to a QIAamp MinElute spin column. The samples were centrifuged at room temperature at 8000 rpm for 1 minute and the spin column was placed in a new collection tube. 500 µl AW1 buffer was added and after centrifugation at room temperature at 8000 rpm for 1 minute, the spin column was again placed in a new collection tube. The same washing step was then performed using 500 µl AW2 buffer. Afterwards, the samples were centrifuged at full speed for 3 minutes to dry the membrane. The spin column was then placed in a 1.5 ml tube and 20 µl of buffer AE were added. After incubation at room temperature for 10 minutes, the samples were centrifuged at full speed for 1 minute to elute the DNA. The eluate was again transferred to the spin column

and centrifugation at full speed for 1 minute was repeated. The DNA concentration was measured using a Qubit device.

5.3.5 Authentication of human cell lines

All human cell lines were authenticated either by Single Nucleotide Polymorphism (SNP)-Profiling or by Short Tandem Repeat (STR) Profiling conducted by Multiplexion (Multiplexion GmbH, Heidelberg, Germany) in August 2022. Only cell lines with confirmed identity and uniqueness were used in this thesis.

5.3.6 Detection of *Kras* mutations in primary human cell lines

Cancer cell line status for all primary human cell lines was confirmed by detection of *Kras* mutations by Sanger Sequencing. To this end, DNA isolated according to Chapter 5.3.2 was sent to Eurofins (Ebersberg, Germany) with the primers hKras_ex2_flank_Fw and hKras_ex2_flank_Rv listed in Table 4-10. The sequences were analyzed using UniPro UGene (Version 35) or Snapgene Viewer (Version 6.0.2).

5.3.7 Polymerase Chain Reaction (PCR)

Taq DNA Polymerase 2x-PreMix was used for mouse regenotyping, mycoplasma and virus contamination testing. The general reaction setup for regenotyping PCRs is shown in Table 5-1. The thermocycler program is shown in Table 5-2. The annealing temperatures and PCR products are listed in Table 5-3.

Table 5-1: Reaction setup for regenotyping PCRs.

Component	Volume
Template DNA	1 µl (ca. 100 ng)
2x PCR Master Mix	12.5 µl
10 µM Forward Primer	1 µl
10 µM Reverse Primer	1 µl
Distilled water	9.5 µl

Table 5-2: Thermocycler program for regenotyping PCRs.

Temperature	Time	
95 °C	3 minutes	
95 °C	30 seconds	
Tm – 5 °C	30 seconds	40 cycles
72 °C	60 seconds/kb	
72 °C	15 minutes	
16 °C	∞	

Table 5-3: Annealing temperatures and PCR products.
(Mut=Mutant Allele; WT=Wild Type Allele; Rec=Recombined Allele).

PCR reaction	Annealing temperature	Size of PCR product(s)
Ptf1a-Cre	60 °C	400 bp (mut), 600 bp (WT)
Pdx1-Cre	64 °C	674 bp (mut), 202 bp (internal control)
Pdx-Flp	56 °C	620 bp (Mut), 300 bp (internal control)
LSL-Kras^{G12D}	55 °C	170 bp (mut), 270 bp (WT), 300 bp (rec)
FSF-Kras^{G12D}	55 °C	351 bp (mut), 270 bp (WT)
LSL-Trp53^{R172H}	60 °C	270 bp (mut), 570 bp (WT), 600 bp (rec)
LSL-Trp53^{R172H} (deleted stop cassette)	55 °C	330 bp (mut), 290 bp (WT)
Trp53^{lox}	64 °C	370 bp (mut), 288 bp (WT)
Trp53^{frt}	57 °C	292 bp (mut), 258 bp (WT)
Pik3ca^{H1047R}	60 °C	629 bp (mut), 550 bp (del)
Cdkn2a^{lox}	58 °C	180 bp (mut), 140 bp (WT), 220 bp (unspecific)
LSL-Braf^{V637E}	55 °C	660 bp (mut), 400 bp (WT)
p16^{Ink4a*}	60 °C	600 bp (mut), 500 bp (WT)

5.3.8 PCR for mycoplasma contamination

For mycoplasma testing, samples were prepared as described in Chapter 5.1.2. A forward primer mix was prepared using 10 µl of each forward primer (listed in Table 4-11) and 30 µl H_2O. A reverse primer mix was prepared using 10 µl of each reverse primer (listed in Table 4-11) and 70 µl H_2O. The reaction setup for mycoplasma test PCRs is shown in Table 5-4. The thermocycler program is listed in Table 5-5. The product size produced by a positive culture is 200 bp.

Table 5-4: Reaction setup for mycoplasma test PCRs.

Component	Volume
15µl Premix	15µl Premix
2µl forward-Primer-Mix	2µl forward-Primer-Mix
2µl reverse-Primer-Mix	2µl reverse-Primer-Mix
9µl H_2O	9µl H_2O
15µl Premix	15µl Premix

Table 5-5: Thermocycler program for mycoplasma test PCRs.

Temperature	Time	
95 °C	15 minutes	
94 °C	60 seconds	
60 °C	60 seconds	40 cycles
74 °C	60 seconds	
72 °C	10 minutes	
16 °C	∞	

5.3.9 Test for human contamination of murine cell lines

To test for human contaminations in murine cell cultures, the primers listed in Table 4-9 were used. The reaction setup is described in Table 5-6. The thermocycler program is listed in Table 5-6.

Table 5-6: Reaction setup for testing for human contamination in murine cell lines

Component	Volume
Template DNA	1 µl (ca. 100 ng)
2x PCR Master Mix	12.5 µl
10 µM Forward Primer Kras_hu_G12D_fw	0.6 µl
10 µM Reverse Primer Kras_hu_G12D_rev	0.6 µl
Distilled water	10.3 µl

Table 5-7: Thermocycler program for testing for human contamination in murine cell lines.

Temperature	Time	
95 °C	3 minutes	
95 °C	45 seconds	
58 °C or 60 °C	60 seconds	40 cycles
72 °C	90 seconds	
72 °C	15 minutes	
16 °C	∞	

5.3.10 Test for murine contamination of human cell lines

All primary human cell lines used in this thesis were tested negative for murine contamination according to the test described below, except for the cell line SMJ98 which was subjected to differential trypsinization (described in Chapter 5.1.4).

To test for murine contaminations in human cell cultures, the primers listed in Table 4-10 were used. The reaction setup is listed in Table 5-8. The thermocycler program is shown in Table 5-9.

Table 5-8: Reaction setup for testing for murine contaminations in human cell cultures.

Component	Volume
Template DNA	1 µl (ca. 10 ng)
2x PCR Master Mix	12.5 µl
10 µM Forward Primer mKras_ex2_flank_Fw	0.6 µl
10 µM Reverse Primer mKras_ex2_flank_Rv	0.6 µl
Distilled water	10.3 µl

Table 5-9: Thermocycler program for testing for murine contaminations in human cell cultures.

Temperature	Time	
95 °C	3 minutes	
95 °C	45 seconds	
58 °C or 60 °C	60 seconds	40 cycles
72 °C	90 seconds	
72 °C	15 minutes	
16 °C	∞	

5.3.11 Test for virus contamination of human cell lines

All human cell lines used in this thesis were tested negative for HIV-1, HIV-2, HBV and HCV. To test for contamination with these pathogenic viruses, DNA was isolated as described in Chapter 5.3.2. For HCV testing, RNA was isolated from cell lines according to Chapter 5.3.13 and reverse transcribed to obtain cDNA as described in Chapter 5.3.14. Subsequently, samples were subjected to PCR as shown in Table 5-10. The thermocycler program is described in Table 5-11 and PCR products are listed in Table 5-12.

Table 5-10: Reaction setup for virus contamination tests

HIV-1		**HIV-2**		**HBV**		**HCV**	
S mix	25 µl	S mix	12.5 µl	S mix	25 µl	S mix	12.5 µl
Primer F-HIV	1.2 µl	Primer F-HIV2	0.4 µl	Primer F-HEBP	1.2 µl	Primer F-HCV	0.1 µl
Primer R-HIV	1.2 µl	Primer R-HIV2	0.4 µl	Primer R-HEBP	1.2 µl	Primer F-HCV-2	0.1 µl
Primer hKras fw	1.25 µl	Primer R-HIV2-2	0.4 µl	Primer hKras fw	1.25 µl	Primer R-HCV	0.1 µl
Primer hKras rv	1.25 µl	Primer Fw-Braf	0.4 µl	Primer hKras rv	1.25 µl	Primer Fw-beta-actin	0.1 µl
		Primer Rv-Braf	0.4 µl			Primer Rv-beta-actin	0.1 µl
						DMSO	1.2 µl
H2O	20.1 µl	H2O	10.5 µl	H2O	19.7 µl	H2O	1.2 µl
DNA	200 ng	DNA	200 ng	DNA	200 ng	cDNA	1 µl
psPAX2	10 ng	pEX-128-HA-MS-2	10 ng	HBV-1.6mer	10 ng	pFR_HCV_xb	10 ng

Table 5-11: Thermocycler program for virus contamination tests

Temperature	Time	
95 °C	2 minutes	
94 °C	30 seconds	
68 °C	30 seconds	15 cycles decreasing 1 °C each cycle (Touchdown PCR)
72 °C	1 minute	
94 °C	30 seconds	
52 °C	30 seconds	40 cycles
72 °C	1 minute	
72 °C	5 minutes	
4 °C	∞	

Table 5-12: PCR products of virus contamination tests

PCR reaction	Size of PCR product(s)
HIV-1	115 bp positive control 250 bp internal control
HIV-2	252 bp positive control 535 bp internal control
HBV	563 bp positive control 250 bp internal control
HCV	255 bp positive control 70 bp internal control

5.3.12 Agarose gel electrophoresis of PCR products

Agarose was dissolved in appropriate volumes of 1x TAE buffer to make 1 % - 2 % agarose gels by boiling for 10 minutes in a microwave. Ethidium bromide was added to the gel mixture before polymerization. The samples were loaded into the gel and the gel was run in 1x TAE buffer at 120 V. 5 µl DNA ladder (GeneRuler™ 100 bp DNA Ladder) was also loaded for estimation of the molecular weight. DNA fragments were visualized with UV light.

5.3.13 RNA isolation from cell cultures

Cells were grown on a 10 cm dish in the appropriate medium until they reached 60-80 % confluency. The cells were washed twice with ice-cold PBS. 500 µl of RLT buffer supplemented with 1:100 ß-mercaptoethanol were added to lyse the cells. The cells were

collected using a cell scraper. The cell solution was then transferred to a QiaShredder column and centrifuged at maximum speed for 2 minutes. The homogenized cells were snap-frozen and stored at -80 °C. RNA was isolated using the RNeasy Mini Kit according to the manufacturer's instructions. RNA concentration was determined using a NanoPhotometer®.

5.3.14 Reverse transcription

The general reaction setup for reverse transcription is shown in Table 5-13. The thermocycler program is detailed in Table 5-14.

Table 5-13: Reaction setup for reverse transcription.

Component	Final concentration
10x TaqMan RT buffer	1x
$MgCl_2$ (25 mM)	5.5 mM
dNTP Mix	500 µM each
Random hexamers	2.5 µM
RNAse inhibitor	0.4 U/µl
Multiscribe Reverse Transcriptase (50 U/µl)	1.25 U/µl
RNA	2 µg
RNase free water	Ad 100 µl

Table 5-14: Thermocycler program for reverse transcription

Temperature	Time
25 °C	10 minutes
48 °C	1 hour
95 °C	5 minutes
4 °C	∞

5.3.15 RNA sequencing and analysis

RNA sequencing was performed by the group of Prof. Roland Rad (TUM). RNA-seq library preparation and sequencing were carried out as described previously (Mueller et al. 2018). Computational analyses for the integration of RNA sequencing and drug screening data were performed by Fabio Boniolo as described in his doctoral dissertation (Boniolo 2022). The DESeq2 R package (version 1.26.0) was used for normalization and log-stabilization. For single-sample gene set enrichment analysis (ssGSEA), the R package GSVA (version 1.34.0) was used. PID pathways (Schaefer et al. 2009) used for pathway-based predictions of drug response were downloaded via the msigdbr R package (version 7.4.1) (Boniolo 2022).

5.4 Whole-genome CRISPR/Cas9 screen

5.4.1 Determination of lentiviral library titration

6 wells of a 12-well plate were seeded at a density of 3×10^6 in 2 mL medium per well with 8 µg/mL polybrene. 400 µl, 200 µl, 100 µl, 50 µl, 25 µl or 0 µl of lentivirus supernatant were added to the respective wells. After thoroughly mixing each well by pipetting up and down, the cells were spinfected by centrifuging at 1000×g for 2 hours at 33 °C. 24 hours after the end of spinfection, the medium was removed, cells were washed with PBS, trypsinized and counted. For each virus condition, 4 wells were seeded at a density of 4×10^3 cells in 100 µl medium in a 96-well clear-bottom tissue culture plate. 100 µl of medium with puromycin at a final concentration of 4 µg/mL were added to two wells and 100 µl of medium without antibiotics to the other two wells for each of the conditions. 96 hours after replating, when the no virus conditions were at 80 to 90 % confluency, cell viability for each condition was determined using CellTiter Glo® Assay (as described in Chapter 5.1.5). The percentage of surviving cells under antibiotics selection compared to the non-puromycin treated cells was plotted against the lentivirus volume. The amount of lentivirus to achieve 25 % survival was determined to be used in the genome-wide CRISPR/Cas9 screens.

5.4.2 Determination of drug concentration

The doses of Afatinib and Paclitaxel for the CRISPR/Ca9-based whole-genome screens were determined by culturing the cells with different concentrations of the compounds. For Afatinib treatment, 1.6 µM, 0.8 µM, 0.4 µM, 0.2 µM and 0.1 µM were used whereas for Paclitaxel, concentrations of 0.04 µM, 0.02 µM, 0.01 µM, 0.005 µM and 0.0025 µM were tested. 50’000 cells were well were seeded in 6-well plates. Treatment was performed in triplicates and was started 24 hours after cell seeding. The cells were passaged every 3-4 days and counted at each passage.

5.4.3 Lentiviral transduction for genome-wide screens

For the whole-genome wide screens, the cell line 9091 stably expressing Cas9 (“9091 Cas9”) provided by Sebastian Widholz (group of Prof. Roland Rad (TUM)) was used. This cell line was generated as previously described (Falcomatà et al. 2022). For screening, at least 140×10^6 cells were transduced per replicate to allow for a 500× coverage. The screen was performed in duplicates for each of the conditions (Afatinib treatment, Paclitaxel treatment, DMSO control) Cells were seeded at a density of 3×10^6 per well in 12-well plates

in a volume of 2 ml per well containing cell suspension, medium, 275 µl virus (as pre-determined according to Chapter 5.4.1) and 2 µl polybrene. The cells were spinfected by centrifuging the plates at 1000×g and 33 °C for 2 hours and then incubated at 37 °C overnight. On the next day, the cells were collected, pooled and plated in medium supplemented with puromycin at a final concentration of 4 µg/ml. After 4 days of puromycin selection, the medium was changed to antibiotics-free medium and the cells were allowed to recover for two days. The cells were then trypsinized, counted and 35×10^6 cells per condition were plated in 10 cm dishes at a density of 3.5×10^6 cells. One of the drugs (Afatinib at a final concentration of 0.2 µM or Paclitaxel at a final concentration of 0.01 µM) or DMSO were added. The cells were cultured in these conditions for two weeks with passaging being performed every three to four days. An appropriate cell number was replated at each passage to maintain the coverage of the library. Cell pellets were collected at each time point. Cell pellets frozen at the final time point were used for downstream processing as described in Chapter 5.4.4.

5.4.4 Isolation of genomic DNA from CRISPR screens

Genomic DNA (gDNA) from frozen cell pellets collected according to Chapter 5.4.3 was isolated using the Qiagen Blood & Cell Culture DNA Maxi Kit following the protocols provided by the manufacturer. The pellets were thawed and resuspended in PBS followed by lysis in Buffer C. The nuclei were then lysed in Buffer G2 and QIAGEN Proteinase K stock solution and incubated at 50 °C overnight. On the following day, the samples were applied to an equilibrated QIAGEN Genomic tip. The tip was then washed twice after which the DNA was eluted from the column, precipitated in Isopropanol and spooled with a Pasteur pipette. The spooled DNA was immediately transferred to a microcentrifuge tube containing 400 µL TE buffer and dissolved at 55 °C for 2 hours. The final DNA concentration was determined using a NanoPhotometer®.

5.4.5 Library preparation of CRISPR screen gDNA with Kapa HiFi

The reaction setup shown in Table 5-15 was used to amplify sgRNA sequences from genomic DNA obtained according to Chapter 5.4.4. The amounts shown in Table 5-15 were pipetted as 38 PCR reactions containing 50 µl each. A 500x coverage of the library was maintained. For each condition, a different combination of forward and reverse primers with unique sequencing-barcode indices was used. The cycling conditions used are shown in Table 5-16. After PCR, all 38 reactions were pooled and 10 µl were used for agarose gel

electrophoresis to confirm the presence of a band at 281 bp indicating successful amplification.

Table 5-15: Reaction setup for amplification of sgRNA sequences after CRISPR/Cas9 screening.

Component	Amount
gDNA	228 µg
Fw primer (10 µM)	76 µl
Rv primer (10 µM)	76 µl
KAPA HiFi Hot Start Master Mix 2X	950 µl
H_2O	ad 1900 µl

Table 5-16: Thermocycler program for amplification of sgRNA sequences.

Temperature	Time	
95 °C	3 minutes	
98 °C	20 seconds	
62 °C	30 seconds	28 cycles
72 °C	45 seconds	
72 °C	5 minutes	
16 °C	∞	

200 µl of the pooled PCR product were subjected to cleanup using the NEB Monarch PCR-cleanup kit according to the manufacturer's instructions. Elution was performed using 20 µl and Lo-Bind tubes.

Subsequent pooling, quantification and sequencing steps were performed by the group of Prof. Roland Rad (TUM) as previously described (Falcomatà et al. 2022).

5.4.6 Whole-genome CRISPR/Cas9 data analysis

Downstream analysis of whole-genome CRISPR/Cas9 data was performed with MAGeCK (version 0.5.9.4) (Li et al. 2014) as previously described (Falcomatà et al. 2022). In brief, reads obtained after sequencing and demultiplexing were aligned to reference sgRNA sequences and counting was performed. ß-scores were calculated using maximum likelihood estimation. Positive ß-scores indicate enrichment whereas negative ß-scores represent depletion of the sgRNAs compared to their initial abundance. To identify genes that are significantly depleted under Afatinib or Paclitaxel treatment, the differences in ß-scores between each of these conditions (Afatinib or Paclitaxel) and DMSO controls were calculated, thereby obtaining differential sensitivity values (ß-scores for DMSO control subtracted from ß-scores for Afatinib or Paclitaxel conditions). For the computation of

enrichment scores, filtering was performed for differential sensitivity values ≤ -0.25 and FDR values ≤ 0.05. The thus obtained genes were then subjected to gene set enrichment analysis using the MSigDB Molecular Signatures Database (MSigDB v2023.1.Mm updated March 2023) (Subramanian et al. 2005; Liberzon et al. 2011; Liberzon et al. 2015).

6 Results

6.1 Declaration of contributions

The monotherapy high-throughput drug screening data presented in this thesis have been generated by myself with contributions from Andrea Coluccio, Raquel Bernad and Julia Manolow. Computational analyses comprising drug response and RNA sequencing data used in Chapters 6.9 to 6.11 were performed by Fabio Boniolo and have already been published in his doctoral dissertation (Boniolo 2022), which also features an overview of the drug screening data with partial similarities to the graphs presented in Chapters 6.2-6.5. Additional contributions are indicated in the respective figure legends.

6.2 An automated high-throughput drug screen for the identification of therapeutic vulnerabilities in pancreatic cancer cell lines

PDAC is a cancer entity with a particularly dismal prognosis and for which treatment options are currently mainly limited to polychemotherapies (Chapter 3.1). The high molecular heterogeneity found among PDAC patients is hypothesized to result in heterogeneous responses to therapy, thereby posing one of the major challenges to the development of effective targeted treatment approaches (Kleeff et al. 2016).

To investigate whether the molecular heterogeneity of PDAC tumors indeed results in variable drug responses, we performed an automated high-throughput drug screen in 250 murine cell lines derived from GEMMs with different genetic backgrounds using a large compound library consisting of 415 drugs (Figure 1).

Before being used in the drug screen, each cell line was subjected to different quality control steps, comprising cell line authentication by regenotyping, tests for mycoplasma contamination and the evaluation of growth rates for determination of optimal seeding density (Figure 1A). Using an automation pipeline, the cell lines were then seeded in technical duplicates and treated with the drug library one day later. CellTiter-Glo® Assay was used as a readout of cell viability (Figure 1B).

Importantly, to reflect the molecular heterogeneity found among PDAC patients, cell lines with different morphologies (Figure 1C), driver oncogenes (Figure 1D) and genotypes (Figure 1E) were used. This heterogeneous set of cell lines was treated with a comprehensive drug library consisting of compounds already approved for clinical use (16 %), in different phases of clinical trials (35 %) or in pre-clinical development (49 %) (Figure 1F). As shown in Figure

1G, various pathways known to be relevant in cancer are targeted by this collection of compounds.

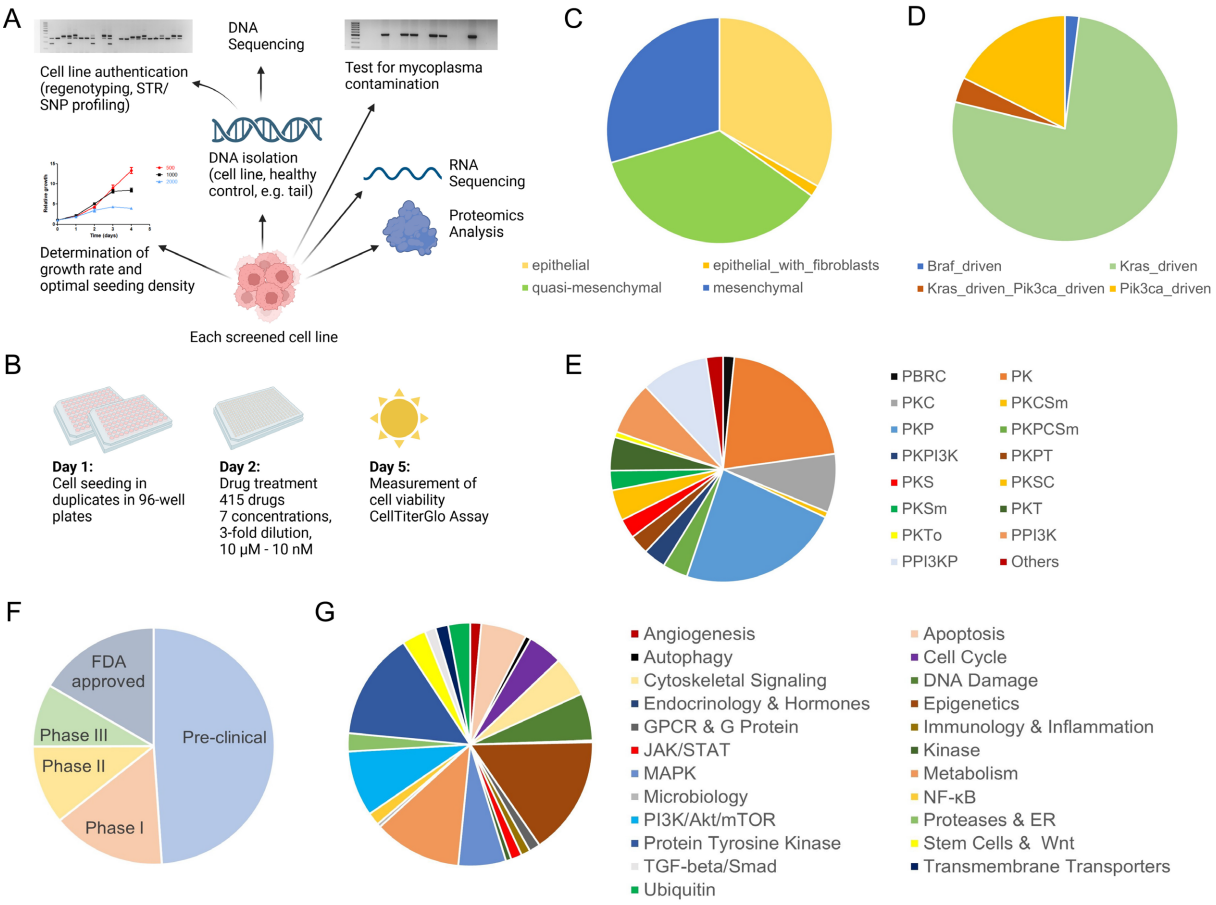

Figure 1: Overview of the automated high-throughput drug screening pipeline.
(A) Quality control procedures performed for each cell line before its use in the automated high-throughput drug screen include cell line authentication, tests for mycoplasma contamination and evaluation of growth rate to determine optimal seeding density. DNA, RNA and protein were also harvested for sequencing purposes. (B) Experimental setup of the drug screen: cells were seeded in technical duplicates on Day 1 and treated with a drug library consisting of 415 drugs on Day 2. Cell viability was measured on Day 5 by CellTiterGlo® Assay (C) Distribution of morphologies (epithelial, epithelial with fibroblasts, quasi-mesenchymal, mesenchymal) in the cohort of 250 screened murine cell lines. Morphology was determined by microscopy. (D) Distribution of oncogenic drivers. (E) Distribution of main genotype groups. Abbreviations and associated genotypes are listed in Table 4-15. (F) Overview of clinical phases of drugs in the compound library. (G) Overview of drug targets. Panels (A) and (B) were created using BioRender.com.

The evaluation of growth rates for the determination of optimal seeding density in the drug screen (Figure 1A) also produced a doubling time for each of the tested cell lines, i.e. the number of hours required for doubling of cell number to occur (Figure 2A). This information was also integrated into the analysis pipeline to generate dose response curves, as exemplarily shown in Figure 2B. From these dose response curves, parameters of drug response were calculated, including area under the curve (AUC) and IC50 values (Figure 2B). Importantly, in this approach, IC50 values could not always be calculated as a relative cell viability of 50 % was not always reached during the assay (Figure 2C). In fact, for less than 50 % of drug – cell line pairs, IC50 values were calculated. Therefore, in general, AUC values will be used in further analyses presented in this thesis.

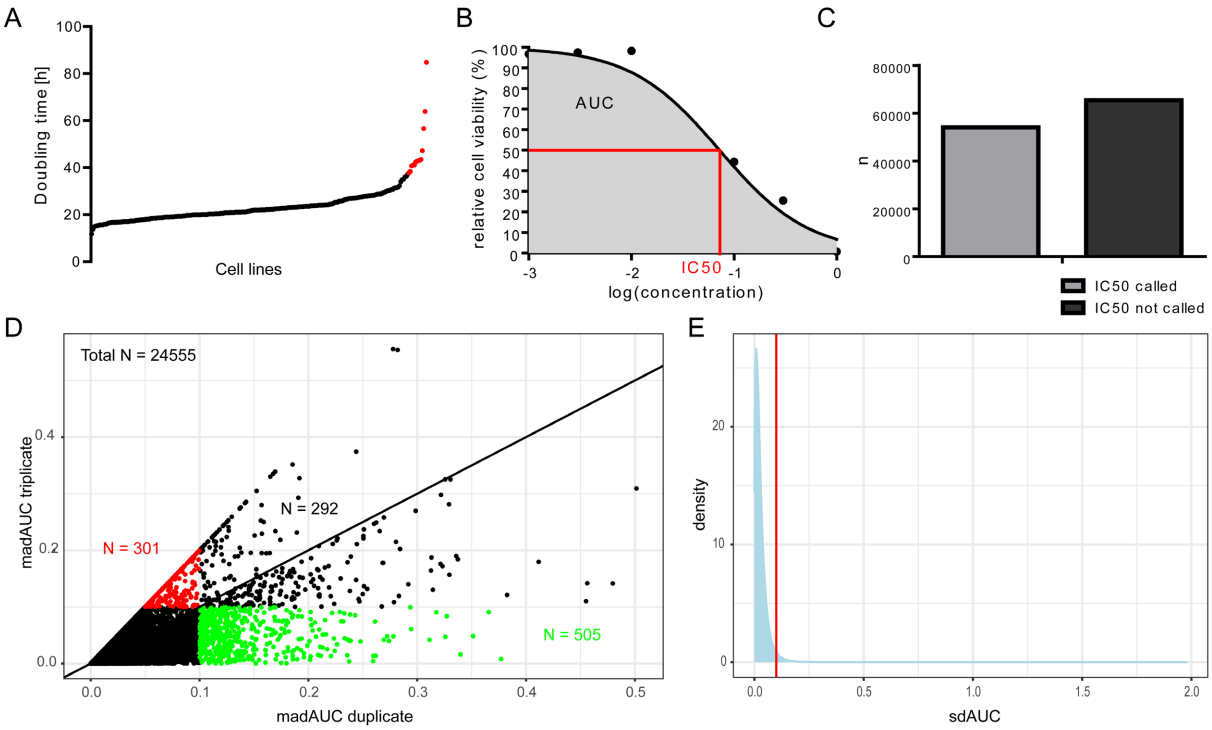

Figure 2: Overview of the analysis of data obtained from the automated high-throughput drug screening pipeline.
(A) Overview of doubling times (in hours) calculated for the tested cell lines. Doubling times were calculated across a time frame of 72 hours based on CellTiter-Glo® measurements. Cell lines with less than two doublings within 72 hours are highlighted in red. (B) Exemplary dose response curve illustrating the commonly used parameters of drug sensitivity, area under the curve (AUC) and IC50 values. (C) Numbers of called IC50 values (n = 47'413) and not called IC50 values (n = 56'332). (D) Comparison of data quality for technical duplicates and technical triplicates. One replicate was randomly removed from drug screening data obtained by triplicate measurements to generate examples of duplicate measurements. When applying a threshold of 0.1 for the mean absolute deviation of the AUC between replicates, 505 datapoints were lost for duplicate measurements, 301 datapoints for triplicate measurements and 292 in both. Total number of datapoints = 24'555. Analysis and graph by Andrea Coluccio. (E) Density plot for the standard deviation of the AUC between replicates (sdAUC) based on the entire dataset (250 murine cell lines treated with 415 drugs (3 cell line – drug pairs excluded according to Chapter 5.2.4)). 2.7 % (2'832 out of 103'745 datapoints) of the AUC values generated have a standard deviation between replicates above 0.1.

The mean absolute deviation of AUC values derived from distinct replicates ($mad_{replicate}$ AUC) was used to assess the utility of performing the high-throughput drug screening assay in duplicate or triplicate measurements. The assay was initially performed in technical triplicates, generating 24'555 datapoints (AUC values for cell line – drug pairs) (Figure 2D). One replicate was randomly removed from the dataset to compare the results for duplicate compared to triplicate measurements. Selection of data based on $mad_{replicate}$ AUC values below 0.1 led to a loss of 3.2 % of datapoints in duplicate measurements and 2.4 % in triplicate measurements. As overall, the difference is not striking, for feasibility reasons, the remaining cell lines were screened in technical duplicates. The vast majority of thereby produced AUC values had a standard deviation below 0.1 between the replicates (Figure 2E).

As demonstrated in Figure 3A, we observed heterogeneous drug responses across the cell line cohort for the 415 tested drugs. The majority of drugs were rather ineffective in the

tested cell lines, with mean AUC values above 0.5 for 91 % of the tested drugs (Figure 3B). Only eight drugs showed AUC values lower than 0.5 in all tested cell lines (Romidepsin, Quisinostat, Carfilzomib, Ganetespib, Chaetocin, STF-118804, NSC319726 and Dinaciclib) indicating their particular effectiveness across PDAC models (Figure 3C, Table 6-1).

Table 6-1: Overview of the eight drugs for which maximum AUC value < 0.5.
Drug, target and mean AUC (mAUC), minimum (min) AUC, maximum (max) AUC values across cell lines are indicated.

Drug	Target	mAUC	minAUC	maxAUC
Romidepsin	HDAC	0.01092399	0.0009105606	0.09384819
Quisinostat	HDAC	0.10063935	0.0239128868	0.30003590
Carfilzomib	Proteasome	0.05221285	0.0015469175	0.33865542
Ganetespib	HSP	0.16013788	0.0141134398	0.41478392
Chaetocin	Histone Methyltransferase	0.08384820	0.0019955046	0.42432457
STF-118804	NAMPT	0.12212811	0.0023496998	0.46251906
NSC 319726	p53	0.17454827	0.0185857422	0.49595341
Dinaciclib	CDK	0.21614449	0.0370722220	0.49898241

Using three examples, Figure 3D illustrates the heterogeneous drug responses which were produced by different drugs in the compound library. We observed both compounds with low efficacy such as Thiomyristoyl which covered only the upper part of the AUC spectrum and drugs such as Romidepsin which produced low AUC values in all tested cell lines (Figure 3D). In addition, we also identified a group of compounds including Adavosertib (Figure 3D), for which variable responses covering a wide range of AUC values were observed.

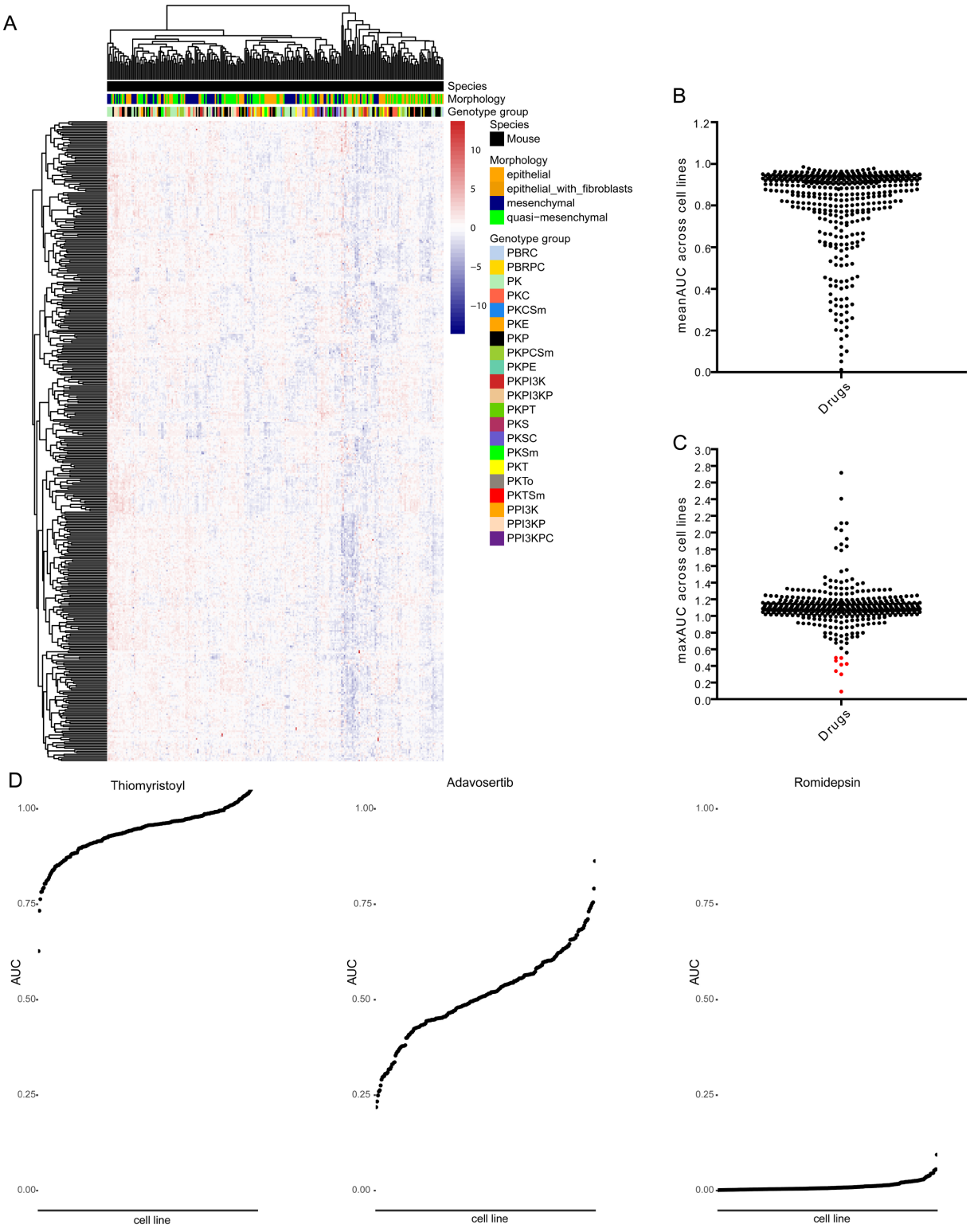

Figure 3: The majority of drugs is ineffective in the murine cell line cohort.
(A) Heatmap of Z scores of AUC values derived from 250 murine cell lines treated with 415 drugs (3 cell line – drug pairs excluded according to Chapter 5.2.4). Clustering is based on Euclidean distance. Morphology and main genotype groups are annotated. (B) Overview of mean AUC values for each drug across all tested cell lines. (C) Overview of maximum AUC values calculated for each drug across all tested cell lines. (D) Overview of AUC values obtained in the different cell lines for three exemplary drugs, Thiomyristoyl, Adavosertib and Romidepsin.

To determine the heterogeneity in the dataset in more detail, the mean absolute deviation of the AUC values (madAUC) across all tested cell lines for each drug can be used (Figure 4A). Drugs with high madAUC values cover a broad range of sensitivities, as is exemplarily shown for Deguelin, the compound with the highest madAUC (madAUC = 0.31) in our cohort. (Figure 4B).

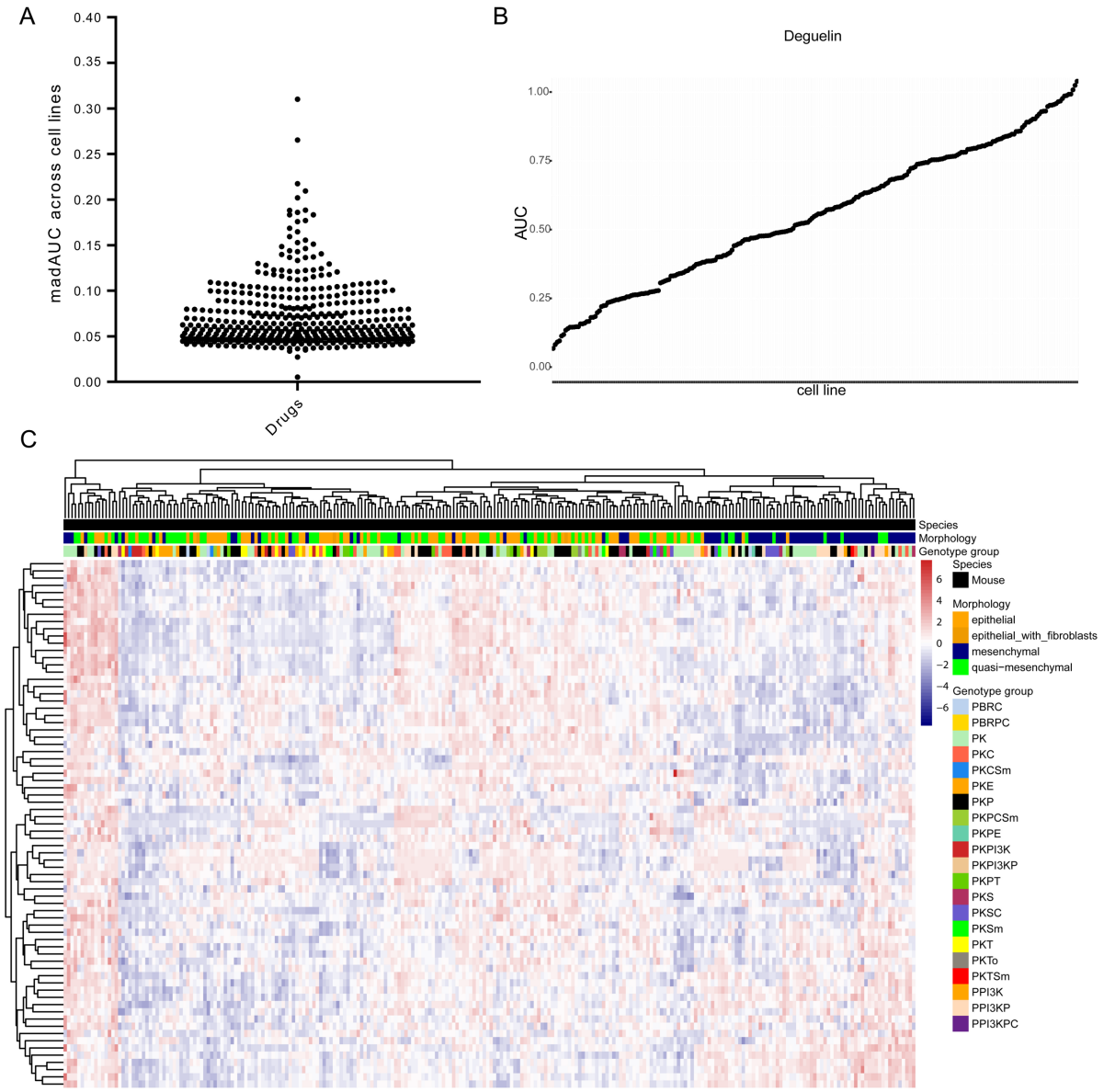

Figure 4: Heterogeneity in drug response becomes evident by selection for high madAUC.
(A) Overview of madAUC values calculated for each drug across all tested 250 murine cell lines (mad = mean absolute deviation). (B) Overview of AUC values obtained for the drug Deguelin. Deguelin is the drug with the highest madAUC (madAUC = 0.31). (C) Heatmap of Z scores of AUC values for all drugs with madAUC > 0.1 (n=73 drugs). Clustering is based on Euclidean distance. Morphology and main genotype groups are annotated.

In addition to Deguelin, other drugs which produced the most variable drug responses include Panobinostat (HDAC inhibitor), RSL3 (ferroptosis inducer), LY2090314 (GSK-3 inhibitor) and Mubritinib (HER2 inhibitor) (Table 6-2).

Table 6-2: Overview of the drugs which produce most heterogeneous drug responses.
Drug, target and mean AUC (mAUC), minimum (min) AUC, maximum (max) AUC and mean absolute deviation of the AUC (madAUC) values across cell lines are indicated.

Drug	Target	mAUC	minAUC	maxAUC	madAUC
Deguelin	AKT	0.55105117	0.0676409	1.03926934	0.31017901
Panobinostat (LBH589)	HDAC	0.43463361	0.04008386	0.99773572	0.26531807
RSL3	Ferroptosis	0.60945884	0.11895309	0.96070352	0.21754248
LY2090314	GSK-3	0.64852836	0.10972772	1.40482019	0.20949062
Mubritinib (TAK 165)	HER2	0.73938619	0.26072047	1.14852693	0.20202032

After selection of drugs with high madAUC (madAUC > 0.1), the heatmap representation of Z scores of AUC values clearly demonstrates the heterogeneity of drug response across the PDAC cell line cohort (Figure 4C). Therefore, we concluded that, as hypothesized, pancreatic cancer represented here by the different cell line models indeed displays high variability in treatment responses, which could be exploited by personalized or subgroup-specific therapeutic approaches.

6.3 Identification of subtype-specific vulnerabilities

Subtype-specific vulnerabilities of pancreatic cancer have previously been reported (Falcomatà et al. 2022; Collisson et al. 2011). As demonstrated in Figure 5A, principal component analysis revealed that likewise in our high-throughput drug screening dataset, the morphology of the tested cell lines can be considered as an important driver of drug response. Specific compounds for which AUC values showed statistically significant differences between morphologies (p value < 0.05, absolute log2-fold change > 0.3) are highlighted in Figure 5B.

We confirm previously known associations between PDAC subtypes and drug sensitivity, namely increased effectiveness of MEK inhibitors in epithelial cell lines (Falcomatà et al. 2022) and of the HDAC inhibitor Panobinostat in the mesenchymal subtype (Krauß et al. 2022). Other subtype-specific vulnerabilities observed in our cohort include, for example, a higher sensitivity of mesenchymal cell lines towards ferroptosis induction by RSL3 and Erastin and of the epithelial cohort towards GLUT inhibition by BAY-876 (Figure 5B).

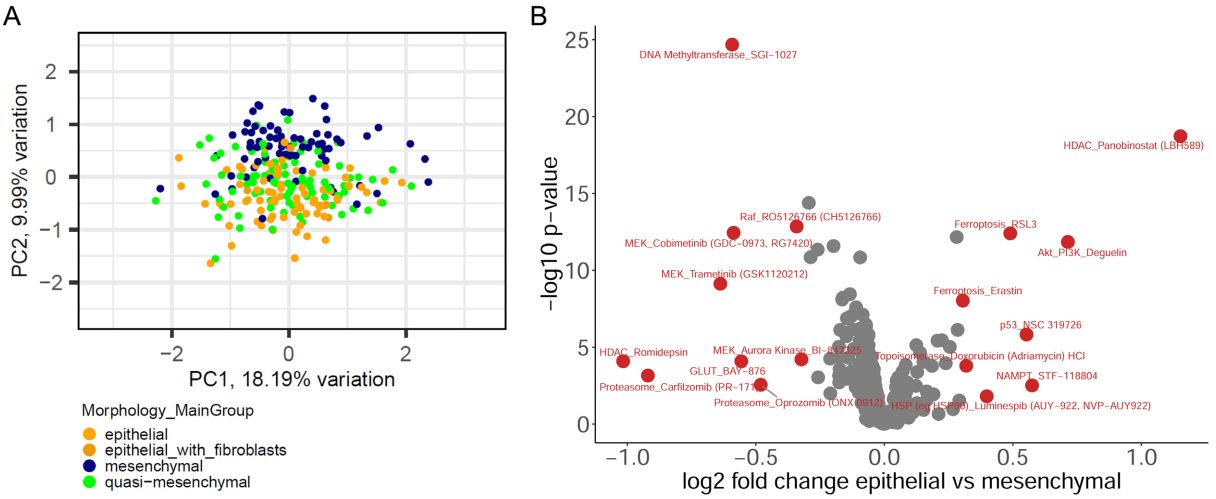

Figure 5: Subtype-specific differences in drug response.
(A) Principal component analysis (PCA) plot for the 250 screened mouse cell lines based on AUC values for 415 drugs (3 cell line – drug pairs excluded according to Chapter 5.2.4). Each dot represents one cell line, colored by morphology. (B) Volcano plot for log2-fold changes for all tested compounds between epithelial and mesenchymal cell lines. Two-sided Student's t tests were performed. Highlighted: *p* value < 0.05, absolute log2-fold change > 0.3.

6.4 Identification of genotype-specific vulnerabilities

In addition to subtype-specific vulnerabilities described in Chapter 6.3, differential drug response can also be observed based on the genotypes of the cell lines. PCA revealed, for example, that the oncogenic driver can have an effect on drug sensitivity (Figure 6A). Due to the high number of different genotype groups, differences in drug response are hard to determine by PCA (Figure 6B), but pairwise comparisons with the PK cohort also showed specific vulnerabilities based on the genotype group of the cell lines (Figure 7A-I).

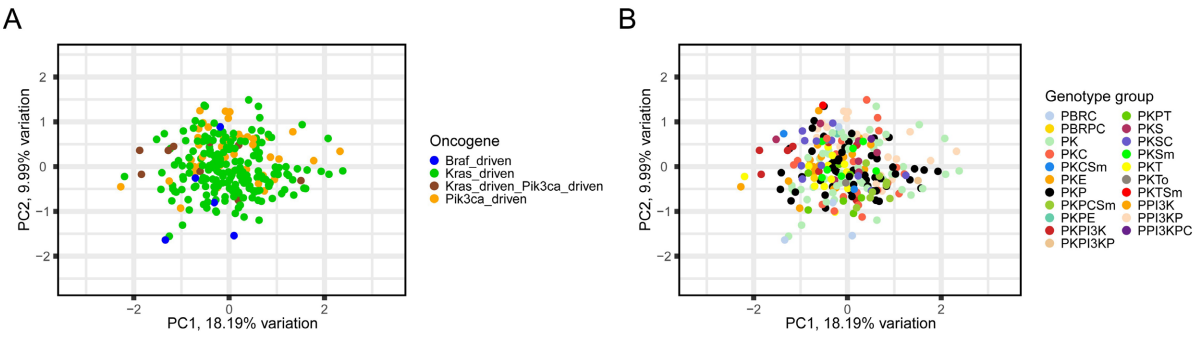

Figure 6: Genotype-specific differences in drug response.
Principal component analysis (PCA) plot for the 250 screened mouse cell lines based on AUC values for 415 drugs (3 cell line – drug pairs excluded according to Chapter 5.2.4). Each dot represents one cell line, colored by (A) driver oncogene or (B) genotype group. A list of the abbreviations for each genotype group is available in Table 4-15.

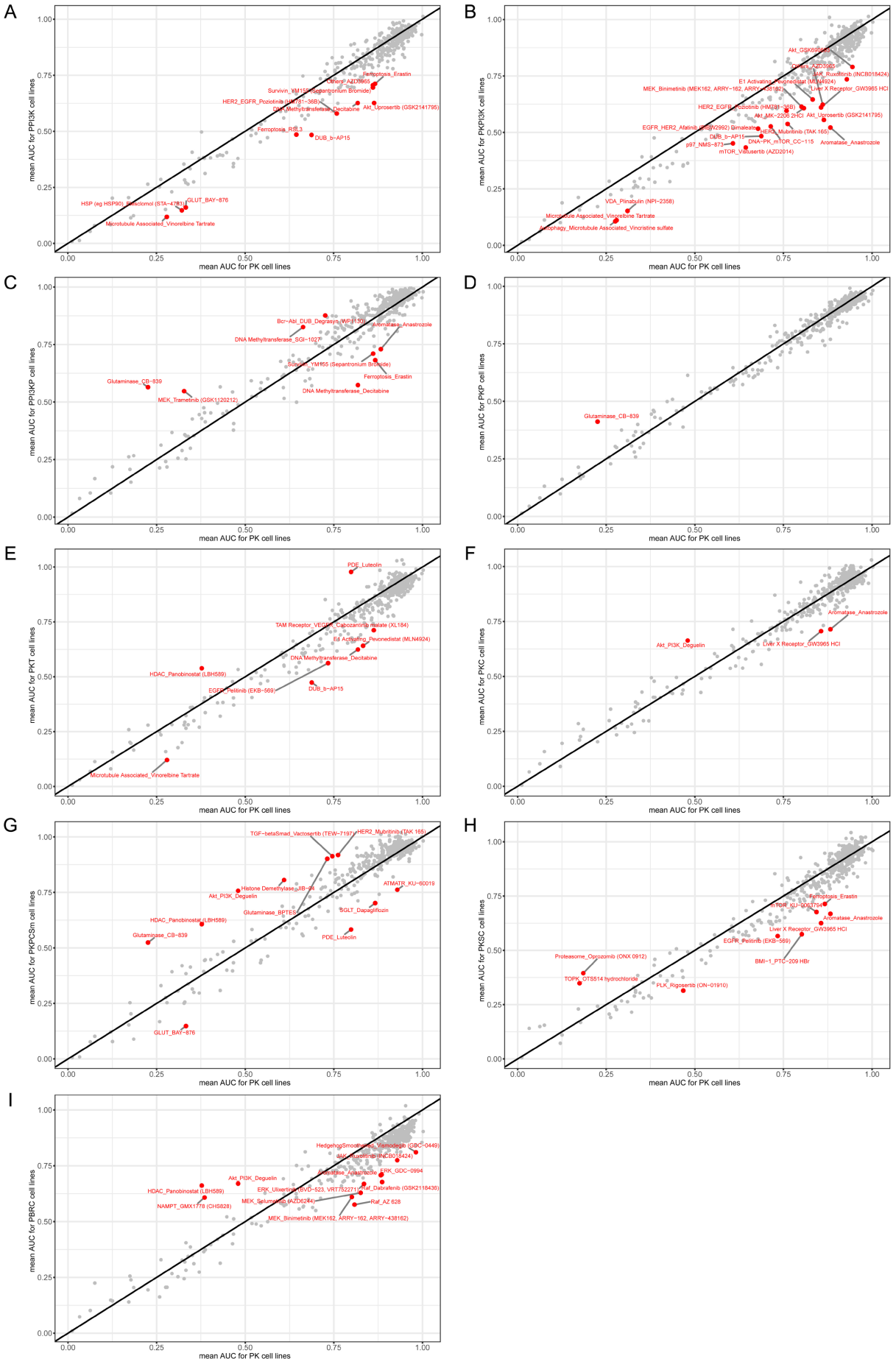
A
mean AUC for PPI3K cell lines
mean AUC for PK cell lines
Ferroptosis_Erastin
Olaparib_AZD2281
Survivin_YM155 (Sepantronium Bromide)
HER2_EGFR_Poziotinib (HM781−36B)
DNA Methyltransferase_Decitabine
Akt_Uprosertib (GSK2141795)
Ferroptosis_RSL3
DUB_b−AP15
GLUT_BAY−876
HSP (eg HSP90)_Retaspimycin (STA−4783)
Microtubule Associated_Vinorelbine Tartrate
B
mean AUC for PKPI3K cell lines
mean AUC for PK cell lines
Akt_GSK690693
Olaparib_AZD2281
TAK1_Ruxolitinib (INCB018424)
E1 Activating_Pevonedistat (MLN4924)
MEK_Binimetinib (MEK162, ARRY−162, ARRY−438162)
Liver X Receptor_GW3965 HCl
HER2_EGFR_Poziotinib (HM781−36B)
Akt_MK−2206 2HCl
Akt_Uprosertib (GSK2141795)
EGFR_HER2_Afatinib (BIBW2992)
Bmalleatine
HER2_Mubritinib (TAK 165)
DUB_b−AP15
DNA−PK_mTOR_CC−115
Aromatase_Anastrozole
p97_NMS−873
mTOR_Vistusertib (AZD2014)
VDA_Plinabulin (NPI−2358)
Microtubule Associated_Vinorelbine Tartrate
Autophagy_Microtubule Associated_Vincristine sulfate
C
mean AUC for PPI3KP cell lines
mean AUC for PK cell lines
Bcr−Abl_DUB_Degrasyn_WP1130
Aromatase_Anastrozole
DNA Methyltransferase_SGI−1027
Survivin_YM155 (Sepantronium Bromide)
Ferroptosis_Erastin
Glutaminase_CB−839
DNA Methyltransferase_Decitabine
MEK_Trametinib (GSK1120212)
D
mean AUC for PKP cell lines
mean AUC for PK cell lines
Glutaminase_CB−839
E
mean AUC for PKT cell lines
mean AUC for PK cell lines
PDE_Luteolin
TAM Receptor_VEGFR_Cabozantinib malate (XL184)
E1 Activating_Pevonedistat (MLN4924)
DNA Methyltransferase_Decitabine
HDAC_Panobinostat (LBH589)
EGFR_Pelitinib (EKB−569)
DUB_b−AP15
Microtubule Associated_Vinorelbine Tartrate
F
mean AUC for PKC cell lines
mean AUC for PK cell lines
Aromatase_Anastrozole
Akt_PI3K_Deguelin
Liver X Receptor_GW3965 HCl
G
mean AUC for PKPCSm cell lines
mean AUC for PK cell lines
TGF−betaSmad_Vactosertib (TEW−7197)
HER2_Mubritinib (TAK 165)
Histone Demethylase_JIB−04
ATMATR_KU−60019
Akt_PI3K_Deguelin
Glutaminase_BPTES
SGLT_Dapagliflozin
HDAC_Panobinostat (LBH589)
Glutaminase_CB−839
PDE_Luteolin
GLUT_BAY−876
H
mean AUC for PKSC cell lines
mean AUC for PK cell lines
Ferroptosis_Erastin
mTOR_KU−0063794
Aromatase_Anastrozole
Liver X Receptor_GW3965 HCl
EGFR_Pelitinib (EKB−569)
Proteasome_Oprozomib (ONX 0912)
BMI−1_PTC−209 HBr
TOPK_OTS514 hydrochloride
PLK_Rigosertib (ON−01910)
I
mean AUC for PBRC cell lines
mean AUC for PK cell lines
HedgehogSmoothened_Vismodegib (GDC−0449)
TAK1_Ruxolitinib (INCB018424)
Aromatase_Anastrozole
ERK_GDC−0994
Akt_PI3K_Deguelin
HDAC_Panobinostat (LBH589)
ERK_Ulixertinib (BVD−523, VRT752271)
Raf_Dabrafenib (GSK2118436)
NAMPT_GMX1778 (CHS828)
MEK_Selumetinib (AZD6244)
Raf_AZ 628
MEK_Binimetinib (MEK162, ARRY−162, ARRY−438162)

Figure 7: Compounds with differential efficacy based on genotype groups.
Mean AUC values across cell lines are plotted for specific genotype groups against the PK cohort. (A) PPI3K vs. PK; (B) PKPI3K vs. PK; (C) PPI3KP vs. PK; (D) PKP vs. PK; (E) PKT vs. PK; (F) PKC vs. PK; (G) PKPCSm vs. PK; (H) PKSC vs. PK; (I) PBRC vs. PK. Highlighted: absolute delta mean AUC > 0.15. A list of the abbreviations for each genotype group is available in Table 4-15.

Some of the identified genotype-specific differences in drug response were mechanistically reasonable. For example, PPI3K and PKPI3K cell lines were on average more susceptible to Akt inhibition by Uprosertib, MK-2206 and GSK690693 (Figure 7A, B). The PPI3K cohort was furthermore more sensitive towards GLUT inhibition by BAY-876 compared to the PK cell lines (Figure 7A). PI3K/Akt activation has previously been shown to promote glucose uptake via glucose transporters (GLUT) (Wright et al. 2021; Wieman et al. 2007). Another example is the higher sensitivity of *Braf* mutant PBRC cells towards Raf inhibition by the inhibitors AZ628 and Dabrafenib (Figure 7I).

Overall, the results presented in chapters 6.3 and 6.4 demonstrate that the generated high-throughput drug screening data, together with annotations of phenotypic and genotypic characteristics of the cell lines, allows for the identification of subgroup-specific vulnerabilities.

6.5 Correlations in drug response can potentially be informative on drugs' mechanisms of action

Another application of high-throughput drug screening studies which has previously been demonstrated is to derive insights on drugs' mechanisms of actions (Seashore-Ludlow et al. 2015). Analyses of correlations between AUC values for each drug-drug pair can be useful to identify potentially inaccurate target annotations. As shown in Figure 8, for the majority of drug-drug pairs, AUC values were positively correlated, indicating that despite the previously described heterogeneity in drug response, a certain degree of general response produced by the drug screening pipeline is present.

Figure 9A is a representation of the highest correlating drug-drug pairs after selection for drugs with at least one Spearman's correlation value above 0.7. Certain clusters of drugs sharing the same target are evident, for example drugs targeting the MAPK pathway and agents acting on epigenetics. These findings can serve as a quality control measure of the drug screening data as they indicate high reproducibility for certain drug targets irrespective of the specific drug used.

Upon closer analysis of Raf, MEK and ERK inhibitors, however, it becomes evident that only two of the tested Raf inhibitors (RO5126766 and AZ 628) cluster with the majority of MEK and ERK inhibitors (Figure 9B). RO5126766 is a dual Raf/MEK inhibitor (Wada et al. 2014)

and AZ 628 is a pan-Raf inhibitor (McDermott et al. 2007) while some of the other inhibitors such as Vemurafenib and Dabrafenib target more specifically mutant $Braf^{V600E}$ (Shelledy and Roman 2015; Kefford et al. 2010). This differential specificity may be reflected in the correlation values presented in Figure 9B.

Cell cycle inhibitors provide another example of strong correlations based on specific targets, as for example Aurora kinase inhibitors and PLK inhibitors show clear clustering (Figure 9A, C).

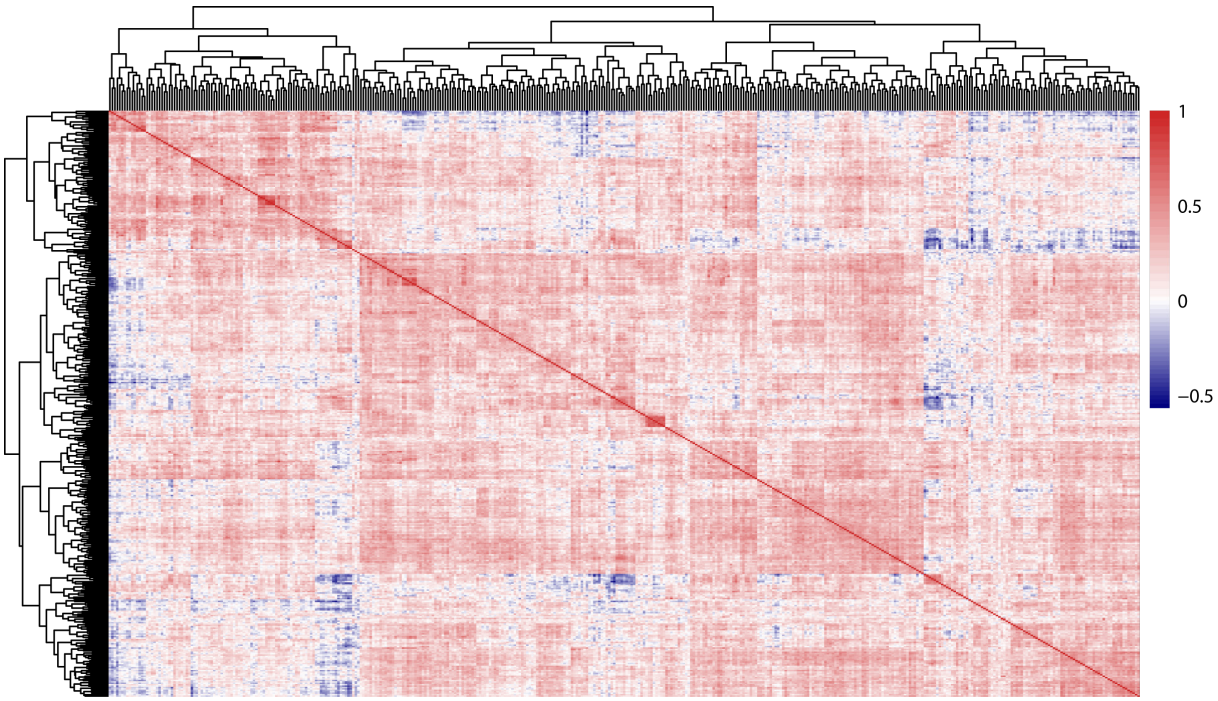

Figure 8: Drug response is overall positively correlated.
Heatmap showing the Spearman's correlation values computed for each drug-drug pair based on AUC values for 250 murine cell lines and 415 drugs (3 cell line – drug pairs excluded according to Chapter 5.2.4). Clustering is based on Euclidean distance.

On the other hand, certain clusters contain drugs with distinct target annotations. One example is the cluster of microtubule inhibitors consisting of the agents Colchicine, Vinorelbine tartrate, Plinabulin, Vincristine sulfate, and in addition the inhibitor KX2-391, for which the annotated target is Src (Fallah-Tafti et al. 2011; Wang et al. 2016) (Figure 9A). Previous cancer cell line profiling studies have made similar observations that KX2-391 clusters with microtubule inhibitors and have also validated that this agent indeed targets microtubule dynamics (Seashore-Ludlow et al. 2015). Further studies have confirmed the dual mechanism of action for this drug (Smolinski et al. 2018).

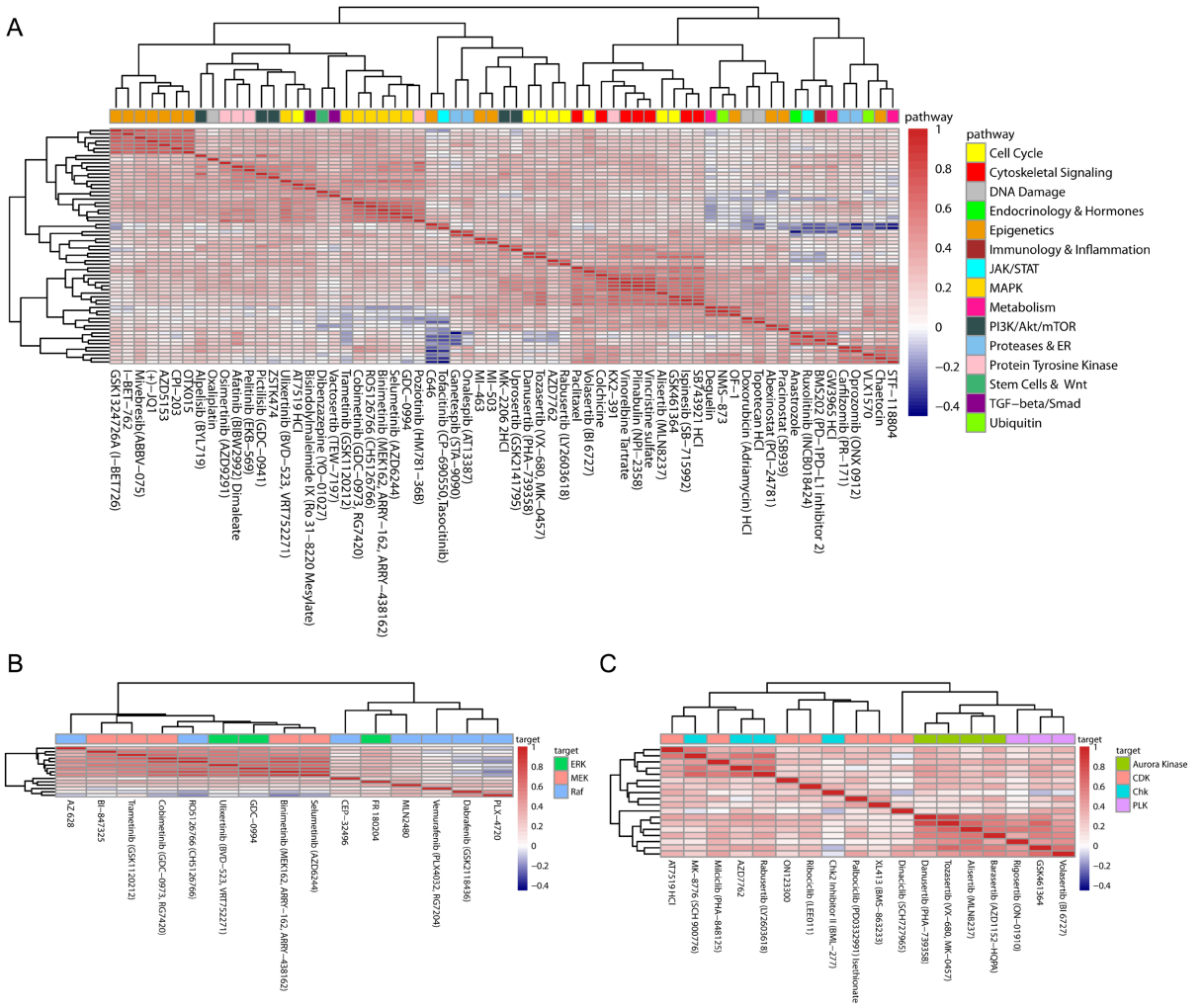

Figure 9: Drug-drug correlation analysis reveals clusters of drugs with similar targets.
(A) Heatmap of Spearman's correlation values for drug-drug pairs after selection for drugs with at least one correlation value > 0.7 (n=65 drugs). Clustering is based on Euclidean distance. Pathways targeted by the compounds are indicated. (B) Heatmap of Spearman's correlation values for each drug-drug pair with the target annotation Raf, MEK or ERK. Clustering is based on Euclidean distance. The specific annotated drug target is indicated. (C) Heatmap of Spearman's correlation values for each drug-drug pair with the pathway annotation "cell cycle". Clustering is based on Euclidean distance. The specific annotated drug target is indicated.

Another unexpected cluster is formed by the drugs Deguelin, NMS-873 and OF-1 (Figure 9A). Multiple targets have been described for Deguelin (Tuli et al. 2021), including Akt inhibition (Jin et al. 2007), but also mitochondrial complex I inhibition (Carpenter et al. 2019) and the induction of reactive oxygen species (ROS) (Xu et al. 2015). Interestingly, the drugs with the highest correlation values with Deguelin target various distinct pathways, which mostly appear to be related to metabolism (Figure 10). Among them are several drugs for which in addition to the originally identified one, an unrelated target has been discovered. For example, for NMS-873, originally identified as an inhibitor of the valosin-containing protein (VCP/p97) (Magnaghi et al. 2013), a dual mechanism of action targeting mitochondrial oxidative phosphorylation has been reported (Bouwer et al. 2021). Furthermore, the known HER2 inhibitor Mubritinib (Nagasawa et al. 2006) has been shown to target the electron transport chain complex I (Baccelli et al. 2019). The compound NSC319726, originally

identified as a p53-mutant reactivator (Yu et al. 2014; Yu et al. 2012) and now recognized as a ROS inducer (Shimada et al. 2018) and affecting the mitochondrial respiratory chain (Tsvetkov et al. 2022), will be investigated in more detail in Chapter 6.8.

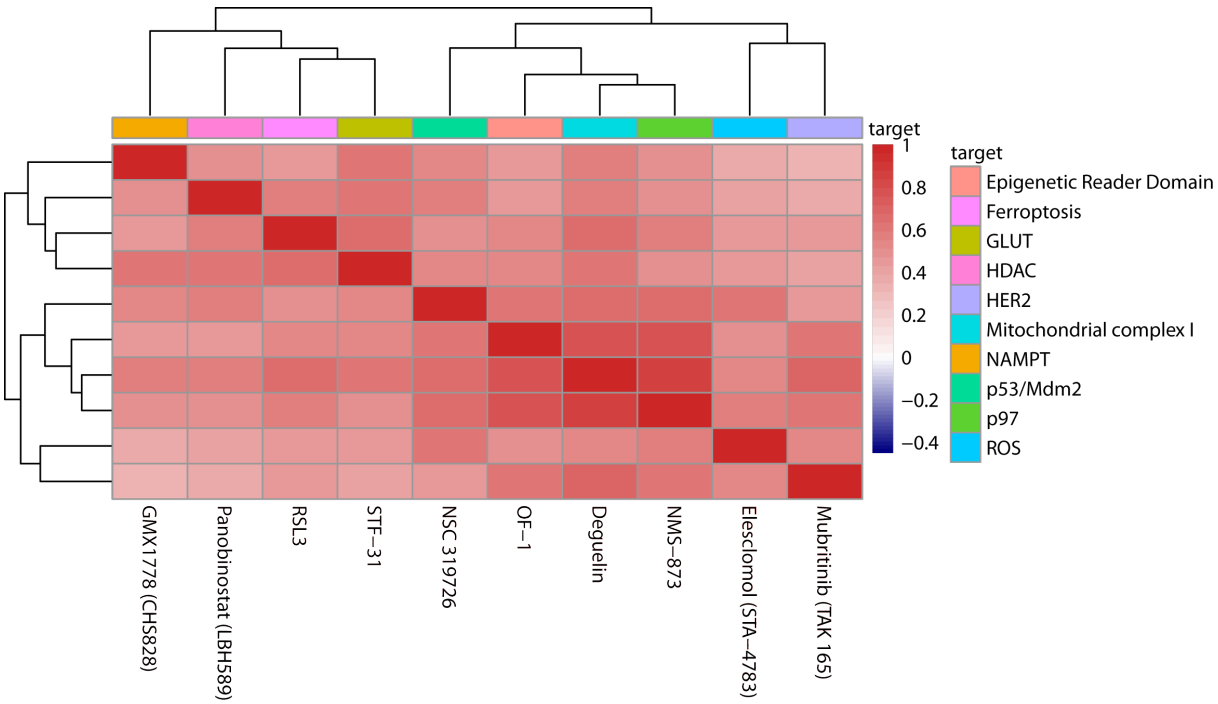

Figure 10: Compounds with the highest correlation values for the multi-target drug Deguelin.
Representation of the ten drugs with the highest correlation values with Deguelin. Shown is the Spearman's correlation value for each drug-drug pair. Clustering is based on Euclidean distance. The specific, originally annotated drug targets are indicated.

Overall, it could be demonstrated in this chapter that several classes of inhibitors, including MAPK inhibitors, drugs targeting epigenetic reader domains or Aurora kinase inhibitors, produce highly correlating drug responses across the cell line cohort, showing the consistency of the high-throughput drug screening approach. Furthermore, it could be shown that unexpected correlations of drugs with deviating targets could help to identify mechanisms of action.

6.6 Comparison of drug screen results for human and mouse cell lines

In addition to the high-throughput drug screening of murine PDAC cell lines presented in the previous chapters, a collection of primary (n=18) and established, commercially available (n=20) human pancreatic cancer cell lines has likewise been included to allow for cross-species validation of the results. The primary human cell lines have been derived directly from patient biopsies (n=9), from PDX models (n=6), from CDX models (n=1) or from

organoid cultures (n=2). These primary human cell lines and the murine cell lines used for this thesis are generally low passaged.

Previous studies have demonstrated that the passage number can affect a cell line's characteristics. Passage number can for instance influence cellular morphology, growth rate and gene expression (O'Driscoll et al. 2006) and lead to accumulation of somatic mutations over time (Kim et al. 2017). The 20 established, commercially available human pancreatic cancer cell lines of unknown total passage number were screened in addition to the primary dataset with two main goals. First, to confirm whether there are indeed differences in drug sensitivity between the primary and the established cell lines, which may for instance be caused by higher passage number. In addition, an important aim was to directly compare the drug screening results with the publicly available datasets (shown in Chapter 6.7).

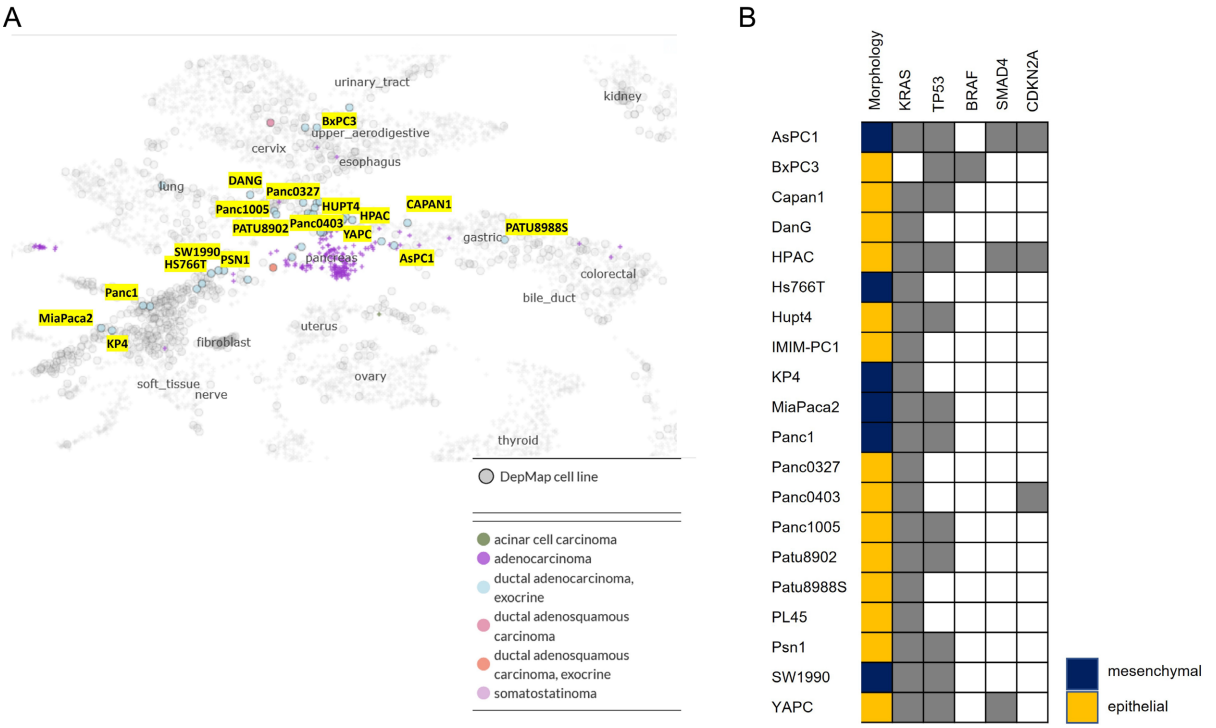

Figure 11: Selection of established human cell lines for high-throughput drug screening.
(A) The Celligner tool (https://depmap.org/portal/celligner/) (Warren et al. 2021) was used to visualize differences in gene expression patterns for established human pancreatic cancer cell lines. Cell line names were manually added. (B) Overview of morphology and genetic alterations for the selected established human cell lines. Grey boxes indicate the presence of a genetic alteration for the specific gene. The information on genetic alterations was obtained from the DepMap Portal (https://depmap.org/portal/). Morphologies were determined by microscopy.

Therefore, 20 established human pancreatic cancer cell lines were selected based on the availability of data on the Depmap portal (https://depmap.org/portal/) and heterogeneity in genomic alterations, morphology, and gene expression. For the latter, the Celligner tool (https://depmap.org/portal/celligner/) was used. It is an unsupervised alignment method that is applied to integrate several large-scale cell line and tumor RNA-Seq datasets (Warren et al. 2021). As shown in Figure 11A, the 20 screened cell lines represent different gene

expression patterns and should therefore reflect heterogeneity. Figure 11B demonstrates that different morphologies and genomic alterations are included.

As shown in Figure 12, overall, human cell line data integrated well with the murine cohort. Nevertheless, specific clustering of primary human and established human cell lines could be observed, indicating that human specific drug responses are also present.

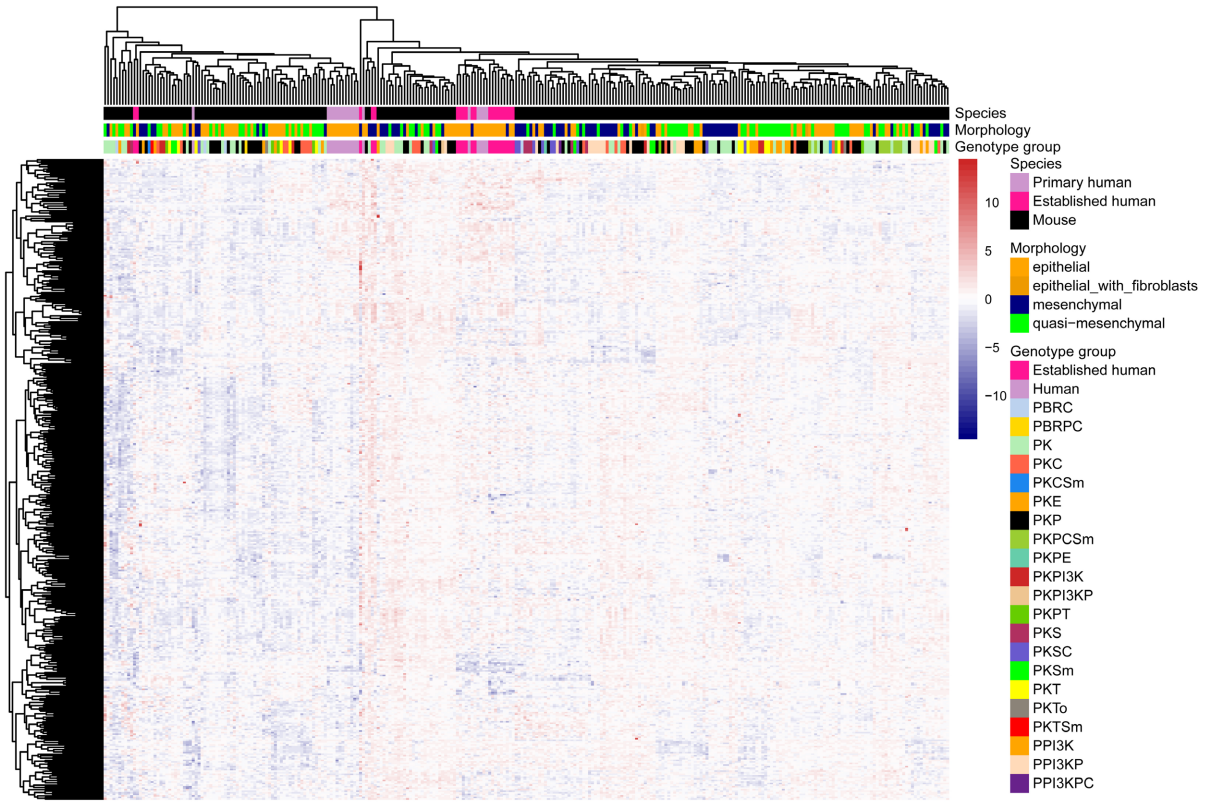

Figure 12: Integration of high-throughput drug screening data for murine and human cell lines.
Heatmap representation of the Z scores of AUC values across 415 drugs for 250 murine (3 cell line – drug pairs excluded according to Chapter 5.2.4), 18 primary and 20 established human cell lines. Clustering is based on Euclidean distance. Species, morphology and genotype groups are indicated.

Such species-specific effects are also indicated by PCA, as shown in Figure 13A. Compounds with significantly higher efficacy in primary human compared to murine cell lines include, for example, the survivin inhibitor YM155, the ferroptosis inducer RSL3 and the NAMPT inhibitor GMX1778 (Figure 13B). By comparison, murine cell lines were generally more susceptible to HDAC inhibitors Romidepsin and Quisinostat and the NAMPT inhibitor STF-118804. It should be noted that the cohorts of murine, primary human and established human cell lines have different representation of morphologies (murine: 34 % epithelial, 31 % mesenchymal (Figure 1C), primary human: 100 % epithelial, 0 % mesenchymal, established human: 70 % epithelial, 30 % mesenchymal (Figure 13E)). Therefore, some of the differences in drug sensitivity between species may also be due to morphology, as this has previously been shown to be an important determinant of drug response (Figure 5).

Nonetheless, for example the survivin inhibitor YM155 was also highly significantly more effective in the established human cell lines compared to the murine cohort (Figure 13C), indicating that human cells are indeed generally more susceptible to this compound. Established human cell lines were also more sensitive to the chemotherapeutic drug 5-FU compared to both murine and primary human cell lines (Figure 13C, D). Overall, less significant differences were observed between primary and established human cell lines than between each of the latter and the murine cohort, in line with the results of the PCA (Figure 13).

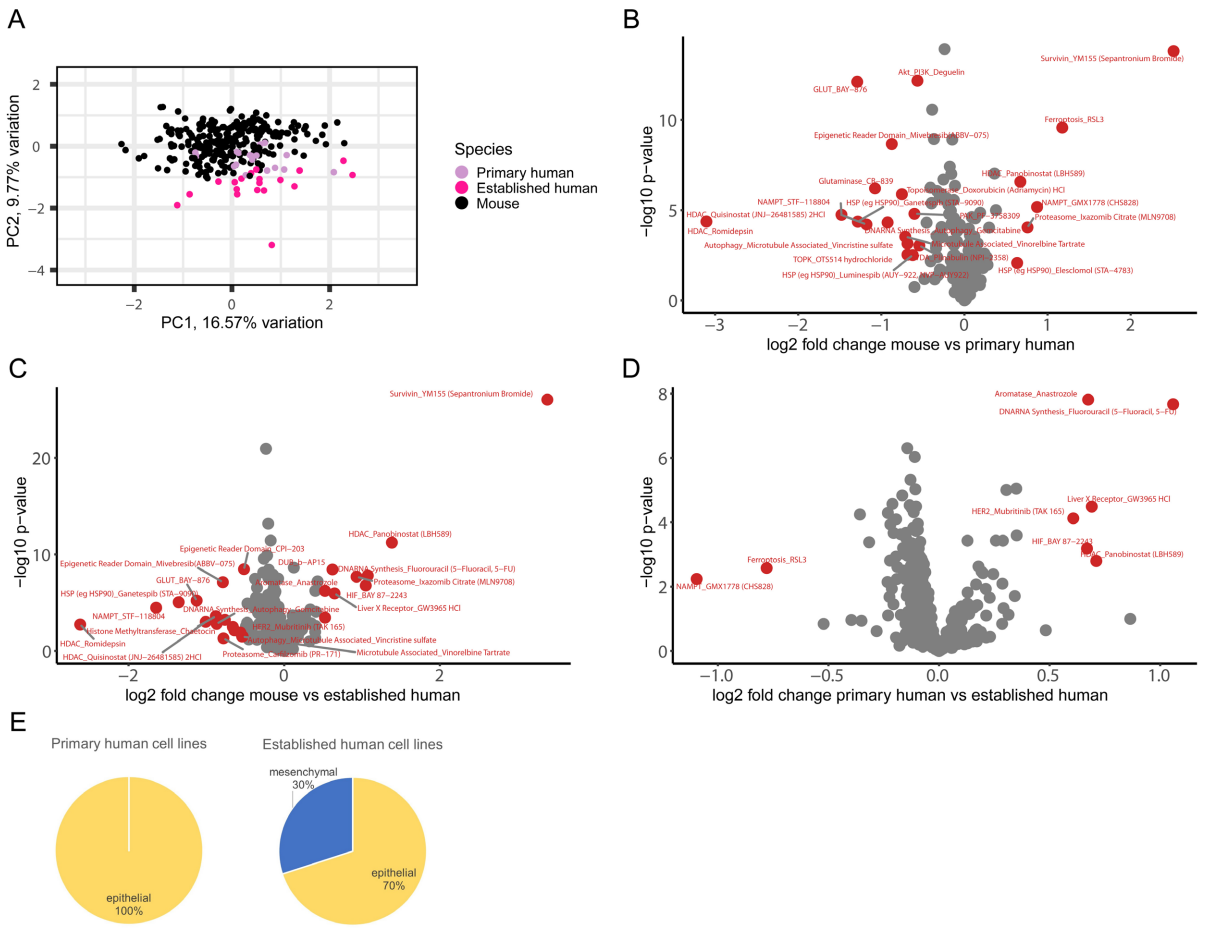

Figure 13: Differences in drug response between murine, primary human and established human cell lines.
(A) PCA plot based on AUC values for 415 drugs and 250 murine (3 cell line – drug pairs excluded according to Chapter 5.2.4), 18 primary human and 20 established human cell lines. Each dot represents one cell line, colored by species. (B) Volcano plot for log2-fold changes between murine and primary human cell line cohorts. Two-sided Student's t tests were performed. Highlighted: log2-fold change > 0.5, *p* value < 0.05. (C) Volcano plot for log2-fold changes between murine and established human cell line cohorts. Two-sided Student's t tests were performed. Highlighted: log2-fold change > 0.5, *p* value < 0.05. (D) Volcano plot for log2-fold changes between primary human and established human cell line cohort. Two-sided Student's t tests were performed. Highlighted: log2-fold change > 0.5, *p* value < 0.05.

The integration of human cell lines into the high-throughput drug screen, as described above, allows for cross-species validation which can be useful when selecting drug candidates for

further validation, as for each individual drug, comparisons can be made between the murine and human dataset.

6.7 Comparison of drug screen results for established human cell lines to publicly available datasets

Differences in drug response between murine, primary human and established human cell lines have been shown previously (Chapter 6.6). As mentioned above, the integration of 20 established human cell lines (Figure 11) into our high-throughput drug screen also enabled us to directly compare our results to publicly available datasets.

As discussed in Chapter 3.4 and Chapter 7.2, the consistency and reproducibility of high-throughput drug screens is the matter of ongoing scientific debate and correlation between datasets is diminished by differences in experimental protocols between institutes (Haibe-Kains et al. 2013; Safikhani et al. 2016b; Pharmacogenomic agreement between two cancer cell line data sets 2015; Smirnov et al. 2016; Safikhani et al. 2016a; Geeleher et al. 2016; Bouhaddou et al. 2016; Mpindi et al. 2016).

Table 6-3: Comparison of important aspects of experimental setups for the generation of the different datasets.
Information derived from (Picco et al. 2019; Seashore-Ludlow et al. 2015; Rees et al. 2016; Corsello et al. 2020).

	GDSC2	CTRP	PRISM	TUM
Plate format	1536-well plates	1536-well plates	384-well plates	96-well plates
Cell seeding	Determination of optimal density for each cell line	500 cells/well	1250 cells/well	Human: 1000 – 3000 cells/well
Drug delivery	Labcyte Echo 555	Labcyte Echo 555	Pintool	Pintool
Drug concentration range	Concentration range adjusted for each compound	16-step, 2-fold dilution, in duplicate	8-step, 4-fold dilution, ranging from 10 µM to 610 pM	7-step, 3-fold dilution, ranging from 10 µM to 10 nM
Viability assay	Cell Titer Glo	Cell Titer Glo	Lysis and mRNA isolation, amplification by PCR, Luminex detection	Cell Titer Glo
Analysis	R package gdscIC50	MATLAB (MathWorks)	R package drc	R package GRMetrics

As demonstrated in Table 6-3, differences in experimental setups are also present between our own drug screening approach and the assays performed by other institutes. I therefore sought to investigate to what extent these datasets nevertheless correlate. To this end, the GDSC2 (Picco et al. 2019), CTRP (Seashore-Ludlow et al. 2015; Rees et al. 2016) and PRISM (Corsello et al. 2020) datasets were downloaded from the DepMap Portal website (https://depmap.org/portal/download/all/) and overlapping data for specific cell line – drug pairs were compared to AUC values generated in our own high-throughput drug screen.

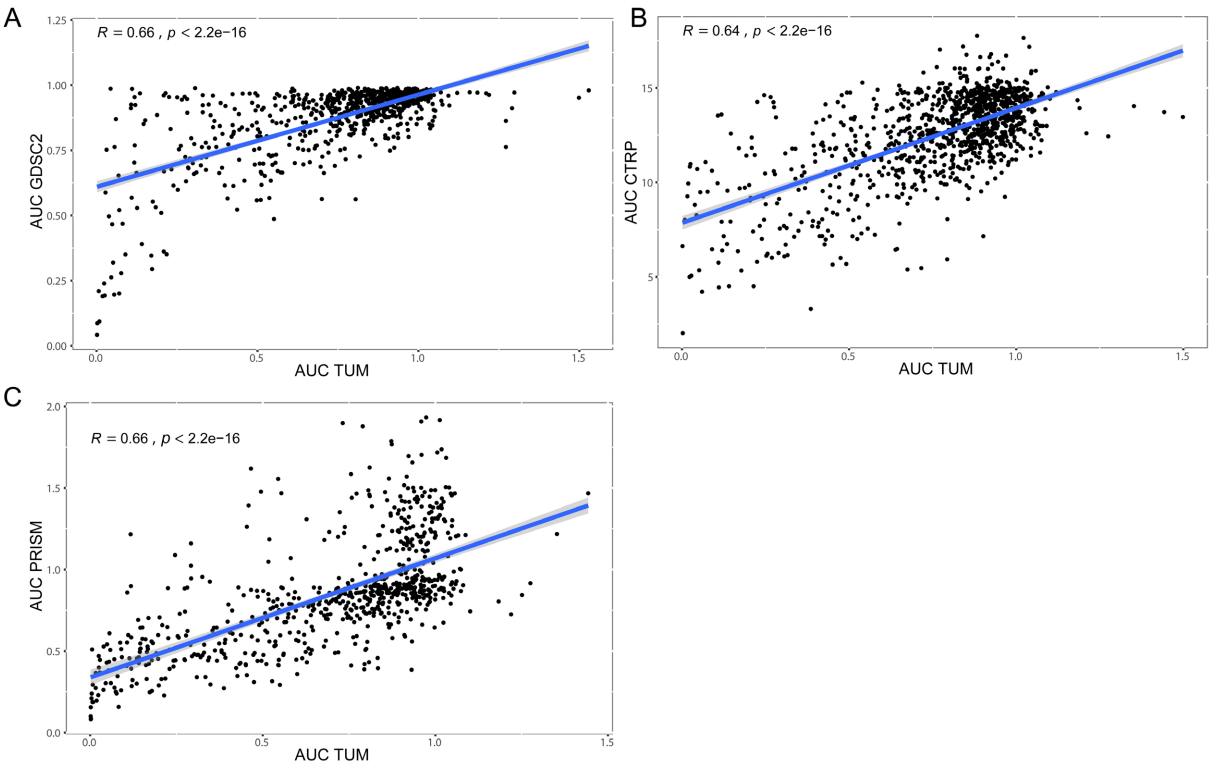

Figure 14: Moderate correlation between our own and publicly available datasets.
AUC values from (A) the GDSC2 screen; (B) the CTRP screen and (C) the PRISM screen are plotted against AUC values for the same drug – cell line pair in our own data (TUM). Each dot therefore represents the AUC value for one specific drug – cell line pair present in both datasets. The publicly available data (Picco et al. 2019; Seashore-Ludlow et al. 2015; Rees et al. 2016; Corsello et al. 2020) were downloaded from https://depmap.org/portal/download/all/ and drug names were manually curated between the datasets. *R* = Pearson correlation coefficient. N = (A) 883, (B) 1056, (C) 728.

As shown in Figure 14, pairwise comparisons between our data (TUM) and the public datasets yielded Pearson correlation values between 0.64 (CTRP vs. TUM) and 0.66 (GDSC2 and PRISM vs. TUM). Moderate Pearson correlations between publicly available datasets in the range of 0.60 and 0.62 could previously be demonstrated (Corsello et al. 2020). As shown in Figure 15, for the subset of pancreatic cancer cell lines used in this study, Pearson correlations determined using the same analysis pipeline as for Figure 14 ranged between 0.48 (PRISM vs. GDSC2) and 0.55 (PRISM vs. CTRP) for pairwise comparisons between the publicly available datasets.

Therefore, as summarized in Figure 15D, while correlation values achieved for all comparisons are only moderate, comparisons including our own dataset did not perform worse than those performed within the publicly available datasets. Overall, this indicates similar robustness of our data compared to previously published pharmacological profiling datasets.

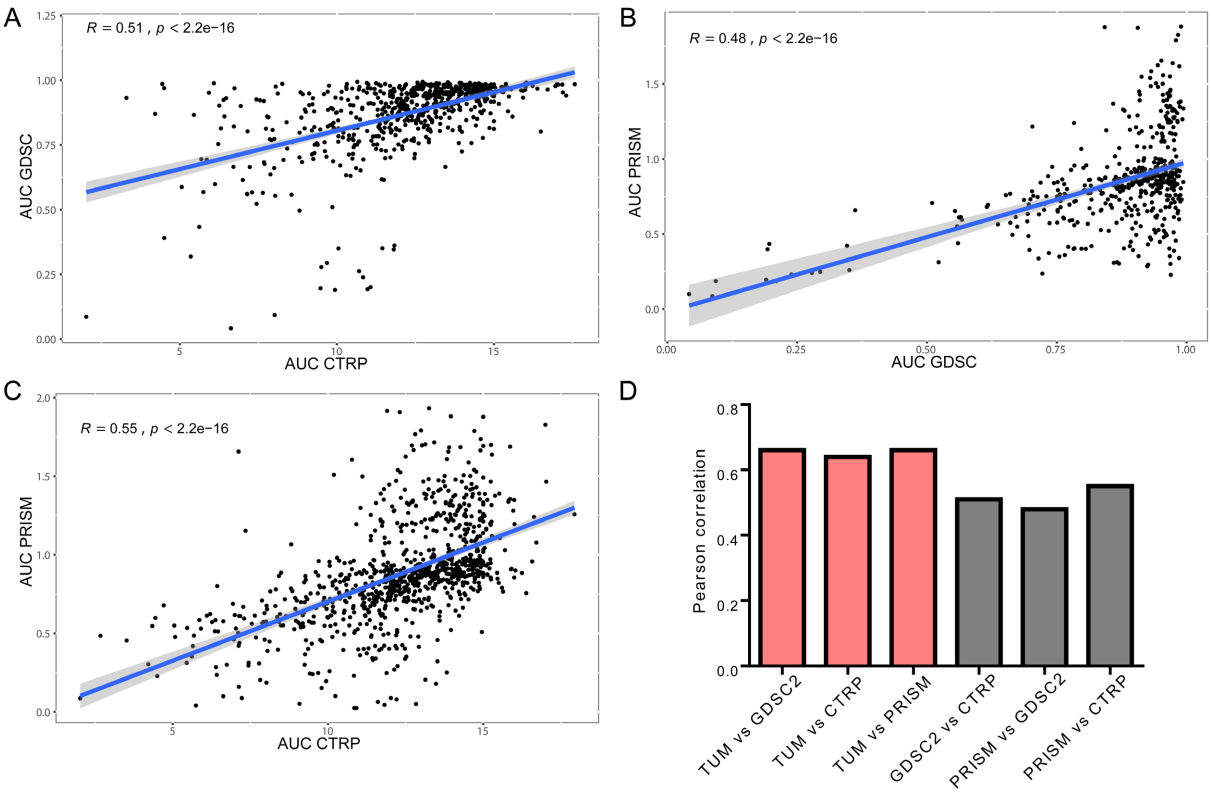

Figure 15: Moderate correlations achieved between TUM dataset and publicly available data are comparable to those achieved within publicly available datasets.
AUC values are plotted against each other for each drug – cell line pair overlapping between the respective datasets. (A) GDSC2 vs. CTRP (n = 651); (B) PRISM vs. GDSC2 (n = 470); (C) PRISM vs. CTRP (n = 937). The publicly available data were downloaded from https://depmap.org/portal/download/all/ and drug names were manually curated between the datasets. *R* = Pearson correlation coefficient. (D) Overview of Pearson correlation coefficients calculated for all pairwise comparisons. Pairs involving our own (TUM) dataset are highlighted.

6.8 NSC319726 is highly effective across PDAC cell lines independently of p53 status

As described in Chapter 6.2, most of the drugs in this study are rather ineffective across the cell line cohort. A small subset of drugs, however, is very efficient with AUC values below 0.5 across all tested cell lines. As demonstrated in Figure 16A, NSC319726 is one of the most efficient drugs in the cohort with a mean AUC value across cell lines of 0.179, which is below, for example, the mean AUC value achieved for the standard of care drug Gemcitabine. AUC values are below 0.5 for almost all tested cell lines, irrespective of species, morphology, or genotype (Figure 16B, C, D). Nevertheless, specific differences in

drug response are observed, with the drug being significantly more effective in murine cell lines compared to primary human (*p* value: 0.0234) and established human cell lines (*p* value < 0.0001) (Figure 16B) and in mesenchymal compared to epithelial cell lines (*p* value < 0.0001) (Figure 16C). Genotype-specific differences can likewise be observed. Compared to the PK cohort, PKC cell lines are significantly more resistant to the drug (*p* value: 0.0371), while PPI3K cell lines are significantly more sensitive (*p* value: 0.0064) (Figure 16D).

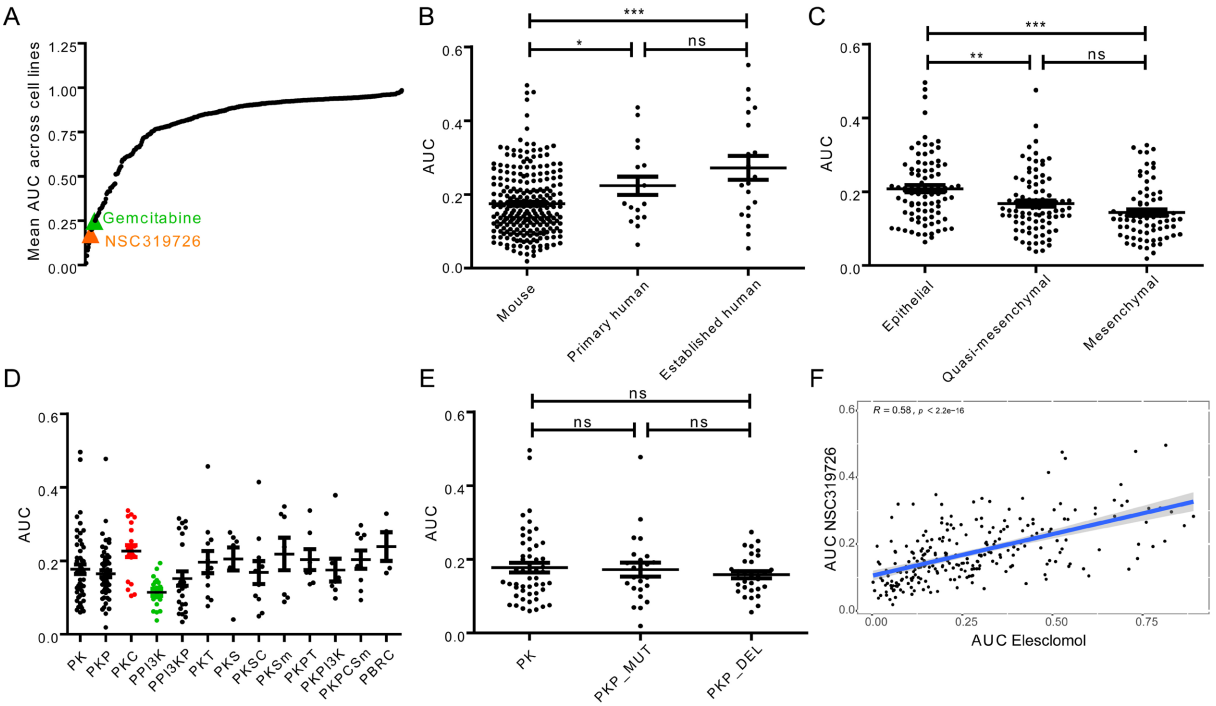

Figure 16: NSC319726 is very efficient in all tested cell lines, independently of p53 status.
(A) Overview of the mean AUC values calculated across the cell line cohort (250 murine cell lines) for each of the 415 drugs. Mean AUC values for NSC319726 and Gemcitabine are highlighted. (B) Distribution of AUC values for mouse, primary human and established human cell lines. Mean values ± SD are shown, *p value ≤ 0.05, ***p value ≤ 0.001, two-tailed student's t test. (C) Distribution of AUC values for epithelial, quasi-mesenchymal and mesenchymal murine cell lines. Mean values ± SD are shown, **p value ≤ 0.01, ***p value ≤ 0.001, two-tailed student's t test. (D) Distribution of AUC values for the different murine genotypes. Mean values ± SD are shown. (E) Distribution of AUC values for PK, PKP_MUT (cell lines with *Trp53* mutation) and PKP_DEL (cell lines with *Trp53* deletion) murine cell lines. Mean values ± SD are shown. (F) AUC values for NSC319726 plotted against AUC values for Elesclomol for each murine cell line. *R* = Pearson correlation coefficient.

NSC319726 is a small molecule that was first discovered as a reactivator of the p53 missense mutant p53-R175H (Yu et al. 2014; Yu et al. 2012). More specifically, NSC319726 was shown to restore the wild-type structure of mutant p53 by functioning as a zinc-metallochaperone that optimizes zinc concentrations in the cell to allow for proper folding (Yu et al. 2014). In addition, an increase in cellular reactive oxygen species has been reported (Yu et al. 2014). Intriguingly, as shown in Figure 16E, in our cohort, we did not observe significant differences in drug response between *Trp53* mutant and *Trp53* wild-type cells. A previous study in glioblastoma patient-derived cells has likewise shown efficiency of NSC319726 in wild-type p53 cell lines (Shimada et al. 2018). Shimada et al. reported that NSC319726 functions as a copper ionophore that induces copper dysregulation, which in

turn can generate reactive oxygen species (ROS) and DNA damage, leading to cell cycle arrest (Shimada et al. 2018).

An involvement of copper in the mechanism of action of NSC319726 has recently been confirmed by Tsvetkov et al. (Tsvetkov et al. 2022). According to this study, NSC319726 induces a copper-dependent, regulated form of cell death that is distinct from previously known death mechanisms and dependent on mitochondrial respiration (Tsvetkov et al. 2022). The authors showed that copper binding to lipoylated components of the tricarboxylic acid (TCA) cycle results in lipoylated protein aggregation which induces iron-sulfur cluster protein loss, proteotoxic stress and subsequently cell death (Tsvetkov et al. 2022).

Based on our results that *Trp53* mutant cell lines did not respond better to NSC319726 treatment than *Trp53* wild-type cells and previous studies indicating divergent mechanisms of actions (Shimada et al. 2018; Tsvetkov et al. 2022), we sought to investigate further the mechanism of action of this drug. In addition, AUC values for NSC319726 moderately correlated with those for Elesclomol giving a further hint that indeed NSC319726 could function via oxidative stress related mechanisms (Figure 16F). NSC319726 is furthermore one of the highest correlating drugs for Deguelin, which forms a cluster with several drugs, for which mitochondrial complex I is a described target (Figure 10).

We selected six *Trp53* wild-type cell lines representing both rather sensitive and resistant phenotypes to NSC319726 treatment (Table 6-4, Figure 17A) for further investigation of this agent's mechanism of action.

Table 6-4: Overview of cell lines selected for investigating the mechanism of action of the drug NSC319726.

Cell line	Genotype	Morphology	AUC drug screen
9091	PK	mesenchymal	0.071202911
C2532	PKT	mesenchymal	0.076639129
C1232	PKE	epithelial	0.085650979
4706	PK	quasi-mesenchymal	0.28287945
S559	PK	mesenchymal	0.319649725
4072	PK	quasi-mesenchymal	0.475292332

First, the effectiveness in the selected cell lines was confirmed by clonogenic assays (Figure 17B). IC50 values ranged from 30 pM to 40 nM (Figure 17C). The cell line S559, in this type of assay, showed a rather sensitive phenotype compared to the original drug screening results. This could be due to diminished growth of this particular cell line at a comparably lower seeding density in clonogenic assays or due to technical problems during the high-throughput drug screen. For the studies on the drug NSC319726, S559 was henceforth

considered as a sensitive rather than resistant cell line and the results for this sample were treated with caution.

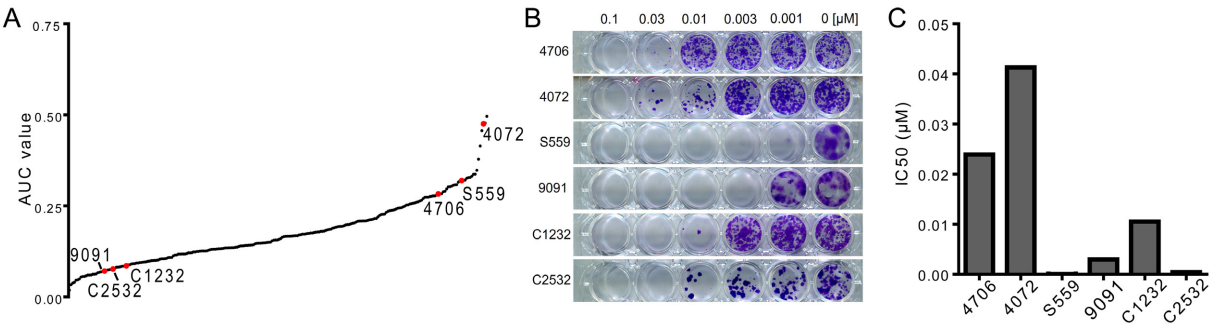

Figure 17: Confirmation of the cytotoxic effects of NSC319726.
(A) Overview of AUC values derived from the high-throughput drug screening experiment for NSC319726 for each of the 250 murine cell lines. The six murine cell lines used for further validation experiments are highlighted. (B) Clonogenic assay results representative of two technical replicates and three independent experiments. The used concentrations of NSC319726 are indicated. 0 µM = DMSO control. (C) IC50 values obtained from quantification of the clonogenic assays shown in (B).

Based on the results of Tsetkov et al. indicating that NSC319726 induces a previously unknown form of cell death (Tsvetkov et al. 2022), we next investigated an involvement of apoptosis, necroptosis and ferroptosis pathways in this drug's mechanism of action. NSC319726 did not induce Caspase 3/7 activation as measured by Caspase-Glo® 3/7 Assay (Figure 18A, B). In addition, the Caspase inhibitor z-VAD-FMK did not decrease the effectiveness of NSC319726 in two tested cell lines (Figure 18C, D). As a control, z-VAD-FMK was shown to affect the response to the drug Bortezomib (Figure 18E, F). Furthermore, the necroptosis inhibitor Necrostatin-1 and the ferroptosis inhibitor Ferrostatin-1 did not affect the response to NSC319726 (Figure 18G) but diminished the sensitivity to the ferroptosis inducer RSL3 (Figure 18H). Overall, an involvement of several known cell death pathways could therefore not be shown, supporting the results published by Tsetkov et al. (Tsvetkov et al. 2022).

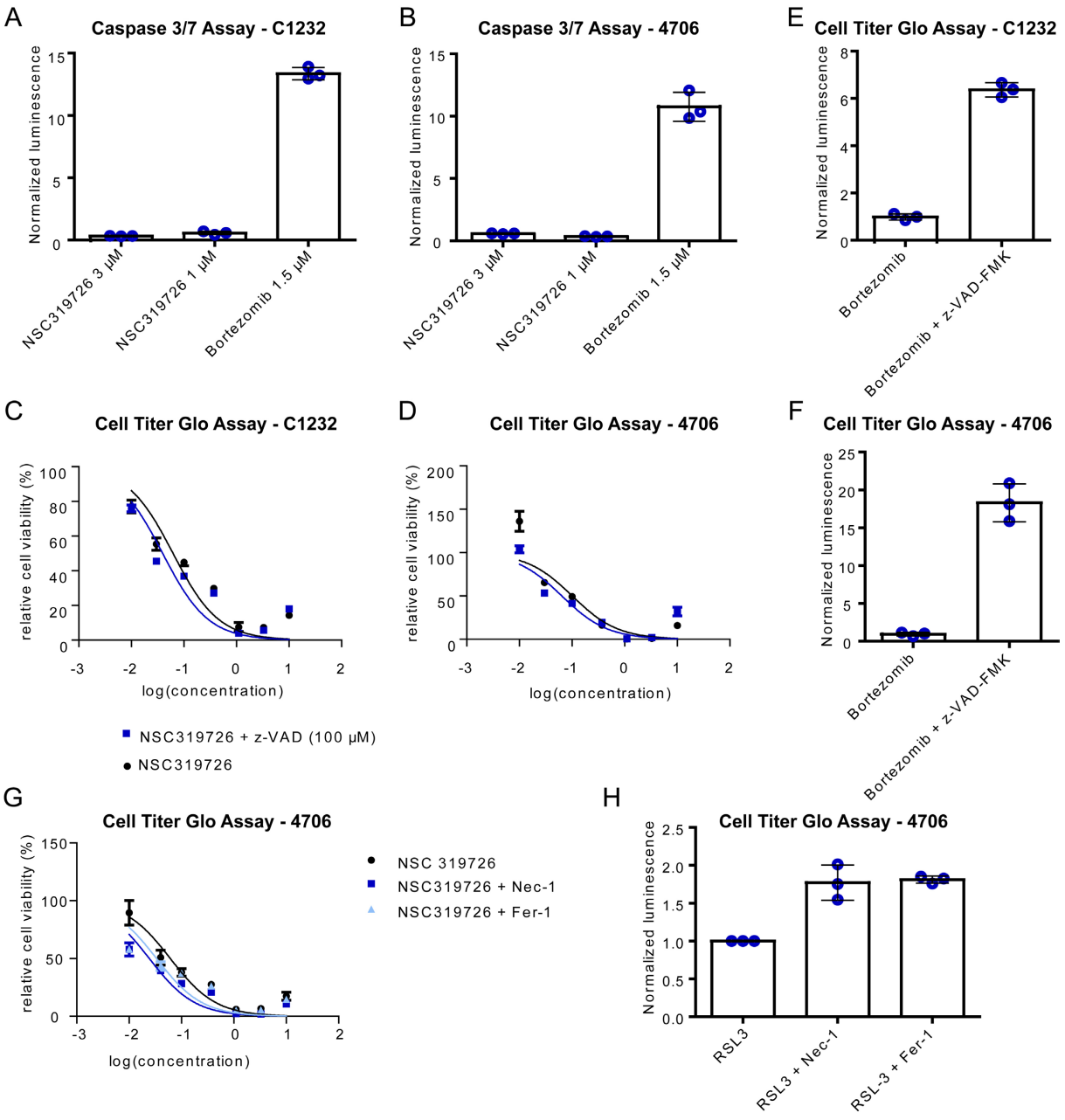

Figure 18: NSC319726 does not induce apoptotic, ferroptotic or necroptotic cell death.
(A) Results of Caspase-Glo®3/7 Assay for cell line C1232. Luminescence values were normalized to DMSO control. Mean values ± SD for three technical replicates are shown. (B) Results of Caspase-Glo®3/7 Assay for cell line 4706. Luminescence values were normalized to DMSO control. Mean values ± SD for three technical replicates are shown. (C) Co-treatment of NSC319726 (concentrations indicated on the x-axis) with 100 µM z-VAD-FMK in the cell line C1232. Relative cell viability was determined by CellTiter-Glo® assay 72 hours after the beginning of treatment. Mean values ± SD for three technical replicates are shown. (D) Co-treatment of NSC319726 (concentrations indicated on the x-axis) with 100 µM z-VAD-FMK in the cell line 4706. Relative cell viability was determined by CellTiter-Glo® assay 72 hours after the beginning of treatment. Mean values ± SD for three technical replicates are shown. (E) CellTiter-Glo® assay for the cell line C1232 treated for 72 hours with 1.5 µM Bortezomib alone or together with 100 µM z-VAD-FMK. Luminescence values are normalized to DMSO control. Mean values ± SD for three technical replicates are shown. (F) CellTiter-Glo® assay for the cell line 4706 treated for 72 hours with 1.5 µM Bortezomib alone or together with 100 µM z-VAD-FMK. Luminescence values are normalized to DMSO control. Mean values ± SD for three technical replicates are shown. (G) Co-treatment for 72 hours with NSC319726 (concentrations shown on x-axis) and 20 µM Necrostatin-1 or 10 µM Ferrostatin-1, respectively. Relative cell viability was determined by CellTiter-Glo® assay. Mean values ± SD for three technical replicates are shown. (H) CellTiter-Glo® assay for the cell line 4706 treated with 1 µM RSL3 alone or together with 20 µM Necrostatin-1 or 10 µM Ferrostatin-1. Luminescence values are normalized to RSL3. Mean values ± SD for three technical replicates are shown.

Tsvetkov et al. claim that Elesclomol and similar agents such as NSC319726 induce cell death by a novel mechanism that they termed cuproptosis (Tsvetkov et al. 2022). As shown in Figure 19, addition of $CuCl_2$ increased sensitivity to NSC319726 in all our tested cell lines, indicating that this compound indeed acts via a copper-related mechanism. Consistently, buthionine sulfoximine (BSO), which lowers the concentration of the copper chelator glutathione in the cell (Drew and Miners 1984), also sensitized the tested cell lines to NSC319726 treatment (Figure 19A-F).

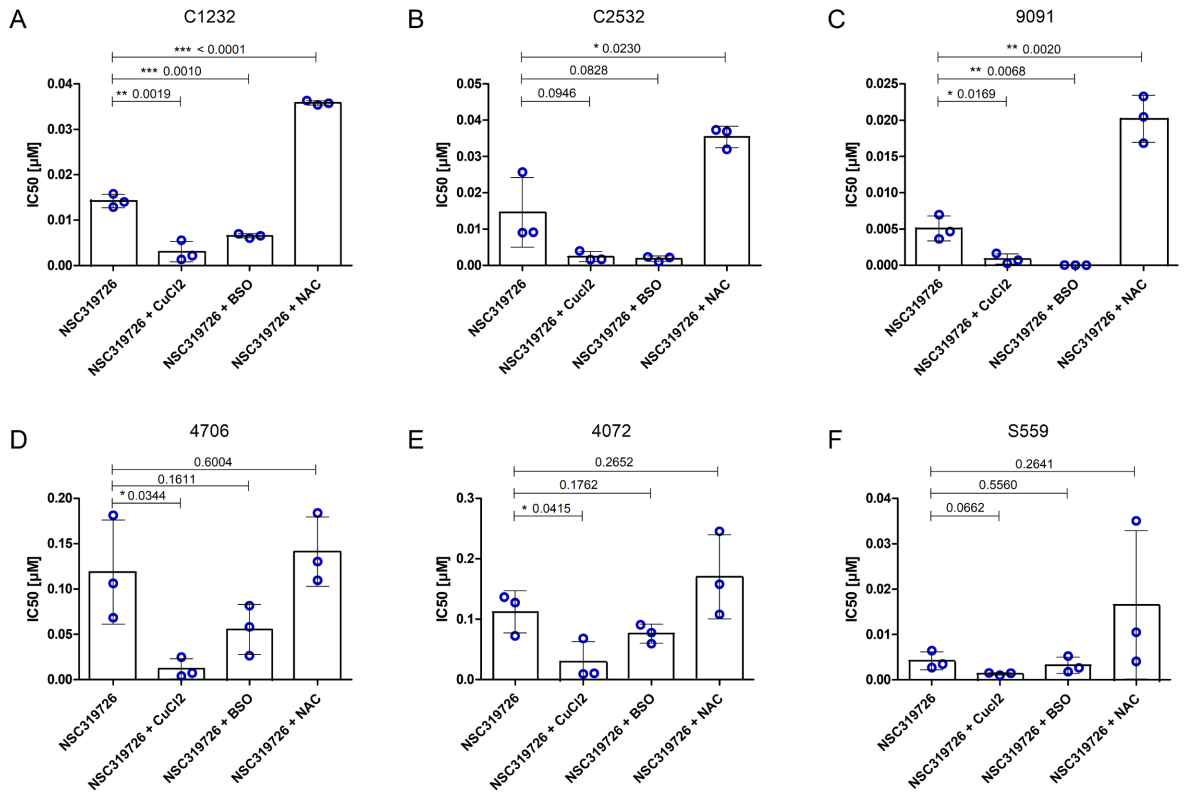

Figure 19: Sensitivity to NSC319726 is increased by $CuCl_2$ and BSO and decreased by NAC.
IC50 values calculated from CellTiter-Glo® assays after 72 hours of drug treatment normalized to DMSO controls for cell lines (A) C1232; (B) C2532; (C) 9091; (D) 4706; (E) 4072; (F) S559. Cells were pretreated with 1 mM NAC, 100 µM BSO or 10 µM $CuCl_2$ for three hours before NSC319726 was added in 7 concentrations (3-fold dilution series, highest concentration = 1 µM). Mean values ± SD for three biological replicates (each biological replicate was calculated from three technical replicates), p-values are indicated, ***p value ≤ 0.001, **p value ≤ 0.01, *p value ≤ 0.05, two-tailed student's t test. The experiment was performed together with Christian Schneeweis.

Glutathione is not only a copper chelator, but is also part of the glutathione (GSH)/GSH reductase (GSR)/GSH peroxidase (GPx)/glutaredoxin (Grx) pathway which controls the redox homeostasis in the cell (Liu et al. 2019; Holmgren et al. 2005). BSO is therefore also commonly used as an inhibitor of anti-oxidative functions in the cell (Han et al. 2008). NAC-acetyl cysteine (NAC) on the other hand can act as a scavenger of reactive oxygen species (ROS) (Liu et al. 2019; Mayer and Noble 1994; Samuni et al. 2013). As shown in Figure 19A-F, NAC reduced the sensitivities of the cell lines to NSC319726, which hints at an

involvement of reactive oxygen species for the compound's mechanism of action in line with the report from Shimada et al. (Shimada et al. 2018).

Tsetkov et al. showed in their study that cells undergoing glycolysis are more resistant to Elesclomol and similar compounds such as NSC319726 than cells that are reliant on mitochondrial respiration (Tsvetkov et al. 2022). These results could be reproduced here as shown in Figure 20A-F. Cells cultured in galactose containing medium had a tendency towards higher sensitivity to NSC319726 treatment than cells that were cultured in glucose conditions, indicating that energy metabolism driven by oxidative phosphorylation favors sensitivity to this drug.

In the same experiment the involvement of copper in the mechanism of action of NSC319726 was additionally further confirmed. As also shown in the report by Tsetkov et al., depletion of serum, which is the source of copper in cell culture media, abrogated the effect of NSC319726 (Figure 20A-F). The effect could be restored by adding $CuCl_2$ to the serum depleted medium (Figure 20A-F).

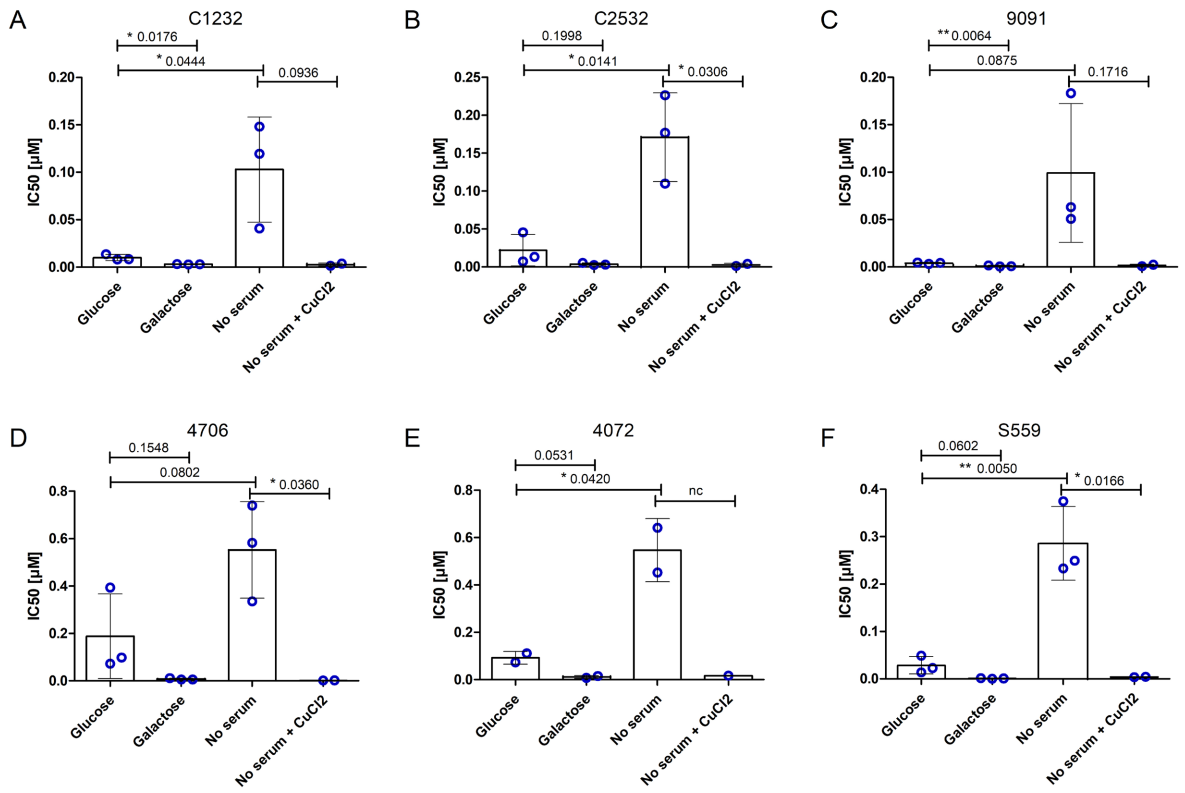

Figure 20: Sensitivity to NSC319726 is increased in galactose and decreased in serum-starved conditions. IC50 values calculated from CellTiter-Glo® assays after 72 hours of drug treatment normalized to DMSO controls for cell lines (A) C1232; (B) C2532; (C) 9091; (D) 4706; (E) 4072; (F) S559. NSC319726 was added in 7 concentrations (3-fold dilution series, highest concentration = 1 µM). Cells were cultured in different conditions as indicated. 10 µM $CuCl_2$ was added three hours before the beginning of NSC319726 treatment. Each dot represents one biological replicate derived from three technical replicates. Mean values ± SD are shown, p values are indicated, ***p value ≤ 0.001, **p value ≤ 0.01, *p value ≤ 0.05, nc = not calculable, two-tailed student's t test. The experiment was performed together with Christian Schneeweis.

To further elucidate whether oxidative phosphorylation and glycolysis play a role in the mechanism of action of NSC319726 as shown by Tsetkov et al. and the data presented in Figure 19 and Figure 20, Seahorse assays were performed measuring oxygen consumption rate (OCR) after treatment with NSC319726 and different inhibitors of the mitochondrial respiratory chain (Figure 21A-F). Across cell lines, decreases in oxygen consumption rate could be observed (Figure 21A-F), affecting all parts of mitochondrial respiration (Figure 22A-F).

Glycolysis was affected by NSC319726 to a weaker extent as shown in Figure 33 and Figure 34 (Supplementary data, Chapter 9).

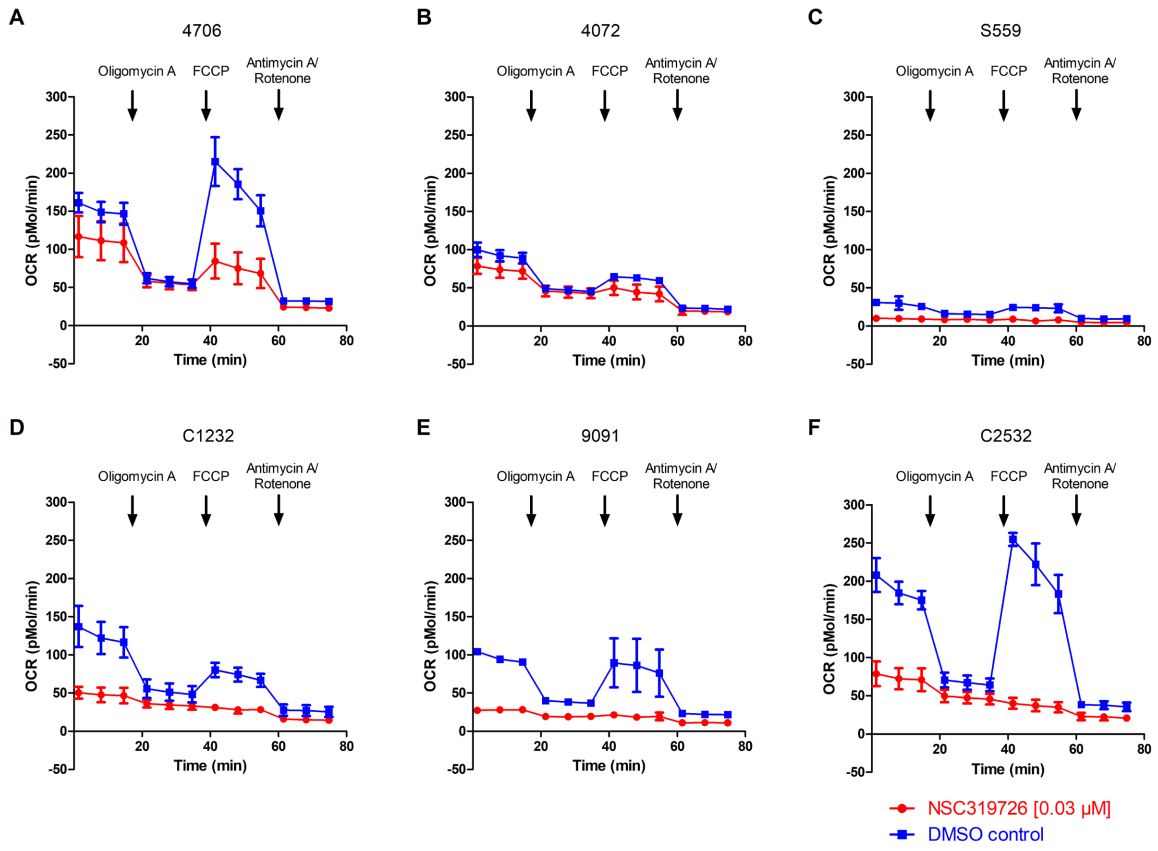

Figure 21: NSC319726 affects the mitochondrial respiratory chain.
Oxygen consumption rate (OCR) measured by Seahorse Assay Cell Mito Stress Test after 24 hours treatment with 0.03 µM NSC319726 for each of the tested cell lines (A) 4706; (B) 4072; (C) S559; (D) C1232; (E) 9091 and (F) C2532. Values for NSC319726 treatment and DMSO controls are normalized to cell viability, for each cell line separately. Mean values ± SD for four technical replicates are shown. Results shown are representative of two independent experiments.

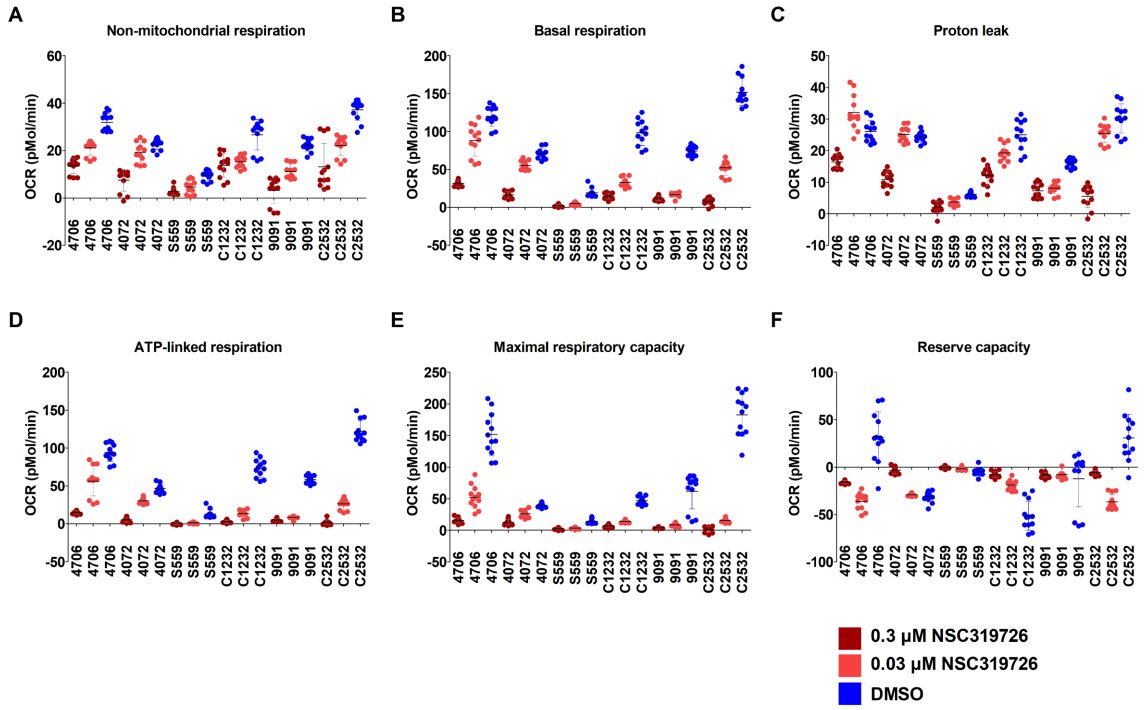

Figure 22: NSC319726 affects all parts of the mitochondrial respiratory chain.
OCR values from Figure 21 summarized for each part of the mitochondrial respiratory chain: (A) Non-mitochondrial respiration; (B) Basal respiration; (C) Proton leak; (D) ATP-linked respiration; (E) Maximal respiratory capacity; (F) Reserve capacity. Mean values ± SD are shown for four replicate OCR values measured at three consecutive time points (12 datapoints per condition).

Overall, it could be demonstrated that NSC319726 is highly efficient *in vitro* across the tested murine and human pancreatic cancer cell line cohort. Although it was originally discovered as a p53 mutant reactivator, the compound did not show significantly better efficacy in *Trp53* mutant cell lines. It could be demonstrated that NSC319726 could elicit its effects via pathways that are related to mitochondrial respiration.

6.9 Integration of drug sensitivity and RNASeq data using a pharmacogenomics pipeline

To identify biomarkers of drug sensitivity and resistance, drug sensitivity data can be integrated with other omics data such as genomic and transcriptomic data. As demonstrated in Figure 23A, for the majority of cell lines used for drug sensitivity profiling, RNA sequencing and genomic sequencing data is available. Since baseline transcriptional profiles have already been generated for almost all drug screened cell lines, we designed the first omics-integration pipeline using drug sensitivity and RNA sequencing data. Detailed descriptions of

the computational methods used are available in the doctoral dissertation of Fabio Boniolo (Boniolo 2022).

In brief, both single gene-based and pathway-based approaches were followed (Figure 23B). Elastic net models were generated based on gene expression alone whereas ridge regression models were calibrated on pathway enrichment scores (Boniolo 2022). For pathway predictions which are also further validated in this thesis (Chapter 6.11), publicly available protein-protein interaction networks and manually curated sets of pathways were used in addition to perform an a priori selection step for the calculation of single sample enrichment scores. These scores together with estimates of general drug response (GDR) were used to build models to predict drug response values (Figure 23B).

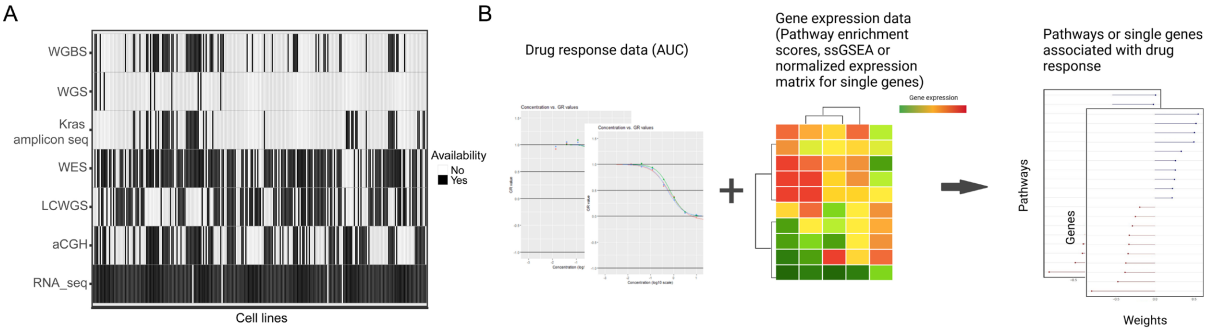

Figure 23: A pharmacogenomic pipeline to predict pathways associated with drug response.
(A) Overview of available omics data for the drug screened cell line cohort (WGBS: Whole Genome Bisulfite Sequencing, WGS: Whole Genome Sequencing, WES: Whole Exome Sequencing, LCWGS: Low-Coverage Whole Genome Sequencing, aCGH: array-based Comparative Genomic Hybridization, RNA_seq: RNA Sequencing). (B) Graphical summary of the input material and output of the pharmacogenomic approach to predict pathways associated with drug response. Panel (B) was created using BioRender.com.

6.10 Validation of an association between CB-839 sensitivity and *Surf1* expression

The large-scale drug response dataset, together with gene expression data generated for the same cell lines, allows for the identification of promising drug – expression associations as described in Chapter 6.9. These associations could hint at potential biomarkers for patient stratification. As an example, I investigated the correlation between drug response to the glutaminase inhibitor CB-839 (Gross et al. 2014) and expression of the gene *Surf1*, which is linked to mitochondrial respiration (Pulliam et al. 2014) (Figure 24A, B). Glutaminase and Surf1 have previously been shown to be interacting proteins (Antonicka et al. 2020). To verify these findings, I selected four cell lines showing high CB-839 AUC values and *Surf1* expression levels, as well as four cell lines with low CB-839 AUC and *Surf1* expression levels (Figure 24B). Subsequently, I performed clonogenic assays with the selected cell lines and

showed that indeed higher *Surf1* expression levels are associated with CB-839 resistance (Figure 24C, D).

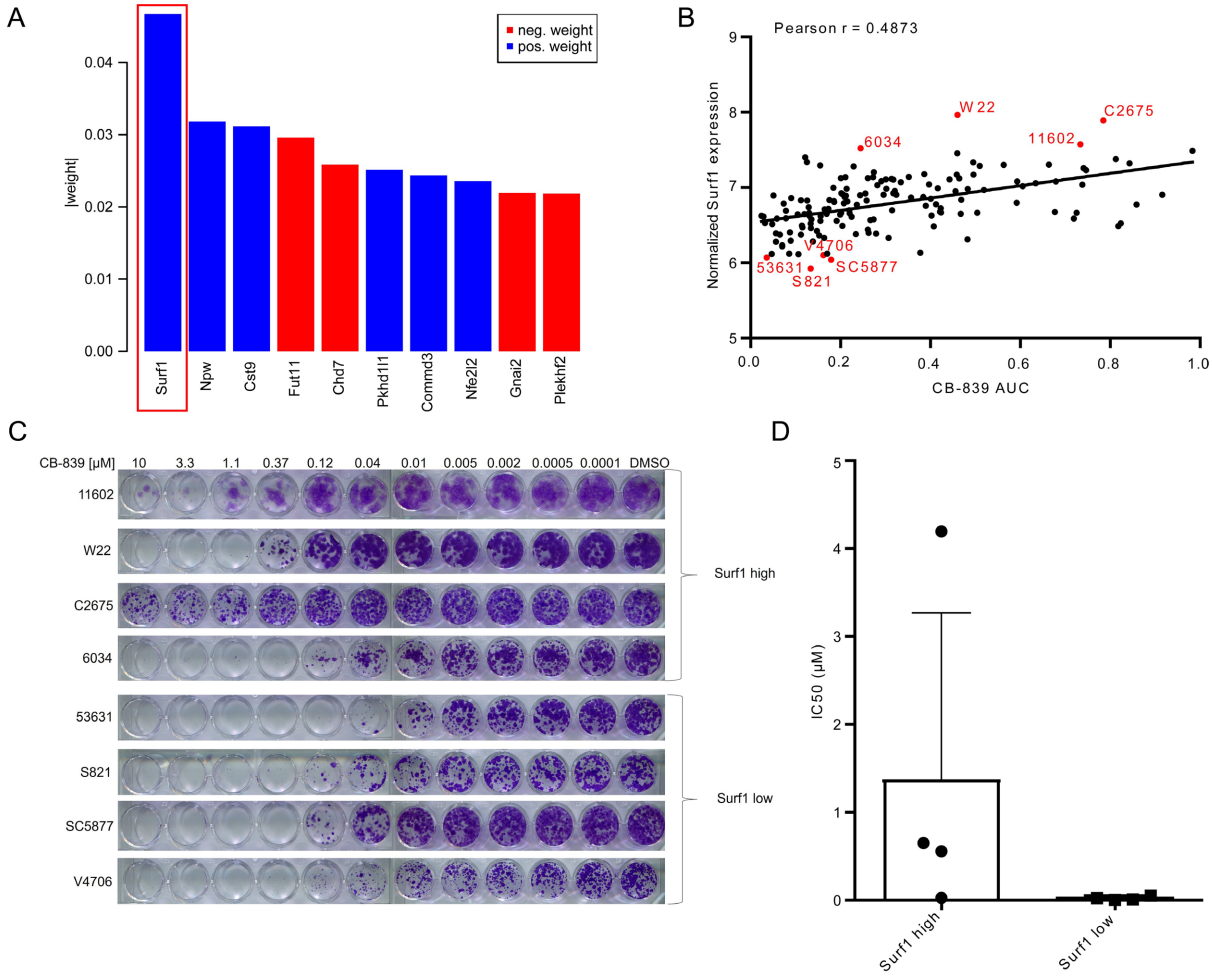

Figure 24: *Surf1* expression as a putative biomarker for CB-839 sensitivity.
(A) Gene expression associated with drug response to CB-839 according to elastic net regression models. The models were generated based on data for 150 cell lines. Analysis and graph by Fabio Boniolo. (B) Normalized *Surf1* expression plotted against AUC values for CB-839. Cell lines used for further validation experiments are highlighted in red. (C) Clonogenic assays using cell lines with low *Surf1* expression and high *Surf1* expression. Cells were treated with eleven concentrations of the drug CB-839 as indicated. Shown are representative results for one replicate out of two technical replicates (D) Representation of IC50 values derived from quantification of the clonogenic assays shown in (C). IC50 values were calculated based on two technical replicates and are shown for four cell lines with low *Surf1* expression and four cell lines with high *Surf1* expression. Mean with SD is indicated.

Overall, this chapter provided evidence that the drug screening results generated in this thesis, together with gene expression data, can be used to generate models of sensitivity and resistance and to identify putative biomarkers of drug response which can be selected for further validation.

6.11 Combinatorial drug screens to validate predictive modelling of drug response based on transcriptomics data

Predictive modelling of drug response based on pathway expression as described in Chapter 6.9 can be validated using different approaches. We chose here to first investigate the relevance of pathways potentially associated with drug resistance or sensitivity by combinatorial drug screening. Of the 90 models generated according to the approach described in Chapter 6.9, 64 models were selected to be of sufficient model performance (Pearson correlation > 0.3) (Figure 25A). The pathways targeted by at least three drugs with sufficient performance are shown in Figure 25B. We selected the pathways represented by the highest numbers of drugs, i.e. MEK, microtubules and multi-receptor tyrosine kinases (multi-RTK) for further validation by combinatorial drug screening. For each pathway, the compound with the highest variability in effectiveness (highest mean absolute deviation of the AUC) was used (Figure 25C). The results for the combinatorial drug screens using Trametinib in combination with the drug library have already been published (Falcomatà et al. 2022). In this thesis, I will present the results for the validation of pathways associated with resistance and sensitivity to the microtubule inhibitor Paclitaxel and the multi-RTK inhibitor Afatinib.

We selected a set of 10 cell lines representing groups of high (“sensitive”), intermediate (“neutral”), and low sensitivity (“resistant”) to the monotherapy treatment for both of these drugs (Figure 25D, E). Afatinib and Paclitaxel were added in a single dose, namely the median IC50 of the 25 % most sensitive cell lines from the monotherapy high-throughput drug screening dataset consisting of 250 murine cells lines (Figure 25F). Expected AUC values based on the Bliss model were derived from the monotherapy screening dataset and subtracted from AUC values calculated from the combinatorial drug screening data to obtain delta AUC values. Negative delta AUC values are used as a proxy for synergy, whereas positive delta AUC values were associated with potential antagonism.

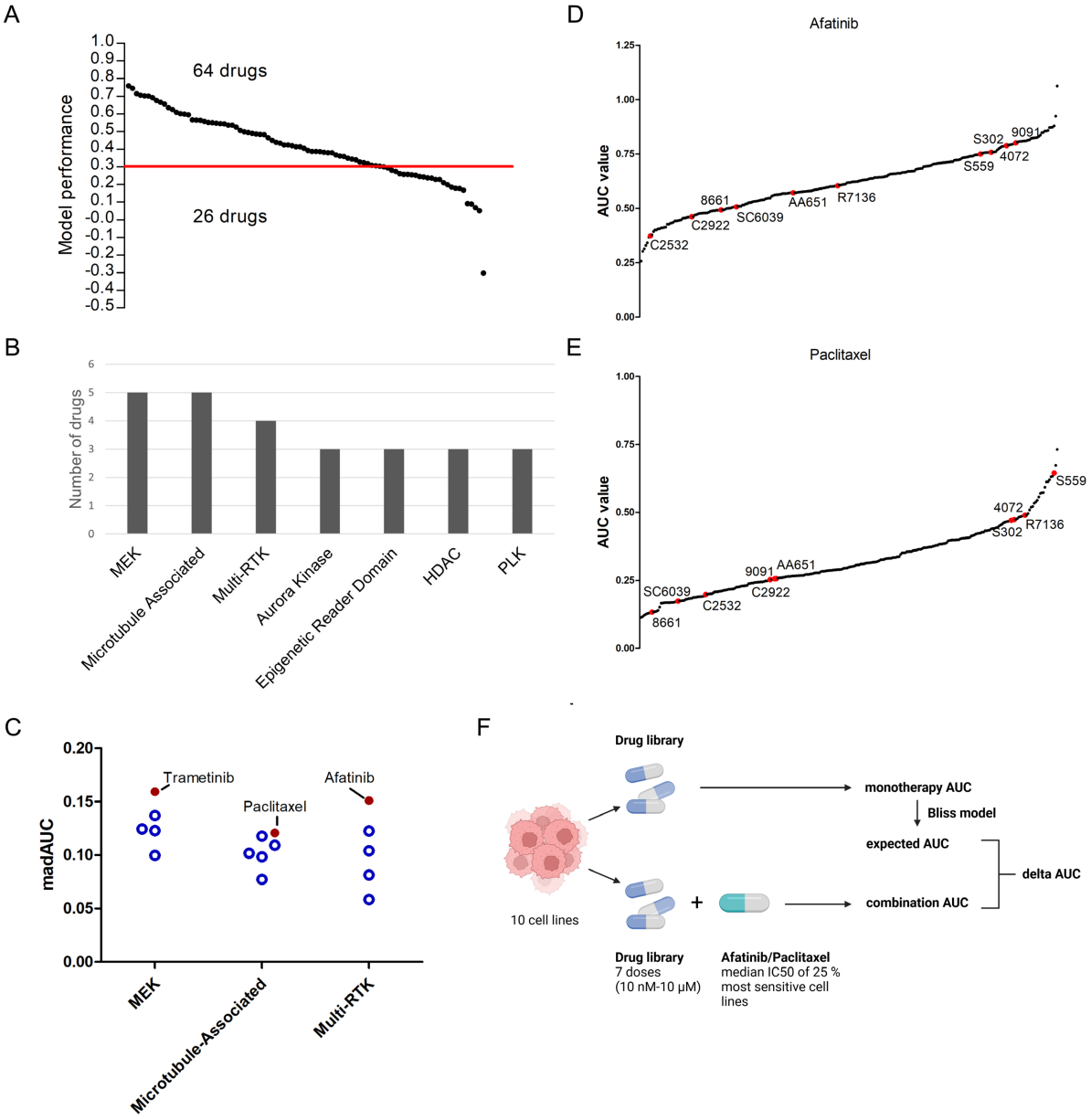

Figure 25: Experimental design for the validation of pathways associated with drug response by combinatorial drug screening.
(A) Overview of the model performance for the 90 generated models. 64 drugs had a performance above 0.3. (B) Overview of the pathways targeted by the highest number of drugs in the selection of 64 drugs (model performance > 0.3, at least 3 drugs targeting the pathway). (C) Median absolute deviation of AUC values for each of the drugs targeting MEK, microtubules or multi-RTK. The median absolute deviation was calculated from the monotherapy dataset for 250 murine cell lines. (D) AUC values from the monotherapy dataset for Afatinib for all screened 250 murine cell lines. Cell lines selected for the combinatorial validation screen are highlighted. (E) AUC values from the monotherapy dataset for Paclitaxel for all screened 250 murine cell lines. Cell lines selected for the combinatorial validation screen are highlighted. (F) Overview of the strategy for the combinatorial drug screen. The drug library (7 concentrations, 3-fold dilution, 10 µM – 10 nM) is given as monotherapy or in combination with the anchors Afatinib (single concentration: 0.2 µM) or Paclitaxel (single concentration: 0.01 µM). Using the Bliss model, an expected AUC value is calculated for each drug based on the monotherapy data and is compared to the AUC value obtained from the combination treatment. Panel (F) was created using BioRender.com. Figures and experimental design were adapted from Chiara Falcomatà.

The results represented by delta AUC values derived from the combination treatment with Afatinib are summarized in Figure 26. As shown in Figure 26A, the occurrence of potential synergism was highly cell line dependent. A large number of potentially synergistic combinations was identified for the cell lines C2532 and S559, whereas for the other tested cell lines, potential synergism was rare. Delta AUC values below certain thresholds, e.g. delta AUC < -0.1, therefore largely reflect the results for the cell lines C2532 and S559 (Figure 26B, C).

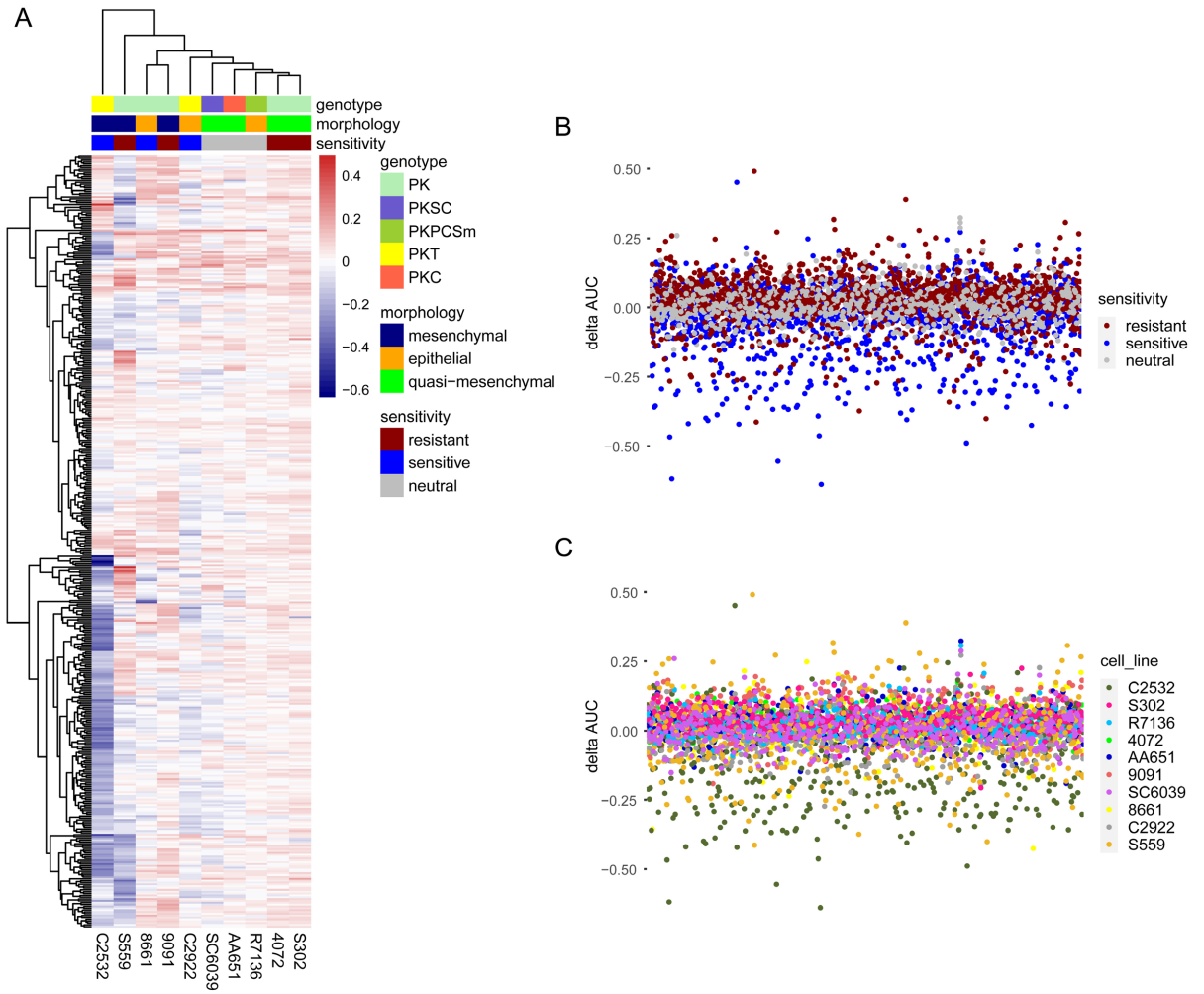

Figure 26: Overview of combinatorial drug screens results for the anchor Afatinib.
(A) Heatmap representation of the delta AUC values ($AUC_{combination} - AUC_{expected}$) with values below 0 indicating potentially synergistic combinations. Clustering is based on Euclidean distance. Genotype, morphology and sensitivity to Afatinib monotherapy are indicated. (B) Overview of the distribution of delta AUC values colored by the sensitivity of the cell lines to the monotherapy treatment. (C) Overview of the distribution of delta AUC values colored by cell line.

A similar pattern of potential synergism was observed for the combinations with Paclitaxel (Figure 27). In this case, the cell line S559 presented with by far the most potentially synergistic combinations as represented in Figure 27A, B and C.

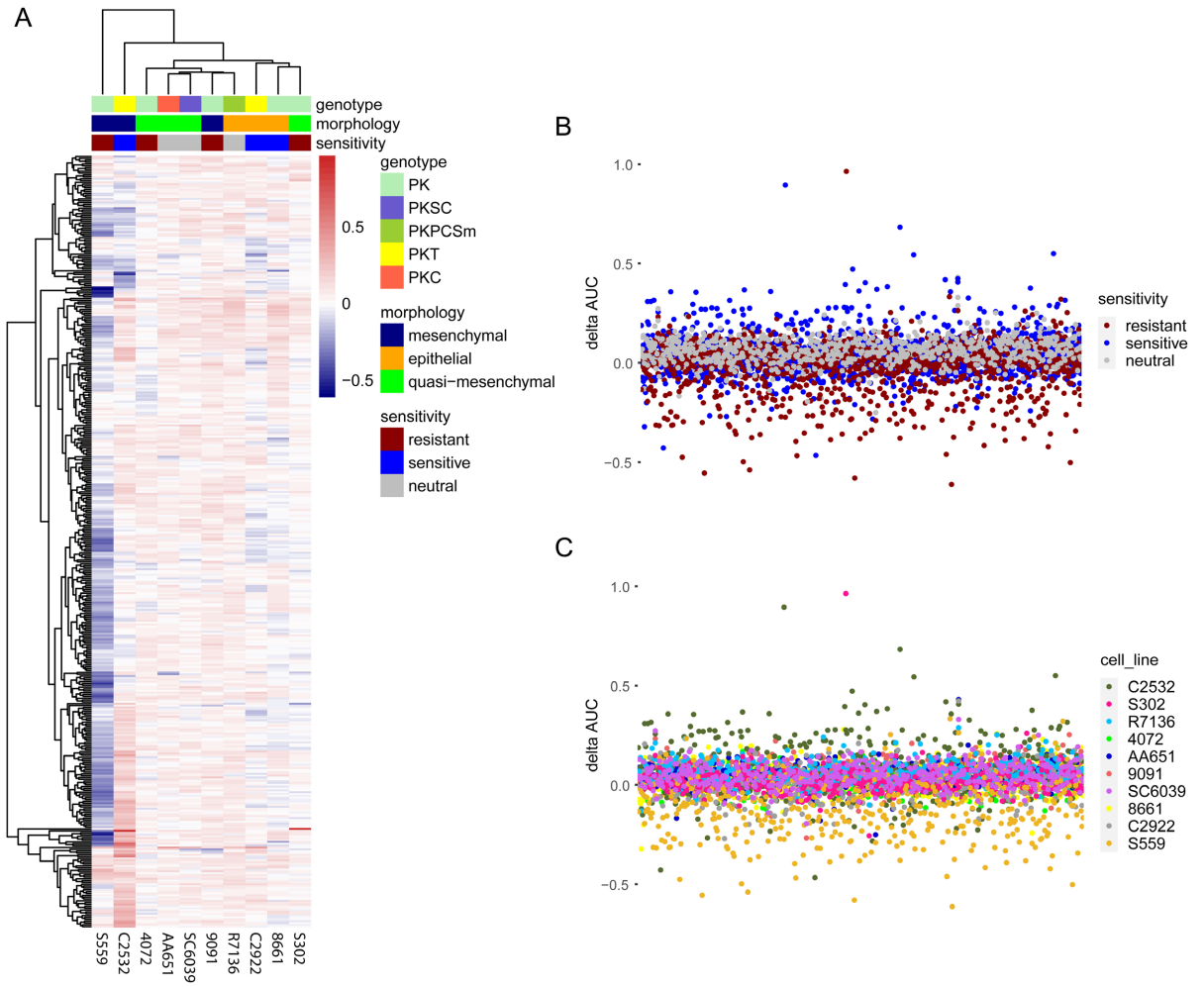

Figure 27: Overview of combinatorial drug screens results for the anchor Paclitaxel.
(A) Heatmap representation of the delta AUC values ($AUC_{combination} - AUC_{expected}$) with values below 0 indicating potentially synergistic combinations. Clustering is based on Euclidean distance. Genotype, morphology and sensitivity to Paclitaxel monotherapy are indicated. (B) Overview of the distribution of delta AUC values colored by the sensitivity of the cell lines to the monotherapy treatment. (C) Overview of the distribution of delta AUC values colored by cell line.

The high variability in the number of potentially synergistic drug combinations across the tested cell lines complicated the identification of common hits to be compared to the pharmacogenomic predictions. We decided to select the most promising combinations based on the median delta AUC across our cell line cohort. The ten best scoring compounds (lowest median delta AUC) were then used for further analysis. These selection criteria revealed the inhibitors Linisitinib (targeting IGF-1R), Orantinib (targeting PDGFR), TPX-0005 (targeting Src and ALK) and Ceritinib (targeting ALK) as potentially synergistic combinations with Afatinib (Figure 28A). While these targets do not exactly match the pathways predicted to be associated with sensitivity to Afatinib, namely for example ERBB and VEGF/VEGFR pathways (Figure 28B), they can nevertheless both be allocated to the group of receptor tyrosine kinases.

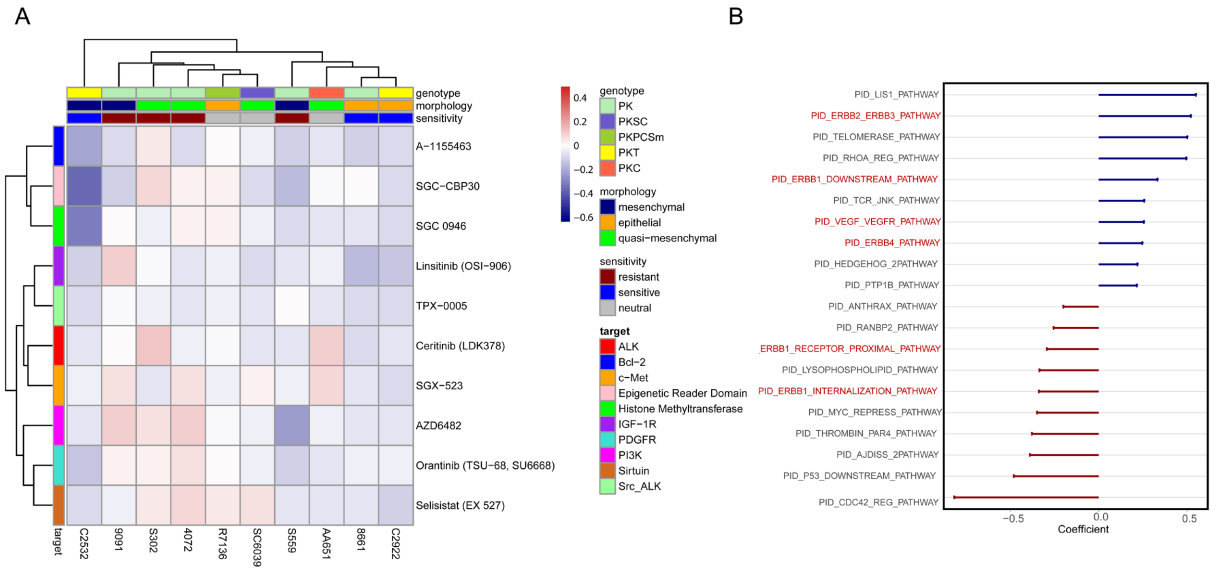

Figure 28: Results from combinatorial drug screen with Afatinib partially reflect predicted pathways.
(A) Heatmap representation of the delta AUC values for the ten drugs with the highest median delta AUC values in combination with Afatinib across the ten tested cell lines. Clustering based on Euclidean distance. Genotype, morphology and sensitivity to Afatinib monotherapy are indicated as well as the drug targets. (B) Pathways predicted to be associated with drug response to Afatinib. Panel (B): Analysis and graph by Fabio Boniolo.

Among others, the autophagy and 6-phosphofructo-2-kinase inhibitor PFK15 and the PI3K inhibitor ZSTK474 were identified as potentially synergistic compounds with Paclitaxel according to the same approach as described for Afatinib (Figure 29A). These targets are related to the pathways predicted to be associated with Paclitaxel sensitivity, namely PI3K and mTOR signaling as well as LKB1 pathways related to autophagy (Figure 29B).

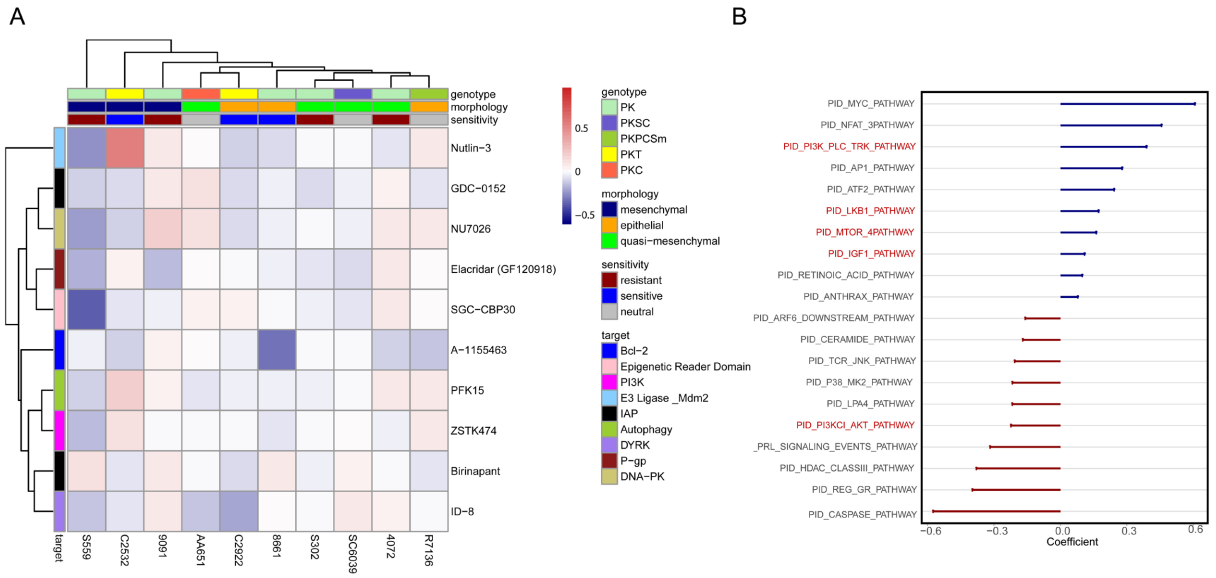

Figure 29: Results from combinatorial drug screen with Paclitaxel partially reflect predicted pathways.
(A) Heatmap representation of the delta AUC values for the ten drugs with the highest median delta AUC values in combination with Paclitaxel across the ten tested cell lines. Clustering based on Euclidean distance. Genotype, morphology and sensitivity to Paclitaxel monotherapy are indicated as well as the drug targets. (B) Pathways predicted to be associated with drug response to Paclitaxel. Panel (B): Analysis and graph by Fabio Boniolo.

Overall, the results from combinatorial drug screens presented in this chapter encouraged further validation by complementary methods such as CRISPR/Cas9-based screens, which is presented in Chapter 6.12.

6.12 CRISPR/Cas9 screens to validate predictive modelling of drug response based on transcriptomics data

Based on the promising results obtained from the validation of predictive modelling of drug response by combinatorial drug screening, we decided to complement these findings by performing CRISPR/Cas9 based screens. An already available cell line stably expressing Cas9 (Falcomatà et al. 2022) was transduced with a genome-scale CRISPR/Cas9 pooled library and divided into two different treatment arms (Afatinib or Paclitaxel) and a control arm (DMSO) (Figure 30A). After a two-week treatment period, DNA was harvested and sequenced to identify genes which were depleted in the presence of Afatinib or Paclitaxel. To this end, ß-scores were calculated for each gene and each of the treatment and control arms. Differences in ß-scores are denoted as differential sensitivity. 165 genes for Afatinib treatment and 196 genes for Paclitaxel treatment were identified which showed significant ß-scores (false discovery rate (FDR) ≤ 0.05 in both control and treatment arm) and differential sensitivity ≤ -0.25 (Figure 30B-C). After exclusion of essential genes, the remaining genes were analyzed for enrichment of PID pathways (Figure 30D-E).

Several overlaps between the thus obtained pathways (Figure 30D-E) and pathways predicted to be associated with drug response (Figure 28B, Figure 29B) were observed. Depletion of TCR-JNK, PTP1B and ERBB1_DOWNSTREAM pathways seen in our CRISPR/Cas9 based screen performed under Afatinib treatment is coherent with the predictions made previously indicating associations with resistance to this drug. Importantly, the association between drug response to Afatinib and ERBB1 and PTP1B pathway expression is also reflected by synergistic combinations observed for receptor tyrosine kinase inhibitors (Figure 28A).

AP1, MYC and LKB1 pathways predicted to be associated with resistance to Paclitaxel treatment (Figure 29B) were also significantly depleted after treatment with this drug as seen in our CRISPR/Cas9 based screen (Figure 30E). The 6-phosphofructo-2-kinase inhibitor PFK15 was identified as potentially synergistic with Paclitaxel in our combinatorial drug screens (Figure 29A), in line with the association seen between drug response and LKB1 pathway expression.

Overall, it could be shown that the drug response data presented in this thesis, together with other omics data such as transcriptomics data, can be used to make predictions of drug sensitivity and resistance based on expression of specific pathways. These predictions could be validated for two exemplary drugs, Afatinib and Paclitaxel, by combinatorial drug screens and CRISPR/Cas9 based screens.

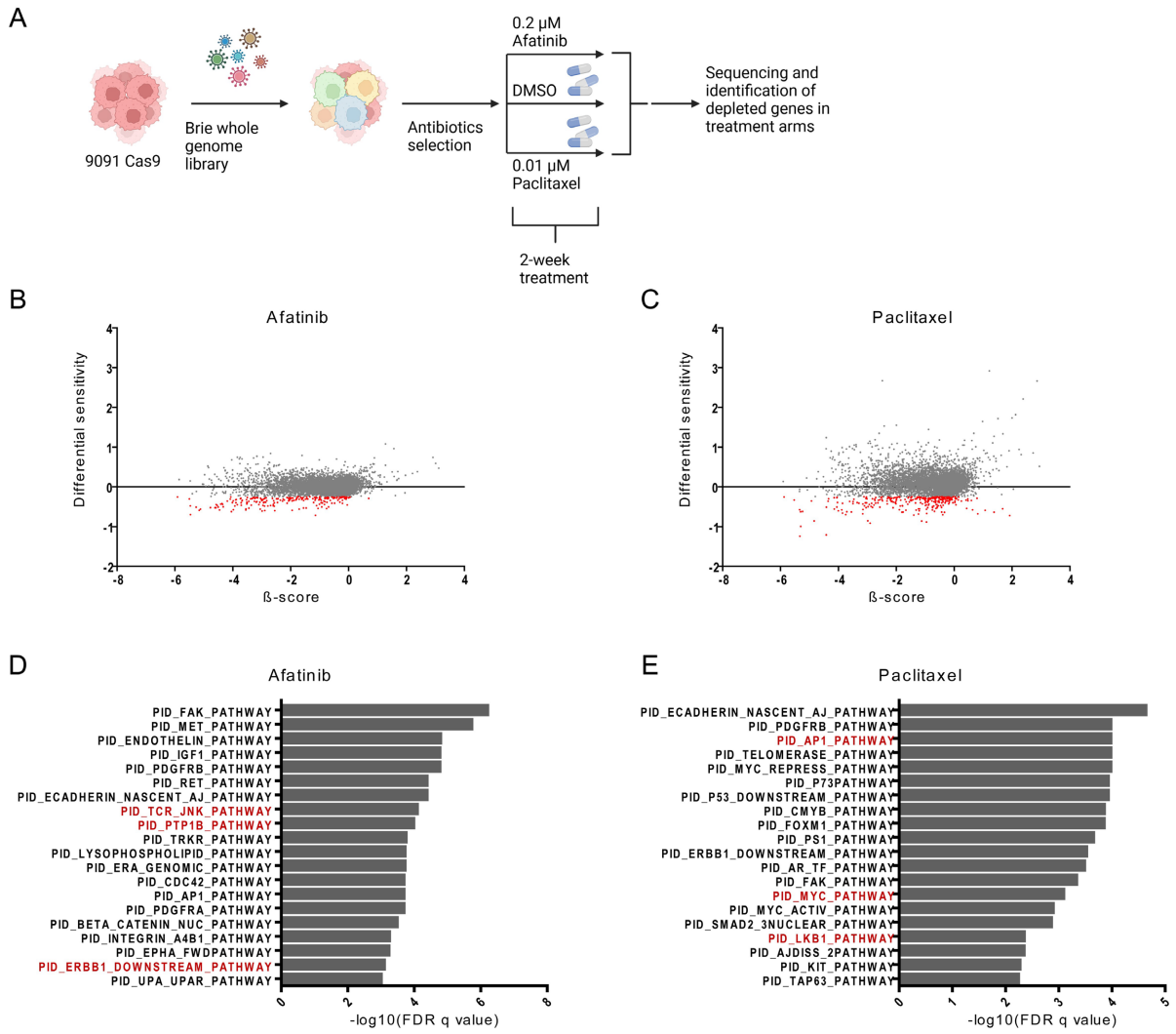

Figure 30: Results from CRISPR/Cas9-based screens support predictions of drug sensitivity and combinatorial drug screens.
(A) Experimental design of the CRISPR/Cas9-based screens: the cell line 9091 stably expressing Cas9 (9091 Cas9) was transduced with a genome-scale library, subjected to antibiotics selection and subsequently divided into two treatment arms and one control arm. Sequencing was performed to identify depleted genes in the treatment arms. Differences in sgRNA representation between treatment and control arms are calculated as ß-scores and differential sensitivity represents differences in ß-scores between each treatment arm and the control arm. Overviews of ß-scores and differential sensitivity are shown for Afatinib (B) and Paclitaxel (C) treatment. Differential sensitivity values ≤ -0.25 are highlighted in red. Gene set enrichment analysis was performed for non-essential genes with differential sensitivity ≤ -0.25 and FDR ≤ 0.05 in both control and treatment arms. The 20 pathways with highest significance are shown for Afatinib (D) and Paclitaxel (E) treatment. Pathways overlapping with predictions of drug resistance shown in Figure 28B and Figure 29B are highlighted in red. The experimental part of the CRISPR/Cas9-based screens was performed by myself with support from Christian Schneeweis. The primary analysis of the data including the calculation of ß-scores was performed by Anantharamanan Rajamani. The pipeline for gene set enrichment analysis was designed by Chiara Falcomatà. Panel (A) was created using Biorender.com.

7 Discussion

7.1 An automated high-throughput drug screen in pancreatic cancer cell lines

In this thesis, I have presented the results of the, to my knowledge, so far largest high-throughput drug screen in pancreatic cancer cell lines. This dataset provides a comprehensive characterization of the landscape of drug response in a large collection of murine cell lines, complemented by a group of primary human cell lines. In addition, I re-tested a cohort of commercially available established human cell lines for which drug screening data have previously been generated by different institutes and which are publicly available (Seashore-Ludlow et al. 2015; Rees et al. 2016; Picco et al. 2019; Corsello et al. 2020).

Overall, the drug sensitivity map presented in this thesis was characterized by resistance to the majority of the drugs. Nevertheless, we could identify several compounds with particularly high efficacy across the PDAC cell line cohort, including the HDAC inhibitor Romidepsin, the proteasome inhibitor Carfilzomib and the histone methyltransferase inhibitor Chaetocin.

The potential of drugs targeting epigenetics pathways, such as HDAC inhibitors, for PDAC treatment has already been shown in various pre-clinical studies (Versemann et al. 2022). Romidepsin is one of the epigenetic compounds which is also being tested in clinical trials involving PDAC patients (Jones et al. 2012; Elrakaybi et al. 2022). Chaetocin is another epigenetic drug for which promising *in vitro* data in PDAC is already available (Mathison et al. 2017). For the proteasome inhibitor Carfilzomib, on the other hand, subtype-specific vulnerabilities in PDAC have been reported (Fraunhoffer et al. 2020). While our study could therefore confirm previously known potential treatment strategies for PDAC with high *in vitro* efficacy, we could also identify novel candidates for further pre-clinical and clinical investigations in pancreatic cancer. For the compound NSC319726, to my knowledge, *in vitro* efficacy in PDAC cell lines has not been demonstrated prior to this study. We carried out further investigations on the mechanism of action of this drug which is discussed in more detail in Chapter 7.2.

In addition to these generally effective or ineffective compounds, we observed high heterogeneity in drug response for a considerable fraction of drugs which also allowed us to identify subgroup-specific vulnerabilities. We observed highly significant differences in sensitivity based on the morphology/subtype of the PDAC cell lines and could confirm previously known associations. These include higher efficacy of MEK inhibition and the proteasome inhibitor Carfilzomib in epithelial cells (Falcomatà et al. 2022; Fraunhoffer et al. 2020) and higher efficacy of HDAC inhibition in mesenchymal cells (Krauß et al. 2022).

Knowledge of such associations between drug response and specific characteristics (e.g. morphology) of the cell lines may be particularly valuable in the case of PDAC as stratification is thought to be an important strategy for the development of more effective treatment regimens (Juiz et al. 2019).

Furthermore, the high-throughput drug screening data, together with other large-scale datasets encompassing transcriptomics, genomics, and proteomics data, can also be used to identify potential biomarkers of drug sensitivity and resistance. Such approaches are discussed in more detail in Chapter 7.4.

An additional application of the drug response data presented in this thesis is the identification of misannotated targets and gaining insights into drugs' mechanism of action. One prominent example shown here is the drug KX2-391, originally annotated as an Src inhibitor (Fallah-Tafti et al. 2011), but which shows clear clustering with microtubule inhibitors. This phenomenon has previously been reported and KX2-391 has been validated as a microtubule inhibitor (Seashore-Ludlow et al. 2015; Smolinski et al. 2018). Such correlation analyses also formed the basis of the investigations of the mechanism of action of NSC319726 presented in this thesis (Chapter 7.3).

All these potential applications of the large-scale drug screening dataset, i.e. identification of effective drugs for pancreatic cancer, identification of therapeutic vulnerabilities in PDAC subgroups with potential biomarkers based on cell line phenotypes or derived from multi-omics data integration and mechanistic studies, can be complemented by the availability of additional data for primary human PDAC cell lines. This allows for cross-species validations of the obtained results. In that regard it should be noted that, even though overall, mice and humans have many similarities on the molecular level, there are nevertheless also differences which can lead to differing responses to therapy (Lin et al. 2014). Therefore, not surprisingly, we observed for example specific drugs with generally higher or lower efficacy in human compared to murine cell lines. Such differences may need to be taken into account when selecting drugs for further validation studies.

7.2 Comparability of large-scale pharmacogenomic datasets

The reproducibility and the utility of large-scale pharmacogenomic approaches have been scientifically debated (Haibe-Kains et al. 2013; Safikhani et al. 2016b; Pharmacogenomic agreement between two cancer cell line data sets 2015; Smirnov et al. 2016; Safikhani et al. 2016a; Geeleher et al. 2016; Bouhaddou et al. 2016; Mpindi et al. 2016). Various confounding factors such as drug concentration range, numbers of cells seeded per well,

numbers of cell doublings achieved, media conditions and growth rate as well as assay readout including the cell viability assay and analytical tools used have been identified which can diminish the achievable correlation values between studies (Pharmacogenomic agreement between two cancer cell line data sets 2015; Mpindi et al. 2016; Hafner et al. 2016).

In our high-throughput drug screening approach, we have strived to reduce the “intra-screen” confounding factors to minimal levels, by for example using the same batch of FCS for all screened cell lines and ordering the compounds always from the same provider who also conducts analytical chemistry to assure identity and purity of the compounds. “Intra-screen” consistency is reflected by the results presented in Chapter 6.5 which demonstrate high correlations of AUC values for drugs with similar targets.

To investigate the degree of consistency of our screen compared to other large-scale screening approaches, I included 20 commercially available established human pancreatic cancer cell lines into the drug screening pipeline. The results can be directly compared to publicly available datasets from the DepMap Portal (https://depmap.org/portal/download/all/).

Previous studies have employed different approaches to measure consistency, for example for each drug separately across all of the cell lines, termed an “across” cell line comparison (Haibe-Kains et al. 2013). Correlation values have been demonstrated to be improved by a “between” cell line comparison approach, where correlation is estimated for pairwise overlapping cell lines over shared sets of compounds (Mpindi et al. 2016). Other groups have calculated correlation coefficients across all shared data points (overlapping cell line – drug pairs) (Pozdeyev et al. 2016; Corsello et al. 2020). While correlation coefficients can be lower or higher for individual drugs (Haibe-Kains et al. 2013; Pharmacogenomic agreement between two cancer cell line data sets 2015), comparisons across shared data points commonly yield moderate correlation values of around 0.6 (Pozdeyev et al. 2016; Corsello et al. 2020).

In this study, I applied a similar approach encompassing all shared data points to obtain an overall view on the levels of consistency of our own with the publicly available datasets GDSC2, CTRP and PRISM. Pearson correlation coefficients obtained from this analysis ranged between 0.64 to 0.66. To put these values into context, I also compared the public datasets for the selected 20 pancreatic cancer cell lines with each other, from which Pearson correlation coefficients between 0.48 and 0.55 were calculated. Overall, our dataset is therefore similarly robust to existing pharmacogenomic datasets (Corsello et al. 2020).

Further analyses that could be performed include the “across” cell line comparison for each individual drug (Haibe-Kains et al. 2013) and applying corrective measures to take

differences in experimental setups, especially used concentration ranges, into consideration. The adjustment of AUC values to the respective overlapping dose range has been proposed in that regard (Bouhaddou et al. 2016; Pozdeyev et al. 2016).

7.3 NSC319726 is highly effective across PDAC cell lines and is putatively targeting mitochondrial metabolism

Among the most effective drugs across the PDAC cell line cohort used in this project is the compound NSC319726, which was originally discovered as a p53-mutant reactivator (Yu et al. 2012; Yu et al. 2014). In the study presented here, AUC values were below 0.5 for almost all tested cell lines and no significant differences were observed between *Trp53* wild-type and *Trp53* mutant cell lines, indicating a predominantly p53-independent mechanism of action. As has been shown in this thesis (Chapter 6.5) and in previous studies (Seashore-Ludlow et al. 2015), clustering of compounds based on their drug response across a cell line cohort can be informative on drugs' mechanism of action. The three drugs with the highest correlation values with NSC319726 were Deguelin, NMS-873 and Elesclomol. Deguelin has been shown to act via DNA damage and repair gene suppression (JI et al. 2012), Akt inhibition (Jin et al. 2007), but also the induction of reactive oxygen species production (Xu et al. 2015). For NMS-873, originally identified as an inhibitor of the valosin-containing protein (VCP/p97), a dual mechanism of action targeting mitochondrial oxidative phosphorylation has been reported (Bouwer et al. 2021). Elesclomol is an accepted inducer of oxidative stress and has in addition been shown to target mitochondrial metabolism and to induce a novel form of cell death called cuproptosis (Zheng et al. 2022; Tsvetkov et al. 2022; Kirshner et al. 2008). For NSC319726, mechanisms of action involving the generation of reactive oxygen species (Shimada et al. 2018) and mitochondrial metabolism, similar to Elesclomol, have likewise been shown (Tsvetkov et al. 2022). Tsetkov et al. also reported on similar killing profiles of Elesclomol and NSC319726 in the PRISM Repurposing dataset (Tsvetkov et al. 2022). Based on these previous studies and the correlations observed in our high-throughput drug screen as well as the lack of *Trp53*-mutant-specific sensitivity, it could be assumed that the relevant mechanism of action of NSC319726 for our cell line cohort is independent of p53 but may involve mitochondrial metabolism and reactive oxygen species.

Before studying the mechanism of action in our PDAC cell lines in more detail, I confirmed the cytotoxicity of NSC319726 by clonogenic assays. IC50 values were shown to be in the picomolar to nanomolar range, confirming the high efficacy of the compound. In line with previous studies (Shimada et al. 2018; Tsvetkov et al. 2022), there was no indication that NSC319726 induced apoptotic, necroptotic or ferroptotic cell death, as shown by co-

treatment with specific inhibitors of these cell death pathways. This drug may therefore act via the recently identified novel cell death mechanism called cuproptosis (Tsvetkov et al. 2022).

We could confirm the role of copper in NSC319726's mechanism of action as $CuCl_2$ increased NSC319726 efficacy, which is in line with what has been previously shown (Tsvetkov et al. 2022). Like Tsetkov et al. did for Elesclomol, we also investigated the effect of BSO and NAC on NSC319726 efficacy. BSO is an inhibitor of gamma-glutamylcysteine synthetase, which is essential for the synthesis of glutathione (GSH) (Griffith 1982). GSH, as the most abundant antioxidant in the cell, plays an important role in the protection against ROS and the regulation of intracellular redox status (Reliene and Schiestl 2006; Anderson 1998). In addition, GSH is also a known copper chelator (Ngamchuea et al. 2016). Co-treatment with BSO increased the effect of NSC319726 and Elesclomol in this study and the report by Tsetkov et al, respectively (Tsvetkov et al. 2022). This may be explained by the involvement of copper, reactive oxygen species or both.

NAC is a synthetic precursor of cysteine and GSH and is therefore a widely accepted inhibitor of oxidative stress (Sun 2010; Zafarullah et al. 2003). Tsetkov et al. did not observe an effect of NAC on Elesclomol activity and therefore concluded that oxidative stress did not play a role in the mechanism of action (Tsvetkov et al. 2022). In our study, however, NAC reduced the activity of NSC319726 in some of the tested cell lines, indicating that for NSC319726 in our PDAC cohort, ROS may play a role. Even though the two inhibitors Elesclomol and NSC319726 have been previously reported to act in an overall similar fashion (Tsvetkov et al. 2022), there may nevertheless be differences in their detailed mechanism of action. In addition, NAC has been shown to reverse ROS production only in specific cells (Zheng et al. 2022; Kirshner et al. 2008; Rushworth and Megson 2014) and the effect of NAC on Elesclomol is also controversial depending on the cell lines and concentrations used (Zheng et al. 2022; Wangpaichitr et al. 2009; Lee et al. 2020; Buccarelli et al. 2021; Tsvetkov et al. 2022). Depending on the context, Elesclomol may therefore exert its effect by either ROS induction and/or targeting mitochondrial metabolism (Zheng et al. 2022) and this may also be the case for NSC319726.

Apart from the effect of NAC on NSC319726 toxicity that we could demonstrate, we could, however, not confirm the induction of ROS in flow cytometric analysis using CellROX™ Deep Red Reagent (data not shown). A previous study in glioblastoma cells which showed ROS induction by NSC319726 performed staining with the ROS detection reagent H_2DCFDA (Shimada et al. 2018), which could also be attempted in our PDAC cell lines in the future. Shimada et al. could not define exactly which ROS is induced by NSC319726 and the specific species generated may not have been detectable by CellROX™ Deep Red Reagent.

While in our study, we could not confirm the induction of ROS by NSC319726, apart from the effect of NAC, we could present strong indications that oxidative phosphorylation and mitochondrial metabolism play an important role for NSC319726's toxic effects. Culturing of cells in galactose, thereby forcing them to predominantly undergo oxidative phosphorylation, tended to increase the effect of NSC319726 in line with previous reports (Tsvetkov et al. 2022). Whereas Elesclomol was shown to reduce the spare capacity of mitochondrial respiration in non-small cell lung cancer and Ewings sarcoma cells (Tsvetkov et al. 2022), I could show that in PDAC cells, NSC319726 affected all components of the mitochondrial respiratory chain. This indicates again that there may be detailed differences between the mode of action of Elesclomol and NSC319726 or that these may depend on the cell culture system and concentrations used.

Overall, I presented evidence that oxidative phosphorylation, and potentially ROS, play an important role in the mode of action of NSC319726. To further elucidate key players that are involved, CRISPR/Cas9 knockout screens could, for example, be performed.

Elesclomol has already been tested in several clinical trials where it has shown a favorable safety profile, but not the desired clinical response (Monk et al. 2018; Hedley et al. 2016; O'Day et al. 2009; Zheng et al. 2022). A retrospective analysis of a phase 3 combination trial in melanoma patients revealed, however, that low plasma lactate dehydrogenase (LDH) levels were associated with higher sensitivity to Elesclomol (O'Day et al. 2009; Tsvetkov et al. 2022). Future clinical trials of Elesclomol and similar compounds such as NSC319726 may therefore be considered for selected patient populations (Tsvetkov et al. 2022; Zheng et al. 2022). NSC319726 has not yet been used in clinical trials. Based on the strong efficacy in PDAC cell lines, such clinical investigations, alone or in combination with for example glycolysis inhibitors, and possibly in selected patient populations may be warranted in the future.

7.4 Multi-omics data integration using the obtained drug sensitivity data

A great strength of the presented large-scale drug sensitivity dataset is that comprehensive molecular characterization is additionally available for the investigated cell lines. In an approach similar to what is being pursued by the DepMap Portal (Barretina et al. 2012; Ghandi et al. 2019), drug response can therefore be integrated with other large-scale datasets to identify biomarkers that could allow for patient stratification. Stratification may be particularly relevant in pancreatic cancer due to high molecular heterogeneity which is widely

thought to hamper the success of targeted therapies in unselected patient cohorts (Juiz et al. 2019).

A subset of the drug response data from the here presented high-throughput screen, including 36 mouse cell lines, has already been successfully used for an integration with (phospho)proteomic data (Giansanti et al. 2022). Associations between Sirt6 protein abundance and sensitivity to Trametinib and Cobimetinib as well as between Shroom2 abundance and responses to KX2-391 and other tubulin polymerization inhibitors could exemplarily be shown (Giansanti et al. 2022).

In addition, advanced machine learning techniques can be applied to the generated large-scale datasets (Boniolo et al. 2021) and such a pharmacogenomic pipeline using drug sensitivity and transcriptomics data has recently been developed in the Saur laboratory (Boniolo 2022). Predictive models based on the expression of single genes on the one hand or of pathways on the other hand were generated. In a next step, these models need to be validated experimentally, as has exemplarily been shown in this thesis for an association identified between the effectiveness of the glutaminase inhibitor CB-839 and *Surf1* mRNA expression. For further biomarker validation studies, *Surf1* mRNA levels will additionally need to be verified by complementary methods such as qPCR and the association will also have to be shown in the human setting. Nevertheless, this study further demonstrates that it is possible to derive candidate biomarkers from our high-throughput drug screening and transcriptomics datasets.

In a second computational approach, the activity of pathways was associated with drug response (Boniolo 2022). Previous work in the Saur laboratory has shown that such predicted pathways can be validated by combinatorial drug screening (Falcomatà et al. 2022) and CRISPR/Cas9-based negative selection screens (Boniolo 2022). In this thesis, I took a similar approach to validate the pathways predicted to be associated with drug response to two additional inhibitors, namely the multi-RTK inhibitor Afatinib and the microtubule inhibitor Paclitaxel. Combinatorial drug screens identified IGF-1R, PDGFR and ALK inhibitors to be cooperating with Afatinib, which correlates with pathways associated with receptor tyrosine kinases predicted to be relevant for Afatinib response. Sensitivity to Paclitaxel was predicted to be associated with PI3K, mTOR and LKB1 pathway activity. In line with these predictions, the autophagy inhibitor PFK15 and the PI3K inhibitor ZSTK474 were shown to potentially synergize with Paclitaxel in combinatorial drug screens.

While the combinatorial drug screens provided first hints at the validity of the predicted pathways, this approach suffers certain limitations, regarding for example potential off-target effects of compounds (Klaeger et al. 2017; Antolin et al. 2020; Lechner et al. 2022) which can complicate the interpretation of associations. Due to constraints in feasibility, the

combinatorial drug screens were performed in only one replicate, further increasing the noise of the data. We therefore decided to complement them by further validation experiments using CRISPR/Cas9 based negative selection screens.

Overall, good agreement between pathways predicted to be associated with drug response and those seen depleted after drug treatment in our CRISPR/Cas9 based experiments was observed. Among the pathways predicted to be associated with the resistance to the compound Afatinib (Figure 28B), TCR-JNK, PTP1B and ERBB1 pathways were also seen significantly depleted within our CRISPR/Cas9 based negative selection screen performed under treatment with the same drug. In general, pathways related to receptor tyrosine kinase signaling are highly represented in all three datasets, in the predictions made based on RNA sequencing data, in our combinatorial drug screen and the CRISPR/Cas9 based screen. Receptor tyrosine kinase inhibitors targeting for example ALK, c-Met, PDGFR and IGF-R are clearly enriched in the set of drugs with potential synergy with Afatinib and pathways depleted in the CRISPR/Cas9 based screen include MET, IGF1, PDGFR and ERBB1 pathways, indicating a strong agreement between the datasets. EGFR (ERBB1) pathway activation, activating *EGFR* and *ALK* mutations and *c-MET* amplifications have previously been reported as resistance mechanism for the compound Afatinib (van der Wekken et al. 2016).

AP1, MYC and LKB1 pathways predicted to be associated with resistance to Paclitaxel treatment (Figure 29B) were also significantly depleted after treatment with this drug as seen in our CRISPR/Cas9 based screen. Interestingly, the 6-phosphofructo-2-kinase and autophagy inhibitor PFK15 was also identified as potentially synergistic with Paclitaxel by combinatorial drug screening. LKB1 is a kinase which directly activates, among others, AMPK, which in turn is a central player in cell growth and metabolism (Shackelford and Shaw 2009). One of the substrates of AMPK is 6-phosphofructo-2-kinase (Shackelford and Shaw 2009) which, as mentioned above, can be targeted by the compound PFK15 (Zhu et al. 2016). Based on our results, it could therefore be hypothesized that LKB1 pathway expression could serve as a potential biomarker for Paclitaxel resistance which could be combated by co-treatment with PFK15. Intriguingly, synergy between Paclitaxel and PFK15 has previously been shown in *in vitro* and *in vivo* breast cancer models (Lu et al. 2021) as well as in a study presenting dual targeting of cancer cells and cancer-associated fibroblasts by nanoparticles (Zang et al. 2022). These previously published findings may warrant further investigations to confirm synergy between Paclitaxel and PFK15 in pancreatic cancer. Given that Paclitaxel, administered together with Gemcitabine is currently part of standard of care therapeutic regimens for this cancer entity (Kleeff et al. 2016), a three-compound combination may also be interesting to analyze.

8 Conclusion and outlook

In summary, this work comprises the so far largest high-throughput drug screening dataset for pancreatic cancer cell lines. It was shown that these data can be used to identify subgroup-specific vulnerabilities and compounds with high efficacy in PDAC and can help to elucidate drugs' mechanisms of action. Additional mechanistic studies were performed for one particular drug, NSC319726, originally identified as a p53 mutant reactivator, which demonstrated that copper and mitochondrial respiration may play an important role in the mechanism of action of this drug. In addition, the integration of the drug response data with other omics data can help to determine specific biomarkers of drug sensitivity or resistance. As exemplarily shown here, expression of single genes or pathway activation can be proposed as potential predictors of drug response and can be validated using different approaches such as combinatorial drug screens and CRISPR/Cas9-based negative selection screens. While this study has focused on transcriptomics data, integration with other large-scale datasets such as genomics and proteomics data is possible in the future and may yield an even more comprehensive view of biomarkers for stratification of sensitive PDAC subgroups. Overall, the high-throughput drug screening data presented in this thesis may be considered as a valuable resource which can hopefully be used to initiate further investigations deciphering therapeutic vulnerabilities in pancreatic cancer.

9 Supplementary data

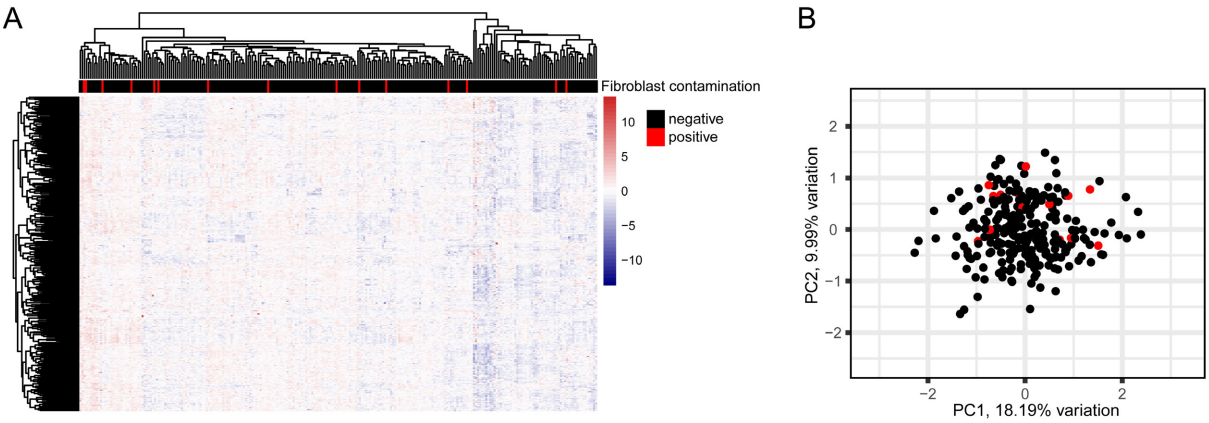

Figure 31: Fibroblast contamination does not affect drug response.
(A) Heatmap of Z scores of AUC values derived from 250 murine cell lines treated with 415 drugs (3 cell line – drug pairs excluded according to Chapter 5.2.4). Clustering is based on Euclidean distance. Fibroblast contamination is annotated. (B) Principal component analysis (PCA) plot for the 250 screened mouse cell lines based on AUC values for 415 drugs (3 cell line – drug pairs excluded according to Chapter 5.2.4). Each dot represents one cell line, colored by fibroblast contamination status. No clustering based on fibroblast contamination can be observed, indicating that fibroblast contamination does not affect drug response.

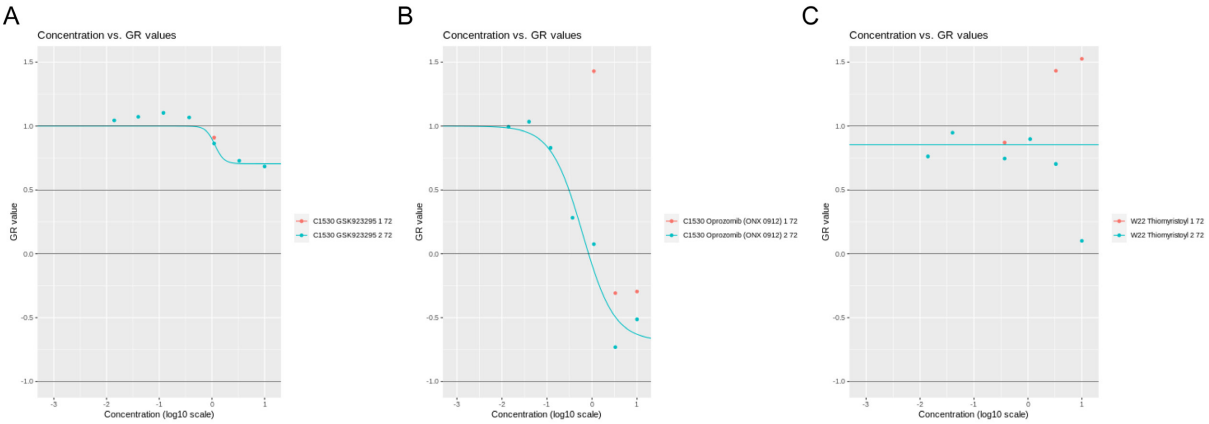

Figure 32: Dose response curves excluded from analysis.
(A) Dose response curves for each replicate of the cell line C1530 treated with GSK923295. Calculated mean AUC = 718, sdAUC = 1015. (B) Dose response curves for each replicate of the cell line C1530 treated with Oprozomib. Calculated mean AUC = 6.1, sdAUC = 8.1. (C) Dose response curves for each replicate of cell line W22 treated with Thiomyristoyl. Calculated mean AUC = 9.5, sdAUC = 10.9.

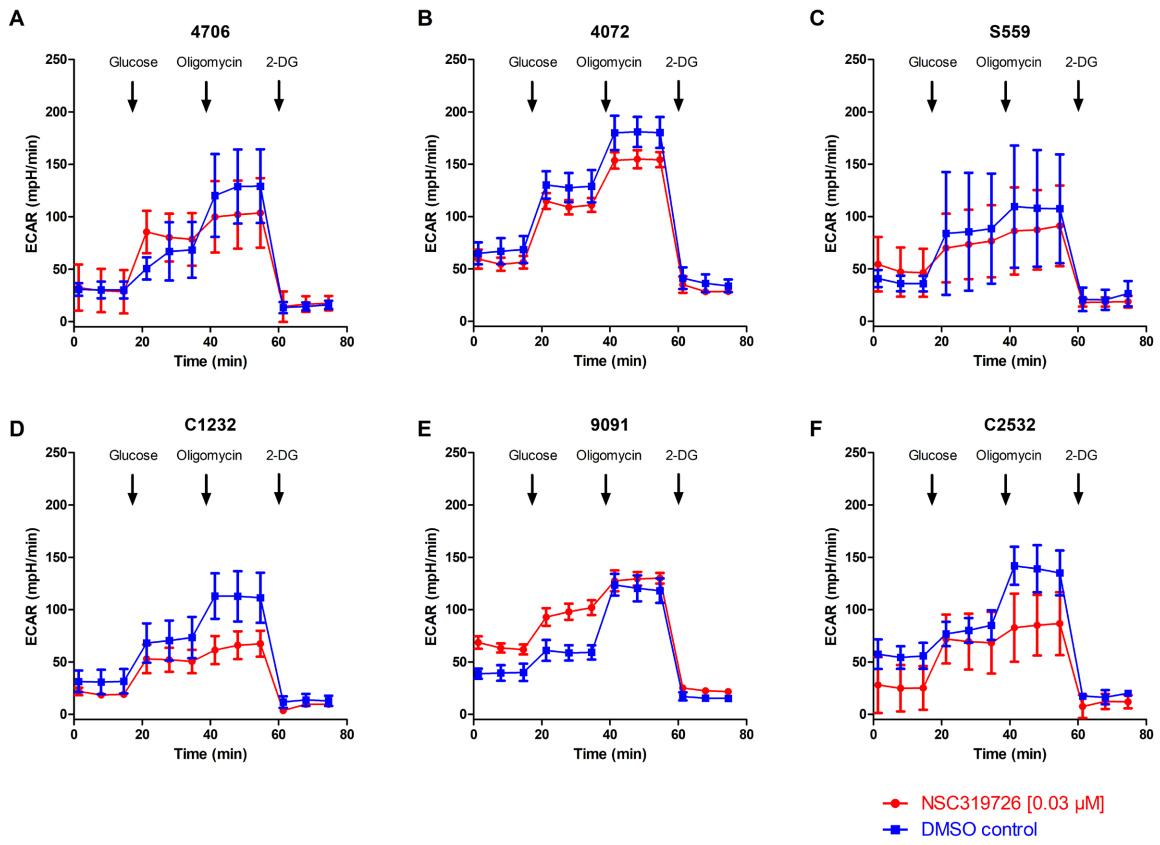

Figure 33: Glycolysis is less affected by NSC319726 than oxidative phosphorylation.
Extracellular acidification rate (ECAR) measured by Seahorse Assay Glycolytic Stress Test after 24 hours treatment with 0.03 µM NSC319726 for each of the tested cell lines (A) 4706; (B) 4072; (C) S559; (D) C1232; (E) 9091 and (F) C2532. Values for NSC319726 treatment and DMSO controls are normalized to cell viability, for each cell line separately. Mean values ± SD for four technical replicates are shown.

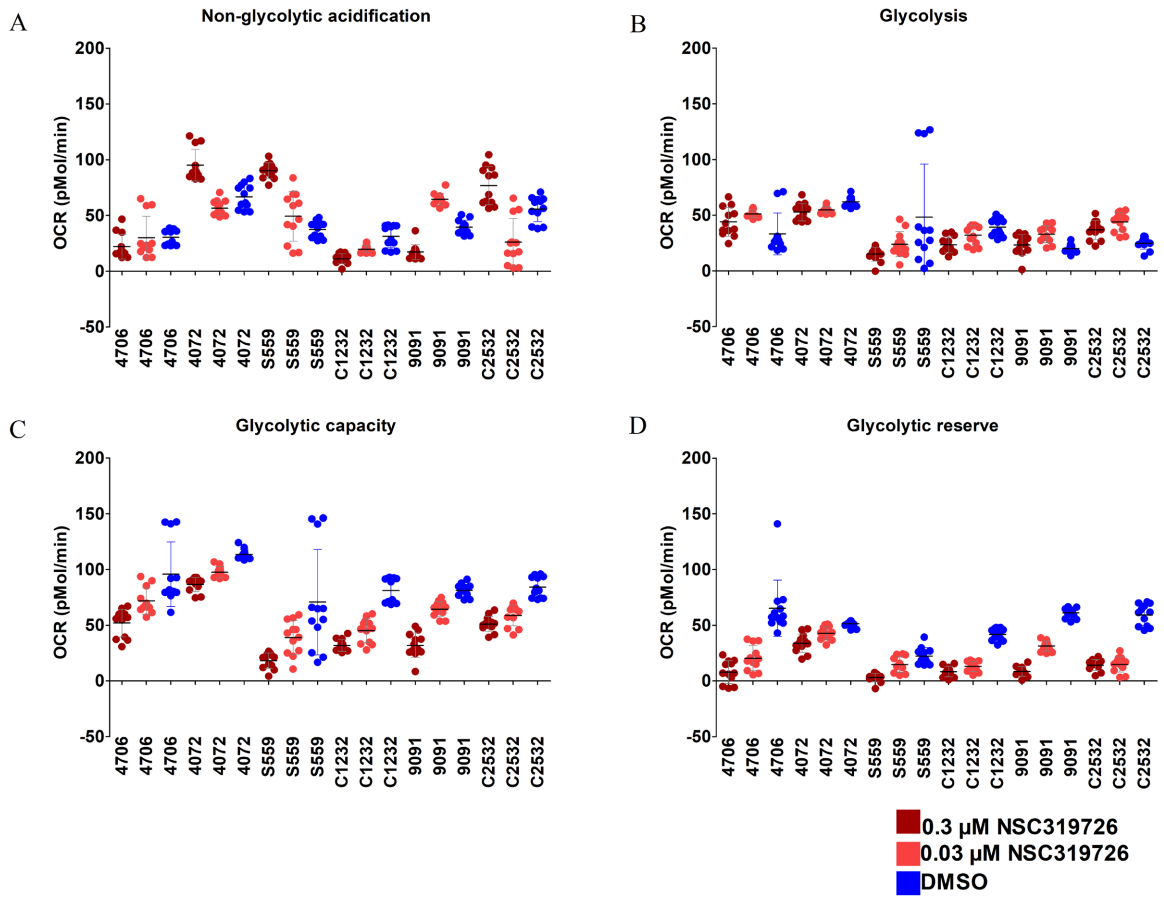

Figure 34: Glycolytic capacity and glycolytic reserve may be affected by NSC319726 to some extent. ECAR values from Figure 33 summarized for (A) Non-glycolytic acidification; (B) Glycolysis; (C) Glycolytic capacity; (D) Glycolytic reserve. Mean values ± SD are shown for four replicate ECAR values measured at three consecutive time points (12 datapoints per condition).

Table 9-1: Detailed genotypes and information on recombined alleles for murine cell lines.
WT = wildtype, REC = recombination, MUT = presence of unrecombined alleles (indicating fibroblast contamination), N.D. = not detected (*Pik3ca*: no band for MUT or REC in Pik3ca recombination PCR indicative of Pik3ca WT status; *Trp53*: no band detected in p53 PCRs indicative of *Trp53* deletion).

Sample ID	Genotype group	Detailed genotype	Recombination in cell line		
			Kras	*Pik3ca*	*Trp53*
10092	PPI3K	*Ptf1a$^{Cre/+}$;Pdx1-Cre;LSL-Pik3ca$^{H1047R/+}$*	WT/WT	REC	WT/WT
10139	PKP	*Ptf1a$^{Cre/+}$;LSL-Kras$^{G12D/+}$;Trp53$^{R172H/+}$*	REC/WT	N.D.	REC/WT
10158	PPI3K	*Ptf1a$^{Cre/+}$;LSL-Pik3ca$^{H1047R/+}$*	WT/WT	REC	WT/WT
10161	PPI3K	*Ptf1a$^{Cre/+}$;LSL-Pik3ca$^{H1047R/+}$*	WT/WT	REC	WT/WT
10193	PPI3KP	*Ptf1a$^{Cre/+}$; LSL-Pik3ca$^{H1047R/+}$;Trp53$^{R172H/+}$*	WT/WT	REC	REC/WT
10232	PKP	*Ptf1a$^{Cre/+}$;LSL-Kras$^{G12D/+}$;Trp53$^{R172H/+}$*	REC/WT	N.D.	REC/WT
10350	PPI3K	*Ptf1a$^{Cre/+}$;LSL-Pik3ca$^{H1047R/+}$*	WT/WT	REC	WT/WT
10502	PKP	*Ptf1a$^{Cre/+}$;LSL-Kras$^{G12D/+}$;Trp53$^{R172H/+}$*	REC/WT	N.D.	REC/WT
10587	PPI3KP	*Ptf1a$^{Cre/+}$;LSL-Pik3ca$^{H1047R/+}$;Trp53$^{R172H/+}$*	WT/WT	REC	REC/WT
10593	PPI3KP	*Ptf1a$^{Cre/+}$;LSL-Pik3ca$^{H1047R/+}$;Trp53$^{R172H/+}$*	WT/WT	REC	REC/WT
10632	PPI3KP	*Ptf1a$^{Cre/+}$;Pdx1-Cre; LSL-Pik3ca$^{H1047R/+}$;Trp53$^{R172H/+}$*	WT/WT	REC	REC/WT
10688	PPI3KP	*Ptf1a$^{Cre/+}$;LSL-Pik3ca$^{H1047R/+}$;Trp53$^{R172H/+}$*	WT/WT	REC	REC/WT
10725	PPI3KP	*Ptf1a$^{Cre/+}$;LSL-Pik3ca$^{H1047R/+}$;Trp53$^{R172H/+}$*	WT/WT	REC	REC/WT
10729	PPI3KP	*Ptf1a$^{Cre/+}$;LSL-Pik3ca$^{H1047R/+}$;Trp53$^{R172H/+}$*	WT/WT	REC/MUT	REC/WT
10731	PPI3KP	*Ptf1a$^{Cre/+}$;LSL-Pik3ca$^{H1047R/+}$;Trp53$^{R172H/+}$*	WT/WT	REC/MUT	REC/WT/ MUT
11343	PKP	*Ptf1a$^{Cre/+}$;LSL-Kras$^{G12D/+}$;Trp53$^{R172H/+}$*	REC/WT	N.D.	REC/WT
11363-2	PKPI3K	*Ptf1a$^{Cre/+}$;LSL-Kras$^{G12D/+}$;Pik3ca$^{H1047R/+}$*	REC/WT	REC	WT/WT
11440	PPI3KP	*Ptf1a$^{Cre/+}$;LSL-Pik3ca$^{H1047R/+}$;Trp53$^{R172H/+}$*	WT/WT	REC/MUT	REC/WT
11600	PPI3KP	*Ptf1a$^{Cre/+}$;Pdx1-Cre;LSL-Pik3ca$^{H1047R/+}$;Trp53$^{R172H/+}$*	WT/WT	REC	REC/WT
11602	PPI3KP	*Ptf1a$^{Cre/+}$;Pdx1-Cre;LSL-Pik3ca$^{H1047R/+}$;Trp53$^{R172H/+}$*	WT/WT	REC/MUT	MUT/MUT
11714	PPI3KP	*Ptf1a$^{Cre/+}$;Pdx1-Cre;LSL-Pik3ca$^{H1047R/+}$;Trp53$^{R172H/+}$*	WT/WT	REC	REC/WT
11987	PPI3KP	*Ptf1a$^{Cre/+}$;Pdx1-Cre; LSL-Pik3ca$^{H1047R/+}$;Trp53$^{R172H/+}$*	WT/WT	REC/MUT	REC/WT/ MUT

Sample ID	Genotype group	Detailed genotype	Recombination in cell line		
			Kras	*Pik3ca*	*Trp53*
12047	PPI3K	*Ptf1a$^{Cre/+}$;LSL-Pik3ca$^{H1047R/+}$*	WT/WT	REC	WT/WT
12128	PPI3KP	*Ptf1a$^{Cre/+}$;LSL-Pik3ca$^{H1047R/+}$;LSL-Trp53$^{R172H/+}$*	WT/WT	REC	REC/WT/ MUT
12508	PK	*Ptf1a$^{Cre/+}$;LSL-Kras$^{G12D/+}$*	REC/WT	N.D.	WT/WT
12690	PPI3K	*Pdx1-Cre;LSL-Pik3ca$^{H1047R/+}$*	WT/WT	REC	WT/WT
13474	PPI3KP	*Pdx1-Cre;LSL-Pik3ca$^{H1047R/+}$;Trp53$^{R172H/+}$*	WT/WT	REC	REC/WT
13871	PKP	*Pdx1-Cre;LSL-Kras$^{G12D/+}$;Trp53$^{lox/lox}$*	REC/WT	N.D.	N.D.
14169	PKP	*Pdx1-Cre;LSL-Kras$^{G12D/+}$;Trp53$^{R172H/+}$*	REC/WT	N.D.	REC/WT
14193	PKP	*Pdx1-Cre;LSL-Kras$^{G12D/+}$;Trp53$^{lox/lox}$*	REC/REC	N.D.	N.D.
14311	PKP	*Pdx1-Cre;LSL-Kras$^{G12D/+}$;Trp53$^{lox/+}$*	REC/WT	N.D.	N.D.
16990	PK	*Ptf1a$^{Cre/+}$;LSL-Kras$^{G12D/+}$*	REC/WT	N.D.	WT/WT
16992	PK	*Ptf1a$^{Cre/+}$;LSL-Kras$^{G12D/+}$*	REC/REC	N.D.	WT/WT
1712	PKP	*Pdx1-Cre;LSL-Kras$^{G12D/+}$;Trp53$^{R172H/+}$*	REC/WT	N.D.	REC/WT
1778	PKP	*Pdx1-Cre;LSL-Kras$^{G12D/+}$;Trp53$^{R172H/+}$*	REC/REC	N.D.	REC/WT
2259	PK	*Pdx1-Cre;LSL-Kras$^{G12D/+}$*	REC/WT	N.D.	WT/WT
271-105	PKPCSm	*Pdx1-Flp;FSF-Kras$^{G12D/+}$;Cdkn2a$^{lox/+}$; Smad4$^{lox/lox}$;Trp53$^{lox/+}$*	REC/WT	N.D.	WT
271-91	PKPCSm	*Pdx1-Flp;FSF-Kras$^{G12D/+}$;Cdkn2a$^{lox/+}$; Smad4$^{lox/lox}$;Trp53$^{lox/+}$*	REC/WT	N.D.	WT
2937	PKPE	*Pdx1-Cre;LSL-Kras$^{G12D/+}$;Trp53$^{R172H/+}$; Cdh1$^{fl/fl}$*	REC/WT	N.D.	REC/WT
3139	PKP	*Ptf1a$^{Cre/+}$;LSL-Kras$^{G12D/+}$;Trp53$^{lox/+}$*	REC/WT	N.D.	WT
3202	PK	*Ptf1a$^{Cre/+}$;LSL-Kras$^{G12D/+}$*	REC/WT	N.D.	WT/WT
3250	PK	*Pdx1-Cre;LSL-Kras$^{G12D/+}$*	REC/WT	N.D.	WT/WT
3862	PPI3KP	*Ptf1a$^{Cre/+}$;Pdx1-Cre; LSL-Pik3ca$^{H1047R/+}$;Trp53$^{R172H/+}$*	WT/WT	REC	REC/WT
4072	PK	*Pdx1-Cre;LSL-Kras$^{G12D/+}$*	REC/WT	N.D.	WT/WT
4130	PPI3KP	*Ptf1a$^{Cre/+}$; LSL-Pik3ca$^{H1047R/+}$;Trp53$^{R172H/+}$*	WT/WT	REC	REC/WT
4134	PPI3K	*Ptf1a$^{Cre/+}$;Pdx1-Cre;LSL-Pik3ca$^{H1047R/+}$*	WT/WT	REC	WT/WT
4140	PPI3K	*Ptf1a$^{Cre/+}$;LSL-Pik3ca$^{H1047R/+}$*	WT/WT	REC	WT/WT
4706	PK	*Pdx1-Flp-o;FSF-Kras$^{G12D/+}$*	REC/WT	N.D.	WT/WT

Sample ID	Genotype group	Detailed genotype	Recombination in cell line		
			Kras	*Pik3ca*	*Trp53*
4888	PPI3K	*Pdx1-Cre;LSL-Pik3ca$^{H1047R/+}$*	WT/WT	REC	WT/WT
4900	PK	*Pdx1-Flp-o;FSF-Kras$^{G12D/+}$*	REC/WT	N.D.	WT/WT
4912	PK	*Pdx1-Flp;FSF-Kras$^{G12D/+}$*	REC/WT	N.D.	WT/WT
4971	PKP	*Pdx1-Flp;FSF-Kras$^{G12D/+}$;LSL-Trp53$^{WT/+}$*	REC/WT	N.D.	MUT/MUT
5123	PK	*Ptf1a$^{Cre/+}$;LSL-Kras$^{G12D/+}$*	REC/WT	N.D.	WT/WT
5320	PK	*Ptf1a$^{Cre/+}$;LSL-Kras$^{G12D/+}$*	REC/WT	N.D.	WT/WT
53578	PK	*Ptf1a$^{Cre/+}$;LSL-Kras$^{G12D/+}$*	REC/WT	N.D.	WT/WT
53631	PK	*Ptf1a$^{Cre/+}$;LSL-Kras$^{G12D/+}$*	REC/WT	N.D.	WT/WT
53646	PK	*Ptf1a$^{Cre/+}$;LSL-Kras$^{G12D/+}$*	REC/WT	N.D.	WT/WT
53704	PK	*Ptf1a$^{Cre/+}$;LSL-Kras$^{G12D/+}$*	REC/WT	N.D.	WT/WT
53909	PK	*Ptf1a$^{Cre/+}$;LSL-Kras$^{G12D/+}$*	REC/REC	N.D.	WT/WT
5671	PK	*Ptf1a$^{Cre/+}$;LSL-Kras$^{G12D/+}$*	REC/WT	N.D.	WT/WT
5748	PK	*Ptf1a$^{Cre/+}$;LSL-Kras$^{G12D/+}$*	REC/WT	N.D.	WT/WT
6021	PKP	*Ptf1a$^{Cre/+}$;LSL-Kras$^{G12D/+}$;Trp53$^{R172H/+}$*	REC/WT	N.D.	REC/WT
6034	PKP	*Pdx1-Cre;LSL-Kras$^{G12D/+}$;Trp53$^{R172H/+}$*	REC/REC	N.D.	REC/WT
6075	PK	*Pdx1-Cre;LSL-Kras$^{G12D/+}$*	REC/WT	N.D.	WT/WT
6127	PK	*Pdx1-Cre;LSL-Kras$^{G12D/+}$*	REC/WT	N.D.	WT/WT
6605	PKP	*Pdx1-Cre;LSL-Kras$^{G12D/+}$;Trp53$^{R172H/+}$*	REC/WT/ MUT	N.D.	REC/WT/ MUT
6719	PKP	*Pdx1-Cre;LSL-Kras$^{G12D/+}$;Trp53$^{R172H/+}$*	REC/WT	N.D.	REC/WT
7725	PKP	*Pdx1-Cre;LSL-Kras$^{G12D/+}$;Trp53$^{lox/+}$*	REC/WT	N.D.	N.D.
7968	PK	*Ptf1a$^{Cre/+}$;LSL-Kras$^{G12D/+}$*	REC/REC	N.D.	WT/WT
8013	PKP	*Pdx1-Cre;LSL-Kras$^{G12D/+}$;Trp53$^{lox/+}$*	REC/WT	N.D.	N.D.
8028	PK	*Ptf1a$^{Cre/+}$;LSL-Kras$^{G12D/+}$*	REC/WT	N.D.	WT/WT
8182	PK	*Ptf1a$^{Cre/+}$;LSL-Kras$^{G12D/+}$*	REC/WT	N.D.	WT/WT
8248	PK	*Ptf1a$^{Cre/+}$;LSL-Kras$^{G12D/+}$*	REC/WT	N.D.	WT/WT
8296	PK	*Ptf1a$^{Cre/+}$;LSL-Kras$^{G12D/+}$*	REC/WT	N.D.	WT/WT
8305	PK	*Ptf1a$^{Cre/+}$;LSL-Kras$^{G12D/+}$*	REC/WT	N.D.	WT/WT
8349	PK	*Ptf1a$^{Cre/+}$;LSL-Kras$^{G12D/+}$*	REC/WT	N.D.	WT/WT
8442	PK	*Ptf1a$^{Cre/+}$;LSL-Kras$^{G12D/+}$*	REC/WT	N.D.	WT/WT
8513	PK	*Ptf1a$^{Cre/+}$;LSL-Kras$^{G12D/+}$*	REC/WT	N.D.	WT/WT
8570	PK	*Ptf1a$^{Cre/+}$;LSL-Kras$^{G12D/+}$*	REC/WT	N.D.	WT/WT
8661	PK	*Ptf1a$^{Cre/+}$;LSL-Kras$^{G12D/+}$*	REC/WT	N.D.	WT/WT
8927	PPI3K	*Ptf1a$^{Cre/+}$;LSL-Pik3ca$^{H1047R/+}$*	WT/WT	REC	WT/WT
8932	PPI3K	*Ptf1a$^{Cre/+}$;LSL-Pik3ca$^{H1047R/+}$*	WT/WT	REC	WT/WT
9063	PKP	*Ptf1a$^{Cre/+}$;Pdx1-Cre;LSL-Kras$^{G12D/+}$; Trp53$^{R172H/+}$*	REC/WT	N.D.	REC/WT
9091	PK	*Ptf1a$^{Cre/+}$;LSL-Kras$^{G12D/+}$*	REC/WT	N.D.	WT/WT

Sample ID	Genotype group	Detailed genotype	Recombination in cell line		
			Kras	*Pik3ca*	*Trp53*
9172	PKP	*Ptf1a$^{Cre/+}$;LSL-Kras$^{G12D/+}$;Trp53$^{R172H/+}$*	REC/WT	N.D.	REC/WT
9203	PK	*Ptf1a$^{Cre/+}$;LSL-Kras$^{G12D/+}$*	REC/WT	N.D.	WT/WT
9255	PKP	*Ptf1a$^{Cre/+}$;Pdx1-Cre;LSL-Kras$^{G12D/+}$;Trp53$^{R172H/+}$*	REC/WT/ MUT	N.D.	REC/WT/ MUT
9366	PKP	*Ptf1a$^{Cre/+}$;Pdx1-Cre;LSL-Kras$^{G12D/+}$;Trp53$^{R172H/+}$*	REC/WT	N.D.	REC/WT
9471	PPI3K	*Ptf1a$^{Cre/+}$;LSL-Pik3ca$^{H1047R/+}$*	WT/WT	REC	WT/WT
9580	PPI3K	*Ptf1a$^{Cre/+}$;LSL-Pik3ca$^{H1047R/+}$*	WT/WT	REC	WT/WT
9591	PK	*Ptf1a$^{Cre/+}$;LSL-Kras$^{G12D/+}$*	REC/WT	N.D.	WT/WT
9784	PKP	*Ptf1a$^{Cre/+}$;LSL-Kras$^{G12D/+}$;Trp53$^{R172H/+}$*	REC/WT/ MUT	N.D.	REC/WT/ MUT
9793	PKPI3KP	*Ptf1a$^{Cre/+}$;LSL-Kras$^{G12D/+}$;Pik3ca$^{H1047R/+}$; Trp53$^{R172H/+}$*	REC/WT/ MUT	REC/MUT	REC/WT/ MUT
9794	PK	*Ptf1a$^{Cre/+}$;LSL-Kras$^{G12D/+}$*	REC/WT/ MUT	N.D.	WT/WT
9795	PKPI3K	*Ptf1a$^{Cre/+}$;LSL-Kras$^{G12D/+}$;Pik3ca$^{H1047R/+}$*	REC/WT	REC	WT/WT
9924	PKP	*Ptf1a$^{Cre/+}$;LSL-Kras$^{G12D/+}$;Trp53$^{R172H/+}$*	REC/WT/ MUT	N.D.	REC/WT/ MUT
9960	PPI3K	*Ptf1a$^{Cre/+}$;LSL-Pik3ca$^{H1047R/+}$*	WT/WT	REC	WT/WT
9964	PK	*Ptf1a$^{Cre/+}$;LSL-Kras$^{G12D/+}$*	REC/WT	N.D.	WT/WT
9965	PKPI3K	*Ptf1a$^{Cre/+}$;LSL-Kras$^{G12D/+}$;Pik3ca$^{H1047R/+}$*	REC/WT	REC	WT/WT
AA120	PKC	*Ptf1a$^{Cre/+}$;LSL-Kras$^{G12D/+}$;Cdkn2a$^{lox/+}$*	REC/WT	N.D.	WT/WT
AA1229	PKC	*Ptf1a$^{Cre/+}$;LSL-Kras$^{G12D/+}$;Cdkn2a$^{lox/lox}$*	REC/WT	N.D.	WT/WT
AA1261	PKC	*Ptf1a$^{Cre/+}$;LSL-Kras$^{G12D/+}$;Cdkn2a$^{lox/lox}$*	REC/REC	N.D.	WT/WT
AA1377	PKC	*Ptf1a$^{Cre/+}$;LSL-Kras$^{G12D/+}$;Cdkn2a$^{lox/lox}$*	REC/REC	N.D.	WT/WT
AA1467	PKC	*Ptf1a$^{Cre/+}$;LSL-Kras$^{G12D/+}$;Cdkn2a$^{lox/lox}$*	REC/WT	N.D.	WT/WT
AA168	PKC	*Ptf1a$^{Cre/+}$;LSL-Kras$^{G12D/+}$;Cdkn2a$^{lox/lox}$*	REC/REC	N.D.	WT/WT
AA169	PKC	*Ptf1a$^{Cre/+}$;LSL-Kras$^{G12D/+}$;Cdkn2a$^{lox/lox}$*	REC/REC	N.D.	WT/WT
AA172	PKC	*Ptf1a$^{Cre/+}$;LSL-Kras$^{G12D/+}$;Cdkn2a$^{lox/lox}$*	REC/REC	N.D.	WT/WT
AA199	PKC	*Ptf1a$^{Cre/+}$;LSL-Kras$^{G12D/+}$;Cdkn2a$^{lox/lox}$*	REC/REC	N.D.	WT/WT
AA651	PKC	*Ptf1a$^{Cre/+}$;LSL-Kras$^{G12D/+}$;Cdkn2a$^{lox/lox}$*	REC/WT	N.D.	WT/WT
AA765	PKC	*Ptf1a$^{Cre/+}$;LSL-Kras$^{G12D/+}$;Cdkn2a$^{lox/+}$*	REC/REC	N.D.	WT/WT

Sample ID	Genotype group	Detailed genotype	Recombination in cell line		
			Kras	*Pik3ca*	*Trp53*
AA766	PKC	*Ptf1a$^{Cre/+}$;LSL-Kras$^{G12D/+}$;Cdkn2a$^{lox/+}$*	REC/WT	N.D.	WT/WT
AA785	PKP	*Pdx1-Cre;LSL-Kras$^{G12D/+}$;LSL-Trp53$^{lox/+}$*	REC/REC	N.D.	N.D.
AA821	PKC	*Ptf1a$^{Cre/+}$;LSL-Kras$^{G12D/+}$;Cdkn2a$^{lox/lox}$*	REC/REC	N.D.	WT/WT
AA852	PKC	*Ptf1a$^{Cre/+}$;LSL-Kras$^{G12D/+}$;Cdkn2a$^{lox/lox}$*	REC/REC	N.D.	WT/WT
AA854	PKC	*Ptf1a$^{Cre/+}$;LSL-Kras$^{G12D/+}$;Cdkn2a$^{lox/lox}$*	REC/WT	N.D.	WT/WT
AA966	PKP	*Pdx1-Cre;LSL-Kras$^{G12D/+}$;LSL-Trp53$^{lox/lox}$*	REC/WT	N.D.	N.D.
AK1301	PPI3K	*Pdx1-Cre;LSL-Pik3ca$^{H1047R/+}$*	WT/WT	REC	WT/WT
AK453	PPI3KP	*Pdx1-Cre;LSL-Pik3ca$^{H1047R/+}$;Trp53$^{R172H/+}$*	WT/WT	REC	REC/WT
AK496	PPI3KP	*Pdx1-Cre;LSL-Pik3ca$^{H1047R/+}$;Trp53$^{lox/lox}$*	WT/WT	REC	N.D.
AK501	PPI3KP	*Pdx1-Cre;LSL-Pik3ca$^{H1047R/+}$;Trp53$^{lox/+}$*	WT/WT	REC	N.D.
AK5299	PPI3K	*Pdx1-Flp;FSF-Pik3ca$^{H1047R/+}$*	WT/WT	REC	WT/WT
AK594	PPI3KP	*Pdx1-Cre;LSL-Pik3ca$^{H1047R/+}$;Trp53$^{lox/+}$*	WT/WT	REC	N.D.
AK596	PPI3KP	*Pdx1-Cre;LSL-Pik3ca$^{H1047R/+}$;Trp53$^{lox/+}$*	WT/WT	REC	N.D.
AK635	PPI3KP	*Pdx1-Cre;LSL-Pik3ca$^{H1047R/+}$;Trp53$^{R172H/+}$*	WT/WT	REC	REC/WT
AK693	PPI3KP	*Pdx1-Cre; LSL-Pik3ca$^{H1047R/+}$;Trp53$^{lox/lox}$*	WT/WT	REC	N.D.
B127	PKP	*Pdx1-Cre;LSL-Kras$^{G12D/+}$;Trp53$^{R172H/+}$*	REC/WT/ MUT	N.D.	REC/WT/ MUT
B191	PKP	*Pdx1-Cre;LSL-Kras$^{G12D/+}$;Trp53$^{R172H/+}$*	REC/WT	N.D.	REC/WT
B212	PKP	*Pdx1-Cre;LSL-Kras$^{G12D/+}$;Trp53$^{lox/lox}$*	REC/WT	N.D.	N.D.
B231	PKP	*Pdx1-Cre;LSL-Kras$^{G12D/+}$;Trp53$^{lox/+}$*	REC/WT	N.D.	N.D.
B590	PK	*Ptf1a$^{Cre/+}$;LSL-Kras$^{G12D/+}$*	REC/WT	N.D.	WT/WT
BR19	PBRC	*Pdx1-Cre;LSL-Braf$^{V637E/+}$;p16$^{Ink4a*/+}$*	WT/WT	N.D.	WT/WT
BR230	PBRC	*Pdx1-Cre;LSL-Braf$^{V637E/+}$;p16$^{Ink4a*/Ink4a*}$*	WT/WT	N.D.	WT/WT
BR55	PBRC	*Pdx1-Cre;LSL-Braf$^{V637E/+}$;p16$^{Ink4a*/Ink4a*}$*	WT/WT	N.D.	WT/WT
BR63	PBRPC	*Pdx1-Cre;LSL-Braf$^{V637E/+}$;p16$^{Ink4a*/+}$; Trp53$^{R172H/+}$*	WT/WT	N.D.	REC/WT
C065	PKT	*Ptf1a$^{Cre/+}$;LSL-Kras$^{G12D/+}$; Tgfβr2$^{lox/lox}$*	REC/WT	N.D.	WT/WT

Sample ID	Genotype group	Detailed genotype	Recombination in cell line		
			Kras	*Pik3ca*	*Trp53*
C1232	PKE	*Pdx1-Flp;FSF-Kras$^{G12D/+}$;Cdh1$^{fl/fl}$*	REC/WT	N.D.	WT/WT
C147	PKPT	*Ptf1a$^{Cre/+}$;LSL-Kras$^{G12D/+}$;Tgfβr2$^{lox/lox}$; Trp53$^{R172H/+}$*	REC/WT	N.D.	REC/WT
C1530	PK	*Pdx1-Flp;FSF-Kras$^{G12D/+}$*	REC/WT	N.D.	WT/WT
C1607	PK	*Pdx1-Flp;FSF-Kras$^{G12D/+}$*	REC/WT	N.D.	WT/WT
C1609	PK	*Pdx1-Flp;FSF-Kras$^{G12D/+}$*	REC/WT	N.D.	WT/WT
C1612	PKPT	*Ptf1a$^{Cre/+}$;LSL-Kras$^{G12D/+}$;Tgfβr2$^{lox/lox}$; Trp53$^{R172H/+}$*	REC/WT	N.D.	REC/WT
C1696	PK	*Pdx1-Flp;FSF-Kras$^{G12D/+}$*	REC/WT	N.D.	WT/WT
C1763	PKPT	*Ptf1a$^{Cre/+}$;Kras$^{G12D/+}$;Tgfβr2 $^{lox/lox}$;LSL-Trp53$^{R172H/+}$*	REC/WT	N.D.	REC/WT
C2118	PK	*Pdx1-Flp;FSF-Kras$^{G12D/+}$*	REC/WT	N.D.	WT/WT
C2473	PKP	*Pdx1-Flp;FSF-Kras$^{G12D/+}$;Trp53$^{frt/+}$*	REC/WT	N.D.	N.D.
C2514	PKP	*Pdx1-Flp;FSF-Kras$^{G12D/+}$;Trp53$^{frt/+}$*	REC/WT	N.D.	N.D.
C2532	PKT	*Ptf1a$^{Cre/+}$;LSL-Kras$^{G12D/+}$; Tgfβr2$^{lox/lox}$*	REC/WT	N.D.	WT/WT
C2552	PKP	*Pdx1-Flp;FSF-Kras$^{G12D/+}$;Trp53$^{frt/+}$*	REC/WT	N.D.	N.D.
C2675	PKP	*Pdx1-Flp;FSF-Kras$^{G12D/+}$;Trp53$^{frt/+}$*	REC/REC	N.D.	N.D.
C2677	PKP	*Pdx1-Flp;FSF-Kras$^{G12D/+}$;Trp53$^{frt/+}$*	REC/WT	N.D.	N.D.
C2810	PKT	*Ptf1a$^{Cre/+}$;LSL-Kras$^{G12D/+}$; Tgfβr2$^{lox/lox}$*	REC/WT	N.D.	WT/WT
C2922	PKT	*Ptf1a$^{Cre/+}$;LSL-Kras$^{G12D/+}$; Tgfβr2$^{lox/+}$*	REC/WT	N.D.	WT/WT
C3356	PKT	*Ptf1a$^{Cre/+}$;LSL-Kras$^{G12D/+}$; Tgfβr2$^{lox/lox}$*	REC/WT	N.D.	WT/WT
C3443	PKT	*Ptf1a$^{Cre/+}$;LSL-Kras$^{G12D/+}$; Tgfβr2$^{lox/lox}$*	REC/WT	N.D.	WT/WT
C4430	PKP	*Pdx1-Flp;FSF-Kras$^{G12D/+}$;Trp53$^{WT/WT}$*	REC/WT	N.D.	MUT/MUT
C4466	PKT	*Ptf1a$^{Cre/+}$;LSL-Kras$^{G12D/+}$; Tgfβr2$^{lox/+}$*	REC/WT	N.D.	WT/WT
C4557	PKP	*Pdx1-Flp;FSF-Kras$^{G12D/+}$;Trp53$^{frt/+}$*	REC/WT	N.D.	N.D.
C4617	PKP	*Pdx1-Flp;FSF-Kras$^{G12D/+}$;Trp53$^{frt/frt}$*	REC/WT	N.D.	N.D.
C4692	PKP	*Pdx1-Flp;FSF-Kras$^{G12D/+}$;Trp53$^{frt/frt}$*	REC/WT	N.D.	N.D.
C4722	PKP	*Pdx1-Flp;FSF-Kras$^{G12D/+}$;Trp53$^{frt/+}$*	REC/WT	N.D.	N.D.
C5081	PKT	*Ptf1a$^{Cre/+}$;LSL-Kras$^{G12D/+}$; Tgfβr2$^{lox/+}$*	REC/WT	N.D.	WT/WT
C5310	PKP	*Pdx1-Flp;FSF-*	REC/WT	N.D.	MUT/MUT

Sample ID	Genotype group	Detailed genotype	Recombination in cell line		
			Kras	*Pik3ca*	*Trp53*
		Kras$^{G12D/+}$;Trp53$^{WT/WT}$			
C5315	PKP	*Pdx1-Flp;FSF-Kras$^{G12D/+}$;Trp53$^{frt/frt}$*	REC/WT	N.D.	N.D.
C5389	PKP	*Pdx1-Flp;FSF-Kras$^{G12D/+}$;Trp53$^{frt/+}$*	REC/REC	N.D.	N.D.
C5599	PK	*Ptf1a$^{Cre/+}$;LSL-Kras$^{G12D/+}$*	REC/WT	N.D.	WT/WT
C5835	PKP	*Pdx1-Flp;FSF-Kras$^{G12D/+}$;Trp53$^{frt/+}$*	REC/WT	N.D.	N.D.
C6037	PKPT	*Ptf1a$^{Cre/+}$;LSL-Kras$^{G12D/+}$;Tgfβr2$^{lox/+}$; Trp53$^{R172H/+}$*	REC/WT	N.D.	REC/WT
CF001-1	PKPI3K	*Ptf1a$^{Cre/+}$;LSL-Kras$^{G12D/+}$;Pik3ca$^{H1047R/+}$*	REC/WT	REC	WT/WT
CF001-2	PKPI3K	*Ptf1a$^{Cre/+}$;LSL-Kras$^{G12D/+}$;Pik3ca$^{H1047R/+}$*	REC/WT	REC	WT/WT
CF002-1	PKPI3K	*Ptf1a$^{Cre/+}$;LSL-Kras$^{G12D/+}$;Pik3ca$^{H1047R/+}$*	REC/WT	REC	WT/WT
CF002-2	PKPI3K	*Ptf1a$^{Cre/+}$;LSL-Kras$^{G12D/+}$;Pik3ca$^{H1047R/+}$*	REC/WT	REC	WT/WT
CR15798	PK	*Ptf1a$^{Cre/+}$;LSL-Kras$^{G12D/+}$*	REC/WT	N.D.	WT/WT
E126	PPI3K	*Ptf1a$^{Cre/+}$;Pdx1-Cre;LSL-Pik3ca$^{H1047R/+}$*	WT/WT	REC/MUT	WT/WT
E208	PPI3K	*Ptf1a$^{Cre/+}$;Pdx1-Cre;LSL-Pik3ca$^{H1047R/+}$*	WT/WT	REC/MUT	WT/WT
E234	PPI3K	*Ptf1a$^{Cre/+}$;LSL-Pik3ca$^{H1047R/+}$*	WT/WT	REC	WT/WT
E440	PPI3KPC	*Pdx1-Cre;LSL-Pik3ca$^{H1047R/+}$;Trp53$^{R172H/}$; Cdkn2a$^{lox/+}$*	WT/WT	REC	REC/WT
E915	PKPI3K	*Ptf1a$^{Cre/+}$;LSL-Kras$^{G12D/+}$;Pik3ca$^{H1047R/+}$*	REC/WT	REC	WT/WT
KG471	PKT	*Ptf1a$^{Cre/+}$;LSL-Kras$^{G12D/+}$; Tgfβr2$^{lox/+}$*	REC/WT	N.D.	WT/WT
KG486	PKPT	*Ptf1a$^{Cre/+}$;LSL-Kras$^{G12D/+}$;Tgfβr2$^{lox/+}$; Trp53$^{R172H/+}$*	REC/WT	N.D.	REC/WT
KG513	PKP	*Pdx1-Flp;FSF-Kras$^{G12D/+}$;Trp53$^{frt/frt}$*	REC/REC	N.D.	N.D.
KG564	PKP	*Pdx1-Flp;FSF-Kras$^{G12D/+}$;Trp53$^{frt/frt}$*	REC/WT	N.D.	N.D.
KG6290	PKP	*Pdx1-Flp;FSF-Kras$^{G12D/+}$;Trp53$^{frt/+}$*	REC/WT	N.D.	N.D.
MG172	PBRC	*Pdx1-Cre;LSL-Braf$^{V637E/+}$;Cdkn2a$^{lox/lox}$*	WT/WT	N.D.	WT/WT
MG846	PKP	*Pdx1-Cre;LSL-Kras$^{G12D/+}$;Trp53$^{lox/+}$*	REC/WT	N.D.	N.D.
MZ1380	PKTo	*Ptf1a$^{Cre/+}$;LSL-Kras$^{G12D/+}$; LSL-Rosa26$^{Tgfβ1/+}$*	REC/WT	N.D.	WT/WT
MZ1730	PKTo	*Ptf1a$^{Cre/+}$;LSL-Kras$^{G12D/+}$; LSL-Rosa26$^{Tgfβ1/+}$*	REC/WT	N.D.	WT/WT

Sample ID	Genotype group	Detailed genotype	Recombination in cell line		
			Kras	*Pik3ca*	*Trp53*
P1162	PKSC	*Ptf1a$^{Cre/+}$;LSL-Kras$^{G12D/+}$;Rosa26$^{Snail/+}$; p16$^{Ink4a*/+}$*	REC/WT	N.D.	WT/WT
P1956	PKSC	*Ptf1a$^{Cre/+}$;LSL-Kras$^{G12D/+}$; Rosa26$^{Snail/+}$; p16$^{Ink4a*/Ink4a*}$*	REC/WT	N.D.	WT/WT
P2313	PKC	*Ptf1a$^{Cre/+}$;LSL-Kras$^{G12D/+}$; p16$^{Ink4a*/+}$*	REC/REC	N.D.	WT/WT
P2324	PKS	*Pdx1-Cre;LSL-Kras$^{G12D/+}$;Rosa26$^{Snail/Snail}$*	REC/WT	N.D.	WT/WT
P2345	PKS	*Pdx1-Cre;LSL-Kras$^{G12D/+}$;Rosa26$^{Snail/Snail}$*	REC/WT	N.D.	WT/WT
P2347	PKS	*Pdx1-Cre;LSL-Kras$^{G12D/+}$;Rosa26$^{Snail/+}$*	REC/WT	N.D.	WT/WT
P3066	PKSC	*Pdx1-Cre;LSL-Kras$^{G12D/+}$;Rosa26$^{Snail/+}$; p16$^{Ink4a*/+}$*	REC/WT	N.D.	WT/WT
P3272	PKS	*Pdx1-Cre;LSL-Kras$^{G12D/+}$;LSL-Rosa26$^{Snail/+}$*	REC/WT	N.D.	WT/WT
P348	PKS	*Ptf1a$^{Cre/+}$;LSL-Kras$^{G12D/+}$;Rosa26$^{Snail/+}$*	REC/WT	N.D.	WT/WT
P3532	PKP	*Pdx1-Flp;FSF-Kras$^{G12D/+}$;Trp53$^{frt/+}$*	REC/WT	N.D.	N.D.
P4162	PKS	*Ptf1a$^{Cre/+}$;LSL-Kras$^{G12D/+}$;Rosa26$^{Snail/+}$*	REC/WT	N.D.	WT/WT
P4470	PKSC	*Ptf1a$^{Cre/+}$;LSL-Kras$^{G12D/+}$; Rosa26$^{Snail/+}$; Cdkn2a$^{lox/+}$*	REC/REC	N.D.	WT/WT
P4492	PKP	*Pdx1-Flp;FSF-Kras$^{G12D/+}$;Trp53$^{frt/+}$*	REC/WT	N.D.	N.D.
P4828	PKS	*Ptf1a$^{Cre/+}$;LSL-Kras$^{G12D/+}$;Rosa26$^{Snail/+}$*	REC/WT	N.D.	WT/WT
P5078	PKC	*Ptf1a$^{Cre/+}$;LSL-Kras$^{G12D/+}$;Cdkn2a$^{lox/lox}$*	REC/WT	N.D.	WT/WT
P5142	PKSC	*Ptf1a$^{Cre/+}$;LSL-Kras$^{G12D/+}$; Rosa26$^{Snail/+}$; Cdkn2a$^{lox/lox}$*	REC/REC	N.D.	WT/WT
P5166	PKSC	*Ptf1a$^{Cre/+}$;LSL-Kras$^{G12D/+}$; Rosa26$^{Snail/+}$; Cdkn2a$^{lox/lox}$*	REC/WT	N.D.	WT/WT
P5187	PKSC	*Ptf1a$^{Cre/+}$;LSL-Kras$^{G12D/+}$; Rosa26$^{Snail/+}$; Cdkn2a$^{lox/lox}$*	REC/WT	N.D.	WT/WT
R1035	PK	*Pdx1-Flp;FSF-Kras$^{G12D/+}$*	REC/WT	N.D.	WT/WT
R211	PKP	*Ptf1a$^{Cre/+}$;LSL-Kras$^{G12D/+}$;Trp53$^{R172H/+}$*	REC/WT	N.D.	REC/WT
R254	PKP	*Ptf1a$^{Cre/+}$;LSL-Kras$^{G12D/+}$;Trp53$^{R172H/+}$*	REC/WT	N.D.	REC/WT
R259	PKP	*Ptf1a$^{Cre/+}$;LSL-Kras$^{G12D/+}$;Trp53$^{R172H/+}$*	REC/WT	N.D.	REC/WT
R4694	PKP	*Pdx1-Flp;FSF-Kras$^{G12D/+}$;Trp53$^{frt/+}$*	REC/WT	N.D.	N.D.
R4765	PKP	*Pdx1-Flp;FSF-*	REC/WT	N.D.	WT

Sample ID	Genotype group	Detailed genotype	Recombination in cell line		
			Kras	*Pik3ca*	*Trp53*
		Kras$^{G12D/+}$;Trp53$^{frt/+}$			
R6827	PKCSm	*Pdx1-Flp;FSF-Kras$^{G12D/+}$;Cdkn2a$^{lox/+}$; Smad4$^{lox/+}$*	REC/WT	N.D.	WT/WT
R6888	PKCSm	*Pdx1-Flp;FSF-Kras$^{G12D/+}$;Cdkn2a$^{lox/+}$; Smad4$^{lox/+}$*	REC/WT	N.D.	WT/WT
R7024-2	PKPCSm	*Pdx1-Flp;FSF-Kras$^{G12D/+}$;Cdkn2a$^{lox/+}$; Smad4$^{lox/lox}$;Trp53$^{lox/+}$*	REC/WT	N.D.	N.D.
R7102	PKPCSm	*Pdx1-Flp;FSF-Kras$^{G12D/+}$;Cdkn2a$^{lox/lox}$; Smad4$^{lox/+}$;Trp53$^{lox/lox}$*	REC/WT	N.D.	WT
R7108	PKPCSm	*Pdx1-Flp;FSF-Kras$^{G12D/+}$;Cdkn2a$^{lox/lox}$; Smad4$^{lox/lox}$;Trp53$^{lox/+}$*	REC/WT	N.D.	WT
R7121	PKPCSm	*Pdx1-Flp;FSF-Kras$^{G12D/+}$;Cdkn2a$^{lox/lox}$; Smad4$^{lox/+}$;Trp53$^{lox/+}$*	REC/WT	N.D.	WT
R7136-1	PKPCSm	*Pdx1-Flp;FSF-Kras$^{G12D/+}$;Cdkn2a$^{lox/+}$; Smad4$^{lox/lox}$;Trp53$^{lox/+}$*	REC/WT	N.D.	N.D.
R7136-2	PKPCSm	*Pdx1-Flp;FSF-Kras$^{G12D/+}$;Cdkn2a$^{lox/+}$; Smad4$^{lox/lox}$;Trp53$^{lox/+}$*	REC/WT	N.D.	N.D.
R7153	PKPCSm	*Pdx1-Flp;FSF-Kras$^{G12D/+}$;Cdkn2a$^{lox/lox}$; Smad4$^{lox/lox}$;Trp53$^{lox/+}$*	REC/WT	N.D.	N.D.
S1145	PKP	*Pdx1-Flp;FSF-Kras$^{G12D/+}$; LSL-Trp53$^{R172H/+}$*	REC/WT	N.D.	REC/WT
S134	PK	*Pdx1-Flp-o;FSF-Kras$^{G12D/+}$*	REC/WT	N.D.	WT/WT
S302	PK	*Pdx1-Flp-o;FSF-Kras$^{G12D/+}$*	REC/WT	N.D.	WT/WT
S411	PK	*Pdx1-Flp-o;FSF-Kras$^{G12D/+}$*	REC/WT	N.D.	WT/WT
S559	PK	*Pdx1-Flp-o;FSF-Kras$^{G12D/+}$*	REC/WT	N.D.	WT/WT
S821	PK	*Pdx1-Flp-o;FSF-Kras$^{G12D/+}$*	REC/WT	N.D.	WT/WT
S908	PKP	*Pdx1-Flp-o;FSF-Kras$^{G12D/+}$; LSL-Trp53$^{R172H/+}$*	REC/WT	N.D.	REC/WT
S914	PK	*Pdx1-Flp;FSF-Kras$^{G12D/+}$*	REC/WT	N.D.	WT/WT
SB1381-1	PKT	*Ptf1a$^{Cre/+}$;LSL-Kras$^{G12D/+}$; Tgfβr2$^{lox/lox}$*	REC/WT	N.D.	WT/WT
SB1382-1	PKSm	*Ptf1a$^{Cre/+}$;LSL-Kras$^{G12D/+}$;Smad4$^{lox/+}$*	REC/WT	N.D.	WT/WT
SB1382-2	PKSm	*Ptf1a$^{Cre/+}$;LSL-Kras$^{G12D/+}$;Smad4$^{lox/+}$*	REC/WT	N.D.	WT/WT
SB1382-3	PKSm	*Ptf1a$^{Cre/+}$;LSL-Kras$^{G12D/+}$;Smad4$^{lox/+}$*	REC/WT	N.D.	WT/WT
SB1412-1	PKPT	*Ptf1a$^{Cre/+}$;LSL-*	REC/WT	N.D.	REC/WT

Sample ID	Genotype group	Detailed genotype	Recombination in cell line		
			Kras	*Pik3ca*	*Trp53*
		Kras$^{G12D/+}$;Tgfβr2$^{lox/lox}$; Trp53$^{R172H/+}$			
SB1437-1	PKT	*Ptf1a$^{Cre/+}$;LSL-Kras$^{G12D/+}$; Tgfβr2$^{lox/lox}$*	REC/WT	N.D.	WT/WT
SB1516-2	PKPT	*Ptf1a$^{Cre/+}$;LSL-Kras$^{G12D/+}$;Tgfβr2$^{lox/+}$; Trp53$^{R172H/+}$*	REC/WT	N.D.	REC/WT
SB1551-1	PKT	*Ptf1a$^{Cre/+}$;LSL-Kras$^{G12D/+}$; Tgfβr2$^{lox/lox}$*	REC/WT	N.D.	WT/WT
SB1614-5	PKSm	*Ptf1a$^{Cre/+}$;LSL-Kras$^{G12D/+}$;Smad4$^{lox/+}$*	REC/REC	N.D.	WT/WT
SB1672-2	PKTSm	*Ptf1a$^{Cre/+}$;LSL-Kras$^{G12D/+}$; Tgfβr2$^{lox/+}$;Smad4$^{lox/+}$*	REC/WT	N.D.	WT/WT
SB1751-1	PKSm	*Ptf1a$^{Cre/+}$;LSL-Kras$^{G12D/+}$;Smad4$^{lox/+}$*	REC/WT	N.D.	WT/WT
SB1751-4	PKSm	*Ptf1a$^{Cre/+}$;LSL-Kras$^{G12D/+}$;Smad4$^{lox/+}$*	REC/WT	N.D.	WT/WT
SB1751-5	PKSm	*Ptf1a$^{Cre/+}$;LSL-Kras$^{G12D/+}$;Smad4$^{lox/+}$*	REC/REC	N.D.	WT/WT
SC3701	PKC	*Ptf1a$^{Cre/+}$;LSL-Kras$^{G12D/+}$; p16$^{Ink4a*/+}$*	REC/WT	N.D.	WT/WT
SC5406	PKC	*Ptf1a$^{Cre/+}$;LSL-Kras$^{G12D/+}$; p16$^{Ink4a*/+}$*	REC/WT	N.D.	WT/WT
SC5711	PKSC	*Ptf1a$^{Cre/+}$;LSL-Kras$^{G12D/+}$; Rosa26$^{Snail/+}$; Cdkn2a$^{lox/+}$*	REC/WT	N.D.	WT/WT
SC5815	PKSC	*Ptf1a$^{Cre/+}$;LSL-Kras$^{G12D/+}$; Rosa26$^{Snail/+}$; Cdkn2a$^{lox/+}$*	REC/REC	N.D.	WT/WT
SC5847	PKC	*Ptf1a$^{Cre/+}$;LSL-Kras$^{G12D/+}$;Cdkn2a$^{lox/+}$*	REC/WT	N.D.	WT/WT
SC5877	PKC	*Ptf1a$^{Cre/+}$;LSL-Kras$^{G12D/+}$;Cdkn2a$^{lox/+}$*	REC/REC	N.D.	WT/WT
SC5881	PKSC	*Ptf1a$^{Cre/+}$;LSL-Kras$^{G12D/+}$; Rosa26$^{Snail/+}$; Cdkn2a$^{lox/+}$*	REC/WT	N.D.	WT/WT
SC6039	PKSC	*Ptf1a$^{Cre/+}$;LSL-Kras$^{G12D/+}$; Rosa26$^{Snail/+}$; Cdkn2a$^{lox/+}$*	REC/WT	N.D.	WT/WT
V4706	PK	*Ptf1a$^{Cre/+}$;LSL-Kras$^{G12D/+}$*	REC/WT	N.D.	WT/WT
W22	PKP	*Ptf1a$^{Cre/+}$;LSL-Kras$^{G12D/+}$;Trp53$^{lox/lox}$*	REC/REC	N.D.	N.D.

10 References

Aguirre, Andrew J.; Bardeesy, Nabeel; Sinha, Manisha; Lopez, Lyle; Tuveson, David A.; Horner, James et al. (2003): Activated Kras and Ink4a/Arf deficiency cooperate to produce metastatic pancreatic ductal adenocarcinoma. In *Genes & development* 17 (24), pp. 3112–3126. DOI: 10.1101/gad.1158703.

Aguirre, Andrew J.; Nowak, Jonathan A.; Camarda, Nicholas D.; Moffitt, Richard A.; Ghazani, Arezou A.; Hazar-Rethinam, Mehlika et al. (2018): Real-time Genomic Characterization of Advanced Pancreatic Cancer to Enable Precision Medicine. In *Cancer discovery* 8 (9), pp. 1096–1111. DOI: 10.1158/2159-8290.CD-18-0275.

Al-Lazikani, Bissan; Banerji, Udai; Workman, Paul (2012): Combinatorial drug therapy for cancer in the post-genomic era. In *Nature biotechnology* 30 (7), pp. 679–692. DOI: 10.1038/nbt.2284.

Anderson, M. E. (1998): Glutathione: an overview of biosynthesis and modulation. In *Chemico-biological interactions* 111-112, pp. 1–14. DOI: 10.1016/s0009-2797(97)00146-4.

Antolin, Albert A.; Ameratunga, Malaka; Banerji, Udai; Clarke, Paul A.; Workman, Paul; Al-Lazikani, Bissan (2020): The kinase polypharmacology landscape of clinical PARP inhibitors. In *Scientific reports* 10 (1), p. 2585. DOI: 10.1038/s41598-020-59074-4.

Antonicka, Hana; Lin, Zhen-Yuan; Janer, Alexandre; Aaltonen, Mari J.; Weraarpachai, Woranontee; Gingras, Anne-Claude; Shoubridge, Eric A. (2020): A High-Density Human Mitochondrial Proximity Interaction Network. In *Cell metabolism* 32 (3), 479-497.e9. DOI: 10.1016/j.cmet.2020.07.017.

Aung, Kyaw L.; Fischer, Sandra E.; Denroche, Robert E.; Jang, Gun-Ho; Dodd, Anna; Creighton, Sean et al. (2018): Genomics-Driven Precision Medicine for Advanced Pancreatic Cancer: Early Results from the COMPASS Trial. In *Clinical cancer research : an official journal of the American Association for Cancer Research* 24 (6), pp. 1344–1354. DOI: 10.1158/1078-0432.CCR-17-2994.

Baccelli, Irène; Gareau, Yves; Lehnertz, Bernhard; Gingras, Stéphane; Spinella, Jean-François; Corneau, Sophie et al. (2019): Mubritinib Targets the Electron Transport Chain Complex I and Reveals the Landscape of OXPHOS Dependency in Acute Myeloid Leukemia. In *Cancer cell* 36 (1), 84-99.e8. DOI: 10.1016/j.ccell.2019.06.003.

Backx, Elyne; Coolens, Katarina; van den Bossche, Jan-Lars; Houbracken, Isabelle; Espinet, Elisa; Rooman, Ilse (2022): On the Origin of Pancreatic Cancer: Molecular Tumor Subtypes in Perspective of Exocrine Cell Plasticity. In *Cellular and molecular gastroenterology and hepatology* 13 (4), pp. 1243–1253. DOI: 10.1016/j.jcmgh.2021.11.010.

Bailey, Peter; Chang, David K.; Nones, Katia; Johns, Amber L.; Patch, Ann-Marie; Gingras, Marie-Claude et al. (2016): Genomic analyses identify molecular subtypes of pancreatic cancer. In *Nature* 531 (7592), pp. 47–52. DOI: 10.1038/nature16965.

Baker, Lindsey A.; Tiriac, Hervé; Clevers, Hans; Tuveson, David A. (2016): Modeling pancreatic cancer with organoids. In *Trends in cancer* 2 (4), pp. 176–190. DOI: 10.1016/j.trecan.2016.03.004.

Bardeesy, Nabeel; Cheng, Kuang-Hung; Berger, Justin H.; Chu, Gerald C.; Pahler, Jessica; Olson, Peter et al. (2006): Smad4 is dispensable for normal pancreas development yet

critical in progression and tumor biology of pancreas cancer. In *Genes & development* 20 (22), pp. 3130–3146. DOI: 10.1101/gad.1478706.

Barretina, Jordi; Caponigro, Giordano; Stransky, Nicolas; Venkatesan, Kavitha; Margolin, Adam A.; Kim, Sungjoon et al. (2012): The Cancer Cell Line Encyclopedia enables predictive modelling of anticancer drug sensitivity. In *Nature* 483 (7391), pp. 603–607. DOI: 10.1038/nature11003.

Behan, Fiona M.; Iorio, Francesco; Picco, Gabriele; Gonçalves, Emanuel; Beaver, Charlotte M.; Migliardi, Giorgia et al. (2019): Prioritization of cancer therapeutic targets using CRISPR-Cas9 screens. In *Nature* 568 (7753), pp. 511–516. DOI: 10.1038/s41586-019-1103-9.

Behrens, Gundula; Jochem, Carmen; Schmid, Daniela; Keimling, Marlen; Ricci, Cristian; Leitzmann, Michael F. (2015): Physical activity and risk of pancreatic cancer: a systematic review and meta-analysis. In *European journal of epidemiology* 30 (4), pp. 279–298. DOI: 10.1007/s10654-015-0014-9.

Berenbaum, M. C. (1989): What is synergy? In *Pharmacological reviews* 41 (2), pp. 93–141.

Biankin, Andrew V.; Waddell, Nicola; Kassahn, Karin S.; Gingras, Marie-Claude; Muthuswamy, Lakshmi B.; Johns, Amber L. et al. (2012): Pancreatic cancer genomes reveal aberrations in axon guidance pathway genes. In *Nature* 491 (7424), pp. 399–405. DOI: 10.1038/nature11547.

Bleijs, Margit; van de Wetering, Marc; Clevers, Hans; Drost, Jarno (2019): Xenograft and organoid model systems in cancer research. In *The EMBO journal* 38 (15), e101654. DOI: 10.15252/embj.2019101654.

BLISS, C. I. (1939): THE TOXICITY OF POISONS APPLIED JOINTLY1. In *Annals of Applied Biology* 26 (3), pp. 585–615. DOI: 10.1111/j.1744-7348.1939.tb06990.x.

Boj, Sylvia F.; Hwang, Chang-Il; Baker, Lindsey A.; Chio, Iok In Christine; Engle, Dannielle D.; Corbo, Vincenzo et al. (2015): Organoid models of human and mouse ductal pancreatic cancer. In *Cell* 160 (1-2), pp. 324–338. DOI: 10.1016/j.cell.2014.12.021.

Boniolo, Fabio (2022): Towards precision medicine: computational approaches for patient stratification and biomarker identification in oncology. With assistance of Jan Baumbach. München: Universitätsbibliothek der TU München.

Boniolo, Fabio; Dorigatti, Emilio; Ohnmacht, Alexander J.; Saur, Dieter; Schubert, Benjamin; Menden, Michael P. (2021): Artificial intelligence in early drug discovery enabling precision medicine. In *Expert opinion on drug discovery* 16 (9), pp. 991–1007. DOI: 10.1080/17460441.2021.1918096.

Bos, Johannes L.; Rehmann, Holger; Wittinghofer, Alfred (2007): GEFs and GAPs: critical elements in the control of small G proteins. In *Cell* 129 (5), pp. 865–877. DOI: 10.1016/j.cell.2007.05.018.

Bosetti, C.; Lucenteforte, E.; Silverman, D. T.; Petersen, G.; Bracci, P. M.; Ji, B. T. et al. (2012): Cigarette smoking and pancreatic cancer: an analysis from the International Pancreatic Cancer Case-Control Consortium (Panc4). In *Annals of oncology : official journal of the European Society for Medical Oncology* 23 (7), pp. 1880–1888. DOI: 10.1093/annonc/mdr541.

Bosetti, C.; Rosato, V.; Li, D.; Silverman, D.; Petersen, G. M.; Bracci, P. M. et al. (2014): Diabetes, antidiabetic medications, and pancreatic cancer risk: an analysis from the

International Pancreatic Cancer Case-Control Consortium. In *Annals of oncology : official journal of the European Society for Medical Oncology* 25 (10), pp. 2065–2072. DOI: 10.1093/annonc/mdu276.

Bouhaddou, Mehdi; DiStefano, Matthew S.; Riesel, Eric A.; Carrasco, Emilce; Holzapfel, Hadassa Y.; Jones, DeAnalisa C. et al. (2016): Drug response consistency in CCLE and CGP. In *Nature* 540 (7631), E9-E10. DOI: 10.1038/nature20580.

Bouwer, Miranda F.; Hamilton, Kathryn E.; Jonker, Patrick B.; Kuiper, Sam R.; Louters, Larry L.; Looyenga, Brendan D. (2021): NMS-873 functions as a dual inhibitor of mitochondrial oxidative phosphorylation. In *Biochimie* 185, pp. 33–42. DOI: 10.1016/j.biochi.2021.03.004.

Buccarelli, Mariachiara; D'Alessandris, Quintino Giorgio; Matarrese, Paola; Mollinari, Cristiana; Signore, Michele; Cappannini, Andrea et al. (2021): Elesclomol-induced increase of mitochondrial reactive oxygen species impairs glioblastoma stem-like cell survival and tumor growth. In *Journal of experimental & clinical cancer research : CR* 40 (1), p. 228. DOI: 10.1186/s13046-021-02031-4.

Burris, H. A.; Moore, M. J.; Andersen, J.; Green, M. R.; Rothenberg, M. L.; Modiano, M. R. et al. (1997): Improvements in survival and clinical benefit with gemcitabine as first-line therapy for patients with advanced pancreas cancer: a randomized trial. In *Journal of clinical oncology : official journal of the American Society of Clinical Oncology* 15 (6), pp. 2403–2413. DOI: 10.1200/JCO.1997.15.6.2403.

Burstin, Johannes von; Eser, Stefan; Paul, Mariel C.; Seidler, Barbara; Brandl, Martina; Messer, Marlena et al. (2009): E-cadherin regulates metastasis of pancreatic cancer in vivo and is suppressed by a SNAIL/HDAC1/HDAC2 repressor complex. In *Gastroenterology* 137 (1), 361-71, 371.e1-5. DOI: 10.1053/j.gastro.2009.04.004.

Bushway, Paul J.; Azimi, Behrad; Heynen-Genel, Susanne; Price, Jeffrey H.; Mercola, Mark (2010): Hybrid median filter background estimator for correcting distortions in microtiter plate data. In *Assay and drug development technologies* 8 (2), pp. 238–250. DOI: 10.1089/adt.2009.0242.

Carpenter, Evan L.; Chagani, Sharmeen; Nelson, Dylan; Cassidy, Pamela B.; Laws, Madeleine; Ganguli-Indra, Gitali; Indra, Arup K. (2019): Mitochondrial complex I inhibitor deguelin induces metabolic reprogramming and sensitizes vemurafenib-resistant BRAFV600E mutation bearing metastatic melanoma cells. In *Molecular carcinogenesis* 58 (9), pp. 1680–1690. DOI: 10.1002/mc.23068.

Chan-Seng-Yue, Michelle; Kim, Jaeseung C.; Wilson, Gavin W.; Ng, Karen; Figueroa, Eugenia Flores; O'Kane, Grainne M. et al. (2020): Transcription phenotypes of pancreatic cancer are driven by genomic events during tumor evolution. In *Nature genetics* 52 (2), pp. 231–240. DOI: 10.1038/s41588-019-0566-9.

Chytil, Anna; Magnuson, Mark A.; Wright, Christopher V. E.; Moses, Harold L. (2002): Conditional inactivation of the TGF-beta type II receptor using Cre:Lox. In *Genesis (New York, N.Y. : 2000)* 32 (2), pp. 73–75. DOI: 10.1002/gene.10046.

Clark, Nicholas A.; Hafner, Marc; Kouril, Michal; Williams, Elizabeth H.; Muhlich, Jeremy L.; Pilarczyk, Marcin et al. (2017): GRcalculator: an online tool for calculating and mining dose-response data. In *BMC cancer* 17 (1), p. 698. DOI: 10.1186/s12885-017-3689-3.

Collisson, Eric A.; Bailey, Peter; Chang, David K.; Biankin, Andrew V. (2019): Molecular subtypes of pancreatic cancer. In *Nature reviews. Gastroenterology & hepatology* 16 (4), pp. 207–220. DOI: 10.1038/s41575-019-0109-y.

Collisson, Eric A.; Sadanandam, Anguraj; Olson, Peter; Gibb, William J.; Truitt, Morgan; Gu, Shenda et al. (2011): Subtypes of pancreatic ductal adenocarcinoma and their differing responses to therapy. In *Nature medicine* 17 (4), pp. 500–503. DOI: 10.1038/nm.2344.

Connor, Ashton A.; Denroche, Robert E.; Jang, Gun Ho; Timms, Lee; Kalimuthu, Sangeetha N.; Selander, Iris et al. (2017): Association of Distinct Mutational Signatures With Correlates of Increased Immune Activity in Pancreatic Ductal Adenocarcinoma. In *JAMA oncology* 3 (6), pp. 774–783. DOI: 10.1001/jamaoncol.2016.3916.

Conroy, Thierry; Desseigne, Françoise; Ychou, Marc; Bouché, Olivier; Guimbaud, Rosine; Bécouarn, Yves et al. (2011): FOLFIRINOX versus gemcitabine for metastatic pancreatic cancer. In *The New England journal of medicine* 364 (19), pp. 1817–1825. DOI: 10.1056/NEJMoa1011923.

Corsello, Steven M.; Nagari, Rohith T.; Spangler, Ryan D.; Rossen, Jordan; Kocak, Mustafa; Bryan, Jordan G. et al. (2020): Discovering the anti-cancer potential of non-oncology drugs by systematic viability profiling. In *Nature cancer* 1 (2), pp. 235–248. DOI: 10.1038/s43018-019-0018-6.

Da Silva, Lais; Jiang, Jinmai; Perkins, Corey; Atanasova, Kalina Rosenova; Bray, Julie K.; Bulut, Gamze et al. (2022): Pharmacological inhibition and reversal of pancreatic acinar ductal metaplasia. In *Cell death discovery* 8 (1), p. 378. DOI: 10.1038/s41420-022-01165-4.

Dardare, Julie; Witz, Andréa; Merlin, Jean-Louis; Gilson, Pauline; Harlé, Alexandre (2020): SMAD4 and the TGFβ Pathway in Patients with Pancreatic Ductal Adenocarcinoma. In *International journal of molecular sciences* 21 (10). DOI: 10.3390/ijms21103534.

Deans, Richard M.; Morgens, David W.; Ökesli, Ayşe; Pillay, Sirika; Horlbeck, Max A.; Kampmann, Martin et al. (2016): Parallel shRNA and CRISPR-Cas9 screens enable antiviral drug target identification. In *Nature chemical biology* 12 (5), pp. 361–366. DOI: 10.1038/nchembio.2050.

Derksen, Patrick W. B.; Liu, Xiaoling; Saridin, Francis; van der Gulden, Hanneke; Zevenhoven, John; Evers, Bastiaan et al. (2006): Somatic inactivation of E-cadherin and p53 in mice leads to metastatic lobular mammary carcinoma through induction of anoikis resistance and angiogenesis. In *Cancer cell* 10 (5), pp. 437–449. DOI: 10.1016/j.ccr.2006.09.013.

Dougan, Stephanie K. (2017): The Pancreatic Cancer Microenvironment. In *Cancer journal (Sudbury, Mass.)* 23 (6), pp. 321–325. DOI: 10.1097/PPO.0000000000000288.

Drew, R.; Miners, J. O. (1984): The effects of buthionine sulphoximine (BSO) on glutathione depletion and xenobiotic biotransformation. In *Biochemical pharmacology* 33 (19), pp. 2989–2994. DOI: 10.1016/0006-2952(84)90598-7.

Driehuis, Else; van Hoeck, Arne; Moore, Kat; Kolders, Sigrid; Francies, Hayley E.; Gulersonmez, M. Can et al. (2019): Pancreatic cancer organoids recapitulate disease and allow personalized drug screening. In *Proceedings of the National Academy of Sciences of the United States of America* 116 (52), pp. 26580–26590. DOI: 10.1073/pnas.1911273116.

Elrakaybi, Asmaa; Ruess, Dietrich A.; Lübbert, Michael; Quante, Michael; Becker, Heiko (2022): Epigenetics in Pancreatic Ductal Adenocarcinoma: Impact on Biology and Utilization in Diagnostics and Treatment. In *Cancers* 14 (23). DOI: 10.3390/cancers14235926.

Eser, Stefan; Reiff, Nina; Messer, Marlena; Seidler, Barbara; Gottschalk, Kathleen; Dobler, Melanie et al. (2013): Selective requirement of PI3K/PDK1 signaling for Kras oncogene-driven pancreatic cell plasticity and cancer. In *Cancer cell* 23 (3), pp. 406–420. DOI: 10.1016/j.ccr.2013.01.023.

Falcomatà, Chiara; Bärthel, Stefanie; Widholz, Sebastian A.; Schneeweis, Christian; Montero, Juan José; Toska, Albulena et al. (2022): Selective multi-kinase inhibition sensitizes mesenchymal pancreatic cancer to immune checkpoint blockade by remodeling the tumor microenvironment. In *Nature cancer* 3 (3), pp. 318–336. DOI: 10.1038/s43018-021-00326-1.

Fallahi-Sichani, Mohammad; Honarnejad, Saman; Heiser, Laura M.; Gray, Joe W.; Sorger, Peter K. (2013): Metrics other than potency reveal systematic variation in responses to cancer drugs. In *Nature chemical biology* 9 (11), pp. 708–714. DOI: 10.1038/nchembio.1337.

Fallah-Tafti, Asal; Foroumadi, Alireza; Tiwari, Rakesh; Shirazi, Amir Nasrolahi; Hangauer, David G.; Bu, Yahao et al. (2011): Thiazolyl N-benzyl-substituted acetamide derivatives: synthesis, Src kinase inhibitory and anticancer activities. In *European journal of medicinal chemistry* 46 (10), pp. 4853–4858. DOI: 10.1016/j.ejmech.2011.07.050.

Feig, Christine; Gopinathan, Aarthi; Neesse, Albrecht; Chan, Derek S.; Cook, Natalie; Tuveson, David A. (2012): The pancreas cancer microenvironment. In *Clinical cancer research : an official journal of the American Association for Cancer Research* 18 (16), pp. 4266–4276. DOI: 10.1158/1078-0432.CCR-11-3114.

Flaherty, Keith T.; Infante, Jeffery R.; Daud, Adil; Gonzalez, Rene; Kefford, Richard F.; Sosman, Jeffrey et al. (2012): Combined BRAF and MEK inhibition in melanoma with BRAF V600 mutations. In *The New England journal of medicine* 367 (18), pp. 1694–1703. DOI: 10.1056/NEJMoa1210093.

Frappart, Pierre-Olivier; Hofmann, Thomas G. (2020): Pancreatic Ductal Adenocarcinoma (PDAC) Organoids: The Shining Light at the End of the Tunnel for Drug Response Prediction and Personalized Medicine. In *Cancers* 12 (10). DOI: 10.3390/cancers12102750.

Fraunhoffer, Nicolas A.; Abuelafia, Analía Meilerman; Bigonnet, Martin; Gayet, Odile; Roques, Julie; Telle, Emmanuel et al. (2020): Evidencing a Pancreatic Ductal Adenocarcinoma Subpopulation Sensitive to the Proteasome Inhibitor Carfilzomib. In *Clinical cancer research : an official journal of the American Association for Cancer Research* 26 (20), pp. 5506–5519. DOI: 10.1158/1078-0432.CCR-20-1232.

Garcia, Patrick L.; Miller, Aubrey L.; Yoon, Karina J. (2020): Patient-Derived Xenograft Models of Pancreatic Cancer: Overview and Comparison with Other Types of Models. In *Cancers* 12 (5). DOI: 10.3390/cancers12051327.

Garnett, Mathew J.; Edelman, Elena J.; Heidorn, Sonja J.; Greenman, Chris D.; Dastur, Anahita; Lau, King Wai et al. (2012): Systematic identification of genomic markers of drug sensitivity in cancer cells. In *Nature* 483 (7391), pp. 570–575. DOI: 10.1038/nature11005.

Geeleher, Paul; Gamazon, Eric R.; Seoighe, Cathal; Cox, Nancy J.; Huang, R. Stephanie (2016): Consistency in large pharmacogenomic studies. In *Nature* 540 (7631), E1-E2. DOI: 10.1038/nature19838.

Ghandi, Mahmoud; Huang, Franklin W.; Jané-Valbuena, Judit; Kryukov, Gregory V.; Lo, Christopher C.; McDonald, E. Robert et al. (2019): Next-generation characterization of the Cancer Cell Line Encyclopedia. In *Nature* 569 (7757), pp. 503–508. DOI: 10.1038/s41586-019-1186-3.

Giansanti, Piero; Samaras, Patroklos; Bian, Yangyang; Meng, Chen; Coluccio, Andrea; Frejno, Martin et al. (2022): Mass spectrometry-based draft of the mouse proteome. In *Nature methods* 19 (7), pp. 803–811. DOI: 10.1038/s41592-022-01526-y.

Gimple, Ryan C.; Wang, Xiuxing (2019): RAS: Striking at the Core of the Oncogenic Circuitry. In *Frontiers in oncology* 9, p. 965. DOI: 10.3389/fonc.2019.00965.

Giovannetti, E.; van der Borden, C. L.; Frampton, A. E.; Ali, A.; Firuzi, O.; Peters, G. J. (2017): Never let it go: Stopping key mechanisms underlying metastasis to fight pancreatic cancer. In *Seminars in cancer biology* 44, pp. 43–59. DOI: 10.1016/j.semcancer.2017.04.006.

Gobbi, Paolo G.; Bergonzi, Manuela; Comelli, Mario; Villano, Lara; Pozzoli, Donatella; Vanoli, Alessandro; Dionigi, Paolo (2013): The prognostic role of time to diagnosis and presenting symptoms in patients with pancreatic cancer. In *Cancer epidemiology* 37 (2), pp. 186–190. DOI: 10.1016/j.canep.2012.12.002.

Golan, Talia; Hammel, Pascal; Reni, Michele; van Cutsem, Eric; Macarulla, Teresa; Hall, Michael J. et al. (2019): Maintenance Olaparib for Germline BRCA-Mutated Metastatic Pancreatic Cancer. In *The New England journal of medicine* 381 (4), pp. 317–327. DOI: 10.1056/NEJMoa1903387.

Gonçalves, Emanuel; Segura-Cabrera, Aldo; Pacini, Clare; Picco, Gabriele; Behan, Fiona M.; Jaaks, Patricia et al. (2020): Drug mechanism-of-action discovery through the integration of pharmacological and CRISPR screens. In *Molecular systems biology* 16 (7), e9405. DOI: 10.15252/msb.20199405.

Griffith, O. W. (1982): Mechanism of action, metabolism, and toxicity of buthionine sulfoximine and its higher homologs, potent inhibitors of glutathione synthesis. In *The Journal of biological chemistry* 257 (22), pp. 13704–13712.

Gross, Matt I.; Demo, Susan D.; Dennison, Jennifer B.; Chen, Lijing; Chernov-Rogan, Tania; Goyal, Bindu et al. (2014): Antitumor activity of the glutaminase inhibitor CB-839 in triple-negative breast cancer. In *Molecular cancer therapeutics* 13 (4), pp. 890–901. DOI: 10.1158/1535-7163.MCT-13-0870.

Guan, Michelle; Bender, R. Joseph; Pishvaian, Michael J.; Halverson, David Charles; Tuli, Richard; Klempner, Samuel Jacob et al. (2018): Molecular and clinical characterization of BRAF mutations in pancreatic ductal adenocarcinomas (PDACs). In *Journal of clinical oncology : official journal of the American Society of Clinical Oncology* 36 (4_suppl), p. 214. DOI: 10.1200/JCO.2018.36.4_suppl.214.

Hafner, Marc; Niepel, Mario; Chung, Mirra; Sorger, Peter K. (2016): Growth rate inhibition metrics correct for confounders in measuring sensitivity to cancer drugs. In *Nature methods* 13 (6), pp. 521–527. DOI: 10.1038/nmeth.3853.

Hafner, Marc; Niepel, Mario; Sorger, Peter K. (2017): Alternative drug sensitivity metrics improve preclinical cancer pharmacogenomics. In *Nature biotechnology* 35 (6), pp. 500–502. DOI: 10.1038/nbt.3882.

Hahn, S. A.; Schutte, M.; Hoque, A. T.; Moskaluk, C. A.; Da Costa, L. T.; Rozenblum, E. et al. (1996): DPC4, a candidate tumor suppressor gene at human chromosome 18q21.1. In *Science (New York, N.Y.)* 271 (5247), pp. 350–353. DOI: 10.1126/science.271.5247.350.

Haibe-Kains, Benjamin; El-Hachem, Nehme; Birkbak, Nicolai Juul; Jin, Andrew C.; Beck, Andrew H.; Aerts, Hugo J. W. L.; Quackenbush, John (2013): Inconsistency in large pharmacogenomic studies. In *Nature* 504 (7480), pp. 389–393. DOI: 10.1038/nature12831.

Han, Yong Hwan; Kim, Sung Zoo; Kim, Suhn Hee; Park, Woo Hyun (2008): Induction of apoptosis in arsenic trioxide-treated lung cancer A549 cells by buthionine sulfoximine. In *Molecules and cells* 26 (2), pp. 158–164.

Hart, Traver; Chandrashekhar, Megha; Aregger, Michael; Steinhart, Zachary; Brown, Kevin R.; MacLeod, Graham et al. (2015): High-Resolution CRISPR Screens Reveal Fitness Genes and Genotype-Specific Cancer Liabilities. In *Cell* 163 (6), pp. 1515–1526. DOI: 10.1016/j.cell.2015.11.015.

Haverty, Peter M.; Lin, Eva; Tan, Jenille; Yu, Yihong; Lam, Billy; Lianoglou, Steve et al. (2016): Reproducible pharmacogenomic profiling of cancer cell line panels. In *Nature* 533 (7603), pp. 333–337. DOI: 10.1038/nature17987.

Hedley, David; Shamas-Din, Aisha; Chow, Sue; Sanfelice, Deborah; Schuh, Andre C.; Brandwein, Joseph M. et al. (2016): A phase I study of elesclomol sodium in patients with acute myeloid leukemia. In *Leukemia & lymphoma* 57 (10), pp. 2437–2440. DOI: 10.3109/10428194.2016.1138293.

Hezel, Aram F.; Kimmelman, Alec C.; Stanger, Ben Z.; Bardeesy, Nabeel; DePinho, Ronald A. (2006): Genetics and biology of pancreatic ductal adenocarcinoma. In *Genes & development* 20 (10), pp. 1218–1249. DOI: 10.1101/gad.1415606.

Hingorani, Sunil R.; Petricoin, Emanuel F.; Maitra, Anirban; Rajapakse, Vinodh; King, Catrina; Jacobetz, Michael A. et al. (2003): Preinvasive and invasive ductal pancreatic cancer and its early detection in the mouse. In *Cancer cell* 4 (6), pp. 437–450. DOI: 10.1016/S1535-6108(03)00309-X.

Hingorani, Sunil R.; Wang, Lifu; Multani, Asha S.; Combs, Chelsea; Deramaudt, Therese B.; Hruban, Ralph H. et al. (2005): Trp53R172H and KrasG12D cooperate to promote chromosomal instability and widely metastatic pancreatic ductal adenocarcinoma in mice. In *Cancer cell* 7 (5), pp. 469–483. DOI: 10.1016/j.ccr.2005.04.023.

Hirt, Christian K.; Booij, Tijmen H.; Grob, Linda; Simmler, Patrik; Toussaint, Nora C.; Keller, David et al. (2022): Drug screening and genome editing in human pancreatic cancer organoids identifies drug-gene interactions and candidates for off-label treatment. In *Cell genomics* 2 (2), p. 100095. DOI: 10.1016/j.xgen.2022.100095.

Hoff, Daniel D. von; Ervin, Thomas; Arena, Francis P.; Chiorean, E. Gabriela; Infante, Jeffrey; Moore, Malcolm et al. (2013): Increased survival in pancreatic cancer with nab-paclitaxel plus gemcitabine. In *The New England journal of medicine* 369 (18), pp. 1691–1703. DOI: 10.1056/NEJMoa1304369.

Holbeck, Susan L.; Camalier, Richard; Crowell, James A.; Govindharajulu, Jeevan Prasaad; Hollingshead, Melinda; Anderson, Lawrence W. et al. (2017): The National Cancer Institute ALMANAC: A Comprehensive Screening Resource for the Detection of Anticancer Drug Pairs with Enhanced Therapeutic Activity. In *Cancer research* 77 (13), pp. 3564–3576. DOI: 10.1158/0008-5472.CAN-17-0489.

Holmgren, A.; Johansson, C.; Berndt, C.; Lönn, M. E.; Hudemann, C.; Lillig, C. H. (2005): Thiol redox control via thioredoxin and glutaredoxin systems. In *Biochemical Society transactions* 33 (Pt 6), pp. 1375–1377. DOI: 10.1042/BST0331375.

Hosein, Abdel N.; Brekken, Rolf A.; Maitra, Anirban (2020): Pancreatic cancer stroma: an update on therapeutic targeting strategies. In *Nature reviews. Gastroenterology & hepatology* 17 (8), pp. 487–505. DOI: 10.1038/s41575-020-0300-1.

Hosein, Abdel Nasser; Dougan, Stephanie K.; Aguirre, Andrew J.; Maitra, Anirban (2022): Translational advances in pancreatic ductal adenocarcinoma therapy. In *Nature cancer* 3 (3), pp. 272–286. DOI: 10.1038/s43018-022-00349-2.

Hruban, R. H.; Goggins, M.; Parsons, J.; Kern, S. E. (2000): Progression model for pancreatic cancer. In *Clinical cancer research : an official journal of the American Association for Cancer Research* 6 (8), pp. 2969–2972.

Huang, Lamei; Guo, Zhixing; Wang, Fang; Fu, Liwu (2021): KRAS mutation: from undruggable to druggable in cancer. In *Signal transduction and targeted therapy* 6 (1), p. 386. DOI: 10.1038/s41392-021-00780-4.

Ianevski, Aleksandr; Giri, Anil K.; Aittokallio, Tero (2020): SynergyFinder 2.0: visual analytics of multi-drug combination synergies. In *Nucleic acids research* 48 (W1), W488-W493. DOI: 10.1093/nar/gkaa216.

Integrated Genomic Characterization of Pancreatic Ductal Adenocarcinoma (2017). In *Cancer cell* 32 (2), 185-203.e13.

Iorio, Francesco; Knijnenburg, Theo A.; Vis, Daniel J.; Bignell, Graham R.; Menden, Michael P.; Schubert, Michael et al. (2016): A Landscape of Pharmacogenomic Interactions in Cancer. In *Cell* 166 (3), pp. 740–754. DOI: 10.1016/j.cell.2016.06.017.

Jaaks, Patricia; Coker, Elizabeth A.; Vis, Daniel J.; Edwards, Olivia; Carpenter, Emma F.; Leto, Simonetta M. et al. (2022): Effective drug combinations in breast, colon and pancreatic cancer cells. In *Nature* 603 (7899), pp. 166–173. DOI: 10.1038/s41586-022-04437-2.

Jackson, E. L.; Willis, N.; Mercer, K.; Bronson, R. T.; Crowley, D.; Montoya, R. et al. (2001): Analysis of lung tumor initiation and progression using conditional expression of oncogenic K-ras. In *Genes & development* 15 (24), pp. 3243–3248. DOI: 10.1101/gad.943001.

JI, BIN-CHUAN; YU, CHIEN-CHIH; YANG, SU-TSO; HSIA, TE-CHUN; YANG, JAI-SING; LAI, KUANG-CHI et al. (2012): Induction of DNA damage by deguelin is mediated through reducing DNA repair genes in human non-small cell lung cancer NCI-H460 cells. In *Oncology Reports* 27 (4), pp. 959–964. DOI: 10.3892/or.2012.1622.

Jiang, Yan; Sohal, Davendra P. S. (2023): Pancreatic Adenocarcinoma Management. In *JCO oncology practice* 19 (1), pp. 19–32. DOI: 10.1200/OP.22.00328.

Jin, Haojie; Wang, Liqin; Bernards, René (2022): Rational combinations of targeted cancer therapies: background, advances and challenges. In *Nature reviews. Drug discovery*. DOI: 10.1038/s41573-022-00615-z.

Jin, Quanri; Feng, Lei; Behrens, Carmen; Bekele, B. Nebiyou; Wistuba, Ignacio I.; Hong, Waun-Ki; Lee, Ho-Young (2007): Implication of AMP-activated protein kinase and Akt-regulated survivin in lung cancer chemopreventive activities of deguelin. In *Cancer research* 67 (24), pp. 11630–11639. DOI: 10.1158/0008-5472.CAN-07-2401.

Jones, Suzanne F.; Infante, Jeffrey R.; Spigel, David R.; Peacock, Nancy W.; Thompson, Dana S.; Greco, F. Anthony et al. (2012): Phase 1 results from a study of romidepsin in combination with gemcitabine in patients with advanced solid tumors. In *Cancer investigation* 30 (6), pp. 481–486. DOI: 10.3109/07357907.2012.675382.

Jonkers, J.; Meuwissen, R.; van der Gulden, H.; Peterse, H.; van der Valk, M.; Berns, A. (2001): Synergistic tumor suppressor activity of BRCA2 and p53 in a conditional mouse model for breast cancer. In *Nature genetics* 29 (4), pp. 418–425. DOI: 10.1038/ng747.

Juiz, Natalia Anahi; Iovanna, Juan; Dusetti, Nelson (2019): Pancreatic Cancer Heterogeneity Can Be Explained Beyond the Genome. In *Frontiers in oncology* 9, p. 246. DOI: 10.3389/fonc.2019.00246.

Kalluri, Raghu; Weinberg, Robert A. (2009): The basics of epithelial-mesenchymal transition. In *The Journal of clinical investigation* 119 (6), pp. 1420–1428. DOI: 10.1172/JCI39104.

Kanda, Mitsuro; Matthaei, Hanno; Wu, Jian; Hong, Seung-Mo; Yu, Jun; Borges, Michael et al. (2012): Presence of somatic mutations in most early-stage pancreatic intraepithelial neoplasia. In *Gastroenterology* 142 (4), 730-733.e9. DOI: 10.1053/j.gastro.2011.12.042.

Kefford, R.; Arkenau, H.; Brown, M. P.; Millward, M.; Infante, J. R.; Long, G. V. et al. (2010): Phase I/II study of GSK2118436, a selective inhibitor of oncogenic mutant BRAF kinase, in patients with metastatic melanoma and other solid tumors. In *Journal of clinical oncology : official journal of the American Society of Clinical Oncology* 28 (15_suppl), p. 8503. DOI: 10.1200/jco.2010.28.15_suppl.8503.

Khoo, Bee Luan; Lee, Soo Chin; Kumar, Prashant; Tan, Tuan Zea; Warkiani, Majid Ebrahimi; Ow, Samuel G. W. et al. (2015): Short-term expansion of breast circulating cancer cells predicts response to anti-cancer therapy. In *Oncotarget* 6 (17), pp. 15578–15593. DOI: 10.18632/oncotarget.3903.

Kim, Myungshin; Rhee, Je-Keun; Choi, Hayoung; Kwon, Ahlm; Kim, Jiyeon; Lee, Gun Dong et al. (2017): Passage-dependent accumulation of somatic mutations in mesenchymal stromal cells during in vitro culture revealed by whole genome sequencing. In *Scientific reports* 7 (1), p. 14508. DOI: 10.1038/s41598-017-15155-5.

Kirshner, Jessica R.; He, Suqin; Balasubramanyam, Vishwasenani; Kepros, Jane; Yang, Chin-Yu; Zhang, Mei et al. (2008): Elesclomol induces cancer cell apoptosis through oxidative stress. In *Molecular cancer therapeutics* 7 (8), pp. 2319–2327. DOI: 10.1158/1535-7163.MCT-08-0298.

Klaeger, Susan; Heinzlmeir, Stephanie; Wilhelm, Mathias; Polzer, Harald; Vick, Binje; Koenig, Paul-Albert et al. (2017): The target landscape of clinical kinase drugs. In *Science (New York, N.Y.)* 358 (6367). DOI: 10.1126/science.aan4368.

Kleeff, Jorg; Korc, Murray; Apte, Minoti; La Vecchia, Carlo; Johnson, Colin D.; Biankin, Andrew V. et al. (2016): Pancreatic cancer. In *Nature reviews. Disease primers* 2, p. 16022. DOI: 10.1038/nrdp.2016.22.

Knox, Jennifer J.; Jaffee, Elizabeth M.; O'Kane, Grainne M.; Plenker, Dennis; Zhang, Amy; Ramotar, Stephanie et al. (2022): PASS-01: Pancreatic adenocarcinoma signature stratification for treatment–01. In *Journal of clinical oncology : official journal of the American Society of Clinical Oncology* 40 (4_suppl), TPS635-TPS635. DOI: 10.1200/JCO.2022.40.4_suppl.TPS635.

Krauß, Lukas; Urban, Bettina C.; Hastreiter, Sieglinde; Schneider, Carolin; Wenzel, Patrick; Hassan, Zonera et al. (2022): HDAC2 Facilitates Pancreatic Cancer Metastasis. In *Cancer research* 82 (4), pp. 695–707. DOI: 10.1158/0008-5472.CAN-20-3209.

Krill-Burger, J. Michael; Dempster, Joshua M.; Borah, Ashir A.; Paolella, Brenton R.; Root, David E.; Golub, Todd R. et al. (2023): Partial gene suppression improves identification of cancer vulnerabilities when CRISPR-Cas9 knockout is pan-lethal. In *Genome biology* 24 (1), p. 192. DOI: 10.1186/s13059-023-03020-w.

Krimpenfort, P.; Quon, K. C.; Mooi, W. J.; Loonstra, A.; Berns, A. (2001): Loss of p16Ink4a confers susceptibility to metastatic melanoma in mice. In *Nature* 413 (6851), pp. 83–86. DOI: 10.1038/35092584.

Laetsch, Theodore W.; DuBois, Steven G.; Mascarenhas, Leo; Turpin, Brian; Federman, Noah; Albert, Catherine M. et al. (2018): Larotrectinib for paediatric solid tumours harbouring NTRK gene fusions: phase 1 results from a multicentre, open-label, phase 1/2 study. In *The Lancet. Oncology* 19 (5), pp. 705–714. DOI: 10.1016/S1470-2045(18)30119-0.

Law, M. R.; Wald, N. J.; Morris, J. K.; Jordan, R. E. (2003): Value of low dose combination treatment with blood pressure lowering drugs: analysis of 354 randomised trials. In *BMJ (Clinical research ed.)* 326 (7404), p. 1427. DOI: 10.1136/bmj.326.7404.1427.

Le, Dung T.; Uram, Jennifer N.; Wang, Hao; Bartlett, Bjarne R.; Kemberling, Holly; Eyring, Aleksandra D. et al. (2015): PD-1 Blockade in Tumors with Mismatch-Repair Deficiency. In *The New England journal of medicine* 372 (26), pp. 2509–2520. DOI: 10.1056/NEJMoa1500596.

Lechner, Severin; Malgapo, Martin Ian P.; Grätz, Christian; Steimbach, Raphael R.; Baron, Agnes; Rüther, Patrick et al. (2022): Target deconvolution of HDAC pharmacopoeia reveals MBLAC2 as common off-target. In *Nature chemical biology* 18 (8), pp. 812–820. DOI: 10.1038/s41589-022-01015-5.

Lee, Chang-Lung; Moding, Everett J.; Huang, Xiaofang; Li, Yifan; Woodlief, Loretta Z.; Rodrigues, Rafaela C. et al. (2012): Generation of primary tumors with Flp recombinase in FRT-flanked p53 mice. In *Disease models & mechanisms* 5 (3), pp. 397–402. DOI: 10.1242/dmm.009084.

Lee, Jin Hee; Cho, Young Seok; Jung, Kyung-Ho; Park, Jin Won; Lee, Kyung-Han (2020): Genipin enhances the antitumor effect of elesclomol in A549 lung cancer cells by blocking uncoupling protein-2 and stimulating reactive oxygen species production. In *Oncology Letters* 20 (6). DOI: 10.3892/ol.2020.12237.

Li, Wei; Xu, Han; Xiao, Tengfei; Le Cong; Love, Michael I.; Zhang, Feng et al. (2014): MAGeCK enables robust identification of essential genes from genome-scale CRISPR/Cas9 knockout screens. In *Genome biology* 15 (12), p. 554. DOI: 10.1186/s13059-014-0554-4.

Liberzon, Arthur; Birger, Chet; Thorvaldsdóttir, Helga; Ghandi, Mahmoud; Mesirov, Jill P.; Tamayo, Pablo (2015): The Molecular Signatures Database (MSigDB) hallmark gene set collection. In *Cell systems* 1 (6), pp. 417–425. DOI: 10.1016/j.cels.2015.12.004.

Liberzon, Arthur; Subramanian, Aravind; Pinchback, Reid; Thorvaldsdóttir, Helga; Tamayo, Pablo; Mesirov, Jill P. (2011): Molecular signatures database (MSigDB) 3.0. In *Bioinformatics (Oxford, England)* 27 (12), pp. 1739–1740. DOI: 10.1093/bioinformatics/btr260.

Lin, Shin; Lin, Yiing; Nery, Joseph R.; Urich, Mark A.; Breschi, Alessandra; Davis, Carrie A. et al. (2014): Comparison of the transcriptional landscapes between human and mouse

tissues. In *Proceedings of the National Academy of Sciences of the United States of America* 111 (48), pp. 17224–17229. DOI: 10.1073/pnas.1413624111.

Liu, Xiehong; Wang, Li; Cai, Jiaodi; Liu, Ke; Liu, Meidong; Wang, Hao; Zhang, Huali (2019): N-acetylcysteine alleviates H2O2-induced damage via regulating the redox status of intracellular antioxidants in H9c2 cells. In *International journal of molecular medicine* 43 (1), pp. 199–208. DOI: 10.3892/ijmm.2018.3962.

LOEWE, S. (1953): The problem of synergism and antagonism of combined drugs. In *Arzneimittel-Forschung* 3 (6), pp. 285–290.

Lopez, Juanita S.; Banerji, Udai (2017): Combine and conquer: challenges for targeted therapy combinations in early phase trials. In *Nature reviews. Clinical oncology* 14 (1), pp. 57–66. DOI: 10.1038/nrclinonc.2016.96.

Lotfollahi, Mohammad; Klimovskaia Susmelj, Anna; Donno, Carlo de; Hetzel, Leon; Ji, Yuge; Ibarra, Ignacio L. et al. (2023): Predicting cellular responses to complex perturbations in high-throughput screens. In *Molecular systems biology* 19 (6), e11517. DOI: 10.15252/msb.202211517.

Lowery, Maeve A.; Jordan, Emmet J.; Basturk, Olca; Ptashkin, Ryan N.; Zehir, Ahmet; Berger, Michael F. et al. (2017): Real-Time Genomic Profiling of Pancreatic Ductal Adenocarcinoma: Potential Actionability and Correlation with Clinical Phenotype. In *Clinical cancer research : an official journal of the American Association for Cancer Research* 23 (20), pp. 6094–6100. DOI: 10.1158/1078-0432.CCR-17-0899.

Lu, Chao; Qiao, Pengyun; Sun, Yonghong; Ren, Chune; Yu, Zhenhai (2021): Positive regulation of PFKFB3 by PIM2 promotes glycolysis and paclitaxel resistance in breast cancer. In *Clinical and Translational Medicine* 11 (4). DOI: 10.1002/ctm2.400.

Maddalena, Martino; Mallel, Giuseppe; Nataraj, Nishanth Belugali; Shreberk-Shaked, Michal; Hassin, Ori; Mukherjee, Saptaparna et al. (2021): TP53 missense mutations in PDAC are associated with enhanced fibrosis and an immunosuppressive microenvironment. In *Proceedings of the National Academy of Sciences of the United States of America* 118 (23). DOI: 10.1073/pnas.2025631118.

Magnaghi, Paola; D'Alessio, Roberto; Valsasina, Barbara; Avanzi, Nilla; Rizzi, Simona; Asa, Daniela et al. (2013): Covalent and allosteric inhibitors of the ATPase VCP/p97 induce cancer cell death. In *Nature chemical biology* 9 (9), pp. 548–556. DOI: 10.1038/nchembio.1313.

Mainardi, Sara; Mulero-Sánchez, Antonio; Prahallad, Anirudh; Germano, Giovanni; Bosma, Astrid; Krimpenfort, Paul et al. (2018): SHP2 is required for growth of KRAS-mutant non-small-cell lung cancer in vivo. In *Nature medicine* 24 (7), pp. 961–967. DOI: 10.1038/s41591-018-0023-9.

Mansoury, Morva; Hamed, Maya; Karmustaji, Rashid; Al Hannan, Fatima; Safrany, Stephen T. (2021): The edge effect: A global problem. The trouble with culturing cells in 96-well plates. In *Biochemistry and biophysics reports* 26, p. 100987. DOI: 10.1016/j.bbrep.2021.100987.

Mao, L.; Merlo, A.; Bedi, G.; Shapiro, G. I.; Edwards, C. D.; Rollins, B. J.; Sidransky, D. (1995): A novel p16INK4A transcript. In *Cancer research* 55 (14), pp. 2995–2997.

Mathison, Angela; Salmonson, Ann; Missfeldt, Mckenna; Bintz, Jennifer; Williams, Monique; Kossak, Sarah et al. (2017): Combined AURKA and H3K9 Methyltransferase Targeting

Inhibits Cell Growth By Inducing Mitotic Catastrophe. In *Molecular cancer research : MCR* 15 (8), pp. 984–997. DOI: 10.1158/1541-7786.MCR-17-0063.

Mayer, M.; Noble, M. (1994): N-acetyl-L-cysteine is a pluripotent protector against cell death and enhancer of trophic factor-mediated cell survival in vitro. In *Proceedings of the National Academy of Sciences of the United States of America* 91 (16), pp. 7496–7500. DOI: 10.1073/pnas.91.16.7496.

McDermott, Ultan; Sharma, Sreenath V.; Dowell, Lori; Greninger, Patricia; Montagut, Clara; Lamb, Jennifer et al. (2007): Identification of genotype-correlated sensitivity to selective kinase inhibitors by using high-throughput tumor cell line profiling. In *Proceedings of the National Academy of Sciences of the United States of America* 104 (50), pp. 19936–19941. DOI: 10.1073/pnas.0707498104.

McGranahan, Nicholas; Swanton, Charles (2017): Clonal Heterogeneity and Tumor Evolution: Past, Present, and the Future. In *Cell* 168 (4), pp. 613–628. DOI: 10.1016/j.cell.2017.01.018.

Mees, Soeren Torge; Mardin, Wolf Arif; Wendel, Claudia; Baeumer, Nicole; Willscher, Edith; Senninger, Norbert et al. (2010): EP300--a miRNA-regulated metastasis suppressor gene in ductal adenocarcinomas of the pancreas. In *International journal of cancer* 126 (1), pp. 114–124. DOI: 10.1002/ijc.24695.

Menden, Michael P.; Wang, Dennis; Mason, Mike J.; Szalai, Bence; Bulusu, Krishna C.; Guan, Yuanfang et al. (2019): Community assessment to advance computational prediction of cancer drug combinations in a pharmacogenomic screen. In *Nature communications* 10 (1), p. 2674. DOI: 10.1038/s41467-019-09799-2.

Meyers, Robin M.; Bryan, Jordan G.; McFarland, James M.; Weir, Barbara A.; Sizemore, Ann E.; Xu, Han et al. (2017): Computational correction of copy number effect improves specificity of CRISPR-Cas9 essentiality screens in cancer cells. In *Nature genetics* 49 (12), pp. 1779–1784. DOI: 10.1038/ng.3984.

Moffitt, Richard A.; Marayati, Raoud; Flate, Elizabeth L.; Volmar, Keith E.; Loeza, S. Gabriela Herrera; Hoadley, Katherine A. et al. (2015): Virtual microdissection identifies distinct tumor- and stroma-specific subtypes of pancreatic ductal adenocarcinoma. In *Nature genetics* 47 (10), pp. 1168–1178. DOI: 10.1038/ng.3398.

Monk, Bradley J.; Kauderer, James T.; Moxley, Katherine M.; Bonebrake, Albert J.; Dewdney, Summer B.; Secord, Angeles Alvarez et al. (2018): A phase II evaluation of elesclomol sodium and weekly paclitaxel in the treatment of recurrent or persistent platinum-resistant ovarian, fallopian tube or primary peritoneal cancer: An NRG oncology/gynecologic oncology group study. In *Gynecologic oncology* 151 (3), pp. 422–427. DOI: 10.1016/j.ygyno.2018.10.001.

Mpindi, John Patrick; Yadav, Bhagwan; Östling, Päivi; Gautam, Prson; Malani, Disha; Murumägi, Astrid et al. (2016): Consistency in drug response profiling. In *Nature* 540 (7631), E5-E6. DOI: 10.1038/nature20171.

Muckenhuber, Alexander; Berger, Anne Katrin; Schlitter, Anna Melissa; Steiger, Katja; Konukiewitz, Björn; Trumpp, Andreas et al. (2018): Pancreatic Ductal Adenocarcinoma Subtyping Using the Biomarkers Hepatocyte Nuclear Factor-1A and Cytokeratin-81 Correlates with Outcome and Treatment Response. In *Clinical cancer research : an official journal of the American Association for Cancer Research* 24 (2), pp. 351–359. DOI: 10.1158/1078-0432.CCR-17-2180.

Mueller, Sebastian; Engleitner, Thomas; Maresch, Roman; Zukowska, Magdalena; Lange, Sebastian; Kaltenbacher, Thorsten et al. (2018): Evolutionary routes and KRAS dosage define pancreatic cancer phenotypes. In *Nature* 554 (7690), pp. 62–68. DOI: 10.1038/nature25459.

Nagasawa, Joji; Mizokami, Atsushi; Koshida, Kiyoshi; Yoshida, Sei; Naito, Kenichiro; Namiki, Mikio (2006): Novel HER2 selective tyrosine kinase inhibitor, TAK-165, inhibits bladder, kidney and androgen-independent prostate cancer in vitro and in vivo. In *International journal of urology : official journal of the Japanese Urological Association* 13 (5), pp. 587–592. DOI: 10.1111/j.1442-2042.2006.01342.x.

Nakhai, Hassan; Sel, Saadettin; Favor, Jack; Mendoza-Torres, Lidia; Paulsen, Friedrich; Duncker, Gernot I. W.; Schmid, Roland M. (2007): Ptf1a is essential for the differentiation of GABAergic and glycinergic amacrine cells and horizontal cells in the mouse retina. In *Development (Cambridge, England)* 134 (6), pp. 1151–1160. DOI: 10.1242/dev.02781.

Nevala-Plagemann, Christopher; Hidalgo, Manuel; Garrido-Laguna, Ignacio (2020): From state-of-the-art treatments to novel therapies for advanced-stage pancreatic cancer. In *Nature reviews. Clinical oncology* 17 (2), pp. 108–123. DOI: 10.1038/s41571-019-0281-6.

Ngamchuea, Kamonwad; Batchelor-McAuley, Christopher; Compton, Richard G. (2016): The Copper(II)-Catalyzed Oxidation of Glutathione. In *Chemistry (Weinheim an der Bergstrasse, Germany)* 22 (44), pp. 15937–15944. DOI: 10.1002/chem.201603366.

Niepel, Mario; Hafner, Marc; Chung, Mirra; Sorger, Peter K. (2017): Measuring Cancer Drug Sensitivity and Resistance in Cultured Cells. In *Current protocols in chemical biology* 9 (2), pp. 55–74. DOI: 10.1002/cpch.21.

Niepel, Mario; Hafner, Marc; Mills, Caitlin E.; Subramanian, Kartik; Williams, Elizabeth H.; Chung, Mirra et al. (2019): A Multi-center Study on the Reproducibility of Drug-Response Assays in Mammalian Cell Lines. In *Cell systems* 9 (1), 35-48.e5. DOI: 10.1016/j.cels.2019.06.005.

O'Day, Steven; Gonzalez, Rene; Lawson, David; Weber, Robert; Hutchins, Laura; Anderson, Clay et al. (2009): Phase II, randomized, controlled, double-blinded trial of weekly elesclomol plus paclitaxel versus paclitaxel alone for stage IV metastatic melanoma. In *Journal of clinical oncology : official journal of the American Society of Clinical Oncology* 27 (32), pp. 5452–5458. DOI: 10.1200/JCO.2008.17.1579.

O'Driscoll, Lorraine; Gammell, Patrick; McKiernan, Eadaoin; Ryan, Eoin; Jeppesen, Per Bendix; Rani, Sweta; Clynes, Martin (2006): Phenotypic and global gene expression profile changes between low passage and high passage MIN-6 cells. In *The Journal of endocrinology* 191 (3), pp. 665–676. DOI: 10.1677/joe.1.06894.

Olive, Kenneth P.; Tuveson, David A.; Ruhe, Zachary C.; Yin, Bob; Willis, Nicholas A.; Bronson, Roderick T. et al. (2004): Mutant p53 gain of function in two mouse models of Li-Fraumeni syndrome. In *Cell* 119 (6), pp. 847–860. DOI: 10.1016/j.cell.2004.11.004.

Orth, Michael; Metzger, Philipp; Gerum, Sabine; Mayerle, Julia; Schneider, Günter; Belka, Claus et al. (2019): Pancreatic ductal adenocarcinoma: biological hallmarks, current status, and future perspectives of combined modality treatment approaches. In *Radiation oncology (London, England)* 14 (1), p. 141. DOI: 10.1186/s13014-019-1345-6.

Palmer, Adam C.; Sorger, Peter K. (2017): Combination Cancer Therapy Can Confer Benefit via Patient-to-Patient Variability without Drug Additivity or Synergy. In *Cell* 171 (7), 1678-1691.e13. DOI: 10.1016/j.cell.2017.11.009.

Paul, Mariel C.; Schneeweis, Christian; Falcomatà, Chiara; Shan, Chuan; Rossmeisl, Daniel; Koutsouli, Stella et al. (2023): Non-canonical functions of SNAIL drive context-specific cancer progression. In *Nature communications* 14 (1), p. 1201. DOI: 10.1038/s41467-023-36505-0.

Payne, S. N.; Maher, M. E.; Tran, N. H.; van de Hey, D. R.; Foley, T. M.; Yueh, A. E. et al. (2015): PIK3CA mutations can initiate pancreatic tumorigenesis and are targetable with PI3K inhibitors. In *Oncogenesis* 4 (10), e169. DOI: 10.1038/oncsis.2015.28.

Pharmacogenomic agreement between two cancer cell line data sets (2015). In *Nature* 528 (7580), pp. 84–87.

Picco, Gabriele; Chen, Elisabeth D.; Alonso, Luz Garcia; Behan, Fiona M.; Gonçalves, Emanuel; Bignell, Graham et al. (2019): Functional linkage of gene fusions to cancer cell fitness assessed by pharmacological and CRISPR-Cas9 screening. In *Nature communications* 10 (1), p. 2198. DOI: 10.1038/s41467-019-09940-1.

Pishvaian, Michael J.; Blais, Edik M.; Brody, Jonathan R.; Lyons, Emily; DeArbeloa, Patricia; Hendifar, Andrew et al. (2020): Overall survival in patients with pancreatic cancer receiving matched therapies following molecular profiling: a retrospective analysis of the Know Your Tumor registry trial. In *The Lancet. Oncology* 21 (4), pp. 508–518. DOI: 10.1016/S1470-2045(20)30074-7.

Pozdeyev, Nikita; Yoo, Minjae; Mackie, Ryan; Schweppe, Rebecca E.; Tan, Aik Choon; Haugen, Bryan R. (2016): Integrating heterogeneous drug sensitivity data from cancer pharmacogenomic studies. In *Oncotarget* 7 (32), pp. 51619–51625. DOI: 10.18632/oncotarget.10010.

Prahallad, Anirudh; Sun, Chong; Huang, Sidong; Di Nicolantonio, Federica; Salazar, Ramon; Zecchin, Davide et al. (2012): Unresponsiveness of colon cancer to BRAF(V600E) inhibition through feedback activation of EGFR. In *Nature* 483 (7387), pp. 100–103. DOI: 10.1038/nature10868.

Puleo, Francesco; Nicolle, Rémy; Blum, Yuna; Cros, Jérôme; Marisa, Laetitia; Demetter, Pieter et al. (2018): Stratification of Pancreatic Ductal Adenocarcinomas Based on Tumor and Microenvironment Features. In *Gastroenterology* 155 (6), 1999-2013.e3. DOI: 10.1053/j.gastro.2018.08.033.

Pulliam, Daniel A.; Deepa, Sathyaseelan S.; Liu, Yuhong; Hill, Shauna; Lin, Ai-Ling; Bhattacharya, Arunabh et al. (2014): Complex IV Deficient Surf1−/− Mice Initiate Mitochondrial Stress Responses. In *The Biochemical journal* 462 (2), pp. 359–371. DOI: 10.1042/BJ20140291.

Pylayeva-Gupta, Yuliya; Grabocka, Elda; Bar-Sagi, Dafna (2011): RAS oncogenes: weaving a tumorigenic web. In *Nature reviews. Cancer* 11 (11), pp. 761–774. DOI: 10.1038/nrc3106.

Quelle, D. E.; Zindy, F.; Ashmun, R. A.; Sherr, C. J. (1995): Alternative reading frames of the INK4a tumor suppressor gene encode two unrelated proteins capable of inducing cell cycle arrest. In *Cell* 83 (6), pp. 993–1000. DOI: 10.1016/0092-8674(95)90214-7.

Rad, Roland; Cadiñanos, Juan; Rad, Lena; Varela, Ignacio; Strong, Alexander; Kriegl, Lydia et al. (2013): A genetic progression model of Braf(V600E)-induced intestinal tumorigenesis

reveals targets for therapeutic intervention. In *Cancer cell* 24 (1), pp. 15–29. DOI: 10.1016/j.ccr.2013.05.014.

Rahib, Lola; Wehner, Mackenzie R.; Matrisian, Lynn M.; Nead, Kevin T. (2021): Estimated Projection of US Cancer Incidence and Death to 2040. In *JAMA Network Open* 4 (4). DOI: 10.1001/jamanetworkopen.2021.4708.

Rees, Matthew G.; Seashore-Ludlow, Brinton; Cheah, Jaime H.; Adams, Drew J.; Price, Edmund V.; Gill, Shubhroz et al. (2016): Correlating chemical sensitivity and basal gene expression reveals mechanism of action. In *Nature chemical biology* 12 (2), pp. 109–116. DOI: 10.1038/nchembio.1986.

Reliene, Ramune; Schiestl, Robert H. (2006): Glutathione depletion by buthionine sulfoximine induces DNA deletions in mice. In *Carcinogenesis* 27 (2), pp. 240–244. DOI: 10.1093/carcin/bgi222.

Rhim, Andrew D.; Mirek, Emily T.; Aiello, Nicole M.; Maitra, Anirban; Bailey, Jennifer M.; McAllister, Florencia et al. (2012): EMT and dissemination precede pancreatic tumor formation. In *Cell* 148 (1-2), pp. 349–361. DOI: 10.1016/j.cell.2011.11.025.

Riley, Todd; Sontag, Eduardo; Chen, Patricia; Levine, Arnold (2008): Transcriptional control of human p53-regulated genes. In *Nature reviews. Molecular cell biology* 9 (5), pp. 402–412. DOI: 10.1038/nrm2395.

Román, Marta; Baraibar, Iosune; López, Inés; Nadal, Ernest; Rolfo, Christian; Vicent, Silvestre; Gil-Bazo, Ignacio (2018): KRAS oncogene in non-small cell lung cancer: clinical perspectives on the treatment of an old target. In *Molecular cancer* 17 (1), p. 33. DOI: 10.1186/s12943-018-0789-x.

Rushworth, Gordon F.; Megson, Ian L. (2014): Existing and potential therapeutic uses for N-acetylcysteine: the need for conversion to intracellular glutathione for antioxidant benefits. In *Pharmacology & therapeutics* 141 (2), pp. 150–159. DOI: 10.1016/j.pharmthera.2013.09.006.

Safikhani, Zhaleh; El-Hachem, Nehme; Quevedo, Rene; Smirnov, Petr; Goldenberg, Anna; Juul Birkbak, Nicolai et al. (2016a): Assessment of pharmacogenomic agreement. In *F1000Research* 5, p. 825. DOI: 10.12688/f1000research.8705.1.

Safikhani, Zhaleh; Smirnov, Petr; Freeman, Mark; El-Hachem, Nehme; She, Adrian; Rene, Quevedo et al. (2016b): Revisiting inconsistency in large pharmacogenomic studies. In *F1000Research* 5, p. 2333. DOI: 10.12688/f1000research.9611.3.

Samuni, Yuval; Goldstein, Sara; Dean, Olivia M.; Berk, Michael (2013): The chemistry and biological activities of N-acetylcysteine. In *Biochimica et biophysica acta* 1830 (8), pp. 4117–4129. DOI: 10.1016/j.bbagen.2013.04.016.

Schaefer, Carl F.; Anthony, Kira; Krupa, Shiva; Buchoff, Jeffrey; Day, Matthew; Hannay, Timo; Buetow, Kenneth H. (2009): PID: the Pathway Interaction Database. In *Nucleic acids research* 37 (Database issue), D674-9. DOI: 10.1093/nar/gkn653.

Schönhuber, Nina; Seidler, Barbara; Schuck, Kathleen; Veltkamp, Christian; Schachtler, Christina; Zukowska, Magdalena et al. (2014): A next-generation dual-recombinase system for time- and host-specific targeting of pancreatic cancer. In *Nature medicine* 20 (11), pp. 1340–1347. DOI: 10.1038/nm.3646.

Seashore-Ludlow, Brinton; Rees, Matthew G.; Cheah, Jaime H.; Cokol, Murat; Price, Edmund V.; Coletti, Matthew E. et al. (2015): Harnessing Connectivity in a Large-Scale

Small-Molecule Sensitivity Dataset. In *Cancer discovery* 5 (11), pp. 1210–1223. DOI: 10.1158/2159-8290.CD-15-0235.

Sebaugh, J. L. (2011): Guidelines for accurate EC50/IC50 estimation. In *Pharmaceutical statistics* 10 (2), pp. 128–134. DOI: 10.1002/pst.426.

Shackelford, David B.; Shaw, Reuben J. (2009): The LKB1-AMPK pathway: metabolism and growth control in tumor suppression. In *Nature reviews. Cancer* 9 (8), pp. 563–575. DOI: 10.1038/nrc2676.

Sharpless, Norman E. (2005): INK4a/ARF: a multifunctional tumor suppressor locus. In *Mutation research* 576 (1-2), pp. 22–38. DOI: 10.1016/j.mrfmmm.2004.08.021.

Shelledy, Lindsay; Roman, Danielle (2015): Vemurafenib: First-in-Class BRAF-Mutated Inhibitor for the Treatment of Unresectable or Metastatic Melanoma. In *Journal of the advanced practitioner in oncology* 6 (4), pp. 361–365. DOI: 10.6004/jadpro.2015.6.4.6.

Shimada, Kenichi; Reznik, Eduard; Stokes, Michael E.; Krishnamoorthy, Lakshmi; Bos, Pieter H.; Song, Yuyu et al. (2018): Copper-Binding Small Molecule Induces Oxidative Stress and Cell-Cycle Arrest in Glioblastoma-Patient-Derived Cells. In *Cell chemical biology* 25 (5), 585-594.e7. DOI: 10.1016/j.chembiol.2018.02.010.

Siegel, Rebecca L.; Miller, Kimberly D.; Fuchs, Hannah E.; Jemal, Ahmedin (2022): Cancer statistics, 2022. In *CA: a cancer journal for clinicians* 72 (1), pp. 7–33. DOI: 10.3322/caac.21708.

Sivapalan, L.; Kocher, H. M.; Ross-Adams, H.; Chelala, C. (2022): The molecular landscape of pancreatic ductal adenocarcinoma. In *Pancreatology : official journal of the International Association of Pancreatology (IAP) … [et al.]* 22 (7), pp. 925–936. DOI: 10.1016/j.pan.2022.07.010.

Smirnov, Petr; Safikhani, Zhaleh; El-Hachem, Nehme; Wang, Dong; She, Adrian; Olsen, Catharina et al. (2016): PharmacoGx: an R package for analysis of large pharmacogenomic datasets. In *Bioinformatics (Oxford, England)* 32 (8), pp. 1244–1246. DOI: 10.1093/bioinformatics/btv723.

Smolinski, Michael P.; Bu, Yahao; Clements, James; Gelman, Irwin H.; Hegab, Taher; Cutler, David L. et al. (2018): Discovery of Novel Dual Mechanism of Action Src Signaling and Tubulin Polymerization Inhibitors (KX2-391 and KX2-361). In *Journal of medicinal chemistry* 61 (11), pp. 4704–4719. DOI: 10.1021/acs.jmedchem.8b00164.

Stott, F. J.; Bates, S.; James, M. C.; McConnell, B. B.; Starborg, M.; Brookes, S. et al. (1998): The alternative product from the human CDKN2A locus, p14(ARF), participates in a regulatory feedback loop with p53 and MDM2. In *The EMBO journal* 17 (17), pp. 5001–5014. DOI: 10.1093/emboj/17.17.5001.

Subramanian, Aravind; Tamayo, Pablo; Mootha, Vamsi K.; Mukherjee, Sayan; Ebert, Benjamin L.; Gillette, Michael A. et al. (2005): Gene set enrichment analysis: a knowledge-based approach for interpreting genome-wide expression profiles. In *Proceedings of the National Academy of Sciences of the United States of America* 102 (43), pp. 15545–15550. DOI: 10.1073/pnas.0506580102.

Sun, Shi-Yong (2010): N-acetylcysteine, reactive oxygen species and beyond. In *Cancer biology & therapy* 9 (2), pp. 109–110. DOI: 10.4161/cbt.9.2.10583.

Takai, Y.; Sasaki, T.; Matozaki, T. (2001): Small GTP-binding proteins. In *Physiological reviews* 81 (1), pp. 153–208. DOI: 10.1152/physrev.2001.81.1.153.

Thiery, Jean Paul; Lim, Chwee Teck (2013): Tumor dissemination: an EMT affair. In *Cancer cell* 23 (3), pp. 272–273. DOI: 10.1016/j.ccr.2013.03.004.

Tiriac, Hervé; Belleau, Pascal; Engle, Dannielle D.; Plenker, Dennis; Deschênes, Astrid; Somerville, Tim D. D. et al. (2018): Organoid Profiling Identifies Common Responders to Chemotherapy in Pancreatic Cancer. In *Cancer discovery* 8 (9), pp. 1112–1129. DOI: 10.1158/2159-8290.CD-18-0349.

Tramacere, Irene; Scotti, Lorenza; Jenab, Mazda; Bagnardi, Vincenzo; Bellocco, Rino; Rota, Matteo et al. (2010): Alcohol drinking and pancreatic cancer risk: a meta-analysis of the dose-risk relation. In *International journal of cancer* 126 (6), pp. 1474–1486. DOI: 10.1002/ijc.24936.

Tsherniak, Aviad; Vazquez, Francisca; Montgomery, Phil G.; Weir, Barbara A.; Kryukov, Gregory; Cowley, Glenn S. et al. (2017): Defining a Cancer Dependency Map. In *Cell* 170 (3), 564-576.e16. DOI: 10.1016/j.cell.2017.06.010.

Tsvetkov, Peter; Coy, Shannon; Petrova, Boryana; Dreishpoon, Margaret; Verma, Ana; Abdusamad, Mai et al. (2022): Copper induces cell death by targeting lipoylated TCA cycle proteins. In *Science (New York, N.Y.)* 375 (6586), pp. 1254–1261. DOI: 10.1126/science.abf0529.

Tuli, Hardeep Singh; Mittal, Sonam; Loka, Mariam; Aggarwal, Vaishali; Aggarwal, Diwakar; Masurkar, Akshara et al. (2021): Deguelin targets multiple oncogenic signaling pathways to combat human malignancies. In *Pharmacological research* 166, p. 105487. DOI: 10.1016/j.phrs.2021.105487.

Turati, F.; Edefonti, V.; Bosetti, C.; Ferraroni, M.; Malvezzi, M.; Franceschi, S. et al. (2013): Family history of cancer and the risk of cancer: a network of case-control studies. In *Annals of oncology : official journal of the European Society for Medical Oncology* 24 (10), pp. 2651–2656. DOI: 10.1093/annonc/mdt280.

van der Wekken, A. J.; Saber, A.; Hiltermann, T. J. N.; Kok, K.; van den Berg, A.; Groen, H. J. M. (2016): Resistance mechanisms after tyrosine kinase inhibitors afatinib and crizotinib in non-small cell lung cancer, a review of the literature. In *Critical reviews in oncology/hematology* 100, pp. 107–116. DOI: 10.1016/j.critrevonc.2016.01.024.

Vasan, Neil; Baselga, José; Hyman, David M. (2019): A view on drug resistance in cancer. In *Nature* 575 (7782), pp. 299–309. DOI: 10.1038/s41586-019-1730-1.

Versemann, Lennart; Hessmann, Elisabeth; Ulisse, Maria (2022): Epigenetic Therapeutic Strategies to Target Molecular and Cellular Heterogeneity in Pancreatic Cancer. In *Visceral medicine* 38 (1), pp. 11–19. DOI: 10.1159/000519859.

Villanueva, Jessie; Vultur, Adina; Lee, John T.; Somasundaram, Rajasekharan; Fukunaga-Kalabis, Mizuho; Cipolla, Angela K. et al. (2010): Acquired resistance to BRAF inhibitors mediated by a RAF kinase switch in melanoma can be overcome by cotargeting MEK and IGF-1R/PI3K. In *Cancer cell* 18 (6), pp. 683–695. DOI: 10.1016/j.ccr.2010.11.023.

Wada, Makoto; Horinaka, Mano; Yamazaki, Toshikazu; Katoh, Norito; Sakai, Toshiyuki (2014): The dual RAF/MEK inhibitor CH5126766/RO5126766 may be a potential therapy for RAS-mutated tumor cells. In *PloS one* 9 (11), e113217. DOI: 10.1371/journal.pone.0113217.

Waddell, Nicola; Pajic, Marina; Patch, Ann-Marie; Chang, David K.; Kassahn, Karin S.; Bailey, Peter et al. (2015): Whole genomes redefine the mutational landscape of pancreatic cancer. In *Nature* 518 (7540), pp. 495–501. DOI: 10.1038/nature14169.

Wang, Shuai; Huang, Shuai; Sun, Yu Ling (2017): Epithelial-Mesenchymal Transition in Pancreatic Cancer: A Review. In *BioMed research international* 2017, p. 2646148. DOI: 10.1155/2017/2646148.

Wang, Yuxi; Zhang, Hang; Gigant, Benoît; Yu, Yamei; Wu, Yangping; Chen, Xiangzheng et al. (2016): Structures of a diverse set of colchicine binding site inhibitors in complex with tubulin provide a rationale for drug discovery. In *The FEBS journal* 283 (1), pp. 102–111. DOI: 10.1111/febs.13555.

Wangpaichitr, Medhi; Wu, Chunjing; You, Min; Maher, Johnathan C.; Dinh, Vy; Feun, Lynn G.; Savaraj, Niramol (2009): N',N'-Dimethyl-N',N'-bis(phenylcarbonothioyl) Propanedihydrazide (Elesclomol) Selectively Kills Cisplatin Resistant Lung Cancer Cells through Reactive Oxygen Species (ROS). In *Cancers* 1 (1), pp. 23–38. DOI: 10.3390/cancers1010023.

Warren, Allison; Chen, Yejia; Jones, Andrew; Shibue, Tsukasa; Hahn, William C.; Boehm, Jesse S. et al. (2021): Global computational alignment of tumor and cell line transcriptional profiles. In *Nature communications* 12 (1), p. 22. DOI: 10.1038/s41467-020-20294-x.

Wieman, Heather L.; Wofford, Jessica A.; Rathmell, Jeffrey C. (2007): Cytokine stimulation promotes glucose uptake via phosphatidylinositol-3 kinase/Akt regulation of Glut1 activity and trafficking. In *Molecular biology of the cell* 18 (4), pp. 1437–1446. DOI: 10.1091/mbc.e06-07-0593.

Wilson, Timothy R.; Fridlyand, Jane; Yan, Yibing; Penuel, Elicia; Burton, Luciana; Chan, Emily et al. (2012): Widespread potential for growth-factor-driven resistance to anticancer kinase inhibitors. In *Nature* 487 (7408), pp. 505–509. DOI: 10.1038/nature11249.

Witkiewicz, Agnieszka K.; McMillan, Elizabeth A.; Balaji, Uthra; Baek, GuemHee; Lin, Wan-Chi; Mansour, John et al. (2015): Whole-exome sequencing of pancreatic cancer defines genetic diversity and therapeutic targets. In *Nature communications* 6, p. 6744. DOI: 10.1038/ncomms7744.

Wood, Kevin B.; Wood, Kris C.; Nishida, Satoshi; Cluzel, Philippe (2014): Uncovering scaling laws to infer multidrug response of resistant microbes and cancer cells. In *Cell reports* 6 (6), pp. 1073–1084. DOI: 10.1016/j.celrep.2014.02.007.

Wright, Sarah Christine Elisabeth; Vasilevski, Natali; Serra, Violeta; Rodon, Jordi; Eichhorn, Pieter Johan Adam (2021): Mechanisms of Resistance to PI3K Inhibitors in Cancer: Adaptive Responses, Drug Tolerance and Cellular Plasticity. In *Cancers* 13 (7). DOI: 10.3390/cancers13071538.

Xu, Huae; Li, Xiaolin; Ding, Wenqiu; Zeng, Xiaoning; Kong, Hui; Wang, Hong; Xie, Weiping (2015): Deguelin induces the apoptosis of lung cancer cells through regulating a ROS driven Akt pathway. In *Cancer cell international* 15, p. 25. DOI: 10.1186/s12935-015-0166-4.

Yachida, Shinichi; White, Catherine M.; Naito, Yoshiki; Zhong, Yi; Brosnan, Jacqueline A.; Macgregor-Das, Anne M. et al. (2012): Clinical significance of the genetic landscape of pancreatic cancer and implications for identification of potential long-term survivors. In *Clinical cancer research : an official journal of the American Association for Cancer Research* 18 (22), pp. 6339–6347. DOI: 10.1158/1078-0432.CCR-12-1215.

Yadav, Bhagwan; Wennerberg, Krister; Aittokallio, Tero; Tang, Jing (2015): Searching for Drug Synergy in Complex Dose-Response Landscapes Using an Interaction Potency Model. In *Computational and structural biotechnology journal* 13, pp. 504–513. DOI: 10.1016/j.csbj.2015.09.001.

Yonesaka, Kimio; Zejnullahu, Kreshnik; Lindeman, Neal; Homes, Alison J.; Jackman, David M.; Zhao, Feng et al. (2008): Autocrine production of amphiregulin predicts sensitivity to both gefitinib and cetuximab in EGFR wild-type cancers. In *Clinical cancer research : an official journal of the American Association for Cancer Research* 14 (21), pp. 6963–6973. DOI: 10.1158/1078-0432.CCR-08-0957.

Yu, Channing; Mannan, Aristotle M.; Yvone, Griselda Metta; Ross, Kenneth N.; Zhang, Yan-Ling; Marton, Melissa A. et al. (2016): High-throughput identification of genotype-specific cancer vulnerabilities in mixtures of barcoded tumor cell lines. In *Nature biotechnology* 34 (4), pp. 419–423. DOI: 10.1038/nbt.3460.

Yu, Min; Bardia, Aditya; Wittner, Ben S.; Stott, Shannon L.; Smas, Malgorzata E.; Ting, David T. et al. (2013): Circulating breast tumor cells exhibit dynamic changes in epithelial and mesenchymal composition. In *Science (New York, N.Y.)* 339 (6119), pp. 580–584. DOI: 10.1126/science.1228522.

Yu, Xin; Blanden, Adam R.; Narayanan, Sumana; Jayakumar, Lalithapriya; Lubin, David; Augeri, David et al. (2014): Small molecule restoration of wildtype structure and function of mutant p53 using a novel zinc-metallochaperone based mechanism. In *Oncotarget* 5 (19), pp. 8879–8892. DOI: 10.18632/oncotarget.2432.

Yu, Xin; Vazquez, Alexei; Levine, Arnold J.; Carpizo, Darren R. (2012): Allele-specific p53 mutant reactivation. In *Cancer cell* 21 (5), pp. 614–625. DOI: 10.1016/j.ccr.2012.03.042.

Zafarullah, M.; Li, W. Q.; Sylvester, J.; Ahmad, M. (2003): Molecular mechanisms of N-acetylcysteine actions. In *Cellular and molecular life sciences : CMLS* 60 (1), pp. 6–20. DOI: 10.1007/s000180300001.

Zang, Shuya; Huang, Kexin; Li, Jiaxin; Ren, Kebai; Li, Ting; He, Xuan et al. (2022): Metabolic reprogramming by dual-targeting biomimetic nanoparticles for enhanced tumor chemo-immunotherapy. In *Acta biomaterialia* 148, pp. 181–193. DOI: 10.1016/j.actbio.2022.05.045.

Zhao, Ming; Mishra, Lopa; Deng, Chu-Xia (2018): The role of TGF-β/SMAD4 signaling in cancer. In *International journal of biological sciences* 14 (2), pp. 111–123. DOI: 10.7150/ijbs.23230.

Zheng, Peijie; Zhou, Chuntao; Lu, Liuyi; Liu, Bin; Ding, Yuemin (2022): Elesclomol: a copper ionophore targeting mitochondrial metabolism for cancer therapy. In *Journal of experimental & clinical cancer research : CR* 41 (1), p. 271. DOI: 10.1186/s13046-022-02485-0.

Zhu, Wei; Ye, Liang; Zhang, Jianzhao; Yu, Pengfei; Wang, Hongbo; Ye, Zuguang; Tian, Jingwei (2016): PFK15, a Small Molecule Inhibitor of PFKFB3, Induces Cell Cycle Arrest, Apoptosis and Inhibits Invasion in Gastric Cancer. In *PloS one* 11 (9), e0163768. DOI: 10.1371/journal.pone.0163768.

11 Publications

Peschke K*, **Jakubowsky H***, Schäfer A, Maurer C, Lange S, Orben F, Bernad R, Harder FN, Eiber M, Öllinger R, Steiger K, Schlitter M, Weichert W, Mayr U, Phillip V, Schlag C, Schmid RM, Braren RF, Kong B, Demir IE, Friess H, Rad R, Saur D, Schneider G, Reichert M. Identification of treatment-induced vulnerabilities in pancreatic cancer patients using functional model systems. EMBO Mol Med. 2022 Apr 7;14(4):e14876. doi: 10.15252/emmm.202114876 (*equal contribution)

Orben F, Lankes K, Schneeweis C, Hassan Z, **Jakubowsky H**, Krauß L, Boniolo F, Schneider C, Schäfer A, Murr J, Schlag C, Kong B, Öllinger R, Wang C, Beyer G, Mahajan UM, Xue Y, Mayerle J, Schmid RM, Kuster B, Rad R, Braun CJ, Wirth M, Reichert M, Saur D, Schneider G. Epigenetic drug screening defines a PRMT5 inhibitor-sensitive pancreatic cancer subtype. JCI Insight. 2022 May 23;7(10):e151353. doi: 10.1172/jci.insight.151353

Giansanti P, Samaras P, Bian Y, Meng C, Coluccio A, Frejno M, **Jakubowsky H**, Dobiasch S, Hazarika RR, Rechenberger J, Calzada-Wack J, Krumm J, Mueller S, Lee CY, Wimberger N, Lautenbacher L, Hassan Z, Chang YC, Falcomatà C, Bayer FP, Bärthel S, Schmidt T, Rad R, Combs SE, The M, Johannes F, Saur D, de Angelis MH, Wilhelm M, Schneider G, Kuster B. Mass spectrometry-based draft of the mouse proteome. Nat Methods. 2022 Jul;19(7):803-811. doi: 10.1038/s41592-022-01526-y

12 Acknowledgement

First, I would like to thank Prof. Dr. Dieter Saur for giving me the opportunity to work in his laboratory on this very interesting project and for his support, advice, and scientific guidance, as well as for reviewing this thesis. In addition, I would like to thank Prof. Dr. Günter Schneider for co-supervising the drug screening project and for giving me the opportunity to work on an exciting side-project, which gave me the chance to publish my first paper. I owe my gratitude to both Prof. Dr. Günter Schneider and Prof. Dr. Roland Rad for their valuable comments as part of my PhD committee.

Furthermore, I am very grateful to Dr. Andrea Coluccio for sharing his knowledge and for his help and support in the beginning of my PhD work. I would also like to thank Dr. Raquel Bernad for her contributions to the drug screening efforts and Julia Manolow for excellent technical assistance.

I would further like to thank Fabio Boniolo, Chiara Falcomatà and Christian Schneeweis for their contributions to the analysis of the drug screening data and Christian Schneeweis for his support during the experimental validation of the results. Regarding the CRISPR/Cas9-based screens, I would also like to thank Sebastian Widholz for providing materials and advice and Anantharamanan Rajamani for the primary analysis of the results.

In addition, I would like to thank the groups of Prof. Maximilian Reichert, PD Dr. Bo Kong and Prof. Elisabeth Heßmann for generating and sharing the primary human cell lines with us, and all the members of the Saur, Schneider and Rad labs for generating the mouse models and murine cell cultures as well as additional primary human cell lines, which made this study possible.

Von Herzen danken möchte ich Benedikt und meiner Familie, besonders meinen Eltern und meinem Opa, für ihre großartige Unterstützung.